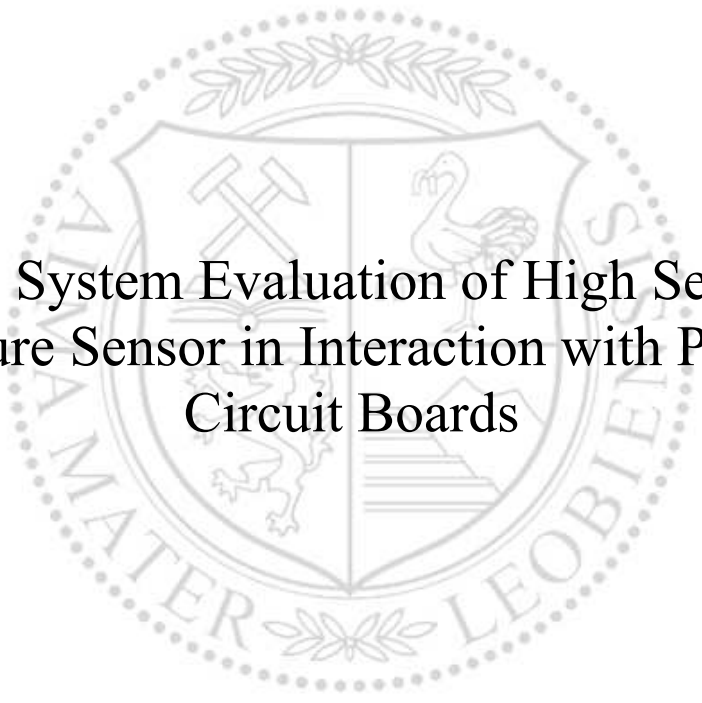




Chair of Mechanics

Doctoral Thesis



Virtual System Evaluation of High Sensitive  
Pressure Sensor in Interaction with Printed  
Circuit Boards

Mahesh Veerappa Yalagach, M.Sc.

May 2021



**AFFIDAVIT**

I declare on oath that I wrote this thesis independently, did not use other than the specified sources and aids, and did not otherwise use any unauthorized aids.

I declare that I have read, understood, and complied with the guidelines of the senate of the Montanuniversität Leoben for "Good Scientific Practice".

Furthermore, I declare that the electronic and printed version of the submitted thesis are identical, both, formally and with regard to content.

Date 31.05.2021

---

Signature Author  
Mahesh Veerappa Yalagach

# DOCTORAL THESIS

---

## VIRTUAL SYSTEM EVALUATION OF HIGH SENSITIVE PRESSURE SENSOR IN INTERACTION WITH PRINTED CIRCUIT BOARDS

---

DISSERTATION  
BY

MAHESH VEERAPPA YALAGACH, MSc



Prepared at the  
POLYMER COMPETENCE CENTER LEOBEN GMBH  
submitted to the  
MONTANUNIVERSITÄT LEOBEN  
INSTITUTE FOR MECHANICS

Leoben, May 2021

MAHESH VEERAPPA YALAGACH, MSc: *Doctoral thesis*, Virtual System Evaluation of High Sensitive Pressure Sensor in Interaction with Printed Circuit Boards, © May-June 2021

*Academic Advisor:*

Univ.-Prof. Dipl.-Ing. Dr. mont. Thomas Antretter

*Academic Mentor:*

Priv.-Doz. Dr. Frank Wiesbrock

*Supervisor:*

Dipl.-Ing. Dr. mont. Peter Filipp Fuchs, MBA

*Location:*

Leoben

*Time Frame:*

May 2017 - May 2021

*Dedicated to my wife Anusha and my family.*

*Cite this thesis as:*

Yalagach, M.V., *Virtual System Evaluation of High Sensitive Pressure Sensor in Interaction with Printed Circuit Boards*, PhD-Thesis, Montanuniversitaet Leoben, Institute of Mechanics, 2021.



# Abstract

---

This work addresses the virtual investigation of a highly sensitive capacitive pressure sensor under the influence of mechanical loads and variable environmental boundary conditions such as temperature and humidity. This type of pressure sensor realized as a micro-electromechanical system (MEMS), with its small size and potential high accuracy, are possible drivers for a variety of new applications such as indoor navigation. To ensure the high accuracies required for specific applications, the design and material selection must be optimized.

In the presented work, methods for characterizing and modeling the deformation behavior of MEMS are developed, implemented, and validated. The influence of mechanical loads, temperature, and humidity on the behavior over different system scales (assembly - PCB - sensor package - chip - membrane) is considered.

In addition to semiconductors and metallic connections, the MEMS sensors consist of a combination of different polymer composites. These composites are partly insulating materials, adhesives, or also conductive connections. Depending on their macromolecular composition or the fillers used, they exhibit pronounced temperature and humidity dependencies. To determine these dependencies, a detailed characterization of the hydro-thermo-mechanical material properties was carried out as part of the work.

The measured material data was then the basis for calibrating selected material models to describe the relevant dependencies. A particular challenge in modeling the influence of material moisture was the discontinuous change in moisture concentration across the material boundaries of the hybrid system. To account for these discontinuities, a solubility approach was chosen. Furthermore, the water activity method was implemented to describe dynamic moisture changes. Based on the material models, a combination of global and local models was implemented to describe the influence of external loads on the deformation behavior of the semiconductor's pressure membrane.

The influence of temperature, humidity, and four-point bending load on the MEMS sensors' behavior was analyzed in a further step by experimental tests. The capacitance signals of selected MEMS pressure sensors were read during defined variable loads. The measured capacitance signals confirmed the results predicted by the simulations.

The characterization and validated modeling of the MEMS sensor serve as a basis

for further possible sensor design optimization. Different design and material variants can be investigated and evaluated against each other in a time-efficient manner, thus enabling more robust and accurate sensors for new applications.



# Zusammenfassung

---

Diese Arbeit befasst sich mit der virtuellen Untersuchung eines hochempfindlichen kapazitiven Drucksensors unter dem Einfluss von mechanischen Lasten und veränderlichen Umgebungsrandbedingungen wie Temperatur und Feuchtigkeit. Diese Art von Drucksensoren, umgesetzt als Mikro-Elektromechanisches System (MEMS), sind mit ihrer geringen Größe und potentiellen hohen Genauigkeit möglicher Treiber für eine Vielzahl neuer Anwendungen wie z.B. für der innerräumliche Navigation. Um die anwendungsspezifisch geforderten hohen Genauigkeiten zu gewährleisten, müssen das Design und die Materialauswahl optimiert werden.

In der präsentierten Arbeit werden Methoden zur Charakterisierung und Modellierung des Verformungsverhaltens von MEMS entwickelt, umgesetzt und validiert. Dabei wird die Beeinflussung des Verhaltens durch mechanische Lasten, Temperatur und Feuchtigkeit über unterschiedliche Systemmaßstäbe (Baugruppe – Leiterplatte – Sensor Package – Chip – Membran) berücksichtigt.

Die MEMS-Sensoren bestehen neben Halbleitern und metallischen Anschlüssen aus einer Kombination unterschiedlicher Polymerer Verbunde. Diese Verbunde sind zum Teil isolierende Trägermaterialien, Kleber oder auch leitfähige Verbindungen. Sie zeigen je nach ihrer makromolekularen Zusammensetzung bzw. den verwendeten Füllstoffen eine ausgeprägte Temperatur- und Feuchtabhängigkeit. Um diese Abhängigkeiten zu bestimmen, wurde im Rahmen der Arbeit eine ausführliche Charakterisierung der hygro-thermo-mechanischen Materialeigenschaften durchgeführt.

Die gemessenen Materialdaten waren dann die Basis zur Kalibrierung ausgewählter Materialmodelle zur Beschreibung der relevanten Abhängigkeiten. Eine spezielle Herausforderung bei der Modellierung des Einflusses der Materialfeuchtigkeit war die abzubildende unstete Änderung der Feuchtigkeitskonzentration über die Materialgrenzen des hybriden Bauteils. Um diese Diskontinuitäten zu berücksichtigen, wurde ein Löslichkeitsansatz gewählt. Weiters wurde zur Beschreibung der dynamisch veränderlichen Feuchte die Wasseraktivitätsmethode implementiert. Basierend auf den Materialmodellen wurden eine Kombination aus globalen und lokalen Modellen umgesetzt, um schließlich im Detail den Einfluss der äußeren Lasten auf das Deformationsverhalten der im Halbleiter integrierten Druckmembran, welcher für das gemessene Sensorsignal ausschlaggebend ist, zu beschreiben.

Der Einfluss von Temperatur, Feuchtigkeit und Biegebelastung auf das Verhalten des MEMS-Sensors wurde in einem weiteren Schritt durch experimentelle Versuche analysiert. Dabei wurden die Kapazitätssignale von ausgewählten MEMS-Drucksensoren während definierten veränderlichen Lasten ausgelesen. Die gemessenen Kapazitätssignale bestätigten dabei die durch die Simulationen vorhergesagten Ergebnisse.

Die erarbeitete Charakterisierung und validierte Modellierung des MEMS Sensors dient als Basis für eine weiterführende mögliche Optimierung des Sensoraufbaus. Unterschiedliche Design- und Materialvarianten können zeiteffizient untersucht und gegeneinander evaluiert werden und ermöglichen so robustere und genauere Sensoren für neue Anwendungen.

# Research Publications

---

The development of this thesis have led to several peer reviewed conference and Journal publications.

## Articles in Refereed Conference and Journal Proceedings

- (a) M. Yalagach et al. **Influence of environmental factors like temperature and humidity on MEMS packaging materials.** In: *2018 7th Electronic System-Integration Technology Conference (ESTC)*. 2018, 1–6. DOI: [10.1109/ESTC.2018.8546484](https://doi.org/10.1109/ESTC.2018.8546484)
- (b) M. Yalagach et al. **Numerical Analysis of the Influence of Polymeric Materials on a MEMS Package Performance Under Humidity and Temperature Loads.** In: *2019 IEEE 69th Electronic Components and Technology Conference (ECTC)*. 2019, 2029–2035. DOI: [10.1109/ECTC.2019.00311](https://doi.org/10.1109/ECTC.2019.00311).
- (c) M. Yalagach et al. **Characterization and Modeling of Prepregs Applied in MEMS Sensor Packages with a Focus on Moisture Dependence.** In: *Microelectronic Devices and Technologies*. Vol. 3. Online: International Frequency Sensor Association (IFSA) Publishing, S. L., Oct. 2020, 5–10. ISBN: 978-84-09-24422-5. URL: [https://sensorsportal.com/MicDAT\\_2020/MicDAT\\_2020\\_Proceedings.pdf](https://sensorsportal.com/MicDAT_2020/MicDAT_2020_Proceedings.pdf)
- (d) M. Yalagach et al. **Numerical analysis of a MEMS sensor’s deformation behavior considering dynamic moisture conditions.** In: *2020 IEEE 22nd Electronics Packaging Technology Conference (EPTC)*. 2020, 380–385. DOI: [10.1109/EPTC50525.2020.9315091](https://doi.org/10.1109/EPTC50525.2020.9315091)
- (e) M. Yalagach et al. **Thermal and Moisture Dependent Material Characterization and Modeling of Glass Fiber Reinforced Epoxy Laminates.** *Sensors & Transducers* 248:1 (Jan. 2021), 1–9. ISSN: 2306-8515. URL: [https://www.sensorsportal.com/HTML/DIGEST/P\\_3196.htm](https://www.sensorsportal.com/HTML/DIGEST/P_3196.htm)
- (f) M. Gschwandl et al. **Modeling of manufacturing induced residual stresses of viscoelastic epoxy mold compound encapsulations.** In: *2017 IEEE 19th Electronics Packaging Technology Conference (EPTC)*. 2017, 1–8. DOI: [10.1109/EPTC.2017.8277557](https://doi.org/10.1109/EPTC.2017.8277557)

Paper (a)-(d) are from conference proceedings and paper (e) from refereed journal are included in this thesis as these publications are directly related to the research of the presented work. These publications can be also found in Appendix A. The contributions of the author to these papers are listed in Table 1. Paper (6) from conference proceedings is related to the thermo-mechanical material characterization of the Bakelite material.

**Table 1:** Contribution of the author to the appended publications in percent.

| <b>Paper</b> | <b>Organization</b> | <b>Experimental</b> | <b>FE modeling</b> | <b>Manuscript preparation</b> |
|--------------|---------------------|---------------------|--------------------|-------------------------------|
| (a)          | 80                  | 100                 | 80                 | 90                            |
| (b)          | 90                  | 100                 | 90                 | 95                            |
| (c)          | 90                  | 100                 | 100                | 85                            |
| (d)          | 85                  | 100                 | 95                 | 80                            |
| (e)          | 100                 | 100                 | 85                 | 90                            |

# Acknowledgments

---

First of all, I would like to express my sincere regards and gratitude to my supervisor Prof. Thomas Antretter and my Mentor Prof. Frank Wiesbrock who continually extended their guidance and support for this research work's successful accomplishment. Without their expertise and competence, this work would not have been possible.

I wholeheartedly thank Peter Fuchs, our divisional manager, for providing me an opportunity to pursue my doctoral research work in the Simulation and Modeling team here at PCCL. I thank him for his constant support and for helping me throughout the journey of this research work. Furthermore, I would like to thank my colleagues at PCCL who have helped me directly or indirectly achieve this work. I would also like to thank Archim Wolfberger from PCCL for introducing me to the world of sensor modules.

Many thanks to Prof. Pinter and his team members Michael Feuchter, Jürgen Grösser, Anja Gosch, and Jürgen Föttinger from Material Science and Testing of Polymers, Montan University of Leoben, for their continuous support and help during my journey towards material characterization and validation tests.

I would like to thank my company partners at Austrian microsystems ams AG and AT&S Austria Technologie & Systemtechnik Aktiengesellschaft. I would particularly like to thank Markus Weber and Anderson Singulani from ams AG for their valuable contribution to my understanding of MEMS sensor packages. Also, I would like to thank Tao Qi, Thomas Krivec, and Julia Zündel for their continuous support and insights towards the knowledge of Printed Circuit Boards (PCB).

I thank my wife, Anusha, for always being with me and continuously supporting me while completing my dissertation. Finally, I thank my parents and all of my family members for supporting me spiritually throughout writing this thesis and my life in general.

The research work of this dissertation was performed within the K-Project "Poly-Therm" at the Polymer Competence Center Leoben GmbH (PCCL, Austria) within the framework of the COMET-program of the Federal Ministry for Transport, Innovation, and Technology, and the Federal Ministry for Digital and Economic Affairs with contributions by the University of Leoben, ams AG and by AT&S Austria Technology &

Systemtechnik Aktiengesellschaft. The PCCL is Funded by the Austrian Government and the State Government of Styria.

# Contents

---

|  |             |
|--|-------------|
| <b>Abstract</b>  | <b>vii</b>  |
| <b>Zusammenfassung</b>                                   | <b>ix</b>   |
| <b>Research Publications</b>                             | <b>xi</b>   |
| <b>Acknowledgments</b>                                   | <b>xiii</b> |
| <b>Contents</b>  | <b>xv</b>   |
| <b>1 Introduction</b>                                    | <b>1</b>    |
| 1.1 Literature Research . . . . .                        | 3           |
| 1.2 MEMS Pressure Sensor . . . . .                       | 5           |
| 1.2.1 Piezoresistive MEMS Pressure Sensor . . . . .      | 5           |
| 1.2.2 Capacitive MEMS Pressure Sensor . . . . .          | 6           |
| 1.3 Aim, Objectives and Challenges . . . . .             | 6           |
| 1.4 Structure of the Thesis . . . . .                    | 8           |
| <b>2 Materials and Characterization</b>                  | <b>11</b>   |
| 2.1 Sensor Materials . . . . .                           | 11          |
| 2.2 Mechanism of Moisture Diffusion . . . . .            | 13          |
| 2.2.1 Moisture diffusion in Epoxy Resins . . . . .       | 14          |
| 2.2.2 Modeling Moisture Diffusion . . . . .              | 15          |
| 2.2.3 Factors Influencing Moisture Diffusion . . . . .   | 17          |
| 2.2.4 Effects of Moisture Diffusion . . . . .            | 18          |
| 2.3 Material Characterization and Test Methods . . . . . | 19          |
| 2.3.1 Material Sample Preparation . . . . .              | 19          |
| 2.3.2 Thermo-mechanical Characterization . . . . .       | 21          |
| 2.3.3 Moisture Dependent Characterization . . . . .      | 29          |
| 2.4 Publication Misprint . . . . .                       | 39          |
| <b>3 Numerical Modeling and Implementation</b>           | <b>41</b>   |
| 3.1 Thermal Analysis . . . . .                           | 41          |
| 3.2 Moisture Diffusion Analysis . . . . .                | 43          |
| 3.3 Verification Simulation . . . . .                    | 45          |
| 3.3.1 Simulation Procedure . . . . .                     | 45          |
| 3.3.2 Results . . . . .                                  | 47          |

|          |   |            |
|----------|---|------------|
| 3.4      | Hygro-Thermo-Mechanical Simulation . . . . .          | 49         |
| 3.4.1    | Simulation Procedure . . . . .                        | 49         |
| 3.4.2    | Global and Local Simulation Approach . . . . .        | 51         |
| 3.4.3    | Results . . . . .                                     | 53         |
| 3.5      | Advanced Hygro-Thermo-Mechanical Simulation . . . . . | 55         |
| 3.5.1    | Implementation . . . . .                              | 56         |
| 3.5.2    | Simulation Procedure . . . . .                        | 58         |
| <b>4</b> | <b>Validation Tests and Simulation</b>                | <b>61</b>  |
| 4.1      | MEMS Sensor System . . . . .                          | 61         |
| 4.2      | Test Setup and Test Conditions . . . . .              | 62         |
| 4.3      | Simulation Procedure . . . . .                        | 64         |
| 4.3.1    | Materials and Boundary Conditions . . . . .           | 64         |
| 4.4      | Results . . . . .                                     | 65         |
| 4.4.1    | Test Condition - 1 . . . . .                          | 66         |
| 4.4.2    | Test Condition - 2 . . . . .                          | 66         |
| 4.4.3    | Test Condition - 3 . . . . .                          | 69         |
| 4.5      | Additional Validation Tests . . . . .                 | 71         |
| <b>5</b> | <b>Membrane Deflection</b>                            | <b>75</b>  |
| 5.1      | Geometry . . . . .                                    | 75         |
| 5.2      | Membrane Analysis . . . . .                           | 77         |
| 5.2.1    | Membrane Center Deflection $w_0$ . . . . .            | 78         |
| 5.2.2    | Deformed Membrane Shape Function $w'(x, y)$ . . . . . | 79         |
| 5.3      | Analytical Capacitance . . . . .                      | 82         |
| 5.4      | Intrinsic Thermal behavior . . . . .                  | 84         |
| 5.4.1    | Results . . . . .                                     | 85         |
| <b>6</b> | <b>Conclusion and Outlook</b>                         | <b>93</b>  |
| 6.1      | Conclusion . . . . .                                  | 93         |
| 6.2      | Outlook . . . . .                                     | 95         |
|          | <b>Bibliography</b>                                   | <b>97</b>  |
| <b>A</b> | <b>List of Publications</b>                           | <b>109</b> |



# List of Figures

---

|      |   |    |
|------|---|----|
| 1.1  | Evolution of MEMS technology in terms of size and power [22]. . . . .   | 1  |
| 1.2  | Illustration of MEMS components [7]. . . . .  | 2  |
| 1.3  | Schematic representation of a Piezoresistive pressure sensor with Wheatstone bridge circuit [1]. <i>The image was taken with consent from avnet.com.</i>  | 6  |
| 1.4  | Size comparison of the considered capacitive pressure sensor with one Euro cent coin. . . . .   | 7  |
| 2.1  | Materials in the considered MEMS pressure sensor system. <i>The graphic was taken with consent from [121] © 2019 IEEE.</i> . . . . .  | 12 |
| 2.2  | Polymers depicting non-Fickian diffusion behavior. [24] . . . . .   | 17 |
| 2.3  | Epoxy adhesive materials prepared after curing for (a) ADH-X-01. (b) ADH-Y-01. (c) ADH-Z-02. . . . .  | 20 |
| 2.4  | Test setup for temperature dependent tensile tests. Left: Test specimens with stochastic pattern after fracture; Right: The tensile test machine along with DIC system. . . . .   | 22 |
| 2.5  | DMA curves obtained for orthotropic BT-epoxy resin (CCL-1078) as a function of frequency and temperature in comparison to tensile tests elastic modulus at different temperature (normalized to maximum modulus). <i>The graphic was taken with consent from [125] © 2018 IEEE.</i> . . . . | 23 |
| 2.6  | DMA curves obtained for isotropic insulating (ADH-X-01) and conductive adhesive (ADH-Z-02) as a function of frequency and temperature (normalized to maximum modulus). <i>The graphic was taken with consent from [125] © 2018 IEEE.</i> . . . . .  | 24 |
| 2.7  | The in-plane CTE measured for different adhesive materials. <i>The graphic was taken with consent from [121] © 2019 IEEE.</i> . . . . .   | 25 |
| 2.8  | The in-plane CTE measured for different FR4-prepregs as a function of temperature. <i>The graphic was taken with consent from [122, 123]</i> . . . .  | 26 |
| 2.9  | The thermal conductivity $\lambda(T)$ measured for different adhesive materials as a function of temperature. . . . .   | 27 |
| 2.10 | The thermal conductivity $\lambda(T)$ measured for different FR4-prepregs as a function of temperature. <i>The graphic was taken with consent from [123]</i>  | 28 |
| 2.11 | Typical moisture uptake/diffusion trend and curve fit using the analytical solutions for insulating (ADH-X-01), conductive adhesive (ADH-Z-02) and BT-epoxy resin (CCL-1078) at (a) 60 °C and (b) 90 °C. <i>The graphic was taken with consent from [125] © 2018 IEEE.</i> . . . . .        | 31 |

|      |  |    |
|------|--|----|
| 2.12 | Typical moisture uptake/diffusion trend and curve fit using the analytical solutions for FR4-prepregs at 23 °C (Immersion) <i>The graphic was taken with consent from [122, 123]</i> . . . . .                             | 32 |
| 2.13 | Typical moisture uptake/diffusion trend and curve fit using the analytical solutions for FR4-prepregs at 85 °C 85%RH. <i>The graphic was taken with consent from [122, 123]</i> . . . . .                                  | 33 |
| 2.14 | Measured change in concentration $\Delta C$ for the epoxy adhesives at 90 °C, 120 °C and 160 °C <i>The graphic was taken with consent from [121] © 2019 IEEE.</i> . . . . .  | 34 |
| 2.15 | Measured hygroscopic swelling strains $\epsilon^\beta$ for the epoxy adhesives at 90 °C, 120 °C and 160 °C <i>The graphic was taken with consent from [121] © 2019 IEEE.</i> . . . . .                                     | 35 |
| 2.16 | Linear relation between the hygroscopic swelling strains and change in moisture concentration for the conductive adhesive (ADH-Z-02) at 160 °C. <i>The graphic was taken with consent from [125] © 2018 IEEE.</i> . . . .  | 36 |
| 2.17 | The measured CME ( $\beta$ ) at different temperatures for the epoxy adhesives. . . . .  | 36 |
| 2.18 | Experimental setup for the humidity-controlled tensile test with climate chamber and a Mercury 3D DIC system. <i>The graphic was taken with consent from [122, 123] © 2021 IFSA Publishing.</i> . . . . .                  | 37 |
| 2.19 | Comparison of controlled humidity tensile tests with DMA and tensile tests in temperature oven for CCL-1078 prepreg (normalized to maximum modulus). <i>The graphic was taken with consent from [123]</i> . . . .          | 39 |
| 2.20 | Misprinted image in the publication (LHS) in page 3 and actual image of the MEMS sensor package (RHS). . . . .   | 40 |
| 2.21 | Misprinted image in the publication (LHS) in page 4 and actual image of the evaluation line in the silicon-die (RHS). . . . .  | 40 |
| 3.1  | Comparison of moisture absorption curve between experimental, analytical and simulation using verification simulation for CCL-1037. . . . .  | 48 |
| 3.2  | Comparison of moisture absorption curve between experimental, analytical and simulation using verification simulation for CCL-1037 and PP2-7628. <i>The graphic was taken with consent from [125] © 2018 IEEE.</i> . . . . | 48 |
| 3.3  | Comparison of moisture absorption curve between experimental, analytical and simulation using verification simulation for conductive adhesive, ADH-Z-02. . . . .   | 49 |
| 3.4  | Hygro-thermo-mechanical simulation modeling approach. <i>The graphic was taken with consent from [125] © 2018 IEEE.</i> . . . . .  | 50 |
| 3.5  | Evaluation line of the silicon die of the MEMS sensor. <i>The graphic was taken with consent from [121] © 2019 IEEE.</i> . . . . .   | 51 |

|      |   |    |
|------|---|----|
| 3.6  | The conventional PCB used for global simulation modeling and Pressure MEMS sensor system soldered on a PCB for local simulation modeling.   | 52 |
| 3.7  | Distribution of moisture concentration (units in %) in the MEMS sensor package. <i>The graphic was taken with consent from [125] © 2018 IEEE.</i>   | 54 |
| 3.8  | Strain levels along the evaluation line using the CASE-1 (MAT-1) and CASE-2 (MAT-2) material combinations in local modeling approach. <i>The graphic was taken with consent from [121] © 2019 IEEE.</i> | 54 |
| 3.9  | Strain levels along the evaluation line using the MAT-1 in a local (CASE-1) and to local submodeling (CASE-3) approach. <i>The graphic was taken with consent from [121] © 2019 IEEE.</i>               | 55 |
| 3.10 | Strain levels along the evaluation line using CASE-3 and CASE-4 in local submodeling approach. <i>The graphic was taken with consent from [121] © 2019 IEEE.</i>  | 56 |
| 3.11 | Hygro-thermo-mechanical simulation modeling approach. <i>The graphic was taken with consent from [124] © 2020 IEEE.</i>   | 59 |
| 4.1  | Typical capacitive pressure sensor.   | 61 |
| 4.2  | Two types of capacitive pressure sensors considered for the validation tests and simulation. <i>The graphic was taken with consent from [124] © 2020 IEEE.</i>  | 62 |
| 4.3  | Validation test setup inside the climate chamber with test board and MEMS sensors. <i>The graphic was taken with consent from [124] © 2020 IEEE.</i>  | 63 |
| 4.4  | Dynamic temperature and moisture loads considered for the validation test conditions 1 and 2 and for the advanced simulation model. <i>The graphic was taken with consent from [124] © 2020 IEEE.</i>   | 65 |
| 4.5  | Validation test results for test condition 1. <i>The graphic was taken with consent from [124] © 2020 IEEE.</i>   | 67 |
| 4.6  | Strain levels using MAT-1 and MAT-2 material combinations for MEMS sensors in CASE-1. <i>The graphic was taken with consent from [124] © 2020 IEEE.</i>   | 67 |
| 4.7  | Validation test results for test condition 2. <i>The graphic was taken with consent from [124] © 2020 IEEE.</i>   | 68 |
| 4.8  | Strain levels using MAT-1 and MAT-2 material combinations for MEMS sensors in CASE-2. <i>The graphic was taken with consent from [124] © 2020 IEEE.</i>   | 69 |
| 4.9  | Validation test results for test condition 3. <i>The graphic was taken with consent from [124] © 2020 IEEE.</i>   | 70 |
| 4.10 | Strain levels using MAT-1 and MAT-2 material combinations for MEMS sensors in CASE-3. <i>The graphic was taken with consent from [124] © 2020 IEEE.</i>   | 71 |

|      |   |    |
|------|---|----|
| 4.11 | Temperature and moisture loads considered for test condiiton 4. . . . .   | 72 |
| 4.12 | Temperature and moisture loads considered for test condiiton 5. . . . .   | 73 |
| 4.13 | Validation test results for test condiiton 4. . . . .   | 74 |
| 4.14 | Validation test results for test condiiton 5. . . . .   | 74 |
| 5.1  | Overview and design of the pressure sensitive membrane using SEM scans. . . . .   | 76 |
| 5.2  | Design consideration for the numerical modeling of silicon die. . . . .   | 76 |
| 5.3  | Schematic representation of the rectangular membrane with dimensions. . . . .   | 77 |
| 5.4  | Comparison of the membrane center deflection between the analytical equation 5.2 and numerical simulation. . . . .  | 79 |
| 5.5  | Comparison of FEA deflection profile of membrane with the existing shape functions. Figure 5.5 (a) X-direction, whereas Figure 5.5 (b) belongs to the Y-direction. . . . .              | 81 |
| 5.6  | Comparison of FEA deflection profile with the considered shape functions, plotted from center along the diagonal axis. . . . .  | 82 |
| 5.7  | Summary of the validation tests. . . . .  | 84 |
| 5.8  | Volumetric thermal expansion of the silicon-die due to intrinsic thermal behavior of the materials at 140 °C. . . . .   | 85 |
| 5.9  | The deflection of the membrane due to thermal loads from test condition-5. . . . .  | 86 |
| 5.10 | Comparsion of simulation+analytical capacitance with the capacitance readout from test condition-5. . . . .   | 87 |
| 5.11 | Comparsion of simulation+analytical capacitance with the capacitance readout from . Figure 5.11 (a) test condition-2 , whereas Figure 5.5 (b) belongs to the test condition-4 . . . . . | 88 |
| 5.12 | Comparsion of simulation+analytical capacitance with the capacitance readout from test condition-1. . . . .   | 89 |
| 5.13 | Comparsion of simulation+analytical capacitance with the capacitance readout from test condition-3. . . . .   | 90 |

# List of Tables

---

|     |   |     |
|-----|---|-----|
| 1   | Contribution of the author to the appended publications in percent. . .   | xii |
| 2.1 | Epoxy adhesives used in MEMS sensor packages. . . . .   | 20  |
| 2.2 | Thickness, dimensions of materials and conditioning environment for gravimetric humidity conditioning . . . . .   | 30  |
| 3.1 | Material properties and boundary conditions for single Fickian diffusion model. . . . .   | 45  |
| 3.2 | Material Properties and Boundary Conditions for dual Fickian diffusion model. . . . .   | 46  |
| 3.3 | Considered material combination's used in MEMS sensor package. <i>The table was taken with consent from [121] © 2019 IEEE.</i> . . . . .                    | 51  |
| 3.4 | Thermal-Moisture analogy between heat transfer and moisture diffusion (water activity) equation. . . . .  | 58  |
| 4.1 | Different temperature and dynamic humidity loads used for the validation tests. <i>The graphic was taken with consent from [124] © 2020 IEEE.</i> . . . . . | 63  |
| 4.2 | Different temperature and humidity loads considered for the additional validation tests. . . . .  | 72  |
| 5.1 | Mechanical and thermal properties of Metalloids. . . . .  | 77  |



Micro-Electro-Mechanical Systems (MEMS) are at the core of advancing human technology. A significant example is its rapid growth in using these systems in consumer products and industrial applications. The high precision sensors and transducers have also shown an increasing demand in many applications, such as the Internet of Things (IoT) applications. The small size, low cost, and exceptionally high precision have made the MEMS technology employed as actuators [52, 104], sensors [54, 100], micro-mirrors [55], and alternatives for logic gates [126]. With an increase in demand for these systems, the whole device's research on miniaturization has taken a progressive trend in recent years. Figure 1.1[22] shows the evolution of miniaturization and more power-efficient MEMS. The MEMS packages are miniaturized integrated devices that incorporate mechanical and electrical components.

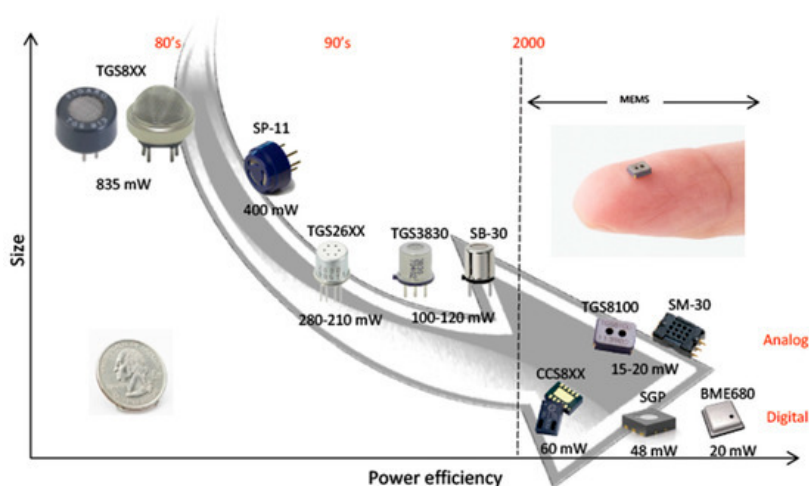


**Figure 1.1:** Evolution of MEMS technology in terms of size and power [22].

The MEMS devices can sense and control on the micro-scale, and thus effects are progressed on to the macro scale. Computer chip IC technology [43] is used in the processing of many traditional electronic packages. In comparison, sophisticated micromachining processes on the silicon-based substrate are used for the fabrication of MEMS components. In general, the micromachining process involves the addition of structural layers on the silicon substrate's surface to form an electromechanical system. As shown in Figure 1.2, MEMS comprises microsensors, micromechanical structures, microactuators, and microelectronics. All these components are embedded

and integrated on the surface of the silicon substrate.

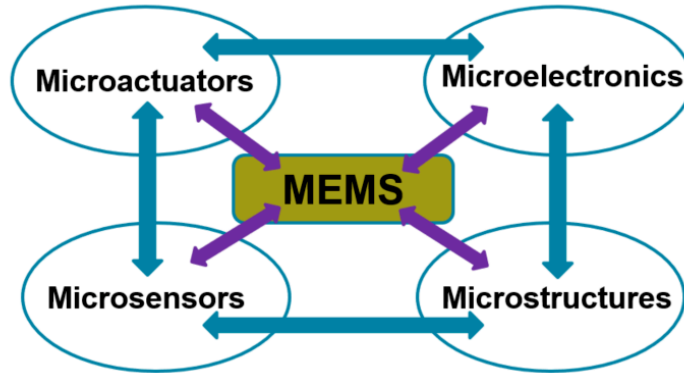


**Figure 1.2:** Illustration of MEMS components [7].

The transducer is the most widely used term in MEMS, and it helps transform signals or energy from one form to another. Consequently, the transducers incorporate a sensor and an actuator to perform this mechanism. A sensor helps in sensing the information from the surroundings and outputs as an electrical signal. In contrast, the actuator converts the output electrical signal into the required action [3]. Based on this functionality of MEMS, these devices have diversified applications across multiple markets like automotive, medical, defense, and electronics.

In the automotive sector, the use of MEMS has enhanced the safety of the passenger. Studies [14, 50] shows a steep reduction in the number of fatalities using MEMS technology in automobiles. The demand for autonomous and electric vehicles enables the development of new technologies in MEMS. The use of a high precision optical camera, Radar, and Lidar sensors' development to detect the surroundings has increased [90] in autonomous vehicles. Electric vehicles being an essential aspect in meeting climate change goals, the use of MEMS technology (for temperature and position sensing) in the core functions of charging and power inversion has taken an upward trend [12]. The use of MEMS technology in the health care sector has its advantages in diagnosis, precision surgery, and therapeutic systems [98]. The developments in BioMEMS help in the precise and early detection of different medical conditions. In the current pandemic crises of COVID-19, for virological diagnosis tests, the BioMEMS is being used [63]. Furthermore, in electronics, the use of MEMS has opened a gateway in protecting the circuits, helping in power conversion and conditioning [127]. In the defense sector, MEMS technology is utilized in aircraft control, surveillance, and munitions guidance



[47].

Increasing demand for MEMS technology in different industrial sectors persists in developing high performance, high sensitivity, low cost, and low power consumption sensor systems. To do so, a proper understanding of MEMS design aspects are necessary. For instance, different operating principles like scaling laws [66] and physics basics play a vital role in developing a MEMS device. The consideration of these laws is highly appreciated both at the macro and micro levels during the MEMS design phase. The continuous miniaturization of the MEMS sensors has led to the development of various functionalities within the sensors. These devices' miniaturization has led to critical issues like a significant increase in atomic forces, complex integration of chips, device packaging, and testing at the component level. Additionally, the critical material-dependent issues like [101]:

- Dissipation of heat is more significant than heat storage.
- Fluid and mass transport in open voids.
- Effect on mechanical properties.

The miniaturization of these devices has led to the development of new design aspects and materials. The new materials being the polymeric materials, the excellent physical and chemical properties [120] of these materials has led to its use for insulation and conduction applications in MEMS packages. However, due to miniaturization, the significant concern is the MEMS sensor's vulnerability to the ambient noise. Unfortunately, in real-world applications, these devices should operate in harsh environmental conditions like temperature and moisture. These conditions may significantly affect the MEMS sensor's response by minimizing and falsifying the MEMS sensing capacity. Therefore, it is always necessary to assess the new designs, materials, and different loading conditions on the MEMS sensors application lifetime. Hence, a virtual study is necessary, using numerical algorithms like Finite Element Modeling (FEM) to understand the material behavior and component sensitivity under different conditions. The virtual study paves the way to develop an accurate and optimal solution for the design process of the MEMS packages.

## 1.1 Literature Research

The durability and performance of polymeric materials are the primary concern due to their sensitivity to harsh environmental conditions. The use of polymeric materials exhibit challenges in the packaging of MEMS sensors. Challenges like the interaction of several polymeric materials, processing conditions, and environmental factors like operating temperature and moisture show a significant impact on the processability

and service lifetime of the MEMS packages. Long term influence from a combination of high temperature, moisture, and stress in the polymeric materials used in MEMS sensors tends to minimize their service lifetime. Only a few experimental studies are available in the literature focusing on deriving temperature and moisture effects on the MEMS sensor's response and reliability.

An experimental investigation on an electrothermally actuated cantilever beam shows a linear reduction of the natural frequency under increasing temperature and humidity [17]. Also, in the silicon beam accelerometer sensor, similar effects of a reduction in the natural frequency were seen [109]. The decrease in natural frequency is attributed to thermal and hygroscopic stresses from temperature and moisture distribution [85] in polymeric epoxy adhesives. Under high temperature and moisture conditions, the damping effects in the MEMS sensors were studied. The experimental studies show that anchor losses were observed due to damping variations at different temperature levels [58].

Studies on multi-layered MEMS show that pressure and temperature significantly impact membrane deflection [16, 94]. [49] investigated the development of thermal hygroscopic stress in multi-layered MEMS sensors due to mismatch in expansion coefficients. Furthermore, this study also explained changes in the polymeric materials' mechanical properties due to ingress of moisture and variation in temperature. The temperature and humidity effects on the MEMS response encouraged new ways of using MEMS for temperature measurements [53] and challenged many researchers to eliminate these effects when sensing other parameters [57, 87]. [80] showed the variation in the output drift of a MEMS vibratory gyroscope under sustained exposure to temperature and moisture environment.

Furthermore, [36] showed the sensitivity of a capacitive MEMS pressure sensor due to absorption of moisture in epoxy-based materials under different temperatures conditions. Additionally, this study also showed that the MEMS pressure sensor's capacitive sensitivity increased with increased temperature and moisture levels. [106] demonstrated the effects of humidity in polysilicon MEMS. This study shows that humidity can lead to very high wear and significantly affects reliability. Consequently, the temperature effects show similar behavior, i.e., poor selection of the material choice leads to lower tolerance for a higher thermal variation [111]. Also, studies [72, 102, 114] show that thermal effects are severe issues for polymeric materials in MEMS sensors. The polymeric materials' thermal expansion coefficients are more significant than metal packaging and metalloids (silicon) materials. These differences in the material properties may lead to the MEMS sensor's failure. As previously mentioned, the MEMS sensors are surface micromachined devices. Studies [102, 112] illustrates that in a humidity environment, the moisture molecules tend to ingress into small voids and

pores on the machined surface.

The effects of temperature and humidity on polymeric materials used in the MEMS sensor need to be accounted for the MEMS functionality's reliability concerns from the above literature review. Due to the growing market and strict safety regulations, the MEMS sensors' reliability assessment has challenged the manufacturers. Therefore, this research focuses on addressing the reliability issues due to environmental factors by concentrating on building a virtual environment using numerical algorithms to assess these effects.

## 1.2 MEMS Pressure Sensor

For the virtual evaluation in this thesis, the behavior of a high sensitive MEMS pressure sensor in interaction with a printed circuit board was examined. Accordingly, this section introduces the definitions of the different types of MEMS pressure sensors currently in use.

A pressure sensor is a device used for pressure measurement. The control and tracking of everyday applications are done by using these sensors. These sensors can indirectly measure different parameters like fluid/gas flow, altitude, and speed. Using MEMS technology, different types of pressure sensors can be built. A brief discussion is made on two commonly used pressure sensors, i.e., piezoresistive and capacitive pressure sensors. These MEMS sensors comprise a flexible membrane deflecting under pressure, but different methods are used to describe the membrane's displacement [118].

### 1.2.1 Piezoresistive MEMS Pressure Sensor

The first MEMS pressure sensor developed was a piezoresistive strain gauge pressure sensor. These sensors have a variety of applications in the field of medical, automobile, and household appliances. On the membrane's surface, conductive elements (piezoresistors) are micromachined [11]. A change in electrical resistance of the conductors leads to a measure of the applied pressure. Furthermore, these piezoresistors form a Wheatstone bridge network to measure the change in resistance accurately [99]. The advantages are being robust, stabilized performance, and calibration over time. The major drawback of this sensor is that it consumes more power than other types of pressure sensors. Therefore, these sensors are not suited for battery-powered systems and applications. Figure 1.3 illustrates the schematic representation of a piezoresistive pressure sensor.

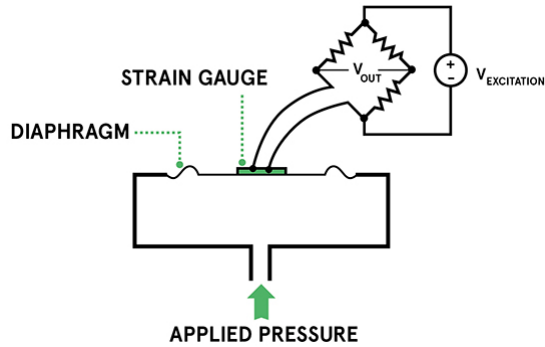


**Figure 1.3:** Schematic representation of a Piezoresistive pressure sensor with Wheatstone bridge circuit [1]. *The image was taken with consent from avnet.com.*

### 1.2.2 Capacitive MEMS Pressure Sensor

The MEMS pressure sensor studied in this research is a capacitive pressure sensor. These sensors are highly sensitive for measuring small pressure changes [6]. The application field is widespread and covers mobile devices, heating, ventilation, air conditioning (HVAC), weather stations, and the automobile industry. A capacitance pressure sensor works on the principle of capacitance between two parallel plates. On the silicon substrate's surface, two conducting layers, i.e., a top flexible pressure-sensitive conductive membrane and a fixed bottom layer, are micromachined. The change in pressure deforms the top membrane, and thus the spacing between the top and bottom layers changes yielding a capacitance. The frequency-dependent oscillator circuits, along with conversion factors, are used to measure the pressure change [61]. As Direct Current (DC) is not considered through the sensor, the capacitive pressure sensor has lower power consumption than the piezoresistive pressure sensor. The drawback of these sensors is that they are sensitive to temperature and moisture changes due to the intrinsic thermal behavior between the silicon substrate and the membrane [16]. Figure 1.4 shows the capacitive MEMS pressure sensor ( $2 \times 2 \times 0.7$  mm) considered in this research. The dimensions of the sensor vary from several millimeters to micrometers.

### 1.3 Aim, Objectives and Challenges

This thesis aims to develop a virtual modeling methodology for predicting temperature and moisture-induced deformation in the materials used in the MEMS sensor. Possible workarounds are compensation algorithms using correction factors taking into account, e.g., temperature or humidity changes. However, the exact deformation behavior of the overall system has to be known in great detail to develop these correlations with the required accuracy. Due to its excellent electrical insulation and conduction properties,

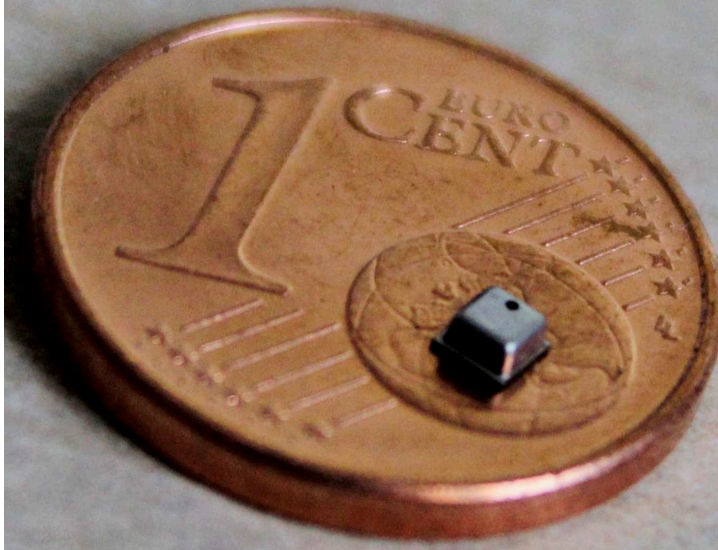


**Figure 1.4:** Size comparison of the considered capacitive pressure sensor with one Euro cent coin.

polymeric materials are the main constituents in nearly all MEMS sensors [60]. Even though these materials help the MEMS sensors from the harsh environment, the material choice for the MEMS designing plays a vital role. Certain polymeric materials tend to have complex reactions when exposed to higher temperature and moisture conditions. Therefore, to understand the material behavior and its effects on MEMS sensor performance, the following objectives were identified to achieve the research's overall scope.

- Thermo-mechanical characterization for the considered thermoset epoxy-based polymeric materials to determine the temperature-dependent mechanical properties for use in numerical algorithms.
- Moisture dependent characterization of the materials to determine the moisture-dependent diffusion and mechanical properties, which also serve as input parameters for the numerical study.
- Development and implementation of a validation mass/moisture diffusion simulation model using different moisture diffusion models for validating the experimental and analytical moisture dependent parameters.
- Development and implementation of a numerical algorithm (Hygro-Thermo-Mechanical simulation model) to account for the moisture concentration discontinuity in a multi-material MEMS sensor system.

- Development and implementation of a numerical algorithm (Advanced Hygro-Thermo-Mechanical simulation model) to consider the dynamic changes in temperature and moisture loads.
- Using the developed virtual simulation strategies to model the accurate silicon-die deformation for a considered MEMS sensor system.
- Experimental Validation tests on the complete assembly of PCB and MEMS sensors under different temperature, moisture, and mechanical loads.
- Development and implementation of a numerical algorithm (Membrane deflection) to validate the experimental validation tests.

Working on the simulation methods gives the manufacturers a competitive edge in developing new products as the prediction quality can be significantly improved. E.g., the deformation of the pressure sensor under environmental loads; consequently, its precision significantly depends on the PCB and IC substrate behavior and the respective interfaces. Thus, the knowledge of the whole system's detailed buildup will be the foundation for an excellent virtual model of the sensor behavior.

The detailed and precise modeling of a sensor's membrane deformation behavior in its structural environment under load implies some specific challenges. The main challenge will be the different dimensional scale of the interacting parts and structures, which have to be considered. A classical PCB dimension for a handheld device is in the range of some centimeters, while the membrane's critical deformation is measured in the micrometer range. Thus, the given limits in computing power and the demand for fast simulation results necessitate effective modeling strategies.

Using the developed material models, the simulations enhanced the prediction of the silicon die deformation. Based on the accomplished material model (Advanced Hygro-Thermo-Mechanical simulation model), different designs and material adaptations (e.g., lower coefficients of thermal expansion and hygroscopic swelling decreased stiffness) were evaluated. The obtained results allowed for a derivation of design guidelines and potential material adaptations, reducing the effect of environmental and mechanical bending loads on the sensor signal.

## 1.4 Structure of the Thesis

In this section, a brief description of the different chapters of the thesis is presented.

- **Chapter 2 Materials and Characterization.** This chapter provides an overview of the different types of materials used in the MEMS pressure sensor. Effects

on the thermosets or Duromers under temperature and moisture environment is briefly described. Furthermore, the moisture diffusion mechanism in epoxy adhesives and epoxy laminates and different analytical models describing moisture diffusion is explained in detail. Doing so, different thermo-mechanical and moisture dependent material characterization methods and results obtained for the considered materials are explained.

- **Chapter 3 Numerical Modeling and Implementation.** This chapter provides details of the virtual modeling strategies using finite element modeling used in this project. The chapter is divided into three main parts. Validation simulation model describing the moisture diffusion in the polymeric materials. Implementation of a hygro-thermo-mechanical simulation model using global and local sub-modeling approaches to solve the moisture concentration's discontinuity. The dynamic changes in the temperature and moisture loads using water activity method and its implementation using advanced hygro-thermo-mechanical simulation.
- **Chapter 4 Validation Tests and Simulation.** The validation tests performed on the two types of MEMS capacitive pressure sensor under different temperature, humidity, and mechanical bending loads has been described in this chapter. A short description of the test procedure and methodology to read the capacitance signals are briefly explained. The use of advanced simulation strategy from chapter 2 is used to describe the validation test results. The details on developed hygrothermal strains due to temperature and moisture distribution and membrane deformation through mechanical bending of the global model are provided.
- **Chapter 5 Membrane Deflection.** The deflection of the rectangular membrane under uniform pressure using different analytical methods is discussed. Furthermore, the equations describing the analytical capacitance using the membrane deformation from the simulation are briefly described. Also, the idea of temperature sensitivity describing the silicon-die and membrane's intrinsic thermal behavior is presented. Additionally, the obtained analytical capacitance from the analytical equation and simulation are compared against the results from validation tests.
- **Chapter 6 Conclusion and Future Work.** The conclusion of the research, along with proposals for future work, are presented in this chapter.





# 2

## Materials and Characterization

---

In this chapter, a brief discussion on the type of materials used in the MEMS sensor system and PCB is illustrated briefly. Additionally, the phenomenon of moisture diffusion and its effects on polymeric materials is described in detail. To this end, different thermo-mechanical and moisture dependent material characterization and the results obtained have been discussed. These characterized material properties serve as material input parameters for the virtual simulation strategies. Based on the virtual simulation models, accurate lifetime prediction on the material behavior defined in the MEMS sensor system can be estimated.

### 2.1 Sensor Materials

To evaluate the reliability and lifetimes prediction accurately, the numerical simulation approaches have to be considered. For these approaches, the material behavior and its properties play a vital role. The MEMS sensor materials are an assembly of both polymeric and non-polymeric materials [125]. The sensor system includes polymeric materials like conductive adhesives, insulating adhesives, FR4-prepregs and, solder masks. The substrate used in the MEMS system is an assembly of solder masks, FR4-prepregs, and copper layers. The conductive adhesive clamps the metal-lid onto the substrate. In contrast, the insulating adhesive is used as an insulation material to attach the silicon-die onto the substrate. The material used for MEMS sensing technology is predominantly silicon. The silicon-die material, a metalloid (non-polymeric material), acts as a semiconductor. The total build-up of a capacitive MEMS pressure sensor is depicted in Figure 2.1.

Polymeric materials have their advantages and disadvantages depending on the type of polymer used. The electrical insulation property, high specific strength, protection from the environment, and low cost are essential uses of using polymeric materials in the MEMS sensors. However, the lower thermal conductivity and stability restrict the polymers to their use where good heat dissipation and low thermal expansion are needed. Based on the temperature applications, the polymeric materials can be classified as thermoplastics and thermosets. Thermoplastics exist in the amorphous or semi-crystalline phase upon heating above  $T_g$ , it deforms and loses its structure. The loss in structure can be regained by merely cooling, or heating [92, 93]. In contrast, the thermosets are duromers, which are highly cross-linked polymers and have lower

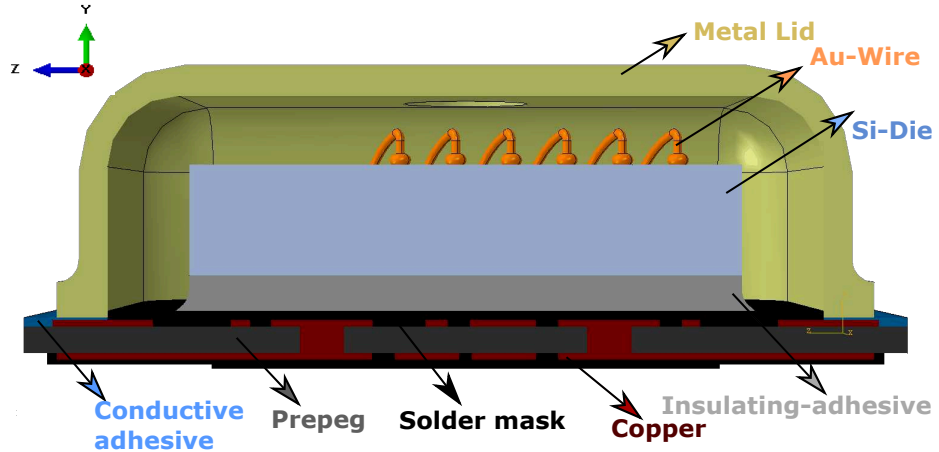


**Figure 2.1:** Materials in the considered MEMS pressure sensor system. *The graphic was taken with consent from [121] © 2019 IEEE.*

susceptibility than thermoplastics. The curing chemical process is utilized to process the thermosetting polymers. Therefore, thermosets strengthen when heated; after initial deformation or change, these polymers cannot be remolded by heating or cooling. Thermosets does not lose their structural integrity at high temperature. As a result of this behavior, the thermoplastics cannot withstand higher temperature compared with thermosets.

The polymeric materials used in the MEMS sensor system are thermosets. Thermoset polymers are commonly used in microelectronics and MEMS sensor packages as adhesives and insulation layers. Introduction fillers can enhance the thermal properties of the thermosets. The fillers improve the technological effectiveness and thermal properties by controlling the shrinkage (curing) during the production [91]. Depending on the applications, the fillers used in the thermosets can be generalized into two parts as thermoset or epoxy adhesives and molding compounds.

Epoxy adhesives are polymers that are used as adhesives. These adhesives are usually available in an uncured stage. The hardening of the adhesives can be accompanied by a curing process in the presence of temperature and light. These adhesives have higher tensile strength, gap-filling capacity, and excellent resistance to heat and moisture. The insulating adhesive used in the MEMS sensor is one-part silicone rubber, acting as an insulation material. This adhesive has unique characteristics like lower Young's modulus, low-stress, rapid heat curing, and an excellent primerless adhesive to substrates. The insulating adhesives serve as excellent insulation in MEMS systems, but conductive adhesives have been developed for die-attach application to ensure lower

a priori ionics. The conductive adhesive is made up of one component, silver-filled epoxy adhesive. The silver powder in the epoxy adhesive is in the range of 70 - 80 %. The conductive adhesives offer excellent bond strength and thermal stability by using them in die attach and bonding components in electronic devices [28]. Furthermore, the solder mask material acts as an insulator for the copper layers and the interfaces between them in the substrate or Printed Circuit Boards (PCB) and avoids short circuits. The solder mask mechanically couples the silicon die and the substrate.

The molding compounds are mixtures of thermosetting resin (e.g., epoxy or acryl resin) with fillers and hardeners (granular). The granular type of molding compounds is used as encapsulating materials in microelectronics [59]. Additional to the granular molding compounds, sheet molding compounds like FR4-prepregs are used in substrate and PCB build-up. Prepregs are a composite material made by pre-impregnated fibers (glass) in a partially cured thermosetting polymer like epoxy resin. FR4-prepregs act as an insulation layer between the copper layers and core in substrates or PCB.

The epoxy resin material (insulating, conductive adhesive, and solder masks) and FR4-prepregs have different mechanical behavior and properties. For the epoxy resins, the fillers are considered to be distributed homogeneously, thus considered as isotropic material behavior, while for FR4-prepregs, due to fiber reinforcement (glass both), this composite material exhibits orthotropic material behavior.

Within the scope of this thesis, the focus is mainly on investigating the moisture dependence of the thermosetting polymeric materials used in MEMS sensor packages. Within the same research program, comprehensive studies were performed to study the thermal behavior on microelectronic components, see [45]. The thermal properties needed as input parameters for numerical modeling are determined by extensive thermo-mechanical characterization as explained in the section 2.3.2 in this chapter.

## 2.2 Mechanism of Moisture Diffusion

To design and manufacture the best MEMS sensor packages, comprehensive studies are necessary to understand the behavior of sensor materials and interfaces exposed to harsh environmental conditions. The absorption of moisture in thermosetting polymers (epoxy resins) is a major reliability concern in MEMS sensor packages. The long term diffusion of moisture molecules in these materials may cause failure during storage, production, and operation [10, 119]. The moisture absorption also leads to the loss of mechanical strength in the polymeric materials. Studies have also shown that moisture intake can be just as damaging as thermal or temperature changes in many polymeric materials [103]. This section presents the mechanisms and effects of moisture diffusion on epoxy resin-based materials.

### 2.2.1 Moisture diffusion in Epoxy Resins

The epoxy resin-based materials are made up of hydroxyl (OH) groups. The absorption of moisture is carried out due to hydrogen bonds forming between the hydroxyl groups and water molecules [64, 78]. The ingress of moisture in the epoxy materials is due to the diffusion process. Diffusion is a concentration gradient-based transport phenomenon of molecules from a region of high concentration to a low concentration until the state of equilibrium is reached.

According to [64], an epoxy resin material features a free volume and an occupied volume. The presence of free volume in polymeric materials is mainly due to the gap between the polymer chains. The higher available free volume, higher the diffusion of moisture in the material. Additionally, the presence of free volume creates a transit for higher diffusion of moisture molecules. Furthermore, many studies [4, 68] have shown that two stages of moisture uptake can be predicted in polymers, i.e., unbounded and bounded stage. The unbounded stage refers to the percentage of moisture molecules that fill the material's cavities and voids. Consequently, hydrogen bonds forming due to the interaction between the polymer chains and water molecules is bounded stage. A volumetric material expansion is observed due to the absorption of water molecules. The volumetric expansion is known to be hygroscopic swelling and is mainly attributed to hydrogen bond formation. The hygroscopic swelling is not observed during the initial moisture diffusion in the free volume of the polymer. Swelling in polymers is seen when most of the free volume is filled with water molecules by altering the polymer chains by increasing the inter-segmental hydrogen bond length [9]. Furthermore, swelling behavior due to moisture uptake is also referred to as plasticization, and it can alter the chemical structure in an epoxy [115]

The absorption of moisture in MEMS sensor packages is mainly attributed to diffusion through the epoxy resin-based materials or via the interface between the materials. [27] describes diffusion as "*the process by which matter is transported from one part of a system to another as a result of random molecular motions.*". Consequently, the heat transfer can also be described in the same representation. Therefore, both moisture diffusion and heat transfer phenomena are analogous to each other. Adolph Eugen Fick described the initial advancement by the analogy between the heat transfer and moisture diffusion in 1855 and published the equations related to this analogy [40]. This equation is now referred to as Fick's first and second law of diffusion.

### 2.2.2 Modeling Moisture Diffusion

The overall moisture diffusion is described using Fick's first law (equation 2.1). Fick's first law is compared to the heat conduction equation described by using Fourier's law (equation 2.2).

$$\mathbf{J} = -D \nabla C \quad (2.1)$$

$$\mathbf{F} = -\mathbf{k} \nabla T \quad (2.2)$$

In equation 2.1,  $\mathbf{J}$  is the diffusion flux,  $C$  is the moisture concentration, and  $D$  is moisture diffusion coefficient, which is typically a constant at a given temperature. As the diffusion occurs in the opposite direction to increasing concentration, therefore, the equation 2.1 has a negative sign. Fick's second law (equation 2.3) is obtained by considering the conservation of mass to the system.

$$\frac{\partial C}{\partial t} = -\nabla \cdot \mathbf{J} \quad (2.3)$$

If the diffusion is considered to be uniform or for isotropic materials, equation 2.3 can be written as equation 2.4.

$$\frac{\partial C}{\partial t} = D \left( \frac{\partial^2 C}{\partial x^2} + \frac{\partial^2 C}{\partial y^2} + \frac{\partial^2 C}{\partial z^2} \right) \quad (2.4)$$

#### Fickian Diffusion or Single Fickian Diffusion Model

Consider an infinitely thin plate (one-dimensional diffusion process) with thickness  $2l$ . It is assumed that surfaces are exposed to constant moisture concentration, under appropriate boundary conditions, the spatial moisture concentration  $C_t$  at time  $t$  is given by equation 2.5 [95].

$$C_t = \left[ 1 - \frac{4}{\pi} \sum_{n=0}^{\infty} \frac{-1}{2n+1} \exp\left(\frac{-D(2n+1)^2 \pi^2 t}{4l^2}\right) \times \cos\left(\frac{(2n+1)\pi x}{2l}\right) \right] \times C_{\infty} \quad (2.5)$$

where  $C_{\infty}$  is the saturated or equilibrium moisture concentration and  $D$  is the Fickian diffusion coefficient. As the moisture concentration  $C_t$  cannot be measured experimentally, the equation 2.5 is integrated over the thickness  $2l$  of the thin plate, and mass uptake as a function of time is computed. This mass uptake process is generally described by the Fickian diffusion or single Fickian diffusion model given by equation 2.6. Most of the polymeric materials (epoxy) follow a single Fickian diffusion model above glass  $T_g$  of a polymer. Above  $T_g$ , the polymeric materials are in a soft state. Therefore, diffusion of water molecules becomes easier [95].

$$M_t = \left( 1 - \frac{8}{\pi^2} \sum_{n=0}^{\infty} \frac{1}{(2n+1)^2} \exp \frac{-D(2n+1)^2 \pi^2 t}{4l^2} \right) \times M_{\infty} \quad (2.6)$$

where  $M_t$  is the overall mass uptake at time  $t$  and  $M_{\infty}$  is the saturated mass uptake or the maximum moisture absorbed by the volume at equilibrium. The important parameters that describe the polymeric materials' diffusion process are the Fickian diffusion coefficient  $D$  and saturated mass uptake  $M_{\infty}$ . Together, these parameters describe the absorption capacity, and rate of diffusion [38]. The  $D$  and  $M_{\infty}$  can be determined by considering experimental moisture conditioning curves (described in detail in section 2.3.3). The initial value for  $D$  is computed by using using equation 2.7 [34].

$$D = \pi \left( \frac{l}{4M_{\infty}} \right)^2 \left( \frac{M_2 - M_1}{\sqrt{t_2} - \sqrt{t_1}} \right)^2 \quad (2.7)$$

where  $M_1$ ,  $M_2$ ,  $\sqrt{t_1}$  and  $\sqrt{t_2}$  is the slope of a moisture absorption plot obtained from experiments.

### Non-Fickian Moisture Diffusion or Dual Fickian Diffusion Model

The single Fickian Diffusion model is valid only above  $T_g$  of the polymer. However, the thermosetting epoxy-based polymers show a non-Fickian diffusion below  $T_g$ . Figure 2.2 shows the schematic curves of polymers depicting a non-Fickian moisture absorption trend. The solid line "LF describes the Fickian diffusion model." It is observed that in epoxy-based polymers, after the initial diffusion state, the diffusion rate changes, and this rate change is described by the non-Fickian diffusion. The traditional method to describe the non-Fickian diffusion is by considering two stages Fickian diffusion (Single Fickian diffusion). This features either two sequential or two parallel single Fickian diffusion models. In the two parallel single Fickian model, the concentration  $C_t$  at any point in the polymer at time  $t$  is given by equation 2.8.

$$C_t = \left[ 1 - \frac{4}{\pi} \sum_{n=0}^{\infty} \frac{-1}{2n+1} \exp \left( \frac{-D_1(2n+1)^2 \pi^2 t}{4l^2} \right) \times \cos \left( \frac{(2n+1)\pi x}{2l} \right) \right] \times C_{1\infty} + \left[ 1 - \frac{4}{\pi} \sum_{n=0}^{\infty} \frac{-1}{2n+1} \exp \left( \frac{-D_2(2n+1)^2 \pi^2 t}{4l^2} \right) \times \cos \left( \frac{(2n+1)\pi x}{2l} \right) \right] \times C_{2\infty} \quad (2.8)$$

where  $C_{1\infty}$  and  $C_{2\infty}$  are the portions of saturated concentrations  $C_{\infty}$ .  $D_1$  and  $D_2$  are the moisture diffusion coefficients. The two parallel single Fickian diffusion model is often referred to as dual Fickian diffusion model. The mass uptake  $M_t$  for dual Fickian diffusion model at time  $t$  is given by equation 2.9.

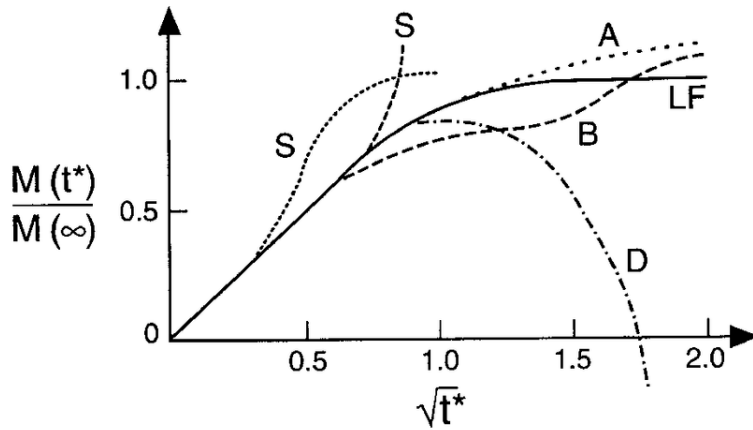


Figure 2.2: Polymers depicting non-Fickian diffusion behavior. [24]

$$M_t = \left(1 - \frac{8}{\pi^2} \sum_{n=0}^{\infty} \frac{1}{(2n+1)^2} \exp \frac{-D_1(2n+1)^2 \pi^2 t}{4l^2}\right) \times M_{1\infty} + \left(1 - \frac{8}{\pi^2} \sum_{n=0}^{\infty} \frac{1}{(2n+1)^2} \exp \frac{-D_2(2n+1)^2 \pi^2 t}{4l^2}\right) \times M_{2\infty} \quad (2.9)$$

where  $M_{1\infty}$  and  $M_{2\infty}$  are the saturated mass uptake and the sum of  $M_{1\infty}$  and  $M_{2\infty}$  is the total saturated mass uptake  $M_{\infty}$ .

### 2.2.3 Factors Influencing Moisture Diffusion

Factors like additives, Relative Humidity  $RH$ , and conditioning temperature influences the changes in moisture diffusion coefficient  $D$  and saturation mass uptake  $M_{\infty}$  during moisture diffusion in polymeric materials. The amount of fillers and additives in epoxy resin-based adhesives affects the saturated moisture concentration. An increase in saturated mass uptake was observed in epoxy-based adhesives with increase fillers (hardners) [32]. The increase in  $M_{\infty}$  is mainly attributed to more hydroxyl groups from the hardners in the epoxy resin matrix.

The increase in relative humidity ( $RH$ ) also increases both  $D$  and  $M_{\infty}$  in many polymers [32, 116]. Many polymers use Henry's law (equation 2.10) to describe the increase in saturated moisture concentration with an increase in relative humidity [76].

$$M_{\infty} = S \times P_{sat} \times RH \quad (2.10)$$

where  $S$  is solubility,  $P_{sat}$  saturated vapor pressure, and  $RH$  is Relative Humidity. The solubility and saturated vapor pressure are expressed as a function of temperature using the Arrhenius relationship [56].

Since the moisture diffusion is activated by temperature, both  $D$  and  $M_{\infty}$  increases with an increase in temperature. The increase in conditioning temperature is used to describe the moisture diffusion process under laboratory conditions, where the material samples are subjected to high humidity and temperature conditioning. Additionally, temperature indirectly increases the aging of the polymers. The dependency of conditioning temperature was studied for different thermosetting polymers under different environmental conditions [38, 56]. Epoxy-based solder mask materials of varying thickness were conditioned in the water at 25, 55, and 85 °C. The diffusion coefficient  $D$  was increased from  $6.2 \times 10^{-6} \text{ mm}^2 \text{ s}^{-1}$  to  $2.5 \times 10^{-5} \text{ mm}^2 \text{ s}^{-1}$  with an increase in the conditioning temperatures from 25 °C to 85 °C. The diffusion coefficient  $D$  is made a function of temperature by considering the Arrhenius relationship [65, 110] given by equation 2.11.

$$D(T) = D_0 \exp\left(-\frac{E}{RT}\right) \quad (2.11)$$

where  $E$  is the diffusion activation energy,  $R$  is the universal gas constant, and  $T$  is temperature. Furthermore, from [56] showed that saturated moisture concentration is also increased from 0.7 to 1.1 % with an increase in temperature. The increase in saturation concentration with an increase in conditioning temperature is mainly attributed to the rapid increase in the mobility of the molecular chains causing thermal expansion due to temperature influence. The thermal expansion introduces free volume thereby increasing the saturated concentration [29].

#### 2.2.4 Effects of Moisture Diffusion

Harsh environmental factors like temperature and moisture may modify the polymeric structure. The changes attributed to thermal expansion and hygroscopic swelling may increase the free volume in the materials. Due to expansion and swelling, the induced stresses causes deformation [103], potential delamination [41], and micro-cracks [8] in the materials.

Many studies [18, 19, 20] have shown that the absorption of moisture in epoxy-based adhesives (insulating and conductive adhesive) deteriorates the adhesion properties and affects the durability of the adhesive joints. Additional to the polymeric structure, the mechanical properties are also affected due to moisture absorption in polymers.



The yield stress and Young's modulus ( $E$  - Elastic modulus) of the prepregs used in MEMS sensor systems decrease with an increase in the moisture uptake [5, 51].

Apart from degradation to the mechanical properties, moisture absorption also affects the glass transition temperature  $T_g$  of the polymeric materials. Studies [5] show that increase in the moisture level in epoxy composite decreases the  $T_g$ . [116] showed that  $T_g$  of the polymer decreases up to 20 °C for an increase in moisture content of 1 %. The plasticizing effect of moisture drives the molecular conformation and lowers the  $T_g$  of the polymer [113].

In the next sections, the different characterization, testing methods, and the results obtained to describe the thermo-mechanical and moisture dependent parameters are described.

## 2.3 Material Characterization and Test Methods

The methods, equipment, and test procedures used for the material characterization during the experimental regime of this research work are described in this section. The material properties for the polymeric materials used were not available in the literature, and these data are required for use in the development of virtual simulation strategies to account for temperature and moisture dependence. The experimental regime was divided into three main parts. The first part involves material sample preparation for epoxy-based adhesives via temperature curing. The second part describes the different thermal analyses like thermal conductivity measurements and thermo-mechanical characterization like temperature-dependent tensile tests, Dynamic Mechanical Analysis (DMA), and measurement of the Coefficient of Thermal Expansion (CTE). Lastly, the third part presents the moisture dependent material characterization methods like moisture conditioning, measurement of the Coefficient of Moisture Expansion (CME), and moisture dependent Young's moduli.

### 2.3.1 Material Sample Preparation

Epoxy-based adhesive samples (insulating and conductive adhesives) were prepared to determine the thermo-mechanical and moisture dependent properties. The epoxy adhesives were stored at -20 °C and thawed to room temperature for further processing. The different adhesives used in the MEMS sensor system and their nomenclature, curing temperature, and time are shown in table 2.1.

To prepare the adhesive material samples, a PTFE rectangular mould for flat embedding with dimensions of 30 × 4 × 1 mm was used. The epoxy adhesives were filled into these molds and were pressed using a stainless steel roller to ensure that the formation of voids (air gaps) is minimal. During the samples' preparation, the major challenge

**Table 2.1:** Epoxy adhesives used in MEMS sensor packages.

| Adhesive   | Nomenclature | Curing Temperature, T °C | Curing Time, t min |
|------------|--------------|--------------------------|--------------------|
| Insulating | ADH-X-01     | 150                      | 45                 |
|            | ADH-Y-01     | 150                      | 60                 |
| Conductive | ADH-Z-02     | 175                      | 60                 |

was to keep the formation of air gaps to a minimum. To ensure this, the adhesive filled molds were kept in a desiccator for 40 min and air inside the desiccator was pumped out. Depending on the type of material used, curing temperature and time was defined, and adhesive filled molds were kept inside a temperature oven for curing.

The cured samples obtained for different adhesive materials are depicted in Figure 2.3. Figure 2.3 (a), the formation of air bubbles or voids can be seen for ADH-X-01. Both ADH-X-01 and ADH-Y-01 are one-part silicone rubber adhesive while, ADH-Z-02 is a one-component silver-filled epoxy adhesive. The prepared material samples were further used for different characterization methods (Thermo-mechanical and Moisture conditioning).

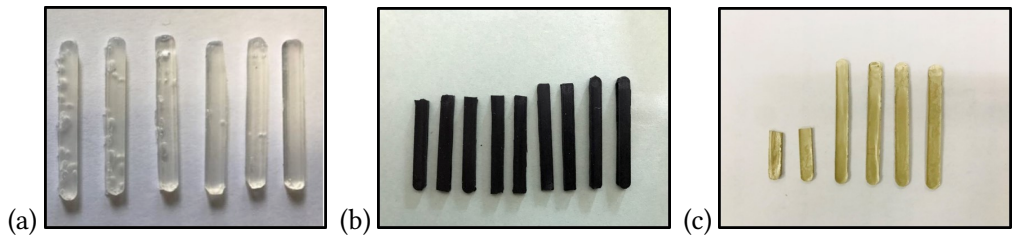


**Figure 2.3:** Epoxy adhesive materials prepared after curing for (a) ADH-X-01. (b) ADH-Y-01. (c) ADH-Z-02.

Furthermore, the FR4-prepregs were received in the form of thin sheets from the material suppliers. Five different prepregs, CCL-1037, CCL-1078, PP1-1037, PP2-7628 and PP3-1037 were considered for the characterization. The considered prepregs vary in their matrix material (epoxy resin), fabric reinforcement type, and thickness. The thickness varied from 60 μm to 1.5 mm. Different test specimens were cut from the thin sheets of the prepregs. The cut specimens were subjected to thermo-mechanical and moisture dependent characterization. The numbers 1037, 1078, and 7628 represents the fabric reinforcement (glass cloth) used in the prepregs. As discussed earlier, due to the prepregs’ composite nature, they show an orthotropic material behavior. The degree of the orthotropic nature of the prepregs is defined by the type of glass cloth used. The glass cloth is woven fibers with fibers aligned along warp (0°) and fill or

weft (90°) directions. The following research work [42, 82, 97] explains in detail the orthotropic behavior of the FR4-prepregs.

### 2.3.2 Thermo-mechanical Characterization

In this section, the measurement of different temperature-dependent material properties obtained by thermo-mechanical characterization techniques for the considered polymeric materials is explained briefly.

#### Temperature dependent Tensile Tests

The standard and most important test method to determine the thermo-mechanical properties is the temperature-dependent tensile tests. The temperature-dependent Young's modulus, Poisson's ratio, and tensile strength are measured from this test. The temperature-dependent tensile test was performed using Zwick Z010 (Zwick Roell AG, Ulm, Germany) machine under defined 23, 100, 180 and 250 °C temperatures. The test specimens and test process were standardized according to ISO-527 : 2019 [84]. The strain data are acquired by combining the Digital Image Correlation (DIC) system (Aramis, GOM GmbH, Braunschweig, Germany) with the tensile testing machine. The DIC system uses optical photogrammetry principles to obtain the surface strain measurements. This system combines the strain gauge and micro-extensometer functionality into a robust non-contact measurement system. Figure 2.4 shows the temperature-dependent tensile test setup with the DIC system.

#### Dynamic Mechanical Analysis (DMA)

Additional to the tensile tests, Dynamic Mechanical Analysis was performed for the materials. The DMA measurements depict the nature of viscoelastic material behavior by measuring the complex modulus and compliance as a function of temperature, time, and frequency [86]. Most epoxy resins show a viscoelastic behavior; due to this, a phase shift [45] between material response and the applied displacement is observed. The storage modulus  $E'$ , loss modulus  $E''$ , and the loss factor  $\tan \delta$  can be determined using this measurement technique. The stress stored in the material sample as mechanical energy is termed as storage modulus  $E'$ . The stress dissipated as heat is loss modulus  $E''$  and  $\tan \delta$  is a measure of phase lag between the stress and strain.  $\tan \delta$  is a measure of damping and energy dissipation. With the help of DMA measurements, the change in modulus of the material below and above the glass transition temperature  $T_g$  can be determined. The following test conditions and parameters were considered during the measurement:

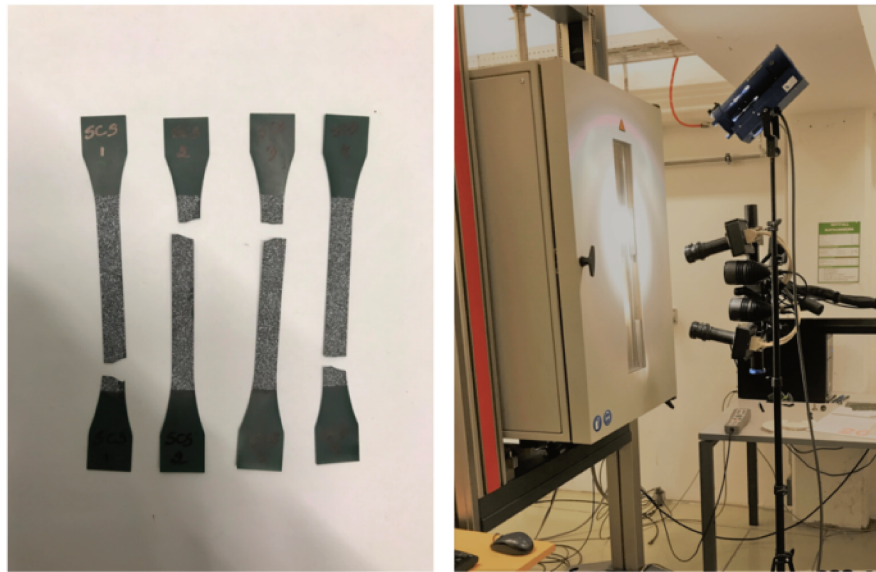


**Figure 2.4:** Test setup for temperature dependent tensile tests. Left: Test specimens with stochastic pattern after fracture; Right: The tensile test machine along with DIC system.

Yalagach et al., ESTC 2018 [125] © 2011 IEEE: Section: Experimental

The DMA measurements were performed using Mettler Toledo DMA/SDTA861 (Mettler-Toledo, Columbus, Ohio, USA) in a tensile mode under a constant displacement excitation. These materials were tested at defined frequencies of 0.1, 1, 10, 100 Hz and over a temperature range of  $-100\text{ }^{\circ}\text{C}$  to  $320\text{ }^{\circ}\text{C}$  with heating rate of 2 K min.

The material samples of dimensions  $20 \times 4 \times 1$  mm were considered for the measurements. Depending on the type of excitation mode, the specimen dimensions also vary [69]. The Young's moduli ( $E$ ) results from the temperature-dependent tensile tests are compared against modulus results from the DMA for prepreg CCL-1078 and are depicted in Figure 2.5:

Yalagach et al., ESTC 2018 [125] © 2011 IEEE: Section: Results and Discussion

The results from the DMA and the tensile test results show the temperature dependent modulus for the individual materials. Figure 2.5 depicts the results for BT – epoxy resin for tensile tests (elevated temperatures) and DMA. The plot shows that the elastic modulus obtained from DMA and tensile tests are in good agreement over a wide temperature range. Small discrepancies may be attributed to the higher fixture compliance in the DMA device. Additionally, Figure 2.5 also shows the DMA results obtained for 45° specimens. The obtained values emphasize the expected anisotropic behavior of the reinforced epoxy resin.

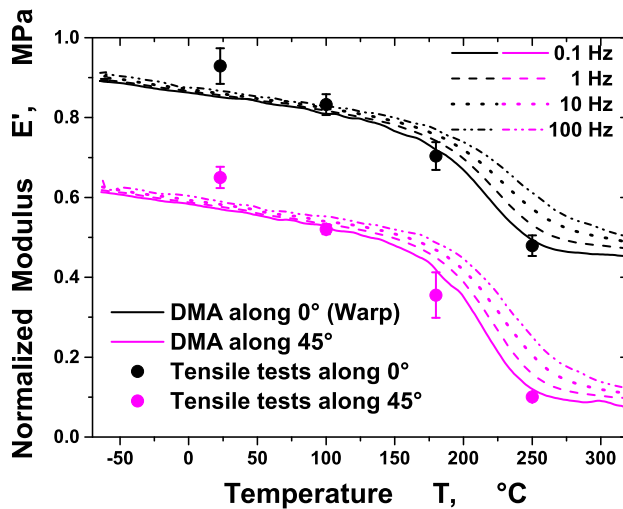


**Figure 2.5:** DMA curves obtained for orthotropic BT-epoxy resin (CCL-1078) as a function of frequency and temperature in comparison to tensile tests elastic modulus at different temperature (normalized to maximum modulus). *The graphic was taken with consent from [125] © 2018 IEEE.*

Typically, the DMA of cured thermosets can be divided into three regions, i.e., glassy region, transition region, and rubbery region. The thermosets are very stiff in the glassy region and show a higher storage modulus but lower loss modulus and  $\tan \delta$ . The thermosets' transition from stiff to soft rubber occurs in the glass transition  $T_g$  region. In this region, the storage modulus decreases, and both loss modulus and  $\tan \delta$  increase to the maximum. The region above the  $T_g$  is the rubbery region. The storage

modulus decreases rapidly and is also proportional to the loss modulus and  $\tan \delta$  in this region - (see Figure 2.5 and 2.6).

The insulating adhesive (ADH-X-01) shows a relatively lower modulus than the conductive adhesive (ADH-Z-02). Furthermore, the insulating adhesive shows a negative  $T_g$  of  $-110^\circ\text{C}$ , this enables the insulating adhesive to be operable over a broad temperature range and also in a harsh environment.

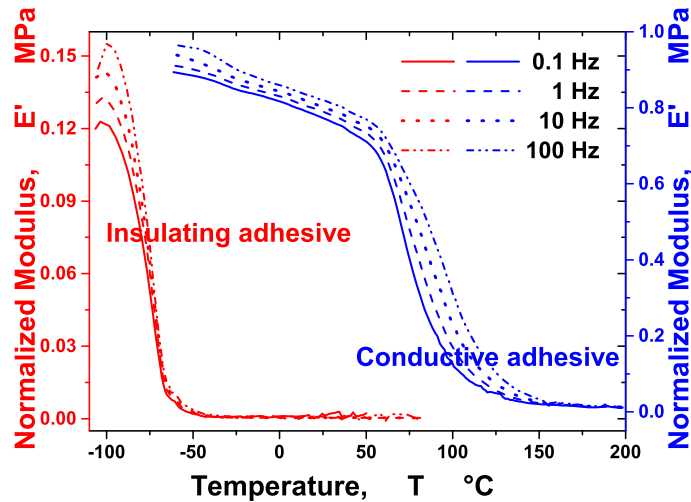


**Figure 2.6:** DMA curves obtained for isotropic insulating (ADH-X-01) and conductive adhesive (ADH-Z-02) as a function of frequency and temperature (normalized to maximum modulus). The graphic was taken with consent from [125] © 2018 IEEE.

**Yalagach et al., ESTC 2018 [125] © 2011 IEEE: Section: Results and Discussion**

On other hand, Figure 2.6 shows the thermal effects from DMA tests obtained for the considered isotropic insulating and conductive adhesives. The conductive adhesive has a significantly higher stiffness compared to the insulating adhesive over the measured frequency and temperature range. As expected the frequency dependence is observed to be pronounced in the  $T_g$  region of the individual materials. Modulus differences of up to 20 % are measured.

## Coefficient of Thermal Expansion - CTE

The reliability and durability of the MEMS sensor packages are often graded by the thermal expansion of the build-up materials. As most of the microelectronic components are multimaterial polymeric systems, these materials are often exposed to extreme temperatures. A strain mismatch in the individual material is generated due to variation in the temperature change. The strains generated are locally strong and may cause errors or malfunctions in the sensor during its operation.

The in-plane strain measurements were performed by using the *Q400 TCT* system (Dantec Dynamics, Ulm, Germany) to compute the CTE ( $\alpha$ ). This measurement system uses the Digital Image Correlation (DIC) method to measure the thermally induced strains in the materials. The DIC systems can be used for the thin material samples showing both isotropic and anisotropic behavior. The samples size used for these measurements are in the range of  $20 \times 4 \times 0.5$  mm (for epoxy adhesives) to  $30 \times 30 \times 0.06 - 1.5$  mm (for FR4 - prepregs). The research work [46] explains the different techniques, procedure, and importance to measure the CTE. The Figure 2.7 and 2.8 shows the in-plane CTE measured for the considered epoxy adhesives and prepregs:

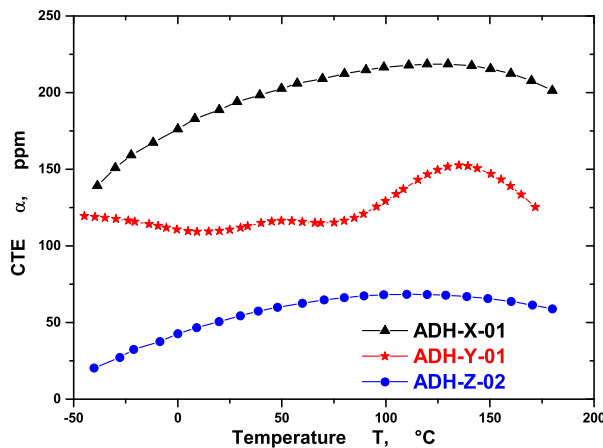


**Figure 2.7:** The in-plane CTE measured for different adhesive materials. *The graphic was taken with consent from [121] © 2019 IEEE.*

Yalagach et al., ECTC 2019 [121] © 2011 IEEE: Section: Results and Discussion

The Figure 2.7 shows the CTE results obtained for the insulating adhesives ADH-X-01 and ADH-Y-01, and the conductive adhesive ADH-Z-02. Within the measurement range of  $-50\text{ }^{\circ}\text{C}$  to  $180\text{ }^{\circ}\text{C}$  there is a substantial difference between the adhesives behavior. ADH-X-01 shows the highest average CTE and ADH-Y-01 shows the lowest CTE. The CTE of ADH-Z-02 is in between. Maximum differences of about 50% emphasize the importance of the material choice.

The changes in the CTE values near and above the  $T_g$  of all the epoxy adhesives can be seen in Figure 2.7. The CTE of the adhesive increases monotonically with temperature. Compared to prepregs (Figure 2.8), the epoxy adhesives show relatively higher CTE. The adhesives' high CTE values are mainly attributed to the rubber-based silicone for insulating adhesive and highly filled silver particles in the conductive adhesive.

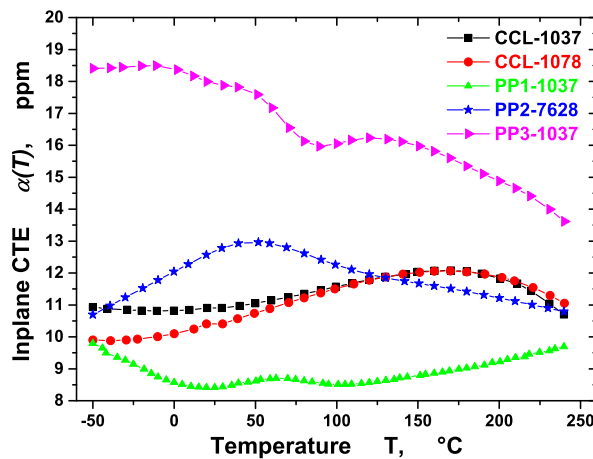


Figure 2.8: The in-plane CTE measured for different FR4-prepregs as a function of temperature. The graphic was taken with consent from [122, 123]

Yalagach et al., [122, 123] , Section: Results and Discussion

Figure 2.8 shows the in-plane CTE  $\alpha(T)$  results obtained for the prepreg materials. The CCL-1037 and CCL-1078 show a similar CTE trend for the overall temperature range of  $-50\text{ }^{\circ}\text{C}$  to  $250\text{ }^{\circ}\text{C}$ . The CCL-1037 has a higher resin content



of 27% than CCL-1078 (23%). Therefore, CCL-1078 has a lower CTE in the initial temperature range ( $-50^{\circ}\text{C}$  -  $150^{\circ}\text{C}$ ). Also, a lower CTE value was measured for PP1-1037 compared with other materials. The PP2-7628 and PP3-1037 showed a higher CTE value in the initial temperature ramp. On close observation, the CTE values decrease due to  $T_g$  for both materials. The CTE values for PP3-1037 is higher than other prepreg materials. Therefore, PP3-1037 is a poor material choice as a substrate in microelectronic packages. The maximum difference of 20% in all the materials emphasize the importance of the material choice.

## Thermal Conductivity

Thermal conductivity  $\lambda$  is the ability of the material to conduct heat. As MEMS sensor packages are operational over a wide range of temperatures, thermal management of the sensor system's materials needs to be accounted for. Along with thermal conductivity  $\lambda$ , specific heat  $C_p$  and density are the essential thermal properties that are necessary to establish a thermal numerical model for reliability assessment.

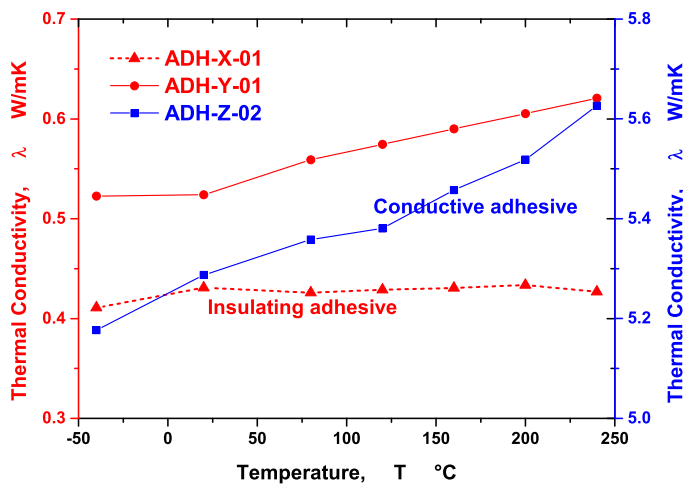


**Figure 2.9:** The thermal conductivity  $\lambda(T)$  measured for different adhesive materials as a function of temperature.

The  $\lambda$  for the polymeric materials were measured using Light Flash Analysis (LFA) [79]. Generally, LFA utilizes a contact-free and non-destructive approach to measure the thermal diffusivity  $a(T)$ . The  $\lambda$  measurements were performed using Netzsch

LFA 467 HyperFlash®(Netzsch GmbH, Selb, Germany). From this approach, thermal conductivity can be measured indirectly using the equation 2.12.

$$\lambda(T) = a(T) \cdot C_p(T) \cdot \rho(T) \tag{2.12}$$

where density  $\rho(T)$  and specific heat capacity  $C_p(T)$  were measured using high-resolution balance and Differential Scanning Calorimetry (DSC), respectively. The dimensions of the material samples and test parameters were considered according to [71]. Figure 2.9 and 2.10 shows the thermal conductivity  $\lambda$  measured for the considered epoxy adhesives and prepregs:

**Yalagach et al., [123] © 2021 IFSA Publishing: Section: Results and Discussion**

Figure 2.10 illustrates a wide range of thermal conductivity  $\lambda(T)$  values for the considered prepreg materials. The  $\lambda(T)$  values measure the ability of the material to conduct heat. The CCL-1037 and CCL-1078 show a similar trend for the measured temperature range. Furthermore, both PP1-1037 and PP2-7628 depict a higher  $\lambda(T)$ . Heat transfer through these prepreg materials occurs at a higher rate compared with other prepregs. Additionally, PP3-1037 shows relatively lower  $\lambda(T)$ . This is mainly attributed to this prepregs' substandard matrix material.

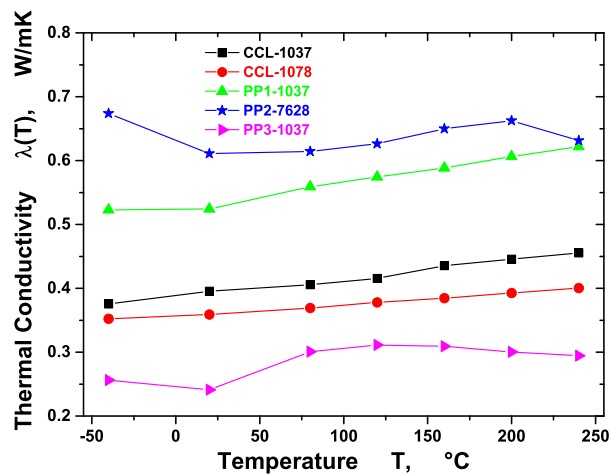


**Figure 2.10:** The thermal conductivity  $\lambda(T)$  measured for different FR4-prepregs as a function of temperature. *The graphic was taken with consent from [123]*

### 2.3.3 Moisture Dependent Characterization

The different test methods and results obtained from moisture dependent characterization have been described in this section. The moisture dependent properties and their test methods used for numerical modeling can be divided into three different parts:

- The moisture diffusion coefficient  $D$  and saturated mass uptake  $M_\infty$  obtained via gravimetric humidity conditioning.
- Coefficient of Moisture Expansion CME measured using a two-step drying process.
- Moisture/Humidity dependent Young's Modulus through uniaxial tensile tests under a controlled environment.

#### Gravimetric Moisture Conditioning

The moisture diffusion properties like moisture diffusion coefficient  $D$  and saturated mass uptake  $M_\infty$  of the polymers considered were determined using the gravimetric method. The following test procedure was involved in gravimetric humidity conditioning:

Yalagach et al., ESTC 2018 [125] © 2011 IEEE: Section: Experimental

The diffusion behavior of materials was measured by immersing them in a demineralized water bath at defined temperatures (60 °C and 90 °C) in a temperature chamber. The material samples were conditioned according to JEDEC-JESD22-A120B standards [107]. Initially, the materials were dried in a temperature oven at 125°C until they achieved a constant weight, before starting the environmental conditioning. Material samples were kept in the temperature chamber in a plastic container with demineralized water. At predefined time intervals, the material samples from the plastic container were removed. The surface was wiped using a paper tissue and they were weighed using a high precision balance (Mettler-Toledo MS-L). The percentage of moisture content  $M_t$  in the samples is computed using (2.13).

$$M_t = \frac{M_2 - M_1}{M_2} \times 100 \quad (2.13)$$

where  $M_1$  is the mass of the material sample after drying and  $M_2$  is the mass of the material sample at time  $t$ .

1 Immersion in demineralized Water.

**Table 2.2:** Thickness, dimensions of materials and conditioning environment for gravimetric humidity conditioning .

| Material       | Thickness, mm | Dimension, mm | Conditioning Environment |   |
|----------------|---------------|---------------|--------------------------|---|
|                |               |               | Temperature, T °C        | Moisture                                      |
| Epoxy Adhesive | 0.3           | 40 × 4        | 23, 60 , 90<br>85        | Immersion <sup>1</sup><br>85% RH <sup>2</sup> |
| FR4-Prepregs   | 0.06 - 0.2    | 50 × 50       | 23, 60 , 90<br>85        | Immersion<br>85% RH                           |

The dimensions and the conditioning environment are presented in table 2.2. Apart from conditioning the prepregs in a distilled water bath [125], a climate chamber was used to measure the moisture diffusion at 85 °C and 85% RH (Relative Humidity). Furthermore, the single and dual Fickian diffusion model parameters  $M_{\infty}$  and  $D$  can be determined by a non-linear least-squares curve-fitting procedure. The curve fitting procedure was performed to the experimental gravimetric moisture conditioning curves using *lsqcurvefit* function available in MATLAB-2020a (The MathWorks, Inc., Natick, Massachusetts, United States). Figure 2.11, shows the experimental and analytical fit moisture diffusion curves for the considered polymers:

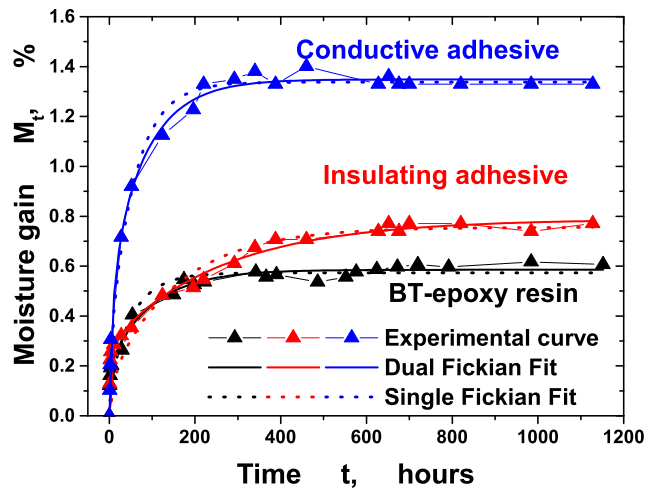
**Yalagach et al., ESTC 2018 [125] © 2011 IEEE: Section: Results and Discussion**

The results obtained for humidity conditioning for conditioning temperatures of 60 °C and 90 °C are depicted in Figures 2.11 (a) and 2.11 (b). The plot indicates a typical moisture gain trend, where both diffusion speed and the mass saturation increases at higher temperatures. The conductive adhesive (ADH-Z-02) absorbs the highest amount of moisture (1.3% and 1.78%) at both conditioning temperatures. The material reaches its saturation state at 120 hours. The insulating adhesive absorbs 0.8% and 1.12% and BT-epoxy resin absorbs nearly 0.65% of moisture. The saturation states for the insulation adhesive and the BT-epoxy resin are reached after 620 and 530 hours.

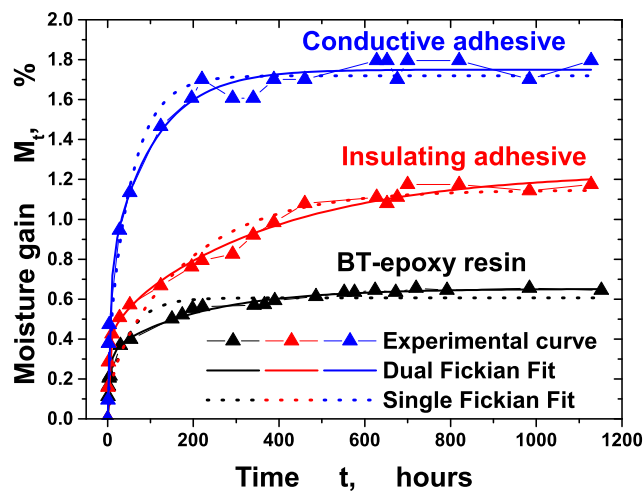
Figures 2.11 (a) and 2.11 (b) also depict the obtained curve fits using equation 2.6 and 2.9. The results show that for single Fickian diffusion the model cannot follow the trend of the experimental data in the initial region while the dual Fickian diffusion model fits the overall behavior of the experimental data well. The saturated mass  $M_{\infty}$  and diffusion coefficient  $D$  obtained from curve fitting

2 Conditioning using a Climate Chamber.

using the dual Fickian diffusion model for all polymeric materials are used in the further numerical hygro-thermo-mechanical simulations.



(a)



(b)

**Figure 2.11:** Typical moisture uptake/diffusion trend and curve fit using the analytical solutions for insulating (ADH-X-01), conductive adhesive (ADH-Z-02) and BT-epoxy resin (CCL-1078) at (a) 60 °C and (b) 90 °C. The graphic was taken with consent from [125] © 2018 IEEE.

Furthermore, the results obtained for moisture uptake at conditioning environment at 23 °C (immersion) and also at 85 °C 85% RH for FR4-Prepregs is depicted in Figure 2.12 and 2.13. Figures show a major difference in the saturated moisture content in the respective prepregs. The saturated moisture content  $M_{\infty}$  is higher for the conditioning environment 23 °C (immersion) compared with conditioning at 85 °C 85% RH. This is attributed to different transport mechanisms at the surface of the test specimen [39].

The absorption process when a polymer is immersed in the demineralized water bath is referred to as water absorption. In contrast, the absorption in a humid environment with a Relative Humidity (RH) less than 100% is termed as moisture absorption. Since the ambient is demineralized water in water absorption, the water molecules diffuse through the whole bulk of the material. Alternatively, moisture in a humid environment is in vapor form; thus, the moisture diffusion is only via the surfaces exposed to the humid air. In both water and moisture absorption, the moisture diffusion mechanism is governed using Fickian kinetics.

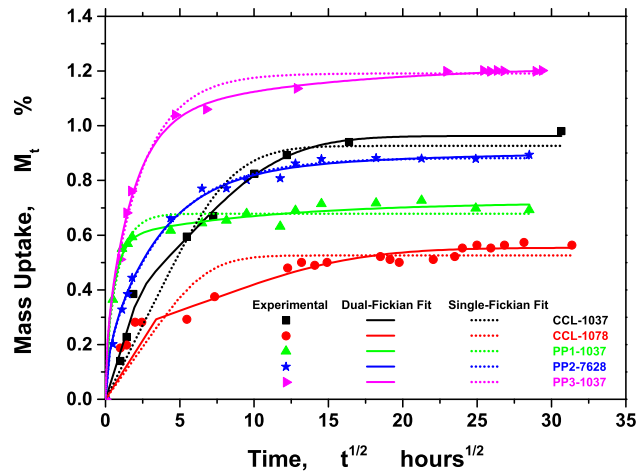


**Figure 2.12:** Typical moisture uptake/diffusion trend and curve fit using the analytical solutions for FR4-prepregs at 23 °C (Immersion) *The graphic was taken with consent from [122, 123]*

The interpretation of more results for the FR4-prepregs under different environmental conditions can be found in [122, 123] in part "Results and Discussion."

### Coefficient of Moisture Expansion (CME)

The Coefficient of Moisture Expansion (CME) or Coefficient of Hygroscopic Swelling (CHE) is a hygro-mechanical material parameter. As discussed in section 2.2.1, the absorption of moisture expands the polymeric materials through hygroscopic swelling

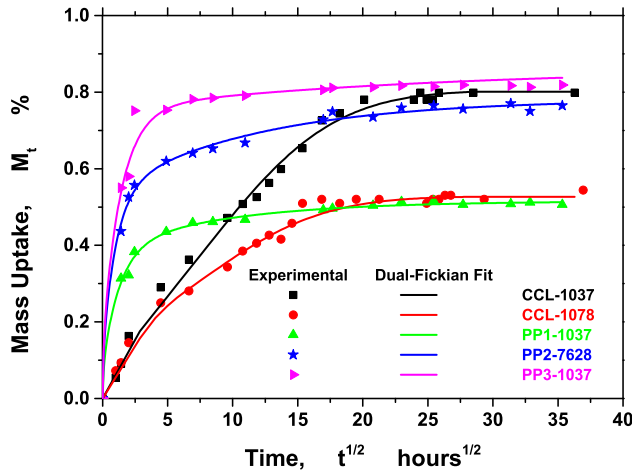


**Figure 2.13:** Typical moisture uptake/diffusion trend and curve fit using the analytical solutions for FR4-prepregs at 85 °C 85%RH. The graphic was taken with consent from [122, 123]

(caused by water molecules bound to the polymer matrix). Research [51] shows that for a temperature change of  $\Delta T = 60\text{ }^{\circ}\text{C}$ , the strain-induced swelling due to mismatch of the CME is twice the thermal strain induced due to CTE mismatch. The induced swelling strains may lead to reliability issues during the lifetime operation of the MEMS sensor packages.

CME can be measured using different thermal techniques like Michelson interferometry [103], or Thermo-Mechanical Analysis (TMA) along with Thermo-Gravimetric Analysis (TGA) [21]. The above measurement techniques can be used when the sample size is relatively small compared with samples used in gravimetric humidity conditioning. Furthermore, the results obtained from these measurement techniques are not accurate due to loss of moisture during the test system's stabilization. Therefore, in this research work, the CME was measured by following test method:

**Yalagach et al., ECTC 2019 [121] © 2011 IEEE: Section: Experimental**

The hygro-mechanical material parameter CME was measured using an approach based on a DIC system monitoring the hygroscopic strains during the drying process. The hygroscopic swelling strains  $\epsilon^{\beta}$  have a linear relation with change in moisture concentration  $\Delta C$  [51][103][125] as shown in (2.14).

$$\epsilon^{\beta} = \beta \Delta C, \quad (2.14)$$

where  $\epsilon^\beta$  is the hygroscopic strain,  $\beta$  is the coefficient of moisture expansion (CME) and  $\Delta C$  is the concentration change.

The following procedure was followed: *a*) humidity conditioning of two samples of the same material and dimension (sample A and sample B) by immersing them in demineralized water, *b*) desorption of moisture at constant temperature using *Q400 TCT* (Dantec Dynamics, Ulm, Germany) using sample A and a conventional temperature oven for sample B. Doing so the swelling strains  $\epsilon^\beta$  and concentration change  $\Delta C$  can be derived from sample A and sample B respectively. The desorption of the saturated material samples is carried out at 90 °C, 120 °C and 160 °C for six hours. A linear curve fit on the  $\epsilon^\beta$  over the  $\Delta C$  is performed to compute the CME  $\beta$ .

The Figures 2.14 and 2.15 depict the concentration change  $\Delta C$  and hygroscopic swelling strains  $\epsilon^\beta$ , respectively measured for the considered epoxy adhesives. The moisture desorption in the adhesives shows pronounced differences between the considered adhesives. The maximum moisture desorbed are varying from 1.7% (ADH-Z-02 - conductive adhesive) and 1.1% (ADH-X-01), 0.55% (ADH-Y-01), respectively for the insulating adhesives. The operating temperature for ADH-Y-01 was limited to 130 °C thus, the  $\Delta C$  and  $\epsilon^\beta$  measurements were not performed at 160 °C.

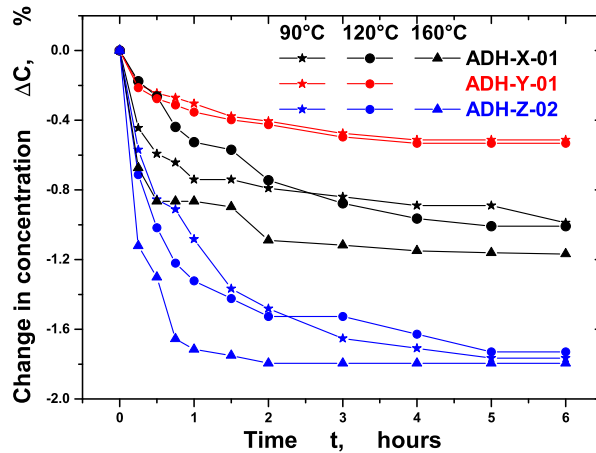


**Figure 2.14:** Measured change in concentration  $\Delta C$  for the epoxy adhesives at 90 °C, 120 °C and 160 °C. The graphic was taken with consent from [121] © 2019 IEEE.

The measured  $\epsilon^\beta$  for the adhesives also show a significant increase. As the conductive



adhesive (ADH-Z-02) absorbed maximum moisture (see Figure 2.11)  $\epsilon^\beta$  reaches a maximum value of 1.4% which is significantly greater than for the insulating adhesives ADH-X-01 and ADH-Y-01. Though the insulating adhesive ADH-X-01 absorbed 1% of moisture in moisture conditioning, no swelling strains were observed during this material's desorption process. Consequently, ADH-Y-01 material showed 1% of  $\epsilon^\beta$  at both 90 °C and 120 °C.

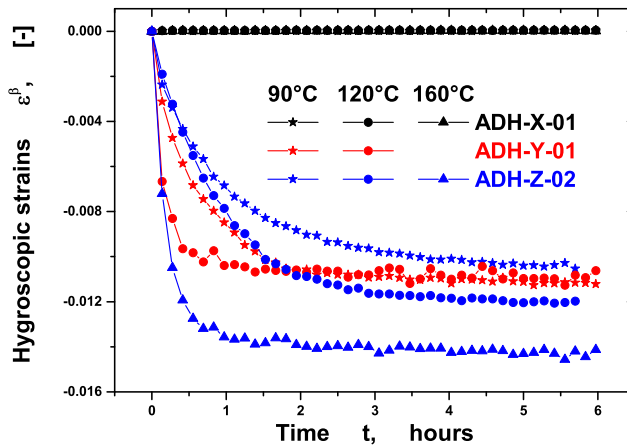


**Figure 2.15:** Measured hygroscopic swelling strains  $\epsilon^\beta$  for the epoxy adhesives at 90 °C, 120 °C and 160 °C The graphic was taken with consent from [121] © 2019 IEEE.

Furthermore, the hygroscopic swelling  $\epsilon^\beta$  behavior of the conductive adhesive versus the change in moisture concentration  $\Delta C$  with linear curve fit at 160 °C is illustrated in the Figure 2.16. The measured CME ( $\beta$ ) at different temperatures for the epoxy adhesives is depicted in the Figure 2.17. Since the insulating adhesive ADH-X-01 did not show any swelling strains, no CME was evaluated for this material.

The assessment of CME measurement, evaluation, and effect of  $T_g$  on hygroscopic swelling for the FR4-prepregs can be found in [122, 123] in "Results and Discussion."

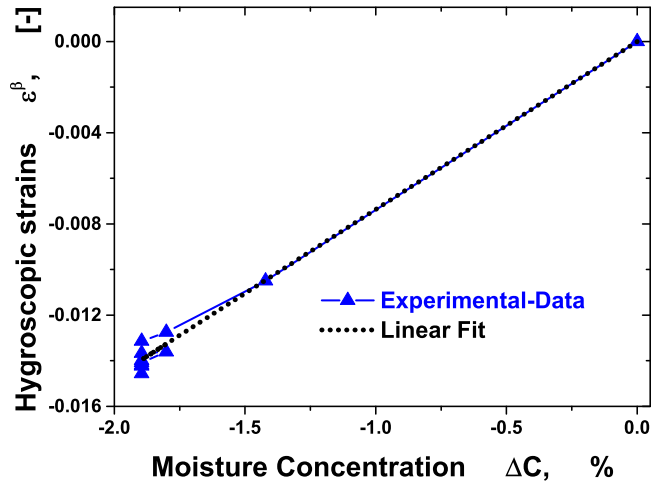


**Figure 2.16:** Linear relation between the hygroscopic swelling strains and change in moisture concentration for the conductive adhesive (ADH-Z-02) at 160 °C. The graphic was taken with consent from [125] © 2018 IEEE.

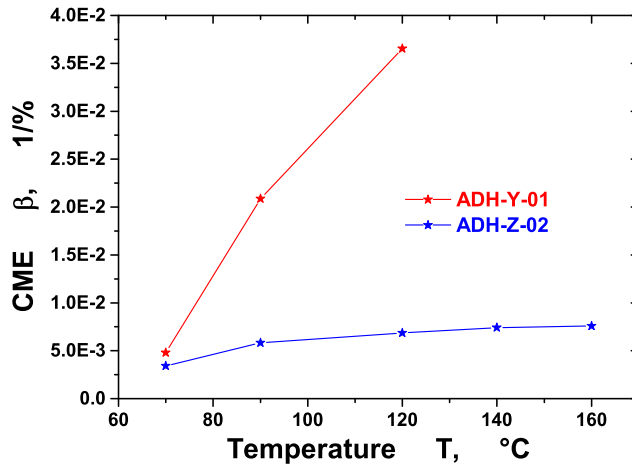


**Figure 2.17:** The measured CME ( $\beta$ ) at different temperatures for the epoxy adhesives.

### Humidity dependent Young’s Modulus

The effect of moisture absorption on the thermoset composites’ mechanical properties (FR4-prepregs) has been described in this section. The Young’s modulus  $E$ , yield

strength  $\sigma_y$  and Poisson's ratio  $\nu$  are measured as a function of temperature and humidity from this test method. These humidity dependent mechanical properties serve as input parameters for numerical modeling. The humidity dependent  $E$  was measured according to the following test procedure:

**Yalagach et al., [122, 123], Section: Experimental**

To assess the humidity effects on Young's modulus, humidity-controlled tensile tests were performed on the prepregs [122]. Before the humidity dependent testing, the prepregs were dried in a temperature chamber at 125 °C for 24 h in the first step and conditioned using a climate chamber in the second step. The defined temperature and humidity levels were 23 °C (50% and 85% RH), 60 °C (50% and 85% RH), and 85 °C (50% and 85% RH). The tests were performed using a Weiss Technik climate chamber and an Instron 4505 universal testing system. For the strain data acquisition, a Mercury 3D DIC system was used. The dimensions of the tensile specimens were prepared according to ISO 527-1BA [84].

The Figure 2.18 illustrates the test setup used for the measurement. The test was performed for the considered FR4-prepregs. Since the tensile specimen preparation is cumbersome, the tests were not performed for the considered epoxy adhesives.

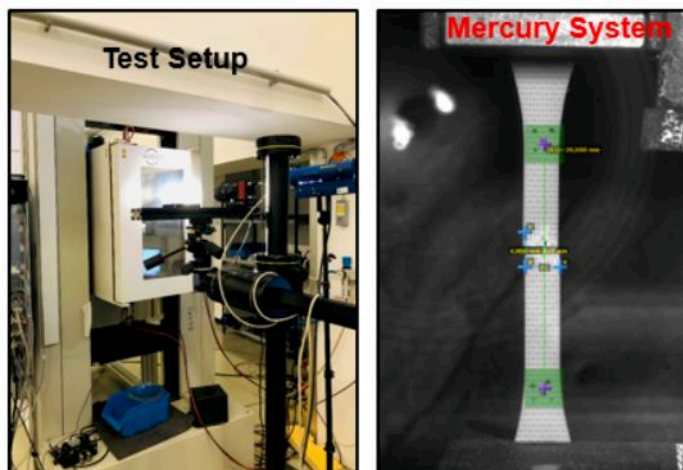


**Figure 2.18:** Experimental setup for the humidity-controlled tensile test with climate chamber and a Mercury 3D DIC system. *The graphic was taken with consent from [122, 123] © 2021 IFSA Publishing.*

The results from the humidity-controlled tensile tests (see Figure 2.19) for CCL-1078 prepreg are compared against the results from thermo-mechanical DMA and the temperature-controlled tensile test results (see Section 2.3.2).

**Yalagach et al., [122, 123], Section: Result and Discussion**

Overall, Young's moduli  $E$  obtained from temperature-controlled tensile tests are in good agreement with DMA results at increased temperatures for the prepregs considered for both Warp ( $0^\circ$ ) and  $45^\circ$  test specimens. Discrepancies at room temperature for CCL-1037, CCL-1078, PP2-7628, and PP3-1037 can be attributed to possible unstable humidity conditions when not using the climate chamber.

To quantify relative humidity effects, the prepregs were tested at 50% RH and 85% RH conditions at temperature levels of  $23^\circ\text{C}$ ,  $60^\circ\text{C}$ , and  $85^\circ\text{C}$ . A decrease in Young's moduli  $E$  for all the prepregs was observed at 50% RH and 85% RH, respectively, at all considered temperature levels. This decrease is mainly attributed due to the presence of moisture in the prepregs during the humidity conditioning. The Young's modulus  $E$  value for 85% RH is relatively smaller than  $E$  at 50% RH. The lower value of  $E$  is mainly due to the presence of higher moisture content at 85% RH than at 50% RH at the same temperature. This hydration difference explains the difference as excess moisture lowers the mechanical strength and stiffness of the prepregs. An increased humidity level leads to a reduced stiffness.

**Yalagach et al., [123], Section: Results and Discussion**

The Young's Modulus  $E$  obtained by performing DMA of the pre-conditioned material (CCL-1078) is shown in Figure 2.19 with black ( $0^\circ$ ) and red ( $45^\circ$ ) dotted lines. CCL-1078 absorbs nearly 0.6% of moisture during the pre-conditioning using gravimetric humidity conditioning. A deviation in the Young's moduli values of 1% in the temperature range of  $-80^\circ\text{C}$  –  $150^\circ\text{C}$  was observed for both  $0^\circ$  and  $45^\circ$  directions test specimen. Furthermore, the increase in temperature from  $150^\circ\text{C}$  desorbs moisture in the specimen. Therefore, the modulus  $E$  above  $150^\circ\text{C}$  follows the DMA trend at 1 Hz without any pre-conditioning. Additionally, Young's moduli measured by DMA are in close agreement with those from humidity-controlled tensile tests.

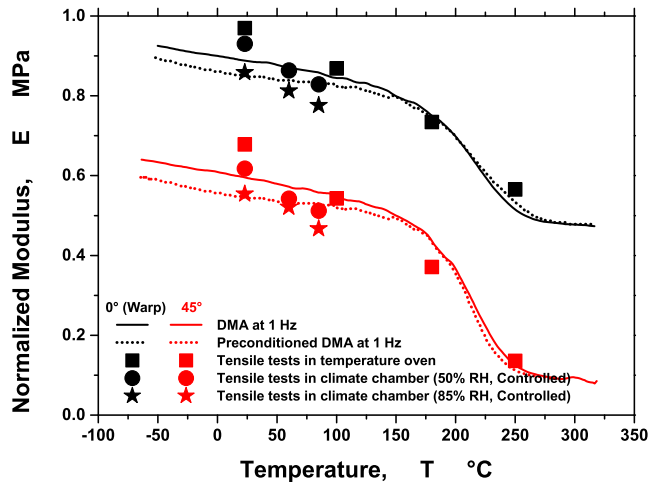


**Figure 2.19:** Comparison of controlled humidity tensile tests with DMA and tensile tests in temperature oven for CCL-1078 prepreg (normalized to maximum modulus). *The graphic was taken with consent from [123]*

## 2.4 Publication Misprint

The following images (Figure 2.20 and 2.21) from the publication M. Yalagach et al. **Numerical Analysis of the Influence of Polymeric Materials on a MEMS Package Performance Under Humidity and Temperature Loads**. In: *2019 IEEE 69th Electronic Components and Technology Conference (ECTC)*. 2019, 2029–2035. DOI: [10.1109/ECTC.2019.00311](https://doi.org/10.1109/ECTC.2019.00311). were misprinted after acceptance in IEEE Xplore. Therefore, the actual and original images used in the publication [121] have been described in this section.

### MEMS sensor package

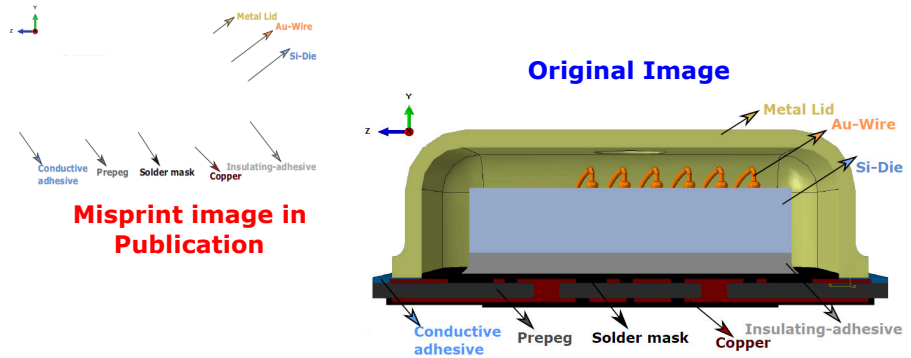


Figure 2.20: Misprinted image in the publication (LHS) in page 3 and actual image of the MEMS sensor package (RHS).

### Evaluation line in the silicon die

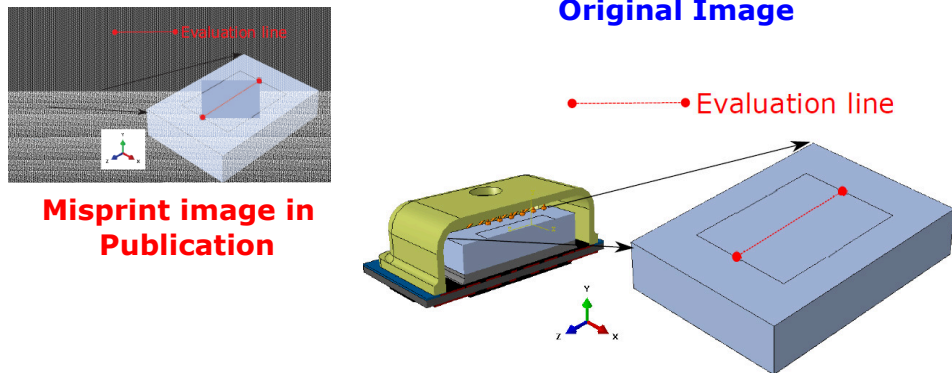


Figure 2.21: Misprinted image in the publication (LHS) in page 4 and actual image of the evaluation line in the silicon-die (RHS).

The Finite Element Method (FEM) was used for the numerical modeling of the MEMS sensor package (pressure sensor) and global modeling of the Printed Circuit Board (PCB). This chapter provides details of several procedures like thermal analysis, moisture (mass) diffusion analysis, and structural analysis to account for the changes from thermal and moisture distribution and mechanical loads. The numerical analysis was carried out using the commercially available finite element code ABAQUS™ (Abaqus 6.17, Dassault Systemes Simulia Corp., Providence, USA). The geometric development, multiphysics setup, and meshing of three-dimensional (3D) models were carried out using a pre-and post-processor for ABAQUS, i.e., Abaqus/CAE. The global simulation (PCB) and local simulation modeling approach (MEMS Sensor) was performed to analyze the detailed local die deformation behavior. The material input parameters for the polymeric materials were considered from the extensive material characterization in chapter 2.

Furthermore, the properties for non-polymeric materials like metal-lid, Au-wire, silicon-die, and copper were taken from literature [15, 81]. Additionally, finite element discretization and element type selection are discussed in this chapter. This chapter starts with a discussion on modeling thermal analysis (Heat-Transfer Simulation) followed by a mass diffusion analysis. A verification simulation is also performed at the material level to analyze the gravimetric moisture conditioning. Furthermore, a detailed description combining heat transfer, mass diffusion, and structural simulation is discussed at the component level. The problem of discontinuity is solved using the solubility approach in hygro-thermo-mechanical simulation. In the end, to account for the dynamic changes in temperature and moisture loads, an advanced hygro-thermo-mechanical simulation is also discussed. Specific analysis details related to a particular model are explained in detail in relevant sections.

### 3.1 Thermal Analysis

The laws of heat transfer are used to analyze a thermal analysis in a system. The heat transfer rate and thermal/temperature distribution are quantified through this analysis. As discussed in the gravimetric moisture conditioning (section 2.3.3), the material samples were conditioned in demineralized water in a plastic container kept in the temperature chamber. A thermal analysis is necessary to account for the temperature effects and estimate the time taken to reach thermal equilibrium. The thermal analysis

can be solved by using different approaches like experimental, analytical and numerical ones. The analytical approach is not considered due to the complexity of the geometry and boundary conditions. Thus, the thermal analysis was performed using a finite element numerical approach due to its accuracy, simplicity, and reliability.

The mathematical model for the analysis involves heat radiation from the temperature oven to the material sample, heat convection between air and material sample, and heat conduction within the material sample. The general energy balance [74] is given by:

$$\int_V \rho \dot{U} dV = \int_S q dS + \int_V r dV \quad (3.1)$$

where  $\rho$  is the density of the material sample,  $\dot{U}$  is the material time derivative of the internal energy,  $q$  is the heat flux per unit area,  $r$  is the volumetric heat source, and  $V$  is the volume of the material with surface area  $S$ . The internal energy is assumed to be a function of temperature as  $U = U(T)$ , where  $T$  is the material's temperature. The Fourier law is used to govern the heat conduction in a body given by equation 3.2.

$$\mathbf{F} = -\mathbf{k} \nabla T \quad (3.2)$$

where  $\mathbf{F}$  is the heat flux,  $\mathbf{k}$  is the conductivity matrix,  $\mathbf{k} = \mathbf{k}(T)$ . For isotropic material,  $\mathbf{k} = k \cdot \mathbf{I}$ , where  $\mathbf{I}$  is the identity matrix. Newton's law of cooling is used to govern the heat transfer by convection and is given by equation 3.3, where  $h$  is the convection or film coefficient and  $T_0$  is the sink temperature. Furthermore, the modified Stefan Boltzmann law is used to model heat transfer through radiation and is given by equation 3.4, where  $\epsilon$  is the unit less surface emissivity of the material (for materials used here,  $\epsilon$  is considered to be 0.8),  $\sigma$  is the Stefan-Boltzmann constant given by  $5.67 \times 10^{-8} \text{ W m}^{-2} \text{ K}^{-4}$  and  $T$  is the surface temperature of the body.

$$q = h(T - T_0) \quad (3.3)$$

$$q = \epsilon \sigma (T^4 - T_0^4) \quad (3.4)$$

Using equation 3.2, 3.3 and 3.4; and since there is no internal heat generation, for the present problem the energy balance is given by equation 3.5.

$$\int_V \rho \dot{U} dV + \int_V \mathbf{k} \nabla T dV = \int_S [h(T - T_0) + \epsilon \sigma (T^4 - T_0^4)] dS \quad (3.5)$$

Standard Galerkin method [2] is used define the variational statement of the energy balance equation. Therefore, equation 3.5 yields:



$$\int_V \rho \dot{U} \delta T dV + \int_V \nabla \delta T \cdot \mathbf{k} \cdot \nabla T dV = \int_S [h(T - T_0) + \epsilon \sigma (T^4 - T_0^4)] \delta T dS \quad (3.6)$$

where  $\delta T$  is an variational field which satisfies the essential boundary conditions. Furthermore, the considered model is descritized with finite number of elements. Thus, the temperature field  $T$  is interpolated as:

$$T(x, y, z) = N^N T^N, \quad N = 1, 2, \dots, \quad (3.7)$$

where  $T^N$  is temperature at nodes. Additionally, Galerkin approach also considers the variational field  $\delta T$  is interpolated by the same functions:

$$\delta T = N^N \delta T^N \quad (3.8)$$

Thus, using the intepolation equations 3.7 and 3.8 in equation 3.6 yields:

$$\delta T^N \left\{ \int_V N^N \rho \dot{U} dV + \int_V \nabla N^N \cdot \mathbf{k} \cdot \nabla T dV - \int_S N^N [h(T - T_0) + \epsilon \sigma (T^4 - T_0^4)] dS \right\} = 0 \quad (3.9)$$

Due to its stability, for time integration, ABAQUS<sup>TM</sup> uses backward difference method given by equation 3.10. Furthermore, the equation 3.11 is further solved using modified Newton method [2] for each time increment  $\Delta t$ .

$$\dot{U}_{t+\Delta t} = \frac{U_{t+\Delta t} - U_t}{\Delta t} \quad (3.10)$$

$$\frac{1}{\Delta t} \int_V N^N \rho (U_{t+\Delta t} - U_t) dV + \int_V \nabla N^N \cdot \mathbf{k} \cdot \nabla T dV - \int_S N^N [h(T - T_0) + \epsilon \sigma (T^4 - T_0^4)] dS = 0 \quad (3.11)$$

## 3.2 Moisture Diffusion Analysis

The absorption/diffusion of moisture is solved using "mass diffusion analysis" option available in ABAQUS<sup>TM</sup>. From conservation of mass, and using Fick's second law (equation 2.3), a mass diffusion analysis is given by equation 3.12. Furthermore, by using the divergence theorem [74] equation 3.12 can be reduced to equation 3.13.

$$\int_V \frac{dC}{dt} dV + \int_S \mathbf{n} \cdot \mathbf{J} dS = 0 \quad (3.12)$$

$$\int_V \left( \frac{dC}{dt} + \nabla \cdot \mathbf{J} \right) dV = 0 \quad (3.13)$$

where  $C$  is the moisture concentration,  $V$  is the volume with surface  $S$  of the material,  $\mathbf{n}$  is the outward normal to  $S$ ,  $\mathbf{J} = -D\nabla C$  is the concentration flux and  $\mathbf{n} \cdot \mathbf{J}$  is the concentration flux leaving  $S$  [2].

For the multi-material system, the discontinuity of the moisture concentration at the material interface can be solved using different approaches considering thermal and moisture analogy. Many studies like wetness theory, normalized concentration analogy [31], "Direct" analogy [128] and advanced normalized concentration analogy [56] have been listed in the literature to solve for this discontinuity. To this end, a normalized concentration analogy was applied for the moisture diffusion analysis. In the normalized concentration analogy, the moisture concentration  $C$  is normalized by the solubility  $S$ . The normalized concentration  $\varphi$  is given by equation 3.14.

$$\varphi = \frac{C}{S} \quad (3.14)$$

Using equation 3.14 in equation 2.6 and by rearranging the terms, concentration flux  $\mathbf{J}$  is given by:

$$\mathbf{J} = -D \cdot (S\nabla\varphi + \varphi\nabla S) \quad (3.15)$$

Assuming uniform distribution of solubility  $S$ , i.e.,  $\nabla S = 0$  and  $D$  as moisture diffusion coefficient. The concentration flux  $\mathbf{J}$  yields equation 3.16.

$$\mathbf{J} = -SD \cdot \nabla\varphi \quad (3.16)$$

Additionally, using equation 3.16 and applying variational principle to equation 3.12, the weak form for the moisture/mass diffusion problem can be obtained. In equation 3.17, the variable  $\delta\phi$  is a scalar and arbitrary field according to variation principle [2].

$$\int_V \left[ \delta\phi \left( S \frac{d\varphi}{dt} \right) + \nabla\delta\phi \cdot SD \cdot \nabla\varphi \right] dV = \int_S \delta\phi - \mathbf{n} \cdot (SD \cdot \nabla\varphi) dS \quad (3.17)$$

ABAQUS<sup>TM</sup> uses Galerkin method for discretization of the mass diffusion problem. Therefore,  $\delta\phi$  is defined as  $\delta\phi = N^N \delta\phi^N$ , where  $N^N$  is the interpolation function [2]. Time integration in transient analysis of mass diffusion is solved by using, the

backward Euler scheme. The discretized version of the mass diffusion problem is given by equation 3.18.

$$\int_V \left[ N^N \left( S \frac{d\varphi}{dt} \right) + \nabla N^N \cdot SD \cdot \nabla \varphi \right] dV = \int_S N^N - \mathbf{n} \cdot (SD \cdot \nabla \varphi) dS \quad (3.18)$$

The use of normalized concentration analogy to solve the discontinuity is valid only when the temperature distribution is uniform and time-independent. Furthermore, this approach does not consider dynamic moisture loads as the solubility is uniform and is temperature independent. Section 3.5 considers these limitations in normalized concentration. Therefore, the dynamic temperature and moisture loads can be solved numerically.

### 3.3 Verification Simulation

The verification simulation numerically computes the moisture absorption in the materials. Furthermore, this simulation considers the analytical fit (single and dual Fickian diffusion models) parameters as boundary conditions to describe experimental moisture uptake curves. The simulation uses combined effects from thermal analysis (heat transfer) and moisture diffusion analysis (mass diffusion) to solve the moisture absorption phenomenon numerically. As discussed earlier, ABAQUS<sup>TM</sup> utilizes Fick's law to model the mass diffusion analysis [2].

**Table 3.1:** Material properties and boundary conditions for single Fickian diffusion model.

| Material Property                | Value   |
|----------------------------------|---|
| Diffusion $D$                    | $5.65 \times 10^{-9} \text{ mm}^2 \text{ s}^{-1}$ |
| Solubility $S$                   | 1   |
| Boundary Condition               | Value   |
| Saturated mass uptake $M_\infty$ | 0.62%   |
| Conditioning Temperature $T$     | 90 °C   |
| Time $t$                         | 792 h   |

#### 3.3.1 Simulation Procedure

Initially, the verification simulation started with the heat transfer analysis. The resulting nodal temperature distribution was further used in mass diffusion analysis as a predefined temperature field to account for the moisture uptake temperature is

dependence. The mass diffusion simulation is solved using both diffusion models, i.e., single-Fickian and dual-Fickian diffusion.

The Fickian diffusion or single Fickian diffusion model involves a single mass diffusion analysis in ABAQUS<sup>TM</sup>. For single Fickian diffusion, the moisture diffusion coefficient  $D$  and solubility  $S$  is a material input parameter while the saturated moisture uptake  $M_{\infty}$  is used as a concentration boundary condition. Furthermore, the dual Fickian diffusion model is numerically solved considering two parallel single Fickian diffusion using the analytically fitted parameters  $D_1$  and  $D_2$  as material parameters;  $M_{1\infty}$  and  $M_{2\infty}$  as concentration boundary conditions.

According to [35], the solubility  $S$  is the maximum amount of a substance that can be dissolved per the amount of solvent and is also defined as the concentration at saturation. The normalized concentration (equation 3.14) uses solubility  $S$ . Therefore, the normalized concentration must be used as boundary conditions. In other words, the boundary condition equal to one is applied, indicating the material surface is in full contact with moisture. Based on the type of boundary conditions used, the solubility  $S$  was considered one, and saturated mass uptake  $M_{\infty}$  was applied as the concentration boundary condition. The material properties and the boundary conditions considered for prepreg CCL-1037 for the verification simulation are given in table 3.1 and 3.2 for single and dual Fickian diffusion models, respectively. The finite element discretization was performed considering the linear hexahedron continuum elements of type DC3D8 for heat transfer and mass diffusion simulations. Additionally, 8 elements were considered along with the specimen thickness (0.06 mm for CCL-1037).

**Table 3.2:** Material Properties and Boundary Conditions for dual Fickian diffusion model.

| Material Property            |  | Value   |
|------------------------------|--|---|
| Diffusion                    | $D_1 \rightarrow$ Stage-1 (0 - 150 h)          | $5.03 \times 10^{-8} \text{ mm}^2 \text{ s}^{-1}$ |
|                              | $D_2 \rightarrow$ Stage-2 (150 - 792 h)        | $1.29 \times 10^{-9} \text{ mm}^2 \text{ s}^{-1}$ |
| Solubility, $S$              |  | 1   |
| Boundary Condition           |  | Value   |
| Saturated mass uptake        | $M_{1\infty} \rightarrow$ Stage-1 (0 -150 h)   | 0.26%   |
|                              | $M_{2\infty} \rightarrow$ Stage-2 (150 -792 h) | 0.38%   |
| Conditioning Temperature $T$ |  | 90 °C   |
| Time                         | Stage-1  | 150 h   |
|                              | Stage-2  | 792 h   |

### 3.3.2 Results

Using the described simulation procedure, the results obtained from a single diffusion simulation model depicting the simulated moisture uptake in CCL-1037 compared against the experimental and analytical fit curves is shown in Figure 3.1.

From a single Fickian diffusion simulation (Figure 3.1), the simulation curve does not follow the trend in the initial region (in between 50 h - 390 h) of the moisture uptake. This diffusion model underestimates the total saturation mass by deviating the time taken to reach the total moisture equilibrium. The results from the dual Fickian diffusion model is depicted in Figure 3.2 for CCL-1037 and PP2-7628 prepreg materials:

**Yalagach et al., ESTC 2018 [122, 123] © 2011 IEEE: Section: Results and Discussion**

The results from the verification simulation have been depicted in Figure 3.2. The verification simulation was performed at the specimen level for the prepregs immersed in a distilled water bath and conditioned at 90 °C. The solid red lines represent the result obtained from a verification simulation; the black dotted lines represent the curve from the analytical fit, and the black and blue squared symbols represent the experimental humidity conditioning curves for CCL-1037 and PP2-7628, respectively. The verification simulation using the dual Fickian diffusion model agrees with both experimental and analytical fit curves' overall behavior. Therefore, this verification simulation model serves as a basis to the hygro-thermo-mechanical modeling [121, 125] approach. The verification simulation was also performed for all the five prepregs considered in this contribution. Overall, the simulation results agree with the experimental data and the analytically fit parameters for all the prepregs

The verification simulation was also performed for the silver filled epoxy adhesive (Conducting adhesive - ADH-Z-02) and Figure 3.3 depicts the simulated moisture uptake using single and dual Fickian diffusion models.

To conclude, the verification simulation using the dual Fickian diffusion model fits the overall behavior from the analytical fit and the experimental trend. Therefore, this diffusion model is further used in the hygro-thermo-mechanical and advanced hygro-thermo-mechanical simulations.

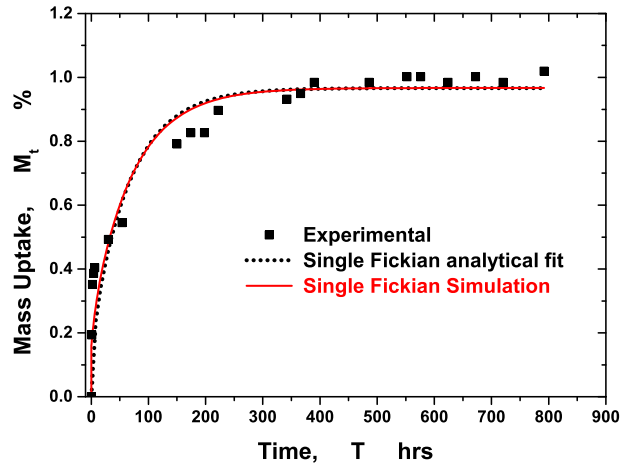


**Figure 3.1:** Comparison of moisture absorption curve between experimental, analytical and simulation using verification simulation for CCL-1037.

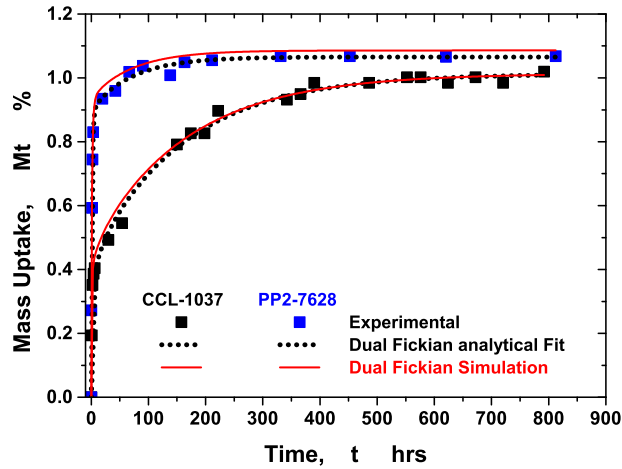


**Figure 3.2:** Comparison of moisture absorption curve between experimental, analytical and simulation using verification simulation for CCL-1037 and PP2-7628. *The graphic was taken with consent from [125] © 2018 IEEE.*

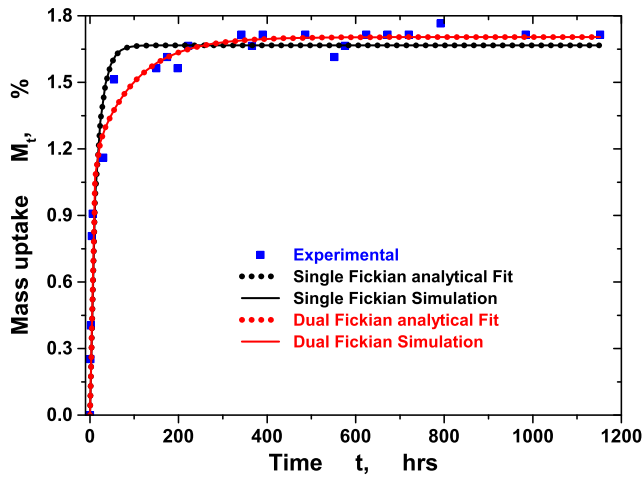


**Figure 3.3:** Comparison of moisture absorption curve between experimental, analytical and simulation using verification simulation for conductive adhesive, ADH-Z-02.

## 3.4 Hygro-Thermo-Mechanical Simulation

The numerical evaluation of thermo-mechanical and hygroscopic stresses due to thermal and moisture distribution is evaluated using the hygro-thermo-mechanical simulation model. In this model, the non-linear strain analysis is performed by considering the combined effect of thermal and hygroscopic deformation. Additionally, the strains due to mechanical loads like bending are also taken into consideration. Furthermore, the solubility approach is implemented to solve discontinuity in the moisture concentration in the multi-material system. For a multi-material system, a pressure MEMS sensor system, as shown in Figure 2.1 was considered. The effect of different material combinations and detailed local silicon-die deformation in the considered MEMS sensor was analyzed using a global and local sub-modeling approach.

### 3.4.1 Simulation Procedure

The modeling approach for the hygro-thermo-mechanical simulation is illustrated in the block diagram in Figure 3.4. This simulation approach involves a heat transfer simulation, two mass diffusion analyses, and a thermo-mechanical step described as:

**Yalagach et al., ESTC 2018 [125] © 2011 IEEE: Section: Hygro-Thermo-Mechanical Simulation**

The hygro-thermo-mechanical modeling approach is initially started with the heat transfer simulation. The resulting nodal temperature values are further used in a mass diffusion analysis as a predefined temperature field to take into account the mass diffusion temperature dependence. The mass diffusion simulation is solved using a dual Fickian diffusion model approach. Doing so, two parallel single Fickian mass diffusion analyses were performed using the analytical fitted parameters  $D_1$ ,  $D_2$ ,  $M_{1\infty}$  and  $M_{2\infty}$ . The resulting single Fickian moisture concentrations were saved in the individual analysis as field variables and summed up to the total moisture concentration using the USDFLD subroutine in the consequent hygro-thermo-mechanical analysis. The resulting moisture concentration and temperature fields are used in the subroutine UEXPAN to compute the thermal and hygroscopic swelling strains.

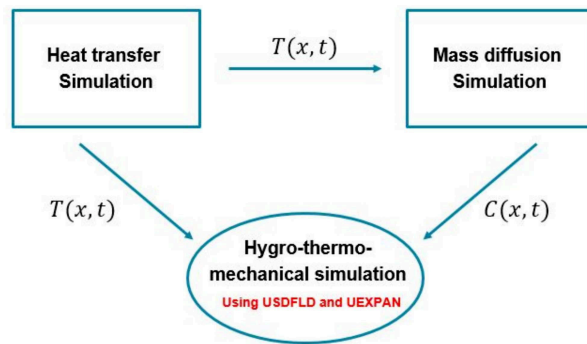


**Figure 3.4:** Hygro-thermo-mechanical simulation modeling approach. *The graphic was taken with consent from [125] © 2018 IEEE.*

The moisture distribution is calculated using the dual Fickian mass diffusion analysis. To this end, the solubility approach is applied to solve for the discontinuity in moisture concentration. In section 3.2, normalized concentration analogy was used to calculate the moisture distribution using mass diffusion analysis in ABAQUS™. The solubility  $S$  was used to normalize the concentration (see equation 3.14). In the verification simulation, the solubility  $S = 1$  was considered due to homogeneous material consideration (single material test). Alternatively, for a multi-material system, the solubility  $S$  is computed using Henry’s Law (equation 3.19) [76].

$$M_{\infty} = S \times P_{VP} \tag{3.19}$$



where  $P_{VP}$  is the ambient vapor pressure. The saturated moisture concentration  $M_{\infty}$  is known from the gravimetric moisture (section 2.3.3) characterization. The values for ambient vapor pressure  $P_{VP}$  at different temperature levels are obtained from literature [62]. The solubility  $S$  at different temperature levels is computed using equation 3.19. Thus, all the parameters necessary to solve discontinuity in a multi-material system using the mass diffusion analysis are defined.

An evaluation line was defined on the upper surface of the silicon-die (see Figure 3.5) to investigate the local deformation behavior (considering maximum principal strains) of the silicon die under the influence of temperature, moisture, and mechanical loads.

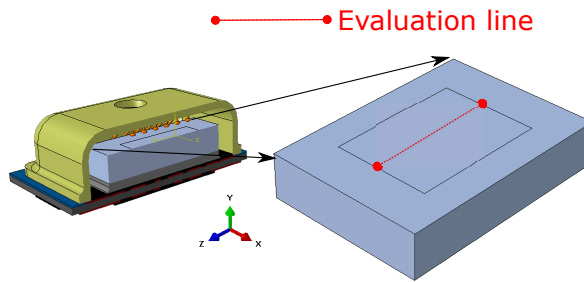


**Figure 3.5:** Evaluation line of the silicon die of the MEMS sensor. *The graphic was taken with consent from [121] © 2019 IEEE.*

**Table 3.3:** Considered material combination's used in MEMS sensor package. *The table was taken with consent from [121] © 2019 IEEE.*

| Materials           | MAT-1    | MAT-2    |
|---------------------|----------|----------|
| Prepreg             | CCL-1078 | PP1-1037 |
| Insulating adhesive | ADH-X-01 | ADH-Y-01 |
| Conductive adhesive | ADH-Z-02 |          |
| Solder mask         | SLM-01   |          |

### 3.4.2 Global and Local Simulation Approach

The global simulation approach analyzes the thermal, moisture, and mechanical effects on a Printed Circuit Board (PCB) structure. Due to the complex structure and material build-up of the PCB, detailed evaluation using FEM is computationally expensive. Therefore, an approach based on homogenization is applied to account for this

complexity. This homogenization method was implemented in an in-house automated PCB generator tool [44]. Using this tool, the complex PCB finite element model was generated. To automatically generate FE models, this tool uses segmentation and clustering algorithms along with the complex PCB design data. A conventional PCB (Figure 3.6) designed according to IPC/JEDEC-9702 standards [70] with dimensions,  $135 \times 77 \times 0.64$  mm was considered for this modeling approach. The finite element discretization was performed using linear hexahedron continuum elements of type C3D8R with 800685 elements.

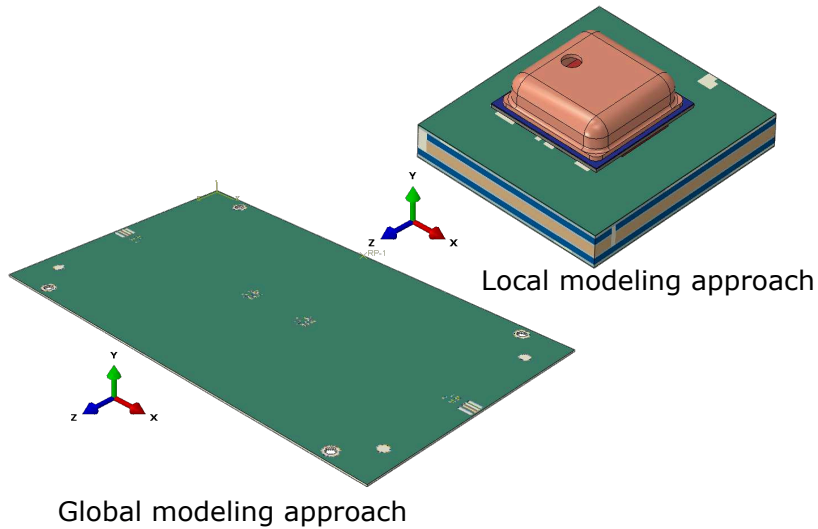


**Figure 3.6:** The conventional PCB used for global simulation modeling and Pressure MEMS sensor system soldered on a PCB for local simulation modeling.

In the local modeling approach, the MEMS pressure sensor soldered onto the PCB (Figure 3.6) was considered. The evaluation of the influence from the thermal, moisture, and mechanical loads is performed on the MEMS sensor. The local modeling approach helps in analyzing the comprehensive and accurate silicon-die deformation due to harsh environmental effects. A MEMS sensor package with dimensions  $2 \times 2 \times 0.7$  mm was considered and the dimensions of the submodel PCB is  $3.1 \times 3.7 \times 0.64$  mm. The used element type for the MEMS sensor package is a linear tetrahedron continuum element of type C3D4, and the total number of elements was 811766. For the local PCB, 181227 linear hexahedral elements of type C3D8.

Furthermore, two polymeric material combinations were considered for the MEMS sensor package to account for the material selection. For prepreg and insulating adhesive, two different materials were considered (see table 3.3). Also, for both material

combinations (MAT-1 and MAT-2), the conductive adhesive (ADH-Z-02) and solder mask (SLM-01) were kept the same. The PCB considered for the global and local modeling approach comprises multiple layers of commonly used solder mask (SLM-01), FR4 prepreg (PP2-7628), and copper layers.

The influence of material combination (MAT-1 and MAT-2), global and local modeling, and mechanical loads were investigated by performing four different simulations. The simulation in CASE-1 and CASE-2 involves possible differences in the type of material combination used. The CASE-1 and CASE-2 simulations are based on considering the local simulation approach. The CASE-3 simulation derives the influence of the combination of global and local simulation approaches. Additional to the temperature and humidity loads, the influence from the mechanical load (bending load of 3mm displacement) was considered in the CASE-4. Furthermore, for all four simulations, the defined moisture load of (100% RH) and temperature (85 °C) were considered. More comprehensive discussion and evaluation of the boundary conditions and the simulation approach can be found in [121].

### 3.4.3 Results

The results obtained from the four simulations are briefly discussed. The main aim of this simulation approach was to solve for the discontinuity in moisture concentration for a multi-material MEMS sensor package. Furthermore, this simulation approach accurately derives the local silicon-die deformation behavior considering global and local simulation approaches.

The continuous distribution of the normalized moisture concentration in a MEMS sensor package is illustrated in Figure 3.7. As the boundary condition normalized concentration was applied to the polymeric surfaces exposed to the environment, the MEMS sensor substrate has the highest moisture concentration of 0.58% compared with other polymer materials. Consequently, due to the continuity of moisture uptake, the conductive adhesive (0.34%) and insulating adhesive (0.15%) show a smaller moisture concentration than the substrate. Furthermore, the moisture diffusion coefficient  $D$  is negligible for non-polymeric materials (metal-lid and silicon-die). Therefore, the distribution of moisture concentration is zero for these materials.

The results from the CASE-1 and CASE-2 simulation cases have been depicted in Figure 3.8. In CASE 2, the principal strains are significantly higher compared with CASE-1. This increase is mainly attributed to the higher hygro-thermal expansion of the material combination in MAT-2. In comparison, the materials in MAT-1 did not show any hygro-thermal expansion during material characterization. The simulation results provide information on the type of material combination necessary to minimize temperature and moisture effects. Therefore, during the MEM sensor package design

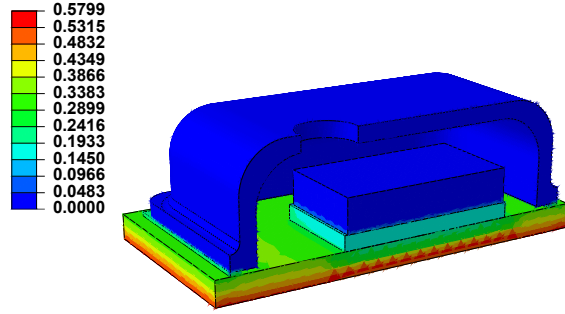


**Figure 3.7:** Distribution of moisture concentration (units in %) in the MEMS sensor package. The graphic was taken with consent from [125] © 2018 IEEE.

phase, polymeric materials showing lower thermal and moisture expansion are always preferred.

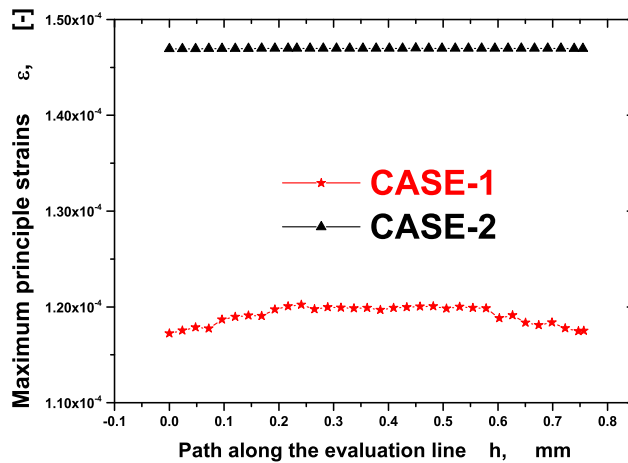


**Figure 3.8:** Strain levels along the evaluation line using the CASE-1 (MAT-1) and CASE-2 (MAT-2) material combinations in local modeling approach. The graphic was taken with consent from [121] © 2019 IEEE.

Figure 3.9 illustrates the results from CASE-1 and CASE-3. The difference in the strain levels is due to the influence of the boundary conditions from the global modeling approach (submodel boundary conditions). CASE-3 yields higher strains compared with CASE-1 (local model only). Therefore, to accurately determine the silicon-die’s

deformation behavior, the global model results are essential.

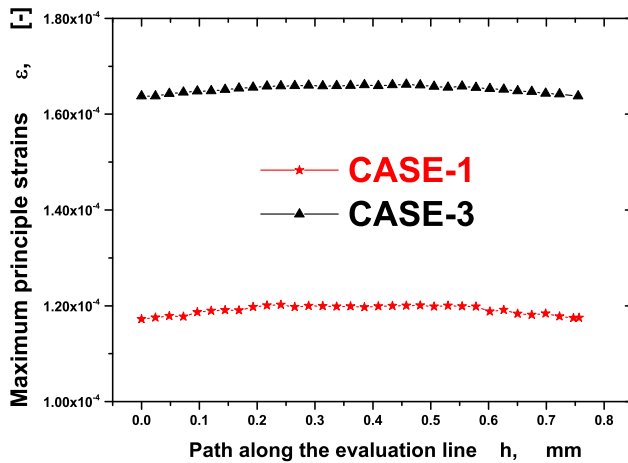


**Figure 3.9:** Strain levels along the evaluation line using the MAT-1 in a local (CASE-1) and to local submodeling (CASE-3) approach. *The graphic was taken with consent from [121] © 2019 IEEE.*

The effect of considering mechanical loads in addition to temperature and moisture distribution is depicted in Figure 3.10. The volumetric changes due to thermal and moisture distribution (CASE-3) are lower than the additional mechanical bending load (CASE-4). The strain levels due to external mechanical loads affect the local silicon-die deformation significantly. Henceforth, along with temperature and moisture loads, mechanical loads should also be considered in the form of four-point bending.

To conclude, the problem of discontinuity in the moisture concentration was solved using the hygro-thermo-mechanical simulation model. Furthermore, the global and local modeling approach can be easily defined and studied using this modeling approach. In this approach, the normalized concentration is a function of temperature alone. Thus, this approach is applied with uniform temperature and moisture loads. This limitation is numerically solved in advanced hygro-thermo-mechanical simulation by considering the effects of dynamic changes in temperature and moisture.

### 3.5 Advanced Hygro-Thermo-Mechanical Simulation

The hygro-thermo-mechanical simulation approach's limitations paved for the development of an advanced simulation strategy considering the dynamic changes in the

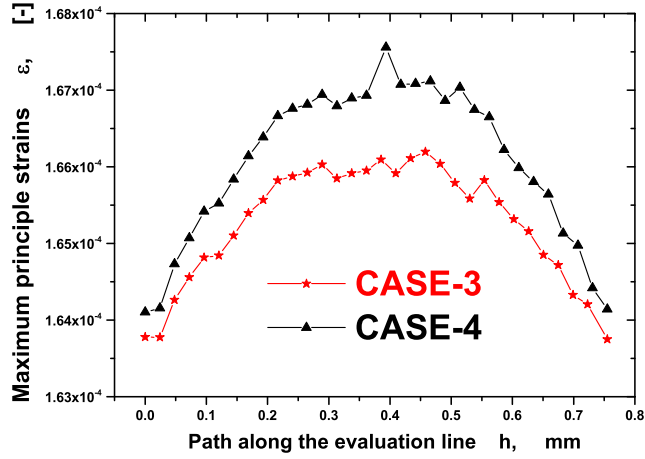


**Figure 3.10:** Strain levels along the evaluation line using CASE-3 and CASE-4 in local submodelling approach. *The graphic was taken with consent from [121] © 2019 IEEE.*

temperature and moisture loads. Furthermore, the method used in this model can also describe the moisture diffusion in the multi-material system without any normalization. The implementation and simulation procedure is briefly discussed in this section.

### 3.5.1 Implementation

Many studies have shown an experimental characterization [37, 83] and numerical modeling [56, 121, 128] approaches to account for moisture absorption and discontinuity under uniform temperature and moisture loads. The method discussed here uses a thermal-moisture analogy to describe the changes in the polymeric system under dynamic temperature and moisture loads. A method based on water activity [23] was considered to define the thermal-moisture analogy to describe the dynamic moisture diffusion. In this method, the water activity ( $\phi$ ) is Relative Humidity ( $RH$ ), considered to be continuous, and is given by equation 3.20. In this,  $P_{VP}$  is ambient vapor pressure, and  $P_{sat}$  is the saturated vapor pressure.

$$\phi = RH = \frac{P_{VP}}{P_{sat}} \tag{3.20}$$

In the water activity method, the moisture concentration  $C$  (see equation 3.21) is computed as the product of water activity  $\phi$  and generalized solubility  $K$ . The generalized solubility  $K$  acts as a driving force for the moisture diffusion [23].

$$C = K \times \phi = K \times RH \tag{3.21}$$

Additionally, the equation 2.4 can also be written as equation of the form;

$$\frac{\partial C}{\partial t} = \nabla \cdot (D \nabla C) \quad (3.22)$$

Now, using equation 3.21 in 3.22, yields

$$\frac{\partial(K\phi)}{\partial t} = \nabla \cdot (K D \nabla \phi) \quad (3.23)$$

The generalized solubility  $K$  is a function of both temperature and relative humidity (water activity). Thus, equation 3.23 can be further written as;

$$\left( K + \phi \frac{\partial K}{\partial \phi} \right) \frac{\partial \phi}{\partial t} = \nabla \cdot (K D \nabla \phi) - \phi \frac{\partial K}{\partial T} \frac{\partial T}{\partial t} \quad (3.24)$$

The equation 3.24 is the nonlinear diffusion equation by considering water activity as field variable. The water activity  $\phi$  being continuous can be used for the multi-material system without any normalization of the concentration. Furthermore, the water activity method is deduced using the fundamental Fick's diffusion equation. Therefore, this approach describes the moisture absorption under dynamic temperature and moisture loads.

The generalized solubility  $K$  is considered to account for the non-linear moisture diffusion in equation 3.24. At equilibrium or when the material reaches its saturation state  $C_\infty$ , from equation 3.21, the  $K$  takes the form;

$$K(\phi, T) = \frac{C_\infty(\phi, T)}{\phi} \quad (3.25)$$

The  $C_\infty(\phi, T)$  can be obtained through gravimetric humidity conditioning experiments at various moisture levels  $RH$  and temperature  $T$ . Thus, the equation 3.25 can be used to compute  $K$  at different temperature and moisture levels.

The heat transfer equation for a non-uniform isotropic medium is given by equation 3.26. In this,  $\rho$  is the density,  $C_p$  is the specific heat,  $k$  is the thermal conductivity, and  $q$  is the volumetric heat source term.

$$C_p \frac{\partial T}{\partial t} = \nabla \cdot (k \nabla T) + q \quad (3.26)$$

The water activity  $\phi$  or relative humidity  $RH$  is considered a field variable in this implementation. Therefore, a thermal-moisture analogy is established by comparing the moisture diffusion equation 3.24 with heat transfer equation 3.26. The table 3.4 describes the established thermal-moisture analogy.

**Table 3.4:** Thermal-Moisture analogy between heat transfer and moisture diffusion (water activity) equation.

| Equation                | Thermal-Moisture Analogy |  |   |
|-------------------------|--------------------------|--|---|
|                         | Field Variable           | Material Properties                                      | Source Term   |
| Heat Transfer 3.26      | $T$                      | $\rho C_p$   | $q$   |
| Moisture Diffusion 3.24 | $\phi$                   | $\left(K + \phi \frac{\partial K}{\partial \phi}\right)$ | $-\phi \frac{\partial K}{\partial T} \frac{\partial T}{\partial t}$ |

### 3.5.2 Simulation Procedure

Based on the established thermal-moisture analogy, the water activity based diffusion model was implemented in ABAQUS™:

**Yalagach et al., EPTC 2020 [124] © 2011 IEEE: Section: Advanced Hygro-Thermo-Mechanical Simulation**

The modeling approach for the advanced hygro-thermo-mechanical simulation is explained in the block diagram in Figure 3.11. This advanced numerical approach is initially started with the heat transfer simulation. The resulting nodal temperature values are considered as a predefined field variable in a humidity simulation to account for the influence of dynamic temperature change from the initial heat transfer step. The humidity simulation is evaluated using a heat transfer step to attain the thermal-moisture analogy. To this end, a combination of user-defined subroutines USDFLD and UMATHT are applied. The USDFLD subroutine is used to compute the incremental temperature change from the heat transfer simulation. This temperature change is further used in a UMATHT subroutine to compute the total concentration change using water activity method [23]. Furthermore in the last step, the resulting temperature field and moisture concentration are used in the subroutine UEXPAN to compute the thermal and moisture induced deformation under dynamic temperature and moisture loads.

The detailed discussion of the considered boundary condition, material properties, and results from this simulation approach can be found in [124] and appendix A. Furthermore, with this simulation approach, the silicon-die deformation is compared with the validation or experimental tests' capacitance readout. The validation experiments performed under different thermal, moisture, and mechanical bending loads has been discussed in detail in chapter 4. Furthermore, the results from the advanced simulation approach are compared with the validation tests.



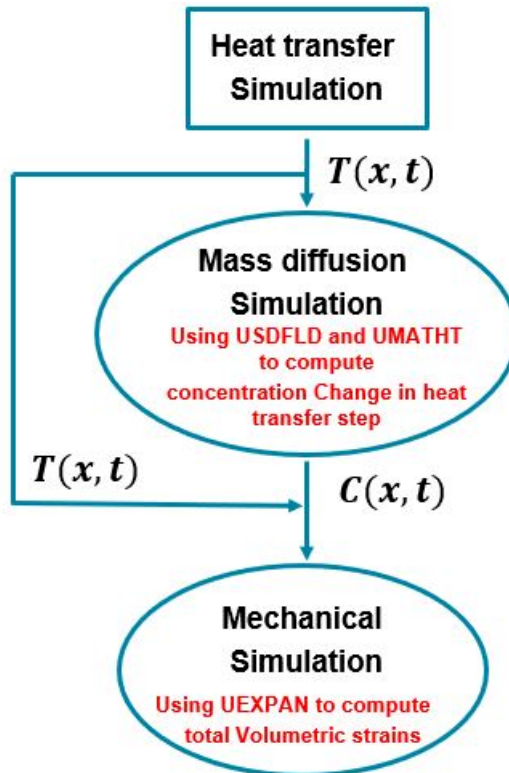


**Figure 3.11:** Hygro-thermo-mechanical simulation modeling approach. *The graphic was taken with consent from [124] © 2020 IEEE.*



# 4

## Validation Tests and Simulation

The sensor must be extensively tested under different environmental conditions to account for the pressure sensor system's sensitivity and accuracy. As a result, the MEMS sensor package's performance is analyzed under different load cases like temperature, moisture, and mechanical bending. This chapter explains the different types of pressure sensors used, test setup, test conditions, and results from the tests. The validation tests results are compared against the simulation's curves using the advanced hygro-thermo-mechanical simulation approach 3.5.

### 4.1 MEMS Sensor System

As discussed in the introduction, capacitive pressure sensors are used for the validation tests. A capacitive pressure sensor measures the pressure change by detecting the electrical capacitance changes due to the movement of the pressure-sensitive membrane. A typical pressure sensor consists of two parallel electrodes, i.e., the top flexible (pressure-sensitive membrane) electrode, and a bottom fixed electrode. The two electrodes are separated by a small gap  $d_0$ . The capacitance between the two parallel electrodes is given by equation 4.1.

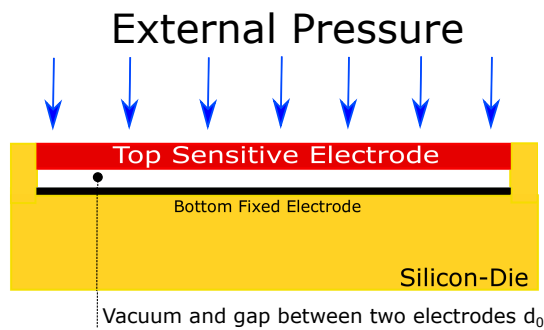


**Figure 4.1:** Typical capacitive pressure sensor.

$$C = C_0 = \epsilon_r \epsilon_0 \frac{A}{d_0} \quad (4.1)$$

where  $\epsilon_r$  is the dielectric constant of the material between the plates ( $\epsilon_r = 1$  for vacuum),  $\epsilon_0$  is the electric constant ( $\epsilon_0 = 8.854 \times 10^{-12} \text{ F m}^{-1}$ ),  $A$  is the area of the

plates. Figure 4.1 shows the build-up of a typical capacitive pressure sensor.

The validation tests were carried out on two types of capacitive pressure sensor packages. The two MEMS sensors are referred to as PAS250 and PAS600, respectively. The design and materials used for the buildup are similar to both flavors. The two sensors vary in their silicon-die thickness (see Figure 4.2). The PAS250 type has a silicon-die thickness of 250  $\mu\text{m}$  while the PAS600 has 600  $\mu\text{m}$

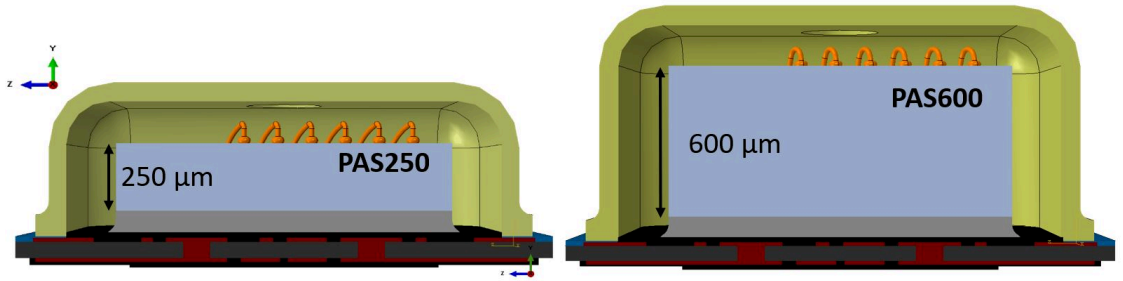


**Figure 4.2:** Two types of capacitive pressure sensors considered for the validation tests and simulation. *The graphic was taken with consent from [124] © 2020 IEEE.*

## 4.2 Test Setup and Test Conditions

The test setup and the different test conditions considered for the validation tests have been described in this section. The validation test setup is illustrated in Figure 4.3:

### Yalagach et al., EPTC 2020 [124] © 2011 IEEE: Section: Experimental Tests

The test board (PCB) with the two flavors of MEMS sensors were kept inside the climate chamber, and the readings from the sensors were measured under different temperature, humidity, and bending conditions. The Table 4.1 shows the different temperature and dynamic humidity loads used for the experimental tests. In test condition-1, at a constant temperature field of 23°C, and the moisture loads were varied from 30 → 85 → 30 % RH. While in the test condition-2, the humidity loads were similar to that of the condition-1, but the temperature was increased from 23 °C to 85 °C at 2 K min<sup>-1</sup>. Furthermore, in test condition-3, additional to temperature (23 °C) and humidity loads (50% RH), a four-point bending load of 5 mm displacement at 2 mm min<sup>-1</sup> was considered.

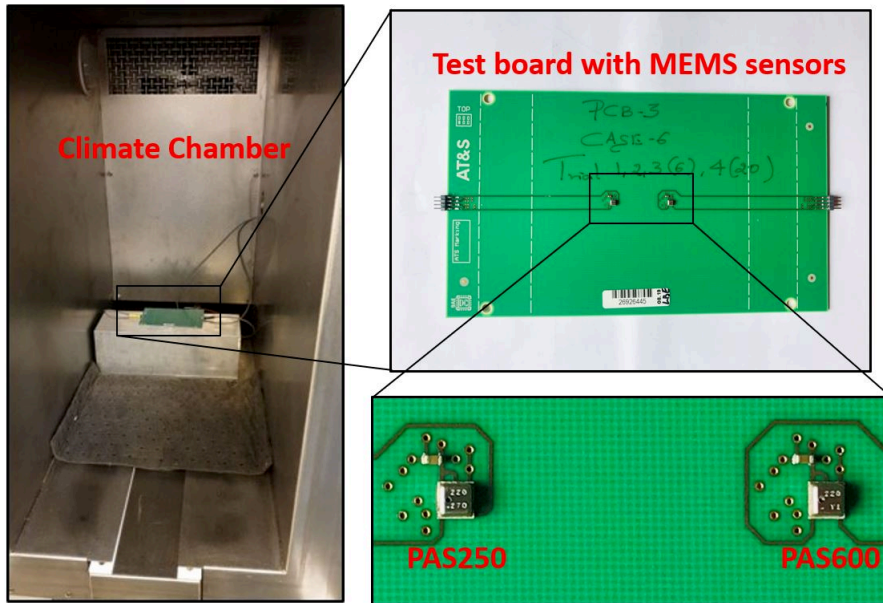


**Figure 4.3:** Validation test setup inside the climate chamber with test board and MEMS sensors. The graphic was taken with consent from [124] © 2020 IEEE.

**Table 4.1:** Different temperature and dynamic humidity loads used for the validation tests. The graphic was taken with consent from [124] © 2020 IEEE.

| Test Condition | Temperature [ °C] | Humidity[%]  |
|----------------|-------------------|--------------|
| 1              | Constant 23       | 30 → 85 → 30 |
| 2              | 23 → 85           | 30 → 85 → 30 |
| 3              | 23                | 50           |

The description of the boundary conditions used for the validation tests has been explained in detail in [124] and appendix A. Furthermore, as capacitance pressure sensors are used for the validation tests, the capacitance change is measured using a frequency-dependent circuit, e.g., an oscillator or an LC-tank circuit (Inductor-Capacitor Tank circuit). Both circuits utilize the change in resonant frequency to measure the capacitance signals with the change in pressure. Doing so, USB- $I^2C$  dongles along with the readout scripts from LabVIEW™ [73] software were used to read the capacitance signals from the respective pressure sensors (PAS250 and PAS600) under different loading conditions.

### 4.3 Simulation Procedure

The simulation models for the validation tests Test Condition-1 and 2 was performed considering the advanced hygro-thermo-mechanical simulation approach. The test conditions 1 and 2 involves dynamic changes in moisture and temperature loads, respectively. Therefore, in this numerical modeling, these dynamic changes are considered to evaluate the silicon die deformation. Furthermore, a comparison is made between the capacitance signals from tests against the silicon-die deformation from the simulation. The material combinations and the boundary conditions used for the advanced simulation model are explained briefly in this section.

#### 4.3.1 Materials and Boundary Conditions

As discussed in the hygro-thermo-mechanical simulation approach (see table 3.3), a similar combination of materials was utilized for the advanced simulation modeling, i.e., MAT-1 and MAT-2. The two material combinations have the following properties:

**Yalagach et al., EPTC 2020 [124] © 2011 IEEE: Section: Advanced Hygro-Thermo-Mechanical Simulation**

- MAT-1 shows lower hygro-thermal expansion and is expected to be best in performance. Therefore, this combination is considered in the experimental tests.
- MAT-2 shows the highest moisture influence during material characterization and lower Young's Moduli ( $E$ ) than MAT-1. Henceforth, this combination is used for the virtual study of the material behavior in the proposed simulation models.

The boundary conditions in the advanced simulation model were applied following the validation tests performed:

**Yalagach et al., EPTC 2020 [124] © 2011 IEEE: Section: Advanced Hygro-Thermo-Mechanical Simulation**

Three sets of simulations (CASE - 1, 2 and 3) were performed considering the test condition - 1, 2 and 3, respectively from the experimental tests. The loads were applied for 12 hours or 43200 seconds for CASE - 1 and 2. In CASE-1, a constant temperature of 23 °C is applied on to the surfaces exposed to the environment in heat transfer simulation. For the mass diffusion simulation, dynamic humidity of 30 → 85 → 30 % RH (see Figure 4.4) is applied on the polymeric materials

exposed to the environment. However, for CASE-2, the initial condition of 23 °C, and the temperature of 85 °C is applied in the heat transfer simulation. The humidity loads for the mass diffusion simulation remained the same as in CASE - 1. Furthermore, for CASE-3, a four-point bending load of 5 mm displacement at 2 mm min<sup>-1</sup> was applied for 420 s. For all the simulations, the temperature, humidity, and the bending loads were considered from the signals obtained from experimental tests.

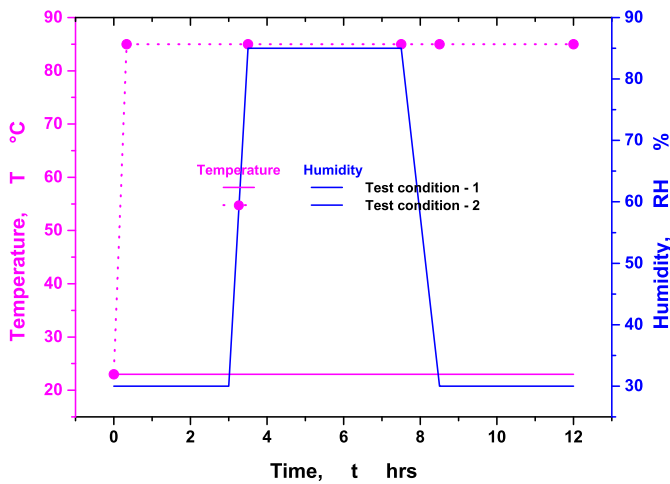


**Figure 4.4:** Dynamic temperature and moisture loads considered for the validation test conditions 1 and 2 and for the advanced simulation model. *The graphic was taken with consent from [124] © 2020 IEEE.*

A more detailed description of the considered material combinations, the evaluation region, and the boundary conditions can be found in [124] and appendix A. In the next section, the validation test results are compared against the silicon-die deformation behavior obtained using an advanced hygro-thermo-mechanical simulation approach.

## 4.4 Results

Using the proposed validation tests and the simulation procedure, the two types of MEMS sensor packages' capacitance signals are compared with the silicon die deformation. The results from the validation test conditions 1, 2 and 3 are compared with the simulations CASE - 1, 2 and 3, respectively. For all the test conditions and simulation

cases, the black-colored lines represent both capacitance signals and strain levels for the PAS250 sensor while the red-colored lines for the PAS600 sensor.

#### 4.4.1 Test Condition - 1

For the test condition 1, results obtained from the validation test are illustrated in the Figure 4.5. The capacitance signals  $C$  from the sensors (PAS250 and PAS600) are compared over time  $t$  for the considered temperature and dynamic moisture loads. The capacitance signals were nearly zero for both sensor types. A small deviation in the negative capacitance was observed for both the sensor types. This deviation is attributed due to decrease in moisture loads from 85 % to 30 %  $RH$ .

The results from the simulation CASE-1 for different material combination MAT-1 and MAT-2 is depicted in Figure 4.6. The maximum principal strain levels on the upper surface of the silicon die are evaluated. The strain levels in MAT-1 is significantly lower than the strain levels for MAT-2. The material combination in MAT-1 exhibit lower hygro-thermal expansion compared with combination MAT-2. Furthermore, Figure 4.6 also justify the effect of change in the silicon-die thickness between PAS250 and PAS600. The strains levels for PAS600 is lower compared with PAS250 sensor:

**Yalagach et al., EPTC 2020 [124] © 2011 IEEE: Section: Results and Discussion**

The simulation results showed relatively low strain levels for both sensors types. The scattering in the strain levels is mainly attributed to the scatter of temperature and humidity during the experimental test. In comparison with the experimental test condition - 1 (see Figure 4.5), no influence on the capacitance signal due to change in humidity was observed. However, in the simulation, a small change in strains was observed at the end of the simulation due to a decrease in humidity from 85  $\rightarrow$  30  $RH$ . Additionally, for the MAT-1 combination, no humidity effects on the capacitance signal are expected, while for the MAT-2 combination for PAS250 sensor, a small influence on the capacitance can be expected.

#### 4.4.2 Test Condition - 2

The results from the test condition 2 of the validation tests show a significant influence on the temperature change. The initial increase in the capacitance readout (see Figure 4.7) is attributed to a rise in temperature from 23 °C to 85 °C. Consequently, no effective change in capacitance was observed under dynamic moisture loads. The



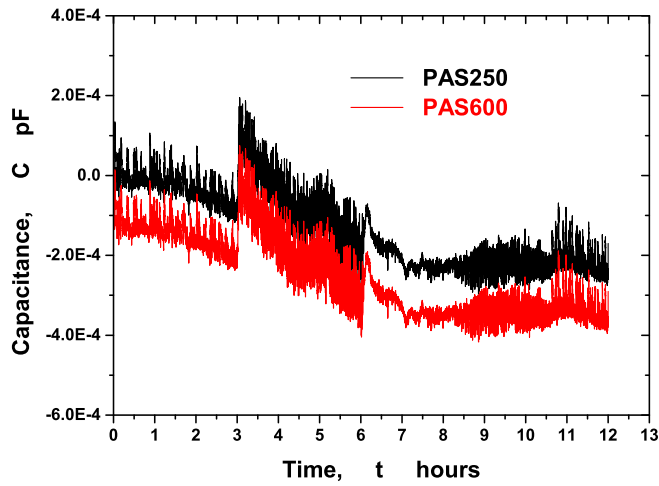


**Figure 4.5:** Validation test results for test condition 1. The graphic was taken with consent from [124] © 2020 IEEE.

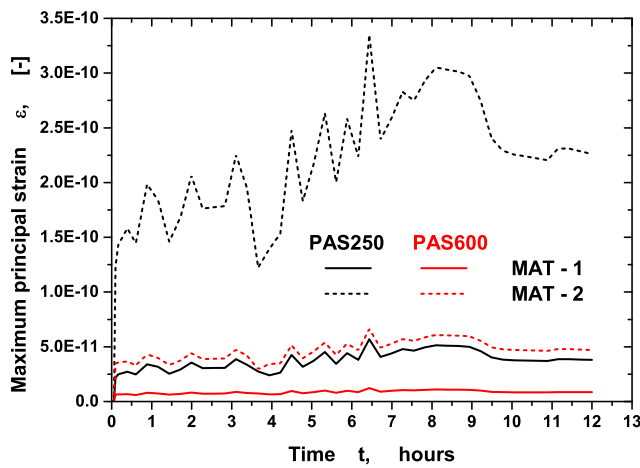


**Figure 4.6:** Strain levels using MAT-1 and MAT-2 material combinations for MEMS sensors in CASE-1. The graphic was taken with consent from [124] © 2020 IEEE.

capacitance signals for PAS250 is higher than PAS600. This increase in capacitance is due to the temperature sensitivity of the considered MEMS sensor (Intrinsic thermal behavior) [16]. The temperature sensitivity and its effects on capacitance signal are explained in detail in chapter 5.

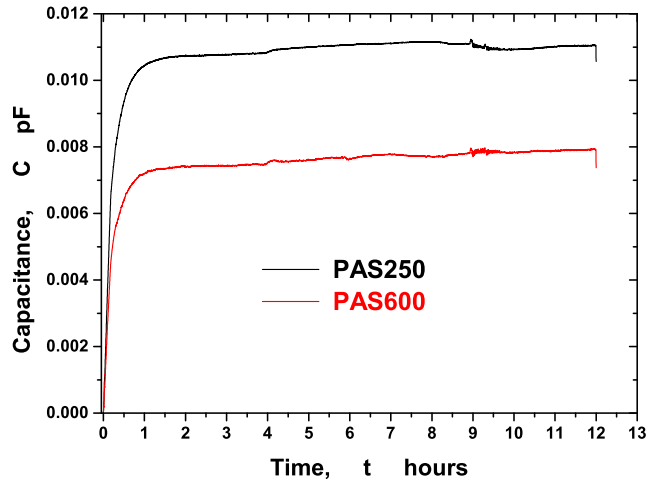


**Figure 4.7:** Validation test results for test condition 2. The graphic was taken with consent from [124] © 2020 IEEE.

The simulation results for the CASE-2 is illustrated in Figure 4.8. The figure shows an increase in the strains levels due to the initial increase in temperature from 23 °C to 85 °C. Therefore, higher strain levels are seen in CASE-2 compared with CASE-1 for the simulation model. Additionally, during conditioning experiments, the MAT-2 combination showed an increase in hygro-thermal expansion. Therefore, higher strains were observed for the MAT-2 combination than MAT-1:

**Yalagach et al., EPTC 2020 [124] © 2011 IEEE: Section: Results and Discussion**

The results from the simulation CASE-2 showed significantly higher strain levels for both MEMS sensors compared with CASE-1. Additionally, comparing the results from simulation to the validation test condition - 2 (see Figure 4.7), both capacitance and strains increased with an increase in temperature. The trends in simulation and experimental tests are in good agreement. Even in the CASE-2, scattering in strain values is due to scatter in temperature in the experimental test. On closer observation, any potential changes in MAT-2 of PAS250 due to humidity loads are overlaid by the significantly larger temperature influence. Therefore, no influence on strain levels is seen for MAT-2 of PAS250 under humidity change. From the experiments and simulations, the effect of dynamic humidity changes is negligible compared with temperature effects.

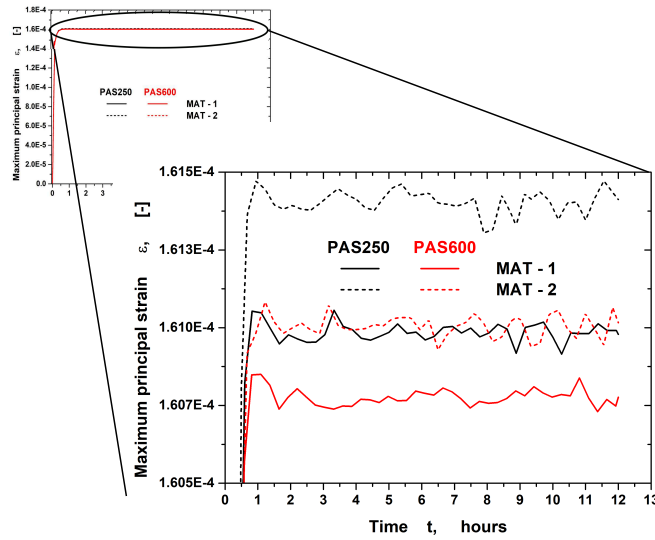


**Figure 4.8:** Strain levels using MAT-1 and MAT-2 material combinations for MEMS sensors in CASE-2. The graphic was taken with consent from [124] © 2020 IEEE.

#### 4.4.3 Test Condition - 3

The effects of bending load on the capacitance signals for the pressure sensor (PAS250 and PAS600) have been described in the results of test condition 3. The obtained results are depicted in Figure 4.9:

##### Yalagach et al., EPTC 2020 [124] © 2011 IEEE: Section: Results and Discussion

The results depict that capacitance values for PAS250 sensor show a significant increase under a four-point bending load. In contrast, the PAS600 sensor does not show any influence under the bending load. The increase in capacitance for PAS250 is mainly due to the lower silicon die thickness of 250  $\mu\text{m}$ . The higher thickness silicon-die (PAS600) minimizes the bending effects during the temperature and humidity loads compared with PAS250. Therefore, the MEMS sensor PAS600 has a lower capacitance.

Furthermore, the results from the four-point bending simulation CASE-3 is illustrated in Figure 4.10:

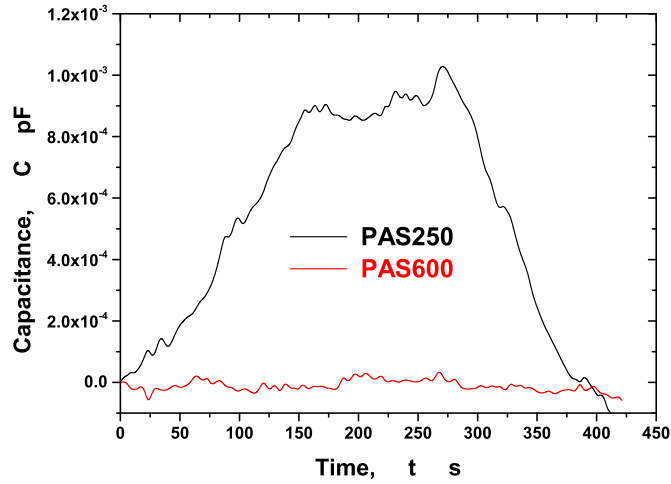


**Figure 4.9:** Validation test results for test condition 3. The graphic was taken with consent from [124] © 2020 IEEE.

#### Yalagach et al., EPTC 2020 [124] © 2011 IEEE: Section: Results and Discussion

The PAS250 sensor showed a higher strain under bending compared to PAS600 sensor. Additionally, the principal strain from material combination MAT-2 shows an increase in strains compared with MAT-1. This can be attributed to the lower Young's Modulus (mechanical properties) of the materials used in MAT-2. The bending effect is minimized by using a thicker silicon die, i.e., PAS600. As a result, the maximum principal strain for PAS250 is higher compared with PAS600. As both temperature and humidity were constant throughout the bending load, these factors did not show any influence on the strain levels.

The strain levels from the simulation CASE-3 is compared to the experimental test condition - 3 (see Figure 4.10). Both capacitance and strain levels increases under the bending load for the PAS250 sensor. Consequently, For the PAS600 sensor, neither the capacitance nor the strains show a significant change under bending. Additionally, the strain levels from the simulation follow a similar trend in comparison with the experimental test. Therefore, both the simulation CASE-3 and experimental test 3 are in good agreement.

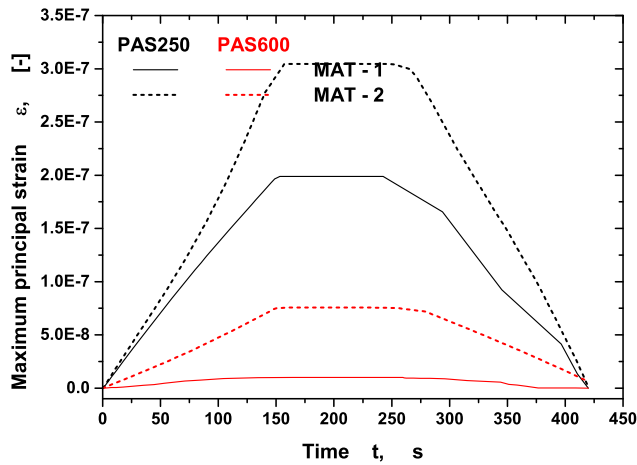


**Figure 4.10:** Strain levels using MAT-1 and MAT-2 material combinations for MEMS sensors in CASE-3. *The graphic was taken with consent from [124] © 2020 IEEE.*

The results from the validation tests conditions and their respective simulation cases provides the following information:

- Influence of different material combinations (MAT-1 and MAT-2) on the local silicon die deformation. The simulation results using material combinations confirmed that a lower thermal and hygroscopic expansion in the materials is highly recommended.
- Influence of the geometric design (PAS250 and PAS600) on the local silicon die deformation. Higher silicon-die thickness (PAS600) is preferred indicating minimal influence under environmental and mechanical loads.
- Deformation of the silicon-die under different dynamic loads like temperature, moisture, and four-point bending using advanced hygro-thermo-mechanical simulation.

## 4.5 Additional Validation Tests

As discussed in the results of the test condition 2 of the validation test, the increase in temperature has a significant impact on the signal sensitivity for the MEMS sensor package. The temperature influence is extensively studied by performing additional temperature-dependent validation tests. The different temperature loads considered for the further temperature sensitivity study is described in table 4.2. In this section,

the test conditions and results obtained from the additional tests have been illustrated for PAS250 and PAS600 pressure sensor.

**Table 4.2:** Different temperature and humidity loads considered for the additional validation tests.

| Test Condition | Temperature [ °C] | Moisture RH [%] |
|----------------|-------------------|-----------------|
| 4              | 23 → 85 → -40     | 50              |
| 5              | 23 → 140 → 23     | -               |

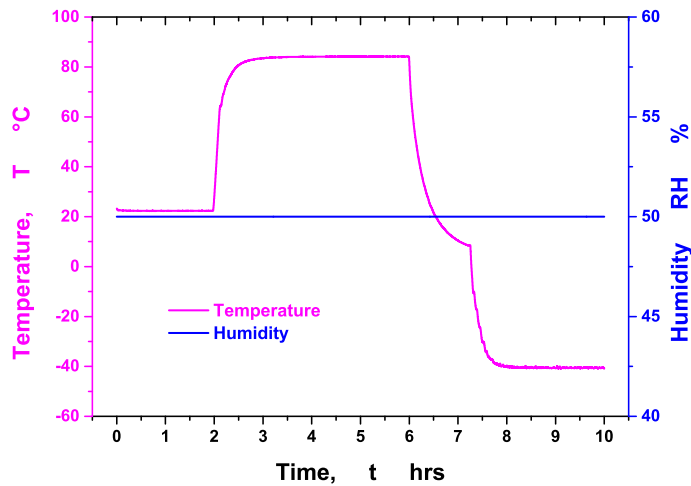


**Figure 4.11:** Temperature and moisture loads considered for test condition 4.

In test condition 4, at a constant moisture field of 50 % RH, the temperature loads were varied from 23 → 85 → -40 °C. While in the test condition 5, the moisture loads were not considered, but the temperature was increased from 23 → 140 → 23 °C to at 2 K min<sup>-1</sup>. The test condition 5 was examined to account for the higher temperature influence on the MEMS sensor system. Similar to the test condition 1, 2 and 3, the capacitance signal from sensors were measured using read out scripts from LabVIEW<sup>TM</sup> [73] software along with USB-I<sup>2</sup>C dongles. The Figure 4.11 and 4.12 represents the temperature loads used for the test condition 4 and test condition 5, respectively.

The results from the additional validation tests are depicted in Figure 4.13 and 4.14 for test condition 4 and 5, respectively. From the test condition 4 (Figure 4.13), the capacitance is constant for both PAS250 and PAS600 sensor at 23 °C. With increase in temperature from 23 °C to 85 °C, capacitance increases. Furthermore, the dependence of

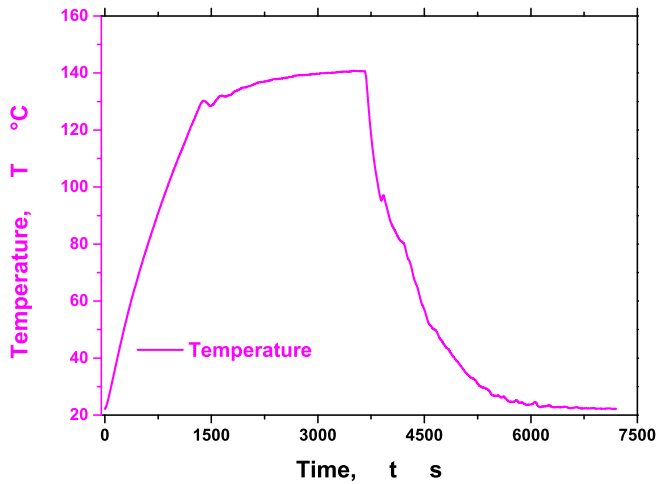


**Figure 4.12:** Temperature and moisture loads considered for test condition 5.

capacitance readout at negative temperatures was also taken into account by reducing the temperature from 85 °C - -40 °C. At negative temperature, the capacitance show a lower value than at 23 °C and 85 °C. The temperature loads in test condition 4 were applied for 10 h or 36 000 s. Compared with moisture (test condition 1) and bending loads (test condition 3), the capacitance signals from test condition 4 show an increasing trend due to temperature sensitivity.

The test condition 5 involves the evaluation of the capacitance readout under higher temperature influence. The temperature loads in this test case were applied for 7200 s. The capacitance signal was relatively higher than the test condition 2 and 4. This increase in temperature is due to higher temperature influence (140 °C).

The temperature sensitivity from test conditions 2, 4, and 5 are extensively studied using the theory of intrinsic thermal behavior in chapter 5. The pressure-sensitive membrane deformation under uniform pressure is considered to validate the capacitance readout from different validation tests performed.

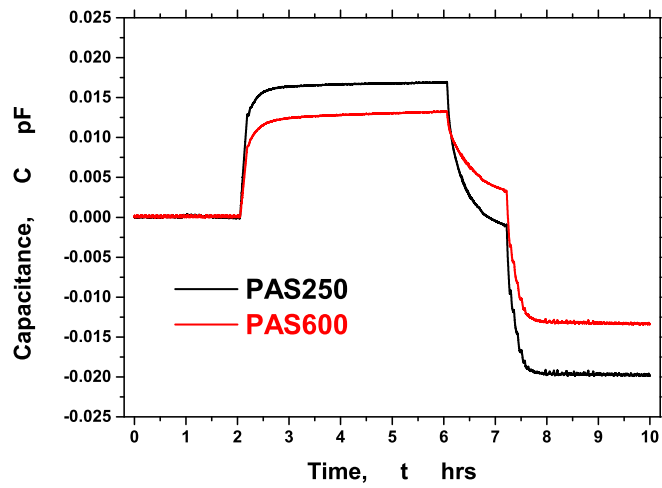


Figure 4.13: Validation test results for test condition 4.

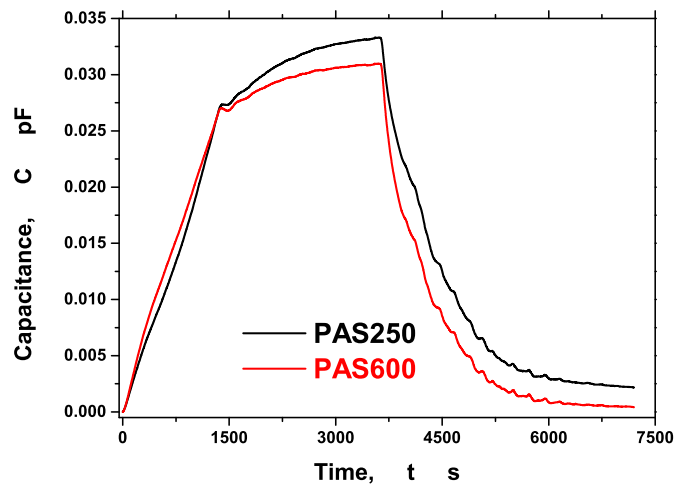


Figure 4.14: Validation test results for test condition 5.



The sensitivity of temperature and moisture loads from the validation test results on the MEMS pressure sensor paved the way for a detailed investigation on the design and structure of the silicon-die. This chapter describes the considered design, deflection of the pressure-sensitive membrane, and a comparison with analytical equations. A brief discussion on equations describing analytical capacitance using the membrane deformation from the simulations is presented. Furthermore, the silicon die's intrinsic thermal behavior is also illustrated by comparing the simulation results against the validation tests under different temperature, moisture, and mechanical bending loads.

## 5.1 Geometry

The validation tests performed under different loading conditions resulted in more substantial influence from the temperature loads (see Figure 4.7) than moisture and mechanical bending loads. A detailed investigation was performed to understand the capacitive pressure sensor's thermal behavior fabricated using the silicon-die and membrane. To do so, SEM (Scanning Electron Microscopy) scans were considered over the cross-section of the considered MEMS sensor. Figure 5.1 describes the detailed description of the silicon-die in the capacitive MEMS pressure sensor. As discussed in section 4.1, two parallel electrodes form a typical capacitive pressure sensor, which is micromachined on the surface of the silicon-die.

The pressure-sensitive membrane (top movable electrode) is a mixture of thin layers of silicon nitride ( $1.25\ \mu\text{m}$ ) and tungsten oxide ( $0.55\ \mu\text{m}$ ), while the bottom fixed electrode is a thin layer of aluminum material ( $< 0.5\ \mu\text{m}$ ). The silicon-die is considered to be made up of a Pyrex-7740 wafer. The distance between electrodes or vacuum distance  $d_0$  (impossible to measure as there is a small deflection of the membrane from atmospheric pressure before the start of the tests) is considered to be ( $\approx 0.8 - 0.9\ \mu\text{m}$ ). Furthermore, the SEM scans also describe the pressure-sensitive membrane geometry; there are two rectangular membranes in parallel. These membranes have a fixed length of  $700\ \mu\text{m}$  and width of  $180\ \mu\text{m}$ . The distance between the two parallel membranes is nearly  $87\ \mu\text{m}$ .

Based on the SEM scan, for the local silicon-die numerical simulation, the model illustrated in Figure 5.2 was used. Two parallel rectangular pressure-sensitive membranes of dimensions  $700 \times 180 \times 1.8\ \mu\text{m}$  were considered. The individual membrane layers were taken into consideration. They are named Membrane - 1 (Silicon Nitride) and

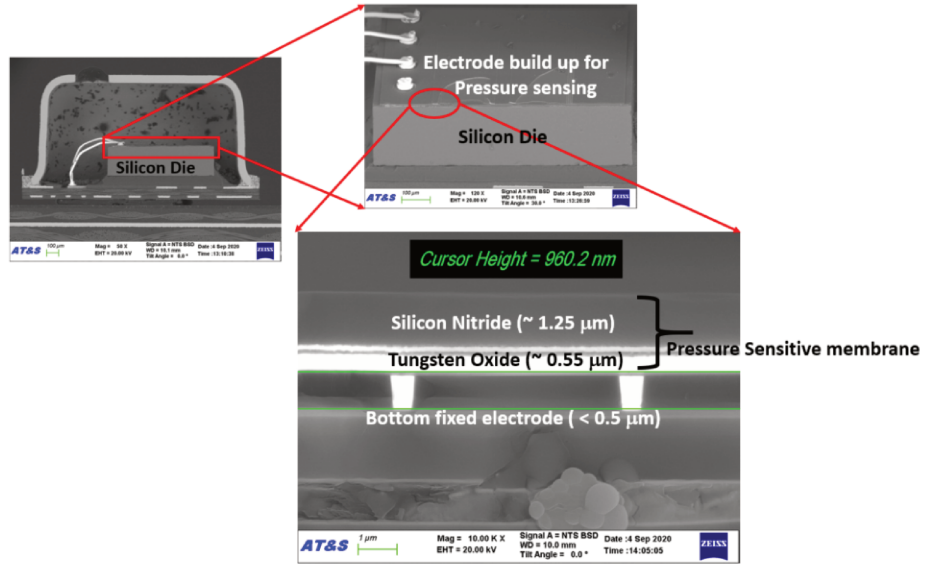


Figure 5.1: Overview and design of the pressure sensitive membrane using SEM scans.

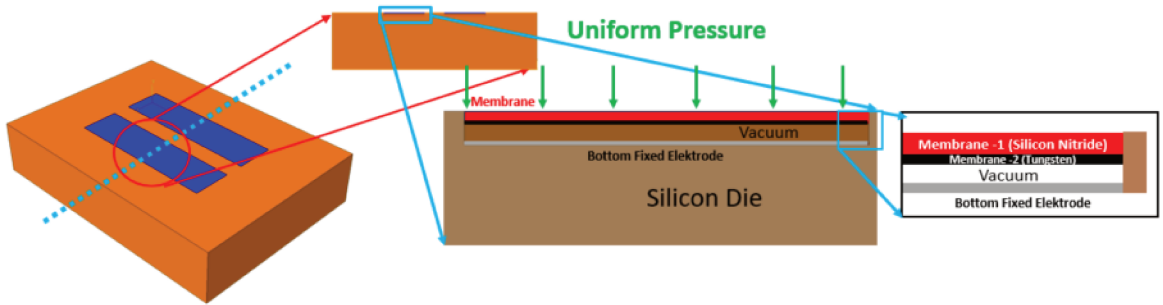


Figure 5.2: Design consideration for the numerical modeling of silicon die.

Membrane - 2 (Tungsten). Furthermore, the vacuum distance between the membrane and bottom electrode is considered to be  $d_0 = 0.9 \mu\text{m}$ .

The material properties for the metalloids (Silicon-die, Silicon nitride, Tungsten, and aluminum) were considered from the literature [16, 25, 48, 88, 96, 129]. The mechanical and thermal material properties for the metalloids are provided in table 5.1.

In the next section, the deflection of the membrane under uniform pressure load is

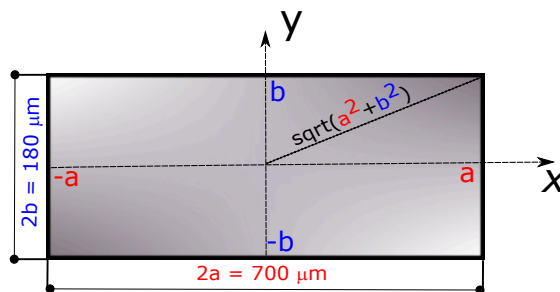
**Table 5.1:** Mechanical and thermal properties of Metalloids.

| Parameter (Unit)                | Membrane-1      | Membrane-2 | Fixed Electrode | Silicon Die |
|---------------------------------|-----------------|------------|-----------------|-------------|
| Material                        | Silicon Nitride | Tungsten   | Aluminum        | Pyrex-7740  |
| Young's modulus (GPa)           | 350             | 450        | 68              | 60          |
| Poisson's Ratio                 | 0.29            | 0.28       | 0.35            | 0.25        |
| CTE( $10^{-6} \text{ K}^{-1}$ ) | 2.33            | 4.4        | 21.5            | 4.6         |

numerically computed. Additionally, the obtained membrane deflection is compared with different analytical deflection shape functions using plate theory.

## 5.2 Membrane Analysis

The capacitive MEMS pressure sensor's sensitivity depends on the change in capacitance [25]. Therefore, to calculate the capacitance between the deformed membrane (for any amount of deformation) and the fixed bottom electrode, accurate analytical models are necessary. The center of the membrane deflects more than the edges of the membrane (edges are rigidly clamped), forming a cosine-like deflection curve. To design an accurate capacitance pressure sensor, both deflection of the membrane's center and deformed shape of the membrane plays a vital role [88]. Therefore, analytical shape functions help in determining the deformation of the membrane under uniform pressure load. Many studies show the use of plate or membrane theory [30, 75, 117] to capture the functional form of the membrane deformation. Therefore, in this section, the simulated membrane deflection is compared with different analytical rectangular shape functions.


**Figure 5.3:** Schematic representation of the rectangular membrane with dimensions.

The deflection of a clamped rectangular membrane (see Figure 5.3) under uniform external pressure is given by;

$$w(x, y) = w_0 \times w'(x, y) \quad (5.1)$$

where  $w_0$  is the maximum deflection at the center of the membrane and  $w'(x, y)$  is the deflection shape function capturing the functional form of the membrane deformation. Furthermore, the membrane is assumed to be homogeneous and isotropic with perfect edge conditions.

### 5.2.1 Membrane Center Deflection $w_0$

The maximum deflection at the center  $w_0$  of the membrane with uniform pressure  $P$  for a prestressed  $\sigma_0$  rectangular membrane is given by equation 5.2 (load deflection model) [105].

$$P = C_1 \left( \frac{\sigma_0 h}{a^2} \right) w_0 + C_2 \left( \frac{E h}{a^4} \right) w_0^3 \quad (5.2)$$

where  $h$  is thickness,  $a$  is longest side length,  $E$  is the Young's modulus of the membrane. The constants  $C_1$  and  $C_2$  can be determined by the membrane shape  $\frac{a}{b} = \frac{1}{n}$  and Poisson's ratio  $\nu$  using the equations 5.3. Furthermore, equation 5.2 is a cubic equation and can be solved using MATLAB-2020a (The MathWorks, Inc., Natick, Massachusetts, United States).

$$C_1 = \frac{\pi^4 (1 + n^2)}{64}$$

$$C_2 = \frac{\pi^6}{32(1 - \nu^2)} \left\{ \frac{9 + 2n^2 + 9n^4}{256} - \left[ \frac{(4 + n + n^2 + 4n^3 - 3n\nu(1 + n))^2}{2\{81\pi^2(1 + n^2) + 128n + \nu[128n - 9\pi^2(1 + n^2)]\}} \right] \right\} \quad (5.3)$$

$C_1$  and  $C_2$  are calculated as 1.6221 and 0.8557 for Poisson's ratio  $\nu = 0.29$ , for the rectangular membrane considered in this research work. The  $w_0$  of the membrane was evaluated both analytically and numerically. The prestress or internal stress in the membrane was considered to be  $\sigma_0 = 200$  MPa and the uniform pressure load  $P$  is applied from 0 to 0.1 MPa (1 bar normal atmospheric pressure) over the intervals of 0.01 MPa.

Figure 5.4 shows the results obtained for center deflection computed using the analytical equation and simulation at different uniform pressures. The deflection of the center from the simulation is in close agreement with the analytically computed deflection. The blue dotted line represents the distance between the pressure-sensitive membrane and the bottom fixed electrode considered to be  $d_0 = 0.9 \mu\text{m}$ . At 0.09 and 0.1 MPa, the pressure-sensitive membrane touches the bottom fixed electrode. If this event occurs in a real-time application, then the capacitance is known as collapse capacitance.

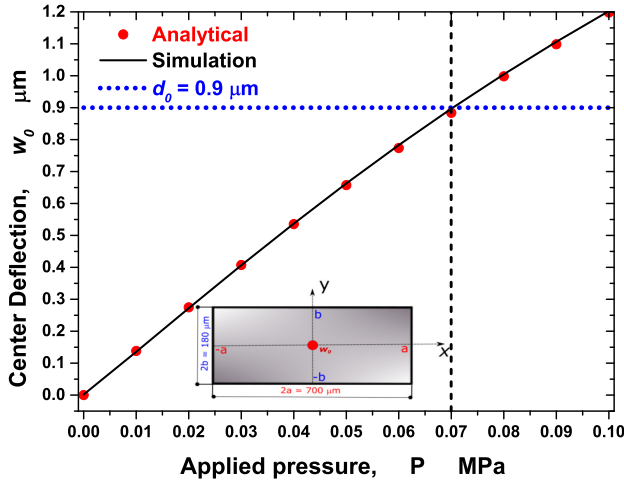


**Figure 5.4:** Comparison of the membrane center deflection between the analytical equation 5.2 and numerical simulation.

The material between the electrodes is considered to be vacuum ( $\epsilon_r = 1$ ). In reality, the vacuum is not ideal, i.e., there is a small pressure in a vacuum, which is assumed to be 0.02 and 0.03 MPa. The applied uniform pressure  $P$  balances with the pressure in a vacuum. Therefore, a uniform pressure load of  $P = 0.07$  MPa is considered for further numerical modeling of shape functions and computation of analytical capacitance. For 0.07 MPa, the membrane is close enough and would not touch the bottom fixed aluminum electrode.

### 5.2.2 Deformed Membrane Shape Function $w'(x, y)$

The shape function  $w'(x, y)$  is necessary to evaluate the membrane's overall deflection. The product of center deflection  $w_0$  and  $w'(x, y)$  (see equation 5.1) is deflection of the membrane. The  $w'(x, y)$ , which is independent of the membrane center deflection  $w_0$ , is computed using the basic shape function from [67, 88, 108, 129]. These shape functions help in capturing the deformed non-linear behavior of the membrane. The basic shape function for  $w'(x, y)$  has been categorized as  $R_1(x, y)$ ,  $R_2(x, y)$ ,  $R_3(x, y)$ , and  $R_4(x, y)$ . These shape functions are chosen for comparison as they are most widely used due to their simplicity.

$$R_1(x, y) = \cos \frac{\pi x}{2a} \cdot \cos \frac{\pi y}{2b} \quad (5.4)$$

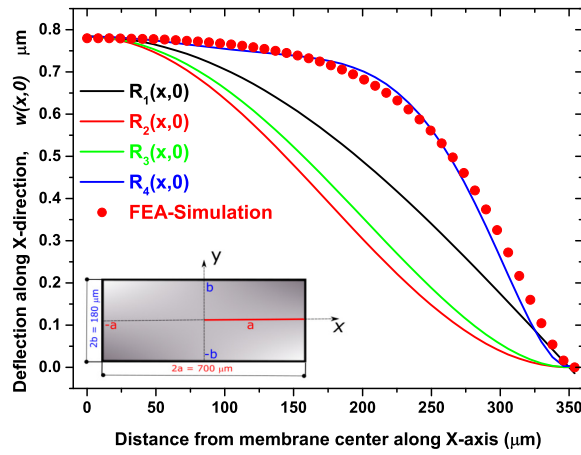
$$R_2(x, y) = \cos^2 \frac{\pi x}{2a} \cdot \cos^2 \frac{\pi y}{2b} \quad (5.5)$$

$$R_3(x, y) = \left(1 - \frac{x^2}{a^2}\right)^2 \left(1 - \frac{y^2}{b^2}\right)^2 \quad (5.6)$$

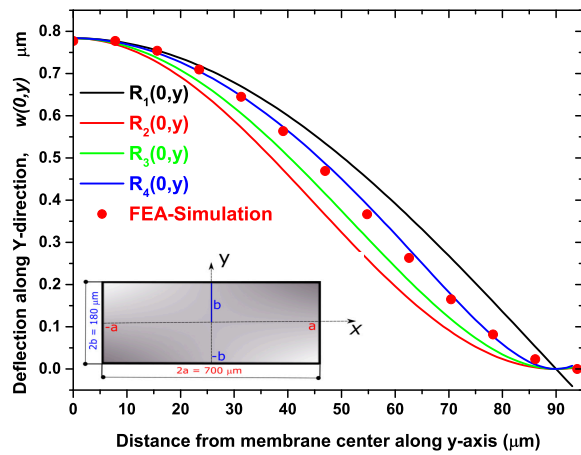
$$R_4(x, y) = \left(1 - \frac{x^2}{a^2}\right)^2 \left(1 - \frac{y^2}{b^2}\right)^2 \left(1 + C_1 \frac{x^2}{a^2} + C_2 \frac{x^4}{a^4} + C_3 \frac{y^2}{b^2} + C_4 \frac{y^4}{b^4}\right) \quad (5.7)$$

The evaluation of the deflection of the rectangular membrane was investigated using the defined shape function in MATLAB and the center deflection  $w_0 = 0.884 \mu\text{m}$  of the membrane at uniform pressure of 0.07 MPa. The results from the membrane deflection simulation using FEA under a uniform pressure load of 0.07 MPa are compared with analytically computed membrane deflection. The analytical shape function equation, which agrees with FEA results, was further considered for analytical capacitance computation. The membrane deflection was evaluated from the membrane center along the x-axis, y-axis, and diagonal direction.

Figures 5.5 show a comparison of FEA determined deflection profiles of the membrane along X (5.5 (a)) and Y (5.5 (b)) direction from the center, respectively. The deflection profiles are obtained using the shape functions  $R_1(x, y)$ ,  $R_2(x, y)$ ,  $R_3(x, y)$ , and  $R_4(x, y)$ . From the figures, it is evident that  $R_4(x, y)$  shape function agrees closely with the deflection profile from FEA along both X and Y-directions. In contrast, the other shape functions predict lower deflection profiles than results from FEA.



(a) X-axis.



(b) Y-axis.

**Figure 5.5:** Comparison of FEA deflection profile of membrane with the existing shape functions. Figure 5.5 (a) X-direction, whereas Figure 5.5 (b) belongs to the Y-direction.

The deflection profile for the membrane along the diagonal direction (center to top right corner) is illustrated in Figure 5.6. From the figure,  $R_4(x, y)$  shape function predicts the membrane’s overall deflection profile along the diagonal direction. Therefore, compared with other shape functions,  $R_4(x, y)$  predicts the membrane’s deflection accurately along X, Y, and diagonal directions. Thus, shape function  $R_4(x, y)$  was

further used for the computation of the analytical capacitance. Furthermore, the constants in  $R_4(x, y)$  were evaluated by performing an analytical fit to FEA's deflection profile. The obtained values are:  $C_1 = 0.4$ ,  $C_2 = 6$ ,  $C_3 = 0.4$ , and,  $C_4 = 0.9$ .

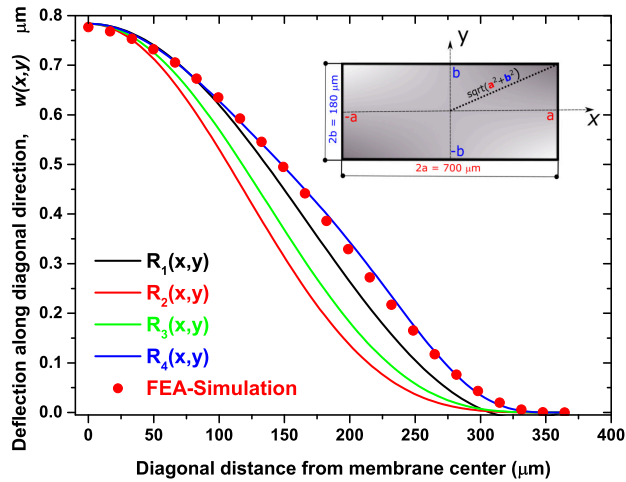


**Figure 5.6:** Comparison of FEA deflection profile with the considered shape functions, plotted from center along the diagonal axis.

### 5.3 Analytical Capacitance

From the validation tests (see chapter 4), the capacitance was measured for the sensors (PAS250 and PAS600) considered under different temperature, moisture, and mechanical loads. To validate the experimental results, with the help of virtual FEA models, an analytical equation for the capacitance is necessary. The numerical evaluation of capacitance using ABAQUS™ is impossible, as one has to perform an electrostatic analysis to evaluate the capacitance between two parallel electrodes. Therefore, an alternative method is necessary to evaluate the capacitance.

Figure 4.1 shows the scheme of the considered capacitive pressure sensor. The thin pressure-sensitive top membrane represents the flexible electrode of the parallel plate capacitor. In contrast, an aluminum electrode acts as a metallic layer deposited on the silicon-die substrate representing a fixed electrode of the capacitor. The deflection of the top flexible membrane due to the external uniform pressure  $P$  changes the sensor's capacitance. Therefore, using the defined analytical equations (see section 5.2) for



the membrane deflection, the analytical capacitance can be easily computed. The capacitance value at rest is known as null capacitance and is given by [33];

$$C_0 = \epsilon_r \epsilon_0 \frac{A}{d_0} \quad (5.8)$$

In equation 5.8,  $\epsilon_r$  is the dielectric constant of the material between the plates ( $\epsilon_r = 1$  for vacuum),  $\epsilon_0$  is the electric constant ( $\epsilon_0 = 8.854 \times 10^{-12} \text{ F m}^{-1}$ ),  $A$  is the area of the plates, and  $d_0$  is the distance between the plates. Furthermore, the parallel plate capacitance between the deflected membrane and the fixed bottom aluminum electrode is given by [33];

$$C_{Deflect} = \epsilon_0 \iint_A \frac{dx dy}{d_0 - w(x, y)} \quad (5.9)$$

where  $w(x, y)$  is the deflection of the rectangular membrane obtained by using equation 5.1. The center deflection of the membrane  $w_0$  can be computed by using the cubic equation 5.2 for applied uniform pressure of 0.07 MPa. The deformed shape function  $w'(x, y)$  is evaluated using the equation 5.7.

Using equation 5.1 in 5.9, and solving the double integrals using binomial expansion of the denominator, the analytical capacitance can be expressed as a function of  $d_0$  (see equation 5.10)

$$C(d_0) = C_0 \left[ 1 + 0.2 \left( \frac{w_0}{d_0} \right) + 5 \left( \frac{w_0}{d_0} \right)^2 \right] \quad (5.10)$$

All equations necessary for the evaluation of the analytical capacitance are established. The following steps were involved for the numerical validation of the experimental tests:

- Initially, the numerical evaluation of distance between the pressure-sensitive membrane and fixed electrode  $d_0$  is performed using different simulation approaches (advanced hygro-thermo-mechanical simulation) for an applied uniform pressure load  $P = 0.07 \text{ MPa}$ .
- The evaluated  $d_0$  from the simulation is used in the equation 5.10 to compute the analytical capacitance

In the next section, the thermal behavior of different materials used in the silicon die for pressure sensing is studied. Furthermore, the results from the temperature-dependent analytical capacitance evaluations are compared against the experimental test results.

## 5.4 Intrinsic Thermal behavior

The validation test results showed that the influence of temperature on capacitance readout was significant compared with moisture and mechanical bending loads. Figure 5.7 shows a summary of the validation tests. To summarize, the temperature loads have a significant influence on the capacitance readout for PAS250 and PAS600 sensors from the validation tests. The moisture loads did not show any change in the capacitance. The influence of bending loads is relatively small compared with temperature loads but higher than moisture loads. In bending, the PAS250 pressure sensor showed a substantial increase compared with PAS600. This capacitance increase is mainly attributed to changes in the silicon-die thickness of the MEM sensors' two flavors.

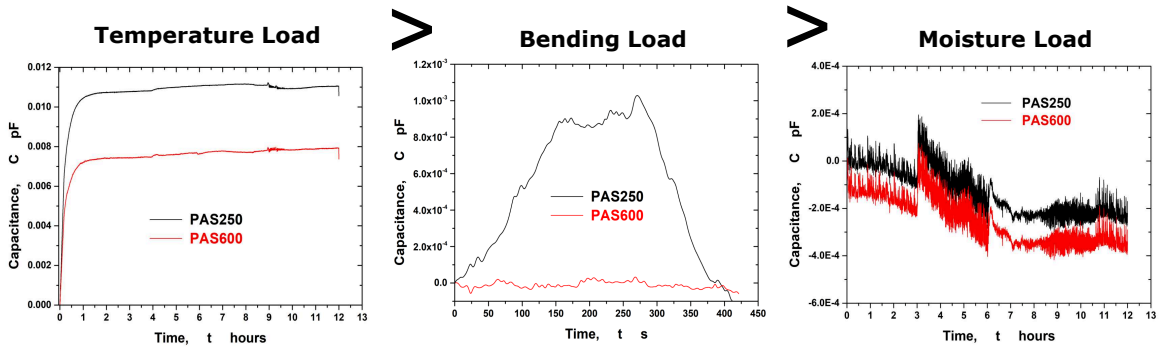


Figure 5.7: Summary of the validation tests.

Many studies [13, 16, 77] have shown that the increase in temperature can modify the membrane thickness  $h$ , the distance between the electrodes  $d_0$  and as a consequence, the capacitance  $C$  is affected. The variations in the capacitive pressure sensor's dimensions due to temperature effects are referred to as intrinsic thermal variations [16]. Thermal expansion [26, 89] of the materials causes the intrinsic thermal behavior. Under  $150^\circ\text{C}$ , the CTE of Silicon Nitride pressure-sensitive membrane ( $2.33 \times 10^{-6} \text{K}^{-1}$ ) is lower than Pyrex 7740 wafer ( $4.6 \times 10^{-6} \text{K}^{-1}$ ). As a result, within the temperature range of  $23^\circ\text{C}$  -  $150^\circ\text{C}$ , the distance between the plates  $d_0$  decreases with an increase in temperature, thus, causing the capacitance to increase.

The thermal influence on the capacitance readout of a pressure sensor fabricated using silicon nitride membrane and silicon-die (Pyrex-7740 Wafer) is analyzed by performing local numerical modeling shown in Figure 5.2. Doing so, the evaluation of change in deflection of the membrane due to thermal variations was performed using advanced hygro-thermo-mechanical simulation (see section 3.5). The numerical modeling for the chip was performed for the temperature conditions from test condition - 5 (see Figure 4.14) of the validation test. Furthermore, to account for the thermal

effects from the polymeric materials in the MEMS pressure sensor, local sub modeling of the PAS250 sensor was performed using the global model's (section 3.4.2) boundary conditions.

### 5.4.1 Results

The test condition-5 of the validation test was performed to determine the higher temperature influence on the MEMS sensor's capacitance signals. In this test case, the moisture loads were not considered. The results obtained from the local model of the chip under thermal distribution are illustrated in Figure 5.8.

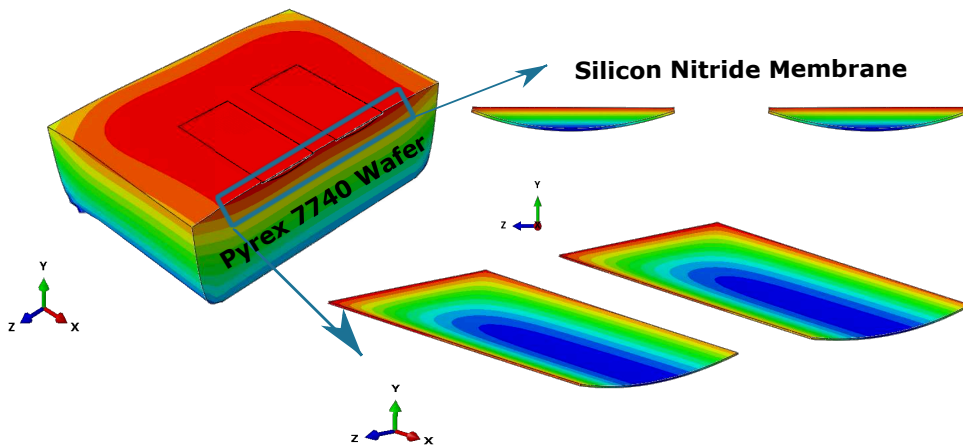


**Figure 5.8:** Volumetric thermal expansion of the silicon-die due to intrinsic thermal behavior of the materials at 140 °C.

The figure represents the deformation behavior of the silicon-die substrate (Pyrex-7740 wafer) compared with the membrane (Silicon Nitride) at a temperature of 140 °C. The CTE of the Pyrex-7740 wafer is higher than the silicon nitride membrane. Therefore, due to the volumetric expansion of the silicon-die with increase in temperature, the distance between the membrane and bottom fixed electrode ( $d_0$ ) decreases with temperature increase. Consequently, according to equation 5.8, with a decrease in the distance  $d_0$ , the capacitance increases.

Furthermore, obtained deflection profiles of the pressure-sensitive membrane from only chip and local sub modeling of a PAS250 pressure sensor are illustrated in Figure 5.9. From the figure, the variation of the membrane under higher temperature loads can be observed. Initially, the deflection of the membrane at 23 °C is zero, but as the temperature increases, the deflection of the membrane or the distance  $d_0$  decreases.

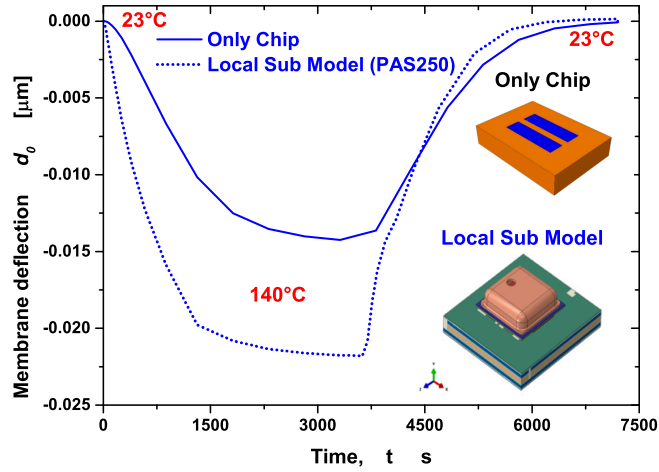
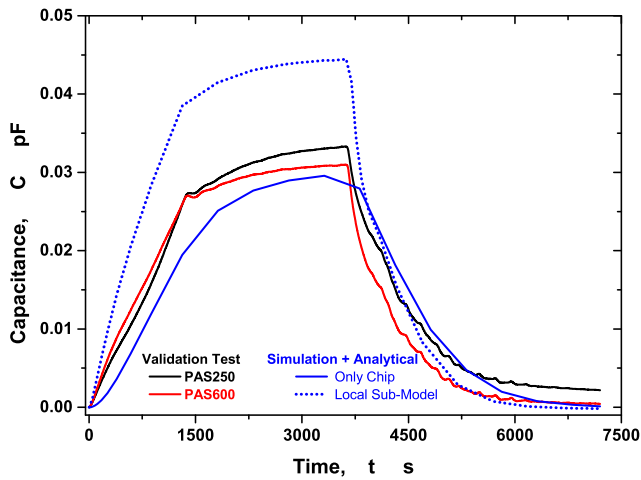


Figure 5.9: The deflection of the membrane due to thermal loads from test condition-5.

The decrease is attributed due to intrinsic thermal behavior between the membrane and the silicon-die. Furthermore, with the decrease in temperature from 140 °C to 23 °C, the deflection of the membrane reduces to zero. The figure also illustrates the dependency of the local sub-model of pressure sensor PAS250. The sub modeling approach considers additional polymeric materials within the entire pressure sensor. Due to different thermal expansion coefficients between the materials, the local sub-model membrane deflection is higher than that of chip only.

Additionally, the only chip model consists of metalloid materials (pressure-sensitive membrane, silicon-die, and bottom fixed aluminum electrode). The deflection of the membrane does not consider the influence of the polymeric materials’ thermal expansion. Henceforth, the deflection of the membrane is smaller than that of the local sub-model. Figure 5.9 also signifies the material dependency in different modeling levels. In the next step, the calculated membrane deflection profiles from the simulation are used as an input for the equation 5.10 to compute the numerical capacitance indirectly.

Figure 5.10 depicts the evaluated capacitance using the deflection profiles from Figure 5.9 for only chip and local sub-model. The analytical capacitance was compared with the temperature-dependent validation test condition-5. The distance  $d_0 = 0.9 \mu\text{m}$  and uniform pressure load of  $P = 0.07 \text{ MPa}$  was considered on the surface of the sensitive membrane while computing the analytical capacitance. As discussed earlier, the distance  $d_0$  is impossible to measure, and this parameter plays a significant role in



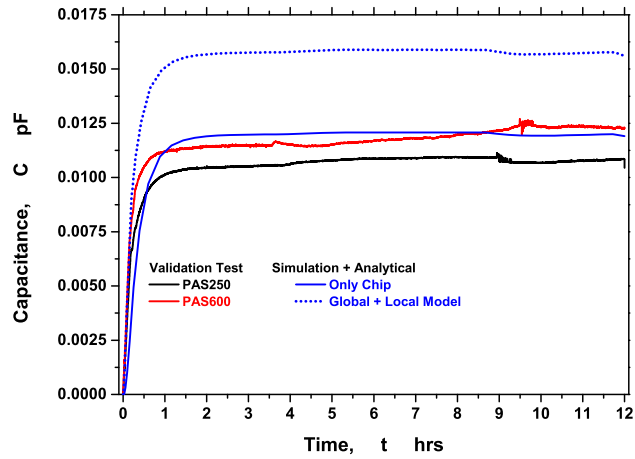
**Figure 5.10:** Comparison of simulation+analytical capacitance with the capacitance readout from test condition-5.

evaluating the analytical capacitance. The increase in  $d_0$  decreases in capacitance and vice versa. Based on the FEA simulation of the only chip model and also from SEM images (see section 5.1), the value of  $d_0 = 0.9 \mu\text{m}$  was considered.<sup>3</sup>

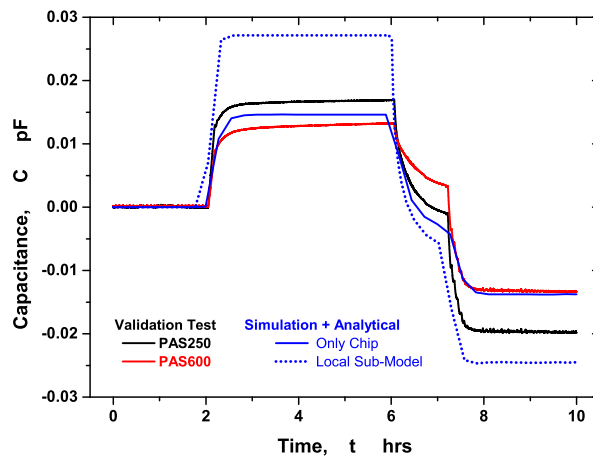
From the Figure 5.10, the calculated analytical capacitance using membrane deflection from the simulation is in close agreement with the capacitance readout from the test. The solid blue lines represent the results for the only chip and blue dotted lines for the local sub-model. The increase in capacitance in the local sub-model is attributed to the consideration of complete pressure sensor assembly (PAS250 and PAS600). The dependency of the polymeric materials plays a significant role in the analytical computation of the capacitance. Due to different thermal and hygroscopic expansion coefficients, a mismatch between the multi-material assembly leads to higher deformation of the pressure-sensitive membrane. As a result, the capacitance increases.

Additional temperature-dependent tests i.e., test condition 2 (figure 4.7) and test condition 4 (figure 4.13) were validated using the similar modeling procedure discussed above. The results obtained for the analytical capacitance were within the range of the experimental capacitance for test conditions 2 and 4. Figure 5.11 depicts the analytical capacitance results from only chip and local sub-model compared against the experi-

<sup>3</sup> The displayed results from Chapter 5 is in the process of publication by Yalagach,M., Fuchs,P.F, Antretter, T., Feuchter, M., Weber,M., and Tao,Q.



(a) Test condition 2.



(b) Test condition 4.

**Figure 5.11:** Comparison of simulation+analytical capacitance with the capacitance readout from . Figure 5.11 (a) test condition-2 , whereas Figure 5.5 (b) belongs to the test condition-4 .

mental capacitance readout from the validation tests (2 and 4).

In the next section, the influence of moisture loads from test condition 1 (see Figure 4.5) and mechanical bending loads from test condition 3 (see Figure 4.9) is validated using the analytical capacitance equation.

### Moisture loads

The discussed modeling procedure was used to compute the analytical capacitance under moisture loads. To do so, the validation test condition 1 (see Figure 4.5) was taken into consideration. In this test, the moisture loads were varied dynamically under constant temperature. The test was validated considering two different material combinations MAT-1 and MAT-2. The MAT-1 shows lower hygro-thermal expansion compared with MAT-2. The description of the material combinations used for this study is explained in detail in chapter 3 and 4. The deflection of the pressure-sensitive membrane was evaluated considering the local sub-model of the PAS250 pressure sensor. The influence of the dynamic moisture loads was computed using the advanced hygro-thermo-mechanical simulation model (section 3.5).

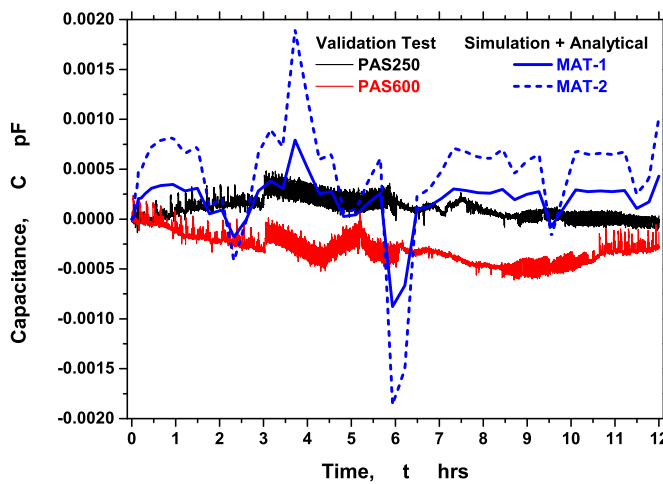


**Figure 5.12:** Comparison of simulation+analytical capacitance with the capacitance readout from test condition-1.

The results obtained from the simulation+analytical capacitance for the test condition 1 is illustrated in Figure 5.12. From the figure, the capacitance results from MAT-1 (solid blue lines) combination is in correlation with test results. In contrast, the material combination MAT-2 (dashed blue lines) depicts a higher capacitance compared with MAT-1. The higher capacitance is due to the material combination MAT-2 exhibiting higher hygro-thermal expansion than combination MAT-1. Furthermore, the scattering in the simulation+analytical capacitance is attributed to the scattering of temperature and moisture loads.

### Four-Point Mechanical Bending loads

The test condition 3 from the validation test involves a four-point bending load at constant room temperature 23 °C and constant moisture or humidity of 50% RH. The test was validated using the modeling procedure discussed above, and to account for temperature and moisture loads, the advanced simulation model (section 3.5) was considered. The test was validated for both PAS250 and PAS600 types of the capacitive pressure sensor. The deflection of the pressure-sensitive membrane was evaluated considering the local sub-model of PAS250 and PAS600 pressure sensors. Furthermore, for PAS250, the change in capacitance due to change in the distance between the electrodes  $d_0$  was also studied for  $d_0 = 0.85, 0.9, 0.95,$  and  $1 \mu\text{m}$ .

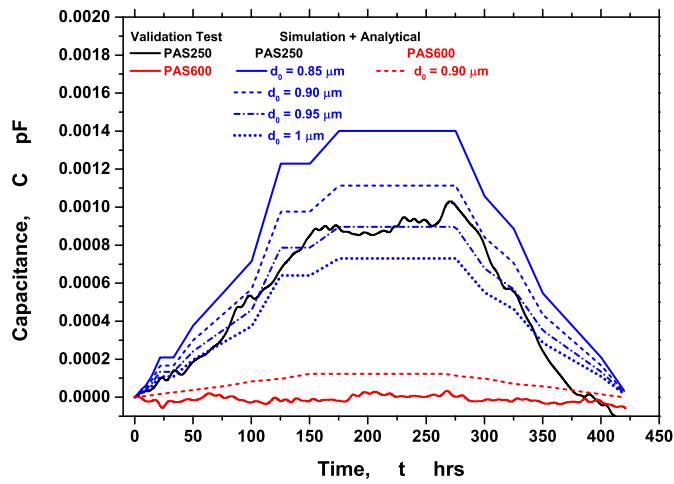


**Figure 5.13:** Comparison of simulation+analytical capacitance with the capacitance readout from test condition-3.

Figure 5.13 depicts the results obtained from the simulation+analytical capacitance for the test condition 3 for PAS250 and PAS600 pressure sensor. The capacitance increases under bending load for the PAS250 sensor. Consequently, for the PAS600 sensor, the test and simulation capacitance did not show significant changes under the four-point bending loads. Additionally, the capacitance from the simulation+analytical approach follows a similar trend compared with the validation test. Therefore, the simulation+analytical and test capacitance are in good agreement for both flavors (PAS250 and PAS600) of the pressure sensor.

Additionally, the dependency of distance  $d_0$  on change in capacitance for PAS250 sensor is illustrated in Figure 5.13. From the equation 5.8, as distance  $d_0$  increases,



the capacitance decreases and vice versa. From the simulation, for  $d_0 = 0.85 \mu\text{m}$ , the capacitance change is higher compared with other  $d_0$  distance's. Thus, the initial distance  $d_0$  between the electrodes describes the capacitance change. Therefore, the sensitivity in  $d_0$  can be predicted with the help of the described simulation model.



As discussed in section 1.3, the aim, objectives, and challenges have been successfully achieved by performing thermal and moisture dependent material characterization for the polymeric materials involved in the MEMS sensor package. Furthermore, with the help of the material properties, virtual simulation strategies were implemented to predict the MEMS package deformation behavior under thermal, moisture, and mechanical loads. The conclusion drawn and the proposed future work of this research has been briefly discussed in this chapter.

## 6.1 Conclusion

In the framework of this research, the following conclusions were drawn;

1. The results from thermo-mechanical and moisture dependent material characterization for the epoxy-based polymers are presented.
2. A change in thermal expansion and mechanical strength of epoxy-based polymeric materials under the influence of temperature is captured.
3. The thermal properties like in-plane CTE  $\alpha(T)$  and thermal conductivity  $\lambda(T)$  help predict the right material choice for the MEMS sensor packages.
4. The absorption of moisture in polymeric materials is attributed to the formation of hydrogen bonds between the water molecules and hydroxyl groups in polymers.
5. The diffusion of moisture described by analytical models like single and dual Fickian depends on the  $T_g$  of the polymers. Below  $T_g$ , dual Fickian diffusion behavior was observed, and above  $T_g$  the material followed a single or Fickian diffusion model.
6. The impact of temperature on moisture absorption was observed by performing experiments under different conditioning environments.
7. The measured moisture expansion coefficient (CME) depends on  $T_g$  and conditioning temperature.
8. The measured in-plane CTE  $\alpha(T)$  and in-plane CME  $\beta(T)$  serve as a material property to analyze the thermal and moisture mismatch in the MEMS sensor package

9. Measured moisture and temperature-dependent Young's moduli provide critical information on shifts in the prepregs' mechanical properties due to moisture absorption and thermal distribution, respectively.
10. The verification simulation model describes the implemented dual-Fickian diffusion model.
11. The virtual numerical model, i.e. the hygro-thermo-mechanical simulation approach describes discontinuity in the moisture concentration using global and local sub-modeling simulation approaches.
12. The deformation behavior of the MEMS sensor packages under dynamic thermal and moisture distribution was numerically solved using an advanced hygro-thermo-mechanical simulation approach. To this end, a thermal-moisture analogy was implemented.
13. The implemented virtual modeling approaches also describe the effects and emphasize the importance of the choice of the material combination.
14. The performed validation tests showed significant effects from temperature loads than from moisture and mechanical bending loads in a capacitive pressure sensor's capacitance readout.
15. The silicon die deformation from the virtual modeling was compared against the validation tests' capacitance readout and found to be in good agreement.
16. The silicon-die thickness plays a significant role in the evaluation of the strains and capacitance. The higher silicon die thickness sensor (PAS600) showed negligible influence compared to the lower silicon die thickness sensor (PAS250).
17. The deformation of the pressure-sensitive membrane describes the capacitance sensitivity of a capacitive pressure sensor.
18. The intrinsic thermal variation between the metalloids micromachined on the silicon-die substrate significantly impacts the capacitance readout during the temperature-dependent validation tests.
19. The tests' results were validated using the membrane deflection approach by computing the simulation + analytical capacitance. The results obtained were in close agreement compared with validation tests' capacitance readouts.
20. The membrane deflection also describes the influence of moisture and mechanical bending loads on the silicon-die deformation behavior.

## 6.2 Outlook

The proposed virtual simulation strategies may be expanded by including the effective residual stresses during the MEMS sensors' processing. This can be achieved by including a curing simulation for the epoxy-based adhesives in a thermal simulation step. The effect of residual stress helps analyzing the material history of the adhesives during the processing of the packages.

The effects of viscoelasticity of the polymeric material can also be included by performing creep and stress relaxation measurements for the polymeric materials. The viscoelastic effects help to predict more realistic deformation behavior of the silicon die when conditioned for long durations.

The effect of cyclic moisture diffusion can also be taken into account by performing the cyclic moisture absorption and desorption for the polymeric materials. The cyclic moisture diffusion predicts the moisture concentration in the polymeric materials after exposure to varying environmental loading situations.

Long-term ingress of moisture into polymeric material causes not only deformation but also potential delamination of the adhesive joints. Modeling delamination can be achieved by considering different failure models (cohesive zone and continuum damage models). This information would give more trust in the utilization of the approach for industrial applications.

Furthermore, it is advisable to consider the parasitic and fringing field capacitance during the analytical computation of the capacitance. This information would consider the effects of metallic materials and predict the capacitance change more accurately in the capacitive pressure sensor system.

To conclude, using the implemented virtual simulation strategies, it is possible to evaluate microelectronic systems' (MEMS sensor packages) deformation behavior accurately and efficiently under different environmental and mechanical loading conditions. These models serve as a basis for the lifetime assessment and reliability of the sensor system design.



# Bibliography

---

- [1] AVNET Abacus. *Piezoresistive pressure sensors*. 2021. URL: <https://www.avnet.com/wps/portal/abacus/solutions/technologies/sensors/pressure-sensors/core-technologies/piezoresistive-strain-gauge/> (visited on 01/25/2021) (see page 6).
- [2] **ABAQUS/Standard User's Manual, Version 6.17**. English. Tech. rep. United States, 2017 (see pages 42–45).
- [3] Thomas M. Adams and Richard A. Layton, 167–210. In: *Introductory MEMS: Fabrication and Applications*. Boston, MA: Springer US, 2010. ISBN: 978-0-387-09511-0. DOI: [10.1007/978-0-387-09511-0\\_7](https://doi.org/10.1007/978-0-387-09511-0_7). URL: [https://doi.org/10.1007/978-0-387-09511-0\\_7](https://doi.org/10.1007/978-0-387-09511-0_7) (see page 2).
- [4] Michael J. Adamson. **Thermal expansion and swelling of cured epoxy resin used in graphite/epoxy composite materials**. *Journal of Materials Science* 15:7 (July 1980), 1736–1745. DOI: [10.1007/bf00550593](https://doi.org/10.1007/bf00550593). URL: <https://doi.org/10.1007/bf00550593> (see page 14).
- [5] Sohaib Akbar and Tao Zhang. **Moisture Diffusion in Carbon/Epoxy Composite and the Effect of Cyclic Hygrothermal Fluctuations: Characterization by Dynamic Mechanical Analysis (DMA) and Interlaminar Shear Strength (ILSS)**. *The Journal of Adhesion* 84:7 (Aug. 2008), 585–600. DOI: [10.1080/00218460802255434](https://doi.org/10.1080/00218460802255434). URL: <https://doi.org/10.1080/00218460802255434> (see page 19).
- [6] Ahmed M. Almassri, W. Z. Wan Hasan, S. A. Ahmad, A. J. Ishak, A. M. Ghazali, D. N. Talib, and Chikamune Wada. **Pressure Sensor: State of the Art, Design, and Application for Robotic Hand**. *Journal of Sensors* 2015 (2015), 1–12. DOI: [10.1155/2015/846487](https://doi.org/10.1155/2015/846487). URL: <https://doi.org/10.1155/2015/846487> (see page 6).
- [7] **An Introduction to MEMS (Micro-electromechanical Systems)**. In: 2002 (see page 2).
- [8] Antonio Apicella, Luigi Nicolais, Gianni Astarita, and Enrico Drioli. **Effect of thermal history on water sorption, elastic properties and the glass transition of epoxy resins**. *Polymer* 20:9 (Sept. 1979), 1143–1148. DOI: [10.1016/0032-3861\(79\)90307-0](https://doi.org/10.1016/0032-3861(79)90307-0). URL: [https://doi.org/10.1016/0032-3861\(79\)90307-0](https://doi.org/10.1016/0032-3861(79)90307-0) (see page 18).
- [9] H. Ardebili, Ee Hua Wong, and M. Pecht. **Hygroscopic swelling and sorption characteristics of epoxy molding compounds used in electronic packaging**. *IEEE Transactions on Components and Packaging Technologies* 26:1 (2003), 206–214. DOI: [10.1109/TCAPT.2002.806172](https://doi.org/10.1109/TCAPT.2002.806172) (see page 14).
- [10] H. Ardebili, C. Hillman, M. A. E. Natishan, P. McCluskey, M. G. Pecht, and D. Peterson. **A comparison of the theory of moisture diffusion in plastic encapsulated microelectronics with moisture sensor chip and weight-gain measurements**. *IEEE Transactions on Components and Packaging Technologies* 25:1 (2002), 132–139. DOI: [10.1109/6144.991185](https://doi.org/10.1109/6144.991185) (see page 13).

- [11] Siddarud Bannikoppa, A.C. Katageri, Kirankumar Balavalad, and Basavaprabhu Sheeparatti. **Design of Piezoresistive pressure sensor for enhanced sensitivity**. In: Apr. 2016, 706–710. DOI: [10.1109/ICEETS.2016.7583841](https://doi.org/10.1109/ICEETS.2016.7583841) (see page 5).
- [12] Aviru Basu, Shreyansh Tatiya, and Shantanu Bhattacharya. In: Jan. 2019. ISBN: 978-981-13-3290-6. DOI: [10.1007/978-981-13-3290-6\\_7](https://doi.org/10.1007/978-981-13-3290-6_7) (see page 2).
- [13] Abdelaziz Beddiaf, Fouad Kerrou, Lazhar Merouani, and Abdelkrim Rachid. **Effect of Thermal Drift in Sensitivity of Pressure Sensor**. In: *Proceedings of the 4th International Conference on Control, Mechatronics and Automation - ICCMA '16*. ACM Press, 2016. DOI: [10.1145/3029610.3029617](https://doi.org/10.1145/3029610.3029617). URL: <https://doi.org/10.1145/3029610.3029617> (see page 84).
- [14] Geeta Bhatt, Kapil Manoharan, Pankaj Chauhan, and Shantanu Bhattacharya, 223–239. In: Jan. 2019. ISBN: 978-981-13-3289-0. DOI: [10.1007/978-981-13-3290-6\\_12](https://doi.org/10.1007/978-981-13-3290-6_12) (see page 2).
- [15] Bruce Billings. **American Institute of Physics handbook**. New York: McGraw-Hill, 1972. ISBN: 978-0070014855 (see page 41).
- [16] G Blasquez, X Chauffleur, P Pons, C Douziech, P Favaro, and Ph Menini. **Intrinsic thermal behaviour of capacitive pressure sensors: mechanisms and minimisation**. *Sensors and Actuators A: Physical* 85:1-3 (Aug. 2000), 65–69. DOI: [10.1016/S0924-4247\(00\)00369-1](https://doi.org/10.1016/S0924-4247(00)00369-1). URL: [https://doi.org/10.1016/S0924-4247\(00\)00369-1](https://doi.org/10.1016/S0924-4247(00)00369-1) (see pages 4, 6, 67, 76, 84).
- [17] T Boltshauser, M Schonholzer, O Brand, and H Baltes. **Resonant humidity sensors using industrial CMOS-technology combined with postprocessing**. *Journal of Micromechanics and Microengineering* 2:3 (1992), 205–207. DOI: [10.1088/0960-1317/2/3/022](https://doi.org/10.1088/0960-1317/2/3/022). URL: <https://doi.org/10.1088/0960-1317/2/3/022> (see page 4).
- [18] M.R. Bowditch. **The durability of adhesive joints in the presence of water**. *International Journal of Adhesion and Adhesives* 16:2 (1996). Special Issue: In honour of Dr K. W. Allen on the occasion of his 70th birthday, 73 –79. ISSN: 0143-7496. DOI: [https://doi.org/10.1016/0143-7496\(96\)00001-2](https://doi.org/10.1016/0143-7496(96)00001-2). URL: <http://www.sciencedirect.com/science/article/pii/0143749696000012> (see page 18).
- [19] D.M. Brewis, J. Comyn, A.K. Raval, and A.J. Kinloch. **The effect of humidity on the durability of aluminium-epoxide joints**. *International Journal of Adhesion and Adhesives* 10:4 (1990), 247 –253. ISSN: 0143-7496. DOI: [https://doi.org/10.1016/0143-7496\(90\)90042-V](https://doi.org/10.1016/0143-7496(90)90042-V). URL: <http://www.sciencedirect.com/science/article/pii/014374969090042V> (see page 18).
- [20] D.M. Brewis, J. Comyn, and S.T. Tredwell. **Diffusion of water in some modified phenolic adhesives**. *International Journal of Adhesion and Adhesives* 7:1 (1987), 30 –32. ISSN: 0143-7496. DOI: [https://doi.org/10.1016/0143-7496\(87\)90051-0](https://doi.org/10.1016/0143-7496(87)90051-0). URL: <http://www.sciencedirect.com/science/article/pii/0143749687900510> (see page 18).
- [21] R. Buchhold, M. Mueller, A. Nakladal, K. Sahre, K.-J. Eichhorn, and G. Gerlach. **Reduction of mechanical stress in micromachined components caused by humidity-induced volume expansion of polymer layers**. *Microsystem Technologies* 5:1 (Oct. 1998), 3–12. DOI: [10.1007/s005420050133](https://doi.org/10.1007/s005420050133). URL: <https://doi.org/10.1007/s005420050133> (see page 33).



- [22] Javier Burgués and Santiago Marco. **Low Power Operation of Temperature-Modulated Metal Oxide Semiconductor Gas Sensors**. *Sensors* 18:2 (Jan. 2018), 339. DOI: [10.3390/s18020339](https://doi.org/10.3390/s18020339). URL: <https://doi.org/10.3390/s18020339> (see page 1).
- [23] Liangbiao Chen, Jiang Zhou, Hsing wei Chu, Guoqi Zhang, and Xuejun Fan. **Modeling nonlinear moisture diffusion in inhomogeneous media**. *Microelectronics Reliability* 75 (2017), 162–170. DOI: [10.1016/j.microrel.2017.06.055](https://doi.org/10.1016/j.microrel.2017.06.055). URL: <https://doi.org/10.1016%2Fj.microrel.2017.06.055> (see pages 56, 58).
- [24] M.Y.M. Chiang and G.B. McKenna. **Conference Report: Hygrothermal Effects on the Performance of Polymers and Polymeric Composites, Gaithersburg, MD - September 21-22, 1995**. *Journal of Research of the National Institute of Standards and Technology* 101:6 (Nov. 1996), 803. DOI: [10.6028/jres.101.077](https://doi.org/10.6028/jres.101.077). URL: <https://doi.org/10.6028/jres.101.077> (see page 17).
- [25] Franck Chollet and Haobing Liu. **A (not so) short introduction to Micro Electro Mechanical Systems**. 5.4. This is an electronic document published under Creative Commons Attribution-NonCommercial 3.0 License (<http://creativecommons.org/licenses/by-nc/3.0/legalcode>). 2018. ISBN: 978-2-9542015-0-4. URL: <http://memscyclopedia.org/introMEMS.html> (see pages 76, 77).
- [26] A Cozma and B Puers. **Characterization of the electrostatic bonding of silicon and Pyrex glass**. *Journal of Micromechanics and Microengineering* 5:2 (1995), 98–102. DOI: [10.1088/0960-1317/5/2/010](https://doi.org/10.1088/0960-1317/5/2/010). URL: <https://doi.org/10.1088/0960-1317/5/2/010> (see page 84).
- [27] John Crank. **The mathematics of diffusion**. Oxford Eng: Clarendon Press, 1975. ISBN: 978-0198534112 (see page 14).
- [28] A. Damasceni, L. Dei, and F. Guasti. *Journal of Thermal Analysis and Calorimetry* 66:1 (2001), 223–232. DOI: [10.1023/a:1012404218926](https://doi.org/10.1023/a:1012404218926). URL: <https://doi.org/10.1023/a:1012404218926> (see page 13).
- [29] B. Duncan, J. Urquhart, and S. Roberts. **Review of measurement and modelling of permeation and diffusion in polymers**. In: 2005 (see page 18).
- [30] P. . Eccardt, P. Wagner, and S. Hansen. **5F-1 Analytical Models for Micromachined Transducers - An Overview (Invited)**. In: *2006 IEEE Ultrasonics Symposium*. 2006, 572–581. DOI: [10.1109/ULTSYM.2006.151](https://doi.org/10.1109/ULTSYM.2006.151) (see page 77).
- [31] Ee Hua Wong, Yong Chua Teo, and Thiam Beng Lim. **Moisture diffusion and vapour pressure modeling of IC packaging**. In: *1998 Proceedings. 48th Electronic Components and Technology Conference (Cat. No.98CH36206)*. 1998, 1372–1378. DOI: [10.1109/ECTC.1998.678922](https://doi.org/10.1109/ECTC.1998.678922) (see page 44).
- [32] L. El-Sa'ad, M. I. Darby, and B. Yates. **Moisture absorption characteristics of rubber particulate filled epoxy adhesives**. *Journal of Materials Science* 24:5 (May 1989), 1653–1659. DOI: [10.1007/bf01105687](https://doi.org/10.1007/bf01105687). URL: <https://doi.org/10.1007/bf01105687> (see page 17).
- [33] Hussam Eldin A. Elgamel. **A simple and efficient technique for the simulation of capacitive pressure transducers**. *Sensors and Actuators A: Physical* 77:3 (Nov. 1999), 183–186. DOI: [10.1016/s0924-4247\(98\)00355-0](https://doi.org/10.1016/s0924-4247(98)00355-0). URL: [https://doi.org/10.1016/s0924-4247\(98\)00355-0](https://doi.org/10.1016/s0924-4247(98)00355-0) (see page 83).

- [34] Fernand Ellyin and Rachel Maser. **Environmental effects on the mechanical properties of glass-fiber epoxy composite tubular specimens.** *Composites Science and Technology* 64:12 (Sept. 2004), 1863–1874. DOI: [10.1016/j.compscitech.2004.01.017](https://doi.org/10.1016/j.compscitech.2004.01.017). URL: <https://doi.org/10.1016/j.compscitech.2004.01.017> (see page 16).
- [35] Shahram Eslami, Abbas Honarbakhsh-Raouf, and Shiva Eslami. **Effects of moisture absorption on degradation of E-glass fiber reinforced Vinyl Ester composite pipes and modelling of transient moisture diffusion using finite element analysis.** *Corrosion Science* 90 (2015), 168 –175. ISSN: 0010-938X. DOI: <https://doi.org/10.1016/j.corsci.2014.10.009>. URL: <http://www.sciencedirect.com/science/article/pii/S0010938X14004661> (see page 46).
- [36] P. Eswaran and Malarvizhi Subramani. **MEMS Capacitive Pressure Sensors: A Review on Recent Development and Prospective.** *International Journal of Engineering and Technology* 5 (June 2013), 2734–2746 (see page 4).
- [37] X. Fan and Jie-Hua Zhao. **Moisture diffusion and integrated stress analysis in encapsulated microelectronics devices.** In: *2011 12th Intl. Conf. on Thermal, Mechanical Multi-Physics Simulation and Experiments in Microelectronics and Microsystems*. 2011, 1/8–8/8. DOI: [10.1109/ESIME.2011.5765793](https://doi.org/10.1109/ESIME.2011.5765793) (see page 56).
- [38] X.J. Fan, S.W.R. Lee, and Q. Han. **Experimental investigations and model study of moisture behaviors in polymeric materials.** *Microelectronics Reliability* 49:8 (2009). Thermal, mechanical and multi-physics simulation and experiments in microelectronics and micro-systems (EuroSimE 2008, 861 –871. ISSN: 0026-2714. DOI: <https://doi.org/10.1016/j.microrel.2009.03.006>. URL: <http://www.sciencedirect.com/science/article/pii/S0026271409000833> (see pages 16, 18).
- [39] Xuejun Fan. **Mechanics of moisture for polymers: Fundamental concepts and model study.** In: *EuroSimE 2008 - International Conference on Thermal, Mechanical and Multi-Physics Simulation and Experiments in Microelectronics and Micro-Systems*. IEEE, 2008. DOI: [10.1109/esime.2008.4525043](https://doi.org/10.1109/esime.2008.4525043). URL: <https://doi.org/10.1109/esime.2008.4525043> (see page 32).
- [40] Adolph Fick. **On liquid diffusion.** *Journal of Membrane Science* 100:1 (1995). The early history of membrane science selected papers celebrating vol. 100, 33 –38. ISSN: 0376-7388. DOI: [https://doi.org/10.1016/0376-7388\(94\)00230-V](https://doi.org/10.1016/0376-7388(94)00230-V). URL: <http://www.sciencedirect.com/science/article/pii/037673889400230V> (see page 14).
- [41] P. Fuchs, K. Fellner, and Gerald Pinter. **Local damage simulations of printed circuit boards based on in-plane cohesive zone parameters.** *Circuit World* 39 (2013), 60–66 (see page 18).
- [42] P.F. Fuchs, G. Pinter, and M. Tonjec. **Determination of the orthotropic material properties of individual layers of printed circuit boards.** *Microelectronics Reliability* 52:11 (Nov. 2012), 2723–2730. DOI: [10.1016/j.microrel.2012.04.019](https://doi.org/10.1016/j.microrel.2012.04.019). URL: <https://doi.org/10.1016/j.microrel.2012.04.019> (see page 21).
- [43] Anthony H. D. Graham, Jon Robbins, Chris R. Bowen, and John Taylor. **Commercialisation of CMOS Integrated Circuit Technology in Multi-Electrode Arrays for Neuroscience and Cell-Based Biosensors.** *Sensors* 11:5 (May 2011), 4943–4971. DOI: [10.3390/s110504943](https://doi.org/10.3390/s110504943). URL: <https://doi.org/10.3390/s110504943> (see page 1).

- [44] M. Gschwandl, P. Fuchs, K. Fellner, T. Antretter, T. Krivec, and T. Qi. **Finite element analysis of arbitrarily complex electronic devices**. In: *2016 IEEE 18th Electronics Packaging Technology Conference (EPTC)*. 2016, 497–500. DOI: [10.1109/EPTC.2016.7861528](https://doi.org/10.1109/EPTC.2016.7861528) (see page 52).
- [45] M. Gschwandl, P. F. Fuchs, I. Mitev, M. Yalagach, T. Antretter, T. Qi, and A. Schingale. **Modeling of manufacturing induced residual stresses of viscoelastic epoxy mold compound encapsulations**. In: *2017 IEEE 19th Electronics Packaging Technology Conference (EPTC)*. 2017, 1–8. DOI: [10.1109/EPTC.2017.8277557](https://doi.org/10.1109/EPTC.2017.8277557) (see pages xi, 13, 21).
- [46] Mario Gschwandl, Markus Frewein, Peter Filipp Fuchs, Thomas Antretter, Gerald Pinter, and Philipp Novak. **Evaluation of Digital Image Correlation Techniques for the Determination of Coefficients of Thermal Expansion for Thin Reinforced Polymers**. In: *2018 20th International Conference on Electronic Materials and Packaging (EMAP)*. IEEE, Dec. 2018. DOI: [10.1109/emap.2018.8660763](https://doi.org/10.1109/emap.2018.8660763). URL: <https://doi.org/10.1109/emap.2018.8660763> (see page 25).
- [47] Ravish Gupta, Jigyasha Maru, and N Pannaga. **MEMS Technology and Application in Defense Navigation System**. *International Journal of Engineering and Technical Research* 2 (Oct. 2013), 1903–1909 (see page 3).
- [48] Scott Habermehl. **Coefficient of thermal expansion and biaxial Young's modulus in Si-rich silicon nitride thin films**. *Journal of Vacuum Science and Technology A: Vacuum, Surfaces, and Films* 36:2 (Mar. 2018), 021517. DOI: [10.1116/1.5020432](https://doi.org/10.1116/1.5020432). URL: <https://doi.org/10.1116/1.5020432> (see page 76).
- [49] Jianqiang Han, Zhu Changchun, Liu Junhua, and Yongning He. **Dependence of the Resonance Frequency of Thermally Excited Microcantilever Resonators on Temperature**. *Sensors and Actuators A: Physical* 101 (Sept. 2002), 37–41. DOI: [10.1016/S0924-4247\(02\)00146-2](https://doi.org/10.1016/S0924-4247(02)00146-2) (see page 4).
- [50] M. Hayashi, Y. Goto, K. Hanzawa, M. Matsumoto, A. Koide, and Heewon Jeong. **Trends in hitachi's MEMS sensors for automobiles**. 58 (Dec. 2009), 335–340 (see page 2).
- [51] Y. He and X. Fan. **In-situ Characterization of Moisture Absorption and Desorption in a Thin BT Core Substrate**. In: *2007 Proceedings 57th Electronic Components and Technology Conference*. 2007, 1375–1383. DOI: [10.1109/ECTC.2007.373974](https://doi.org/10.1109/ECTC.2007.373974) (see pages 19, 33).
- [52] T. Hirano, M. White, Henry Yang, K. Scott, S. Pattanaik, S. Arya, and Fu-Ying Huang. **A moving-slider MEMS actuator for high-bandwidth HDD tracking**. *IEEE Transactions on Magnetics* 40:4 (2004), 3171–3173. DOI: [10.1109/TMAG.2004.829840](https://doi.org/10.1109/TMAG.2004.829840) (see page 1).
- [53] M. A. Hopcroft, B. Kim, S. Chandorkar, R. Melamud, M. Agarwal, C. M. Jha, G. Bahl, J. Salvia, H. Mehta, H. K. Lee, R. N. Candler, and T. W. Kenny. **Using the temperature dependence of resonator quality factor as a thermometer**. *Applied Physics Letters* 91:1 (July 2007), 013505. DOI: [10.1063/1.2753758](https://doi.org/10.1063/1.2753758). URL: <https://doi.org/10.1063/1.2753758> (see page 4).
- [54] X. M. H. Huang, M. Manolidis, Seong Chan Jun, and J. Hone. **Nanomechanical hydrogen sensing**. *Applied Physics Letters* 86:14 (Apr. 2005), 143104. DOI: [10.1063/1.1897445](https://doi.org/10.1063/1.1897445). URL: <https://doi.org/10.1063/1.1897445> (see page 1).

- [55] Saad Ilyas, Abdallah Ramini, Armando Arpys Arevalo Carreno, and Mohammad Younis. **An Experimental and Theoretical Investigation of a Micromirror Under Mixed-Frequency Excitation**. *Journal of Microelectromechanical Systems* 24 (Aug. 2015), 1–1. doi: [10.1109/JMEMS.2014.2386285](https://doi.org/10.1109/JMEMS.2014.2386285) (see page 1).
- [56] Changsoo Jang, Seungbae Park, Bongtae Han, and Samson Yoon. **Advanced Thermal-Moisture Analogy Scheme for Anisothermal Moisture Diffusion Problem**. *Journal of Electronic Packaging* 130:1 (Jan. 2008). doi: [10.1115/1.2837521](https://doi.org/10.1115/1.2837521). URL: <https://doi.org/10.1115/1.2837521> (see pages 18, 44, 56).
- [57] Han Jianqiang, Zhu Changchun, Liu Junhua, and Li Peng. **A novel temperature-compensating structure for micromechanical bridge resonator**. *Journal of Micromechanics and Microengineering* 15:4 (2005), 702–705. doi: [10.1088/0960-1317/15/4/005](https://doi.org/10.1088/0960-1317/15/4/005). URL: <https://doi.org/10.1088/0960-1317/15/4/005> (see page 4).
- [58] B. Kim, M. A. Hopcroft, R. N. Candler, C. M. Jha, M. Agarwal, R. Melamud, S. A. Chandorkar, G. Yama, and T. W. Kenny. **Temperature Dependence of Quality Factor in MEMS Resonators**. *Journal of Microelectromechanical Systems* 17:3 (2008), 755–766. doi: [10.1109/JMEMS.2008.924253](https://doi.org/10.1109/JMEMS.2008.924253) (see page 4).
- [59] Noriyuki Kinjo, Masatsugu Ogata, Kunihiko Nishi, Aizou Kaneda, and K. Duek. **Epoxy Molding Compounds as Encapsulation Materials for Microelectronic Devices**. In: *Speciality Polymers/Polymer Physics*. Berlin, Heidelberg: Springer Berlin Heidelberg, 1989, 1–48. ISBN: 978-3-540-46010-7 (see page 13).
- [60] Brian Knapp and Paul A. Kohl. **Polymers for microelectronics**. *Journal of Applied Polymer Science* 131:24 (Sept. 2014), n/a–n/a. doi: [10.1002/app.41233](https://doi.org/10.1002/app.41233). URL: <https://doi.org/10.1002/app.41233> (see page 7).
- [61] Tamás Kárpáti, Andrea Pap, and Sándor Kulinyi. **Prototype MEMS Capacitive Pressure Sensor Design and Manufacturing**. *Periodica Polytechnica Electrical Engineering* 57 (Jan. 2013), 3. doi: [10.3311/PPee.2066](https://doi.org/10.3311/PPee.2066) (see page 6).
- [62] Norbert Lange. **Lange’s handbook of chemistry**. New York: McGraw-Hill, 2005. ISBN: 978-0071432207 (see page 51).
- [63] Thierry Leïchlé, Liviu Nicu, and Thomas Alava. **MEMS Biosensors and COVID-19: Missed Opportunity**. *ACS Sensors* 5:11 (2020), 3297–3305. doi: [10.1021/acssensors.0c01463](https://doi.org/10.1021/acssensors.0c01463). URL: <https://doi.org/10.1021/acssensors.0c01463> (see page 2).
- [64] CDM Liljedahl, AD Crocombe, Magd Abdel Wahab, and IA Ashcroft. **Modelling the environmental degradation of adhesively bonded aluminium and composite joints using a CZM approach**. *INTERNATIONAL JOURNAL OF ADHESION AND ADHESIVES* 27:6 (2007), 505–518. ISSN: 0143-7496. URL: <http://dx.doi.org/10.1016/j.ijadhadh.2006.09.015> (see page 14).
- [65] Y.C. Lin and Xu Chen. **Investigation of moisture diffusion in epoxy system: Experiments and molecular dynamics simulations**. *Chemical Physics Letters* 412:4-6 (Sept. 2005), 322–326. doi: [10.1016/j.cplett.2005.07.022](https://doi.org/10.1016/j.cplett.2005.07.022). URL: <https://doi.org/10.1016/j.cplett.2005.07.022> (see page 18).
- [66] Marc Madou. **Fundamentals of microfabrication**. Boca Raton, Fla: CRC Press, 1997. ISBN: 0-8493-9451-1 (see page 3).

- [67] D. Maier-Schneider, J. Maibach, and E. Obermeier. **A new analytical solution for the load-deflection of square membranes.** *Journal of Microelectromechanical Systems* 4:4 (1995), 238–241. DOI: [10.1109/84.475551](https://doi.org/10.1109/84.475551) (see page 79).
- [68] L. Masaro and X. X. Zhu. **Physical models of diffusion for polymer solutions, gels and solids.** *Progress in Polymer Science* 24 (1999), 731–775 (see page 14).
- [69] Kevin P. Menard and Noah R. Menard. *Dynamic Mechanical Analysis in the Analysis of Polymers and Rubbers.* Sept. 2015. DOI: [10.1002/0471440264.pst102.pub2](https://doi.org/10.1002/0471440264.pst102.pub2). URL: <https://doi.org/10.1002/0471440264.pst102.pub2> (see page 22).
- [70] **Monotonic Bend Characterization of Board-Level Interconnects.** Standard. Arlington, VA: JEDEC Solid State Technology Association, 2004 (see page 52).
- [71] Matthias Morak, Philipp Marx, Mario Gschwandl, Peter Filipp Fuchs, Martin Pfof, and Frank Wiesbrock. **Heat Dissipation in Epoxy/Amine-Based Gradient Composites with Alumina Particles: A Critical Evaluation of Thermal Conductivity Measurements.** *Polymers* 10:10 (Oct. 2018), 1131. DOI: [10.3390/polym10101131](https://doi.org/10.3390/polym10101131). URL: <https://doi.org/10.3390/polym10101131> (see page 28).
- [72] C.L. Muhlstein, E.A. Stach, and R.O. Ritchie. **A reaction-layer mechanism for the delayed failure of micron-scale polycrystalline silicon structural films subjected to high-cycle fatigue loading.** *Acta Materialia* 50:14 (Aug. 2002), 3579–3595. DOI: [10.1016/s1359-6454\(02\)00158-1](https://doi.org/10.1016/s1359-6454(02)00158-1). URL: [https://doi.org/10.1016/s1359-6454\(02\)00158-1](https://doi.org/10.1016/s1359-6454(02)00158-1) (see page 4).
- [73] National Instruments. *LabVIEW.* Version 2020 SP1. May 25, 2020. URL: <https://www.ni.com/labview> (see pages 63, 72).
- [74] Javier Oliver and Carlos Agelet de Saracibar. **Continuum Mechanics for Engineers. Theory and Problems. First Edition.** Sept. 2016 (see pages 42, 43).
- [75] Onursal Onen and Rasim Guldiken. **Detailed investigation of capacitive micro-machined ultrasonic transducer design space.** *Microsystem Technologies* 18:4 (Feb. 2012), 399–408. DOI: [10.1007/s00542-012-1449-5](https://doi.org/10.1007/s00542-012-1449-5). URL: <https://doi.org/10.1007/s00542-012-1449-5> (see page 77).
- [76] Tim Osswald. **Material science of polymers for engineers.** Munich Germany: Hanser Publishers, 2012. ISBN: 9781569905241 (see pages 17, 50).
- [77] R. Otmani, N. Benmoussa, and B. Benyoucef. **The Thermal Drift Characteristics of Piezoresistive Pressure Sensor.** *Physics Procedia* 21 (2011), 47–52. DOI: [10.1016/j.phpro.2011.10.008](https://doi.org/10.1016/j.phpro.2011.10.008). URL: <https://doi.org/10.1016/j.phpro.2011.10.008> (see page 84).
- [78] D. E. Packham. **Handbook of adhesion.** Chichester, England: John Wiley, 2005. ISBN: 978-0-471-80874-9 (see page 14).
- [79] W. J. Parker, R. J. Jenkins, C. P. Butler, and G. L. Abbott. **Flash Method of Determining Thermal Diffusivity, Heat Capacity, and Thermal Conductivity.** *Journal of Applied Physics* 32:9 (Sept. 1961), 1679–1684. DOI: [10.1063/1.1728417](https://doi.org/10.1063/1.1728417). URL: <https://doi.org/10.1063/1.1728417> (see page 27).
- [80] Chandradip Patel, F. McCluskey, and David Lemus. **Temperature and Humidity Effects on MEMS Vibratory Gyroscope.** In: Jan. 2011. DOI: [10.4071/2011DPC-wa22](https://doi.org/10.4071/2011DPC-wa22) (see page 4).

- [81] Donald Peckner. **Handbook of stainless steels**. New York: McGraw-Hill, 1977. ISBN: 007049147X (see page 41).
- [82] Permadi and Jose M. Castro. **Development of an environmentally friendly solventless process for electronic prepregs**. *Journal of Applied Polymer Science* 91:2 (2003), 1136–1146. DOI: [10.1002/app.13195](https://doi.org/10.1002/app.13195). URL: <https://doi.org/10.1002/app.13195> (see page 21).
- [83] Mark D. Placette, Xuejun Fan, Jie-Hua Zhao, and Darvin Edwards. **Dual stage modeling of moisture absorption and desorption in epoxy mold compounds**. *Microelectronics Reliability* 52:7 (July 2012), 1401–1408. DOI: [10.1016/j.microrel.2012.03.008](https://doi.org/10.1016/j.microrel.2012.03.008). URL: <https://doi.org/10.1016/j.microrel.2012.03.008> (see page 56).
- [84] **Plastics – Determination of tensile properties – Part 1: General principles**. Standard. Geneva, CH: International Organization for Standardization, Mar. 2019 (see pages 21, 37).
- [85] Michele Pozzi, Musaab Hassan, Alun J Harris, Jim S Burdess, Liudi Jiang, Kin K Lee, Rebecca Cheung, Gordon J Phelps, Nick G Wright, Christian A Zorman, and Mehran Mehregany. **Mechanical properties of a 3C-SiC film between room temperature and 600°C**. *Journal of Physics D: Applied Physics* 40:11 (May 2007), 3335–3342. DOI: [10.1088/0022-3727/40/11/012](https://doi.org/10.1088/0022-3727/40/11/012). URL: <https://doi.org/10.1088/0022-3727/40/11/012> (see page 4).
- [86] Bruce Prime. **Report**. Tech. rep. ATT GLOBAL, 2010. ruc.udc.es:2183/11494: <https://core.ac.uk/reader/61908910> (see page 21).
- [87] Qingming Chen, Tao Zhang, and Qing-Ming Wang. **Frequency-temperature compensation of piezoelectric resonators by electric DC bias field**. *IEEE Transactions on Ultrasonics, Ferroelectrics, and Frequency Control* 52:10 (2005), 1627–1631. DOI: [10.1109/TUFFC.2005.1561617](https://doi.org/10.1109/TUFFC.2005.1561617) (see page 4).
- [88] Md Mosaddequr Rahman and Sazzadur Chowdhury. **Square Diaphragm CMUT Capacitance Calculation Using a New Deflection Shape Function**. *Journal of Sensors* 2011 (2011), 1–12. DOI: [10.1155/2011/581910](https://doi.org/10.1155/2011/581910). URL: <https://doi.org/10.1155/2011/581910> (see pages 76, 77, 79).
- [89] T. Rogers and J. Kowal. **Selection of glass, anodic bonding conditions and material compatibility for silicon-glass capacitive sensors**. *Sensors and Actuators A: Physical* 46:1-3 (Jan. 1995), 113–120. DOI: [10.1016/0924-4247\(94\)00872-f](https://doi.org/10.1016/0924-4247(94)00872-f). URL: [https://doi.org/10.1016/0924-4247\(94\)00872-f](https://doi.org/10.1016/0924-4247(94)00872-f) (see page 84).
- [90] Francisca Rosique, Pedro J. Navarro, Carlos Fernández, and Antonio Padilla. **A Systematic Review of Perception System and Simulators for Autonomous Vehicles Research**. *Sensors* 19:3 (Feb. 2019), 648. DOI: [10.3390/s19030648](https://doi.org/10.3390/s19030648). URL: <https://doi.org/10.3390/s19030648> (see page 2).
- [91] Roger Rotheron, 111–124. In: *Fillers for Polymer Applications*. Ed. by Roger Rotheron. Cham: Springer International Publishing, 2017. ISBN: 978-3-319-28117-9. DOI: [10.1007/978-3-319-28117-9\\_77](https://doi.org/10.1007/978-3-319-28117-9_77). URL: [https://doi.org/10.1007/978-3-319-28117-9\\_77](https://doi.org/10.1007/978-3-319-28117-9_77) (see page 12).

- [92] N. Saba, M. Jawaid, Othman Y. Allothman, I.M. Inuwa, and A. Hassan. **A review on potential development of flame retardant kenaf fibers reinforced polymer composites.** *Polymers for Advanced Technologies* 28:4 (Sept. 2016), 424–434. DOI: [10.1002/pat.3921](https://doi.org/10.1002/pat.3921) (see page 11).
- [93] Naheed Saba and Mohammad Jawaid. “3 - Epoxy resin based hybrid polymer composites.” In: *Hybrid Polymer Composite Materials*. Ed. by Vijay Kumar Thakur, Manju Kumari Thakur, and Asokan Pappu. Woodhead Publishing, 2017, 57–82. ISBN: 978-0-08-100787-7. DOI: <https://doi.org/10.1016/B978-0-08-100787-7.00003-2> (see page 11).
- [94] R Sandberg, Winnie Svendsen, Kristian Molhave, and Anja Boisen. **Temperature and pressure dependence of resonance in multi-layer microcantilevers.** *Journal of Micromechanics and Microengineering* 15 (June 2005), 1454. DOI: [10.1088/0960-1317/15/8/011](https://doi.org/10.1088/0960-1317/15/8/011) (see page 4).
- [95] Chi-Hung Shen and George S. Springer. **Moisture Absorption and Desorption of Composite Materials.** *Journal of Composite Materials* 10:1 (1976), 2–20. DOI: [10.1177/002199837601000101](https://doi.org/10.1177/002199837601000101). URL: <https://doi.org/10.1177/002199837601000101> (see page 15).
- [96] A. P. Singulani, H. Ceric, and S. Selberherr. **Thermo-mechanical simulations of an open tungsten TSV.** In: *2012 IEEE 14th Electronics Packaging Technology Conference (EPTC)*. 2012, 107–111. DOI: [10.1109/EPTC.2012.6507061](https://doi.org/10.1109/EPTC.2012.6507061) (see page 76).
- [97] Alexey Sokolov, Chunlei Liu, and Fabian Mohn. **Reliability assessment of SiC power module stack based on thermo-structural analysis.** In: *2018 19th International Conference on Thermal, Mechanical and Multi-Physics Simulation and Experiments in Microelectronics and Microsystems (EuroSimE)*. IEEE, Apr. 2018. DOI: [10.1109/eurosime.2018.8369879](https://doi.org/10.1109/eurosime.2018.8369879). URL: <https://doi.org/10.1109/eurosime.2018.8369879> (see page 21).
- [98] Vaibhavi Sonetha, Poorvi Agarwal, Smeet Doshi, Ridhima Kumar, and Bhavya Mehta. **Microelectromechanical Systems in Medicine.** *Journal of Medical and Biological Engineering* 37:4 (2017), 580–601. DOI: [10.1007/s40846-017-0265-x](https://doi.org/10.1007/s40846-017-0265-x). URL: <https://doi.org/10.1007/s40846-017-0265-x> (see page 2).
- [99] Peishuai Song, Chaowei Si, Mingliang Zhang, Yongmei Zhao, Yurong He, Wen Liu, and Xiaodong Wang. **A Novel Piezoresistive MEMS Pressure Sensors Based on Temporary Bonding Technology.** *Sensors* 20:2 (Jan. 2020), 337. DOI: [10.3390/s20020337](https://doi.org/10.3390/s20020337). URL: <https://doi.org/10.3390/s20020337> (see page 5).
- [100] D. R. Southworth, L. M. Bellan, Y. Linzon, H. G. Craighead, and J. M. Parpia. **Stress-based vapor sensing using resonant microbridges.** *Applied Physics Letters* 96:16 (Apr. 2010), 163503. DOI: [10.1063/1.3393999](https://doi.org/10.1063/1.3393999). URL: <https://doi.org/10.1063/1.3393999> (see page 1).
- [101] S. Spearing. **Material Issues in Microelectromechanical Systems (MEMS).** *Acta Materialia* 48 (Jan. 2000), 179–196. DOI: [10.1016/S1359-6454\(99\)00294-3](https://doi.org/10.1016/S1359-6454(99)00294-3) (see page 3).
- [102] B. Stark. **MEMS reliability assurance guidelines for space applications.** Tech. rep. National Aeronautics, Space Administration (NASA), and Jet Propulsion Laboratory (JPL), 1999 (see page 4).

- [103] E. Stellrecht, Bongtae Han, and M. Pecht. **Characterization of hygroscopic swelling behavior of mold compounds and plastic packages**. *IEEE Transactions on Components and Packaging Technologies* 27 (2004), 499–506 (see pages 13, 18, 33).
- [104] R Syms, H. Zou, J Yao, Deepak Uttamchandani, and J Stagg. **Scalable electrothermal MEMS actuator for optical fibre alignment**. *J. Micromech. Microeng* 14 (Dec. 2004), 1633–1639. DOI: [10.1088/0960-1317/14/12/006](https://doi.org/10.1088/0960-1317/14/12/006) (see page 1).
- [105] Osamu Tabata, Ken Kawahata, Susumu Sugiyama, and Isemi Igarashi. **Mechanical property measurements of thin films using load-deflection of composite rectangular membranes**. *Sensors and Actuators* 20:1-2 (Nov. 1989), 135–141. DOI: [10.1016/0250-6874\(89\)87111-2](https://doi.org/10.1016/0250-6874(89)87111-2). URL: [https://doi.org/10.1016/0250-6874\(89\)87111-2](https://doi.org/10.1016/0250-6874(89)87111-2) (see page 78).
- [106] D. M. Tanner, J. A. Walraven, L. W. Irwin, M. T. Dugger, N. F. Smith, W. P. Eaton, W. M. Miller, and S. L. Miller. **The effect of humidity on the reliability of a surface micromachined microengine**. In: *1999 IEEE International Reliability Physics Symposium Proceedings. 37th Annual (Cat. No.99CH36296)*. 1999, 189–197. DOI: [10.1109/RELPHY.1999.761611](https://doi.org/10.1109/RELPHY.1999.761611) (see page 4).
- [107] **Test Method for the Measurement of Moisture Diffusivity and Water Solubility in Organic Materials Used in Electronic Devices**. Standard. Arlington, VA: JEDEC Solid State Technology Association, 2014 (see page 29).
- [108] Stephen Timoshenko. **Theory of plates and shells**. New York: McGraw-Hill, 1959. ISBN: 0070647798 (see page 79).
- [109] MJ Tudor, MV Andres, KWH Foulds, and JM Naden. **Silicon resonator sensors: interrogation techniques and characteristics**. 1988. URL: <https://eprints.soton.ac.uk/256662/> (see page 4).
- [110] M. R. Vanlandingham, R. F. Eduljee, and J. W. Gillespie. **Moisture diffusion in epoxy systems**. *Journal of Applied Polymer Science* 71:5 (1999), 787–798. DOI: [10.1002/\(sici\)1097-4628\(19990131\)71:5<787::aid-app12>3.0.co;2-a](https://doi.org/10.1002/(sici)1097-4628(19990131)71:5<787::aid-app12>3.0.co;2-a) (see page 18).
- [111] Jeremy Walraven. **Failure mechanisms in mems**. In: vol. 1. Jan. 2003, 828–833. ISBN: 0-7803-8106-8. DOI: [10.1109/TEST.2003.1270915](https://doi.org/10.1109/TEST.2003.1270915) (see page 4).
- [112] X.D. Wang, J.X. Yu, L. Chen, L.M. Qian, and Z.R. Zhou. **Effects of water and oxygen on the tribochemical wear of monocrystalline Si(100) against SiO<sub>2</sub> sphere by simulating the contact conditions in MEMS**. *Wear* 271:9-10 (July 2011), 1681–1688. DOI: [10.1016/j.wear.2010.11.043](https://doi.org/10.1016/j.wear.2010.11.043). URL: <https://doi.org/10.1016/j.wear.2010.11.043> (see page 4).
- [113] I. M. Ward. **An introduction to the mechanical properties of solid polymers**. Chichester, West Sussex, England: Wiley, 2004. ISBN: 978-0-471-49626-7 (see page 19).
- [114] Jonathan D. Weiss. **Magnetic Force and Thermal Expansion as Failure Mechanisms of Electrothermal MEMS Actuators Under Electrostatic Discharge Testing**. *Journal of Applied Mechanics* 74:5 (Jan. 2007), 996–1005. DOI: [10.1115/1.2723813](https://doi.org/10.1115/1.2723813). URL: <https://doi.org/10.1115/1.2723813> (see page 4).
- [115] Y. Jack Weitsman. **Fluid Effects in Polymers and Polymeric Composites**. Springer US, 2012. DOI: [10.1007/978-1-4614-1059-1](https://doi.org/10.1007/978-1-4614-1059-1). URL: <https://doi.org/10.1007/978-1-4614-1059-1> (see page 14).



- [116] W.W. Wright. **The effect of diffusion of water into epoxy resins and their carbon-fibre reinforced composites.** *Composites* 12:3 (July 1981), 201–205. DOI: [10.1016/0010-4361\(81\)90505-x](https://doi.org/10.1016/0010-4361(81)90505-x) (see pages 17, 19).
- [117] I. O. Wygant, M. Kupnik, and B. T. Khuri-Yakub. **Analytically calculating membrane displacement and the equivalent circuit model of a circular CMUT cell.** In: *2008 IEEE Ultrasonics Symposium*. 2008, 2111–2114. DOI: [10.1109/ULTSYM.2008.0522](https://doi.org/10.1109/ULTSYM.2008.0522) (see page 77).
- [118] Fenlan Xu, Xiuyan Li, Yue Shi, Luhai Li, Wei Wang, Liang He, and Ruping Liu. **Recent Developments for Flexible Pressure Sensors: A Review.** *Micromachines* 9 (Nov. 2018), 580. DOI: [10.3390/mi9110580](https://doi.org/10.3390/mi9110580) (see page 5).
- [119] Xuejun Fan, Jiang Zhou, and A. Chandra. **Package structural integrity analysis considering moisture.** In: *2008 58th Electronic Components and Technology Conference*. 2008, 1054–1066. DOI: [10.1109/ECTC.2008.4550106](https://doi.org/10.1109/ECTC.2008.4550106) (see page 13).
- [120] M. Yalagach. **Study of process simulation and integrity analysis using short fiber reinforced polymers.** English. MA thesis. Stuttgart: University of Stuttgart, 2017 (see page 3).
- [121] M. Yalagach, P. Filipp Fuchs, A. Wolfberger, M. Gschwandl, T. Antretter, M. Feuchter, C. Tak, and Q. Tao. **Numerical Analysis of the Influence of Polymeric Materials on a MEMS Package Performance Under Humidity and Temperature Loads.** In: *2019 IEEE 69th Electronic Components and Technology Conference (ECTC)*. 2019, 2029–2035. DOI: [10.1109/ECTC.2019.00311](https://doi.org/10.1109/ECTC.2019.00311) (see pages xi, 12, 25, 26, 33–35, 39, 47, 51, 53–56, 116).
- [122] M. Yalagach, P. F. Fuchs, T. Antretter, M. Feuchter, M. Weber, and T. Qi. **Characterization and Modeling of Prepregs Applied in MEMS Sensor Packages with a Focus on Moisture Dependence.** In: *Microelectronic Devices and Technologies*. Vol. 3. Online: International Frequency Sensor Association (IFSA) Publishing, S. L., Oct. 2020, 5–10. ISBN: 978-84-09-24422-5. URL: [https://sensorsportal.com/MicDAT\\_2020/MicDAT\\_2020\\_Proceedings.pdf](https://sensorsportal.com/MicDAT_2020/MicDAT_2020_Proceedings.pdf) (see pages xi, 26, 32, 33, 35, 37, 38, 47, 124).
- [123] M. Yalagach, P. F. Fuchs, T. Antretter, M. Feuchter, M. Weber, and T. Qi. **Thermal and Moisture Dependent Material Characterization and Modeling of Glass Fiber Reinforced Epoxy Laminates.** *Sensors & Transducers* 248:1 (Jan. 2021), 1–9. ISSN: 2306-8515. URL: [https://www.sensorsportal.com/HTML/DIGEST/P\\_3196.htm](https://www.sensorsportal.com/HTML/DIGEST/P_3196.htm) (see pages xi, 26, 28, 32, 33, 35, 37–39, 47, 142).
- [124] M. Yalagach, P. F. Fuchs, T. Antretter, T. Qi, and M. Weber. **Numerical analysis of a MEMS sensor’s deformation behavior considering dynamic moisture conditions.** In: *2020 IEEE 22nd Electronics Packaging Technology Conference (EPTC)*. 2020, 380–385. DOI: [10.1109/EPTC50525.2020.9315091](https://doi.org/10.1109/EPTC50525.2020.9315091) (see pages xi, 58, 59, 62–71, 135).
- [125] M. Yalagach, P. F. Fuchs, I. Mitev, T. Antretter, M. Feuchter, A. Wolfberger, and T. Qi. **Influence of environmental factors like temperature and humidity on MEMS packaging materials.** In: *2018 7th Electronic System-Integration Technology Conference (ESTC)*. 2018, 1–6. DOI: [10.1109/ESTC.2018.8546484](https://doi.org/10.1109/ESTC.2018.8546484) (see pages xi, 11, 22–24, 29–31, 33, 36, 47, 48, 50, 54, 109).

- [126] Atsushi Yao and Takashi Hikihara. **Logic-memory device of a mechanical resonator**. *Applied Physics Letters* 105:12 (Sept. 2014), 123104. DOI: [10.1063/1.4896272](https://doi.org/10.1063/1.4896272). URL: <https://doi.org/10.1063/1.4896272> (see page 1).
- [127] Eric Yeatman. **Applications of MEMS in power sources and circuits**. *J. Micromech. Microeng* 17 (July 2007), 184–188. DOI: [10.1088/0960-1317/17/7/S16](https://doi.org/10.1088/0960-1317/17/7/S16) (see page 2).
- [128] Samson Yoon, Bongtae Han, and Zhaoyang Wang. **On Moisture Diffusion Modeling Using Thermal-Moisture Analogy**. *Journal of Electronic Packaging* 129:4 (Apr. 2007), 421–426. DOI: [10.1115/1.2804090](https://doi.org/10.1115/1.2804090). URL: <https://doi.org/10.1115/1.2804090> (see pages 44, 56).
- [129] Zhou Zheng, Weijie Sun, Xudong Suo, Lawrence L.P. Wong, Zhendong Sun, and John T.W. Yeow. **A novel deflection shape function for rectangular capacitive micro-machined ultrasonic transducer diaphragms**. *Sensing and Bio-Sensing Research* 5 (Sept. 2015), 62–70. DOI: [10.1016/j.sbsr.2015.07.006](https://doi.org/10.1016/j.sbsr.2015.07.006). URL: <https://doi.org/10.1016/j.sbsr.2015.07.006> (see pages 76, 79).

# A

## List of Publications

---

Yalagach et al., ESTC 2018

© 2018 IEEE. Reprinted, with permission, from:

M. Yalagach et al. **Influence of environmental factors like temperature and humidity on MEMS packaging materials.** In: *2018 7th Electronic*

*System-Integration Technology Conference (ESTC)*. 2018, 1–6. DOI:

[10.1109/ESTC.2018.8546484](https://doi.org/10.1109/ESTC.2018.8546484)

# *Influence of environmental factors like temperature and humidity on MEMS packaging materials.*

Mahesh Yalagach\*, Peter Filipp Fuchs\*, Ivaylo Mitev\*, Thomas Antretter†, Michael Feuchter‡, Archim Wolfberger§, Tao Qi¶

\*Polymer Competence Center Leoben GmbH  
Leoben, Austria  
mahesh.yalagach@pcccl.at

† Montanuniversitaet Leoben, Institute of Mechanics  
Leoben, Austria

‡ Montanuniversitaet Leoben, Institute of Material Science and Testing of Polymers  
Leoben, Austria

§ams AG  
Premstaetten, Austria

¶Austria Technologie & Systemtechnik Aktiengesellschaft  
Leoben, Austria

**Abstract**—Microelectromechanical systems (MEMS) and MEMS packaging solutions are gaining increased interests for electronic applications. These packages feature a variety of polymeric materials and composites e.g. fiber reinforced polymer laminates, insulating and conductive adhesives. Due to the sensitivity of MEMS devices to mechanical stress and environmental factors such as temperature and humidity, the influence of these factors on the device's performance needs to be accounted for. In this contribution, a fabric woven glass fiber reinforced epoxy resin (BT - epoxy resin) and two chosen adhesives commonly used in semiconductor and MEMS packaging have been considered and their dependency on environmental parameters have been studied with different testing methods. Based on the measured material properties a simulation process predicting the package under defined environmental loads is presented.

**Index Terms**—Thermo-mechanical characterization, moisture diffusion, hygroscopic swelling, hygro-thermo-mechanical simulation

## I. INTRODUCTION

MEMS packages are known to be highly sensitive to environmental loads [1] [2]. These packages feature several composite materials with different hygro and the thermo-mechanical properties. The hygro and thermo-mechanical mismatch between the individual materials lead to stresses during their application. The induced stresses again can cause deformation, delamination, and cracks in the package and are important to be understood and evaluated in order to be able to optimize MEMS performance and reliability.

In this work, besides the analysis of the thermo-mechanical behavior a special focus was set on the moisture dependent material behavior. Uptake of water molecules in the polymeric materials can be considered in two stages i.e. unbounded and bounded. The unbounded stage refers to the percentage

of the water molecules which can fill cavities and voids while the bounded stage refers to water molecules interacting with polymer chains by forming hydrogen bonds [3]. Due to absorption of moisture by polymeric materials and adhesives a material volume expansion can be observed. This expansion is termed as hygroscopic swelling and is mainly caused by hydrogen bonds between water molecules and hydroxyl groups in polymers. Formation of these bonds leads to the disintegration of inter-chain hydrogen bonding which again leads to an increase of inter-segmental hydrogen bond length [4] [5]. Many efforts have been made to understand the effects of hygro-thermo-mechanical stresses caused in MEMS packages [6] [7].

In this contribution, the effects from thermo-mechanical stress and hygroscopic stresses on materials have been extensively studied with the help of hygro and thermo-mechanical material characterization. The measured data has been applied in numerical studies to perform a hygro-thermo-mechanical simulation.

## II. EXPERIMENTAL

An extensive material characterization was performed on three representative polymeric materials applied commonly in MEMS packages: BT-epoxy resin (woven fabric glass fiber reinforced epoxy resin), insulating adhesive (silicone) and conductive adhesive (silver filled epoxy). The following section explains briefly the measurement techniques used:

### A. Temperature dependent uni-axial tensile tests and dynamic mechanical analysis (DMA)

To evaluate the temperature dependent behavior of the material samples, BT-epoxy resin, insulating and conductive

adhesive were subjected to temperature dependent tensile tests and dynamic mechanical analysis (DMA). The tensile tests were performed for the defined temperatures  $23^{\circ}\text{C}$ ,  $100^{\circ}\text{C}$ ,  $180^{\circ}\text{C}$  and  $250^{\circ}\text{C}$  using Zwick Z010 (Zwick Roell AG, Ulm, Germany) tensile test machine with ISO 527 - 1BA specimens. Strain data acquisition was performed using the digital image correlation (DIC) system (Aramis, GOM GmbH, Braunschweig, Germany). The DMA measurements were performed using Mettler Toledo DMA/SDTA861 (Mettler-Toledo, Columbus, Ohio, USA) in a tensile mode under a constant displacement excitation. These materials were tested at defined frequencies of 0.1, 1, 10, 100 Hz and over a temperature range of  $-100^{\circ}\text{C}$  to  $320^{\circ}\text{C}$  with heating rate of  $2\text{K}/\text{min}$ .

### B. Humidity conditioning

The moisture diffusion properties were measured using the gravimetric method. The diffusion behavior of materials was measured by immersing them in a demineralized water bath at defined temperatures ( $60^{\circ}\text{C}$  and  $90^{\circ}\text{C}$ ) in a temperature chamber. The material samples were conditioned according to JEDEC-JESD22-A120B standards [10]. Initially, the materials were dried in a temperature oven at  $125^{\circ}\text{C}$  until they achieved a constant weight, before starting the environmental conditioning. Material samples were kept in the temperature chamber in a plastic container with demineralized water. At predefined time intervals, the material samples from the plastic container were removed. The surface was wiped using a paper tissue and they were weighed using a high precision balance (Mettler-Toledo MS-L). The percentage of moisture content  $M_t$  in the samples is computed using (1).

$$M_t = \frac{M_2 - M_1}{M_2} \times 100, \quad (1)$$

where  $M_1$  is the mass of the material sample after drying and  $M_2$  is the mass of the material sample at time  $t$ .

### C. Coefficient of moisture expansion CME

To access the effect of hygroscopic swelling in the materials used in MEMS semiconductor packages, CME is measured. Developed hygroscopic strains  $\epsilon^{\beta}$  are supposed to have a linear relationship with moisture concentration [11] as shown in (2).

$$\epsilon^{\beta} = \beta \Delta C, \quad (2)$$

where  $\epsilon^{\beta}$  is the hygroscopic strain,  $\beta$  is the coefficient of moisture expansion (CME) and  $\Delta C$  is the concentration change. Measuring CME follows different techniques like Michelson interferometry [12] or thermo-mechanical analysis (TMA) along with thermo-gravimetric analysis (TGA) [13]. In this contribution, the concentration change  $\Delta C$  is measured by monitoring the weight of initially saturated material samples during the desorption process in a temperature oven. To measure the hygroscopic swelling strains  $\epsilon^{\beta}$  the digital image correlation (DIC) method is employed using the system Q400 TCT (Dantec Dynamics, Ulm, Germany). The desorption and DIC processes were measured at  $160^{\circ}\text{C}$  for six hours for all the material samples.

## III. MODELING MOISTURE DIFFUSION

A mathematical model for moisture diffusion process was presented by Fick [15] [16] [19] using the mathematical equation of the heat diffusion. It is generally referred to as Fickian diffusion or single Fickian diffusion. In this diffusion model, the moisture flux is directly proportional to the concentration gradient in the polymer. For the assumed infinite plate the overall mass uptake  $M_t$  at time  $t$  of a plate of the thickness  $2l$  is given by

$$M_t = \left( 1 - \frac{8}{\pi^2} \sum_{n=0}^{\infty} \frac{1}{(2n+1)^2} e^{-\frac{D(2n+1)^2 \pi^2 t}{4l^2}} \right) \times M_{\infty}, \quad (3)$$

where  $M_{\infty}$  is the saturated mass and  $D$  is the moisture diffusion coefficient.

Most of the polymers like BT-epoxy resins, insulating and conductive adhesives follow single Fickian diffusion above their glass transition temperature ( $T_g$ ) [17]. However, these polymers show a non Fickian moisture diffusion behavior at a temperature below  $T_g$ . A common way to model non single Fickian diffusion are dual Fickian diffusion models. They feature either two sequential or parallel single Fickian processes. In parallel dual Fickian models the overall mass uptake of  $M_t$  at time  $t$  of a plate of thickness  $2l$  is given by

$$M_t = \left( 1 - \frac{8}{\pi^2} \sum_{n=0}^{\infty} \frac{1}{(2n+1)^2} e^{-\frac{D_1(2n+1)^2 \pi^2 t}{4l^2}} \right) \times M_{1\infty} + \left( 1 - \frac{8}{\pi^2} \sum_{n=0}^{\infty} \frac{1}{(2n+1)^2} e^{-\frac{D_2(2n+1)^2 \pi^2 t}{4l^2}} \right) \times M_{2\infty}, \quad (4)$$

where  $M_{1\infty}$  and  $M_{2\infty}$  are the saturated masses and the sum of  $M_{1\infty}$  and  $M_{2\infty}$  is the total saturated mass  $M_{\infty}$ .  $D_1$  and  $D_2$  are moisture diffusion coefficients.

In this work, both single Fickian and the parallel dual Fickian model have been applied to fit the experimental data. The saturated moisture mass  $M_{\infty}$  and mass diffusion coefficient  $D$  were determined based on experimental moisture conditioning curves. An initial value for  $D$  could be computed by using (5) [10].

$$D = \pi \left( \frac{l}{4M_{\infty}} \right)^2 \left( \frac{M_2 - M_1}{\sqrt{t_2} - \sqrt{t_1}} \right)^2, \quad (5)$$

where  $M_1$ ,  $M_2$ ,  $\sqrt{t_1}$  and  $\sqrt{t_2}$  is the slope of the moisture absorption plot in the initial linear part of the experimental curve.

To determine the final parameters for  $M_{\infty}$  and  $D$  a non-linear least squared curve fitting procedure was applied. The curve fitting procedure was carried out for both, single Fickian and dual Fickian moisture diffusion models using the lsqcurvefit function available in MATLAB-2017a (The MathWorks, Inc., Natick, Massachusetts, United States).

## IV. HYGRO-THERMO-MECHANICAL SIMULATION

To determine the thermomechanical and the hygroscopic stresses, a hygro-thermo-mechanical simulation is set up in Abaqus (Abaqus 6.14, Dassault Systemes Simulia Corp., Providence, USA). To this end, user-defined subroutines USDFLD

and UEXPAN are applied. The total deformation consists of mechanical, thermal and hygroscopic strains. To determine the thermal and hygroscopic strains, the temperature and the moisture distribution needs to be known. The temperature distribution is determined by a heat transfer simulation and the moisture distribution is determined by a mass diffusion analysis. The modeling approach for the hygro-thermo-mechanical simulation is explained in the block diagram in Figure 1.

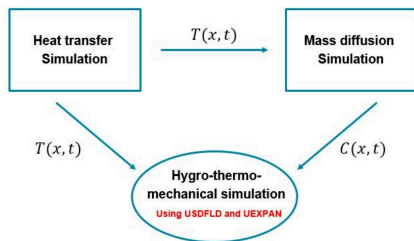


Fig. 1. Hygro-thermo-mechanical simulation modeling approach.

The hygro-thermo-mechanical modeling approach is initially started with the heat transfer simulation. The resulting nodal temperature values are further used in a mass diffusion analysis as a predefined temperature field to take into account the mass diffusion temperature dependence. The mass diffusion simulation is solved using a dual Fickian diffusion model approach. Doing so, two parallel single Fickian mass diffusion analyses were performed using the analytical fitted parameters  $D_1$ ,  $D_2$ ,  $M_{1\infty}$  and  $M_{2\infty}$ . The resulting single Fickian moisture concentrations were saved in the individual analysis as field variables and summed up to the total moisture concentration using the USDFLD subroutine in the consequent hygro-thermo-mechanical analysis. The resulting moisture concentration and temperature fields are used in the subroutine UEXPAN to compute the thermal and hygroscopic swelling strains.

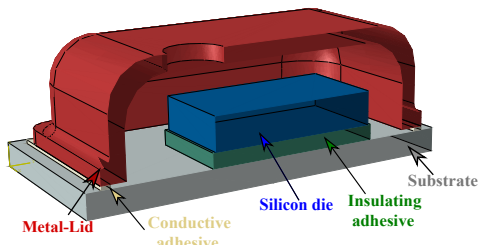


Fig. 2. MEMS package used for the hygro-thermo-mechanical modeling.

This modeling approach is set up for a commonly used MEM semiconductor package as shown in Figure 2. In this package, the connecting wires and the printed circuit board (PCB) are neglected for the simplicity of the model. The material data for silicon die and metal lid were taken from literature [8] [9] and the material data for substrate (BT-epoxy resin), insulation and conductive adhesive were taken from the conducted material characterization. For the heat transfer simulation, the temperature boundary condition of  $90^\circ\text{C}$  is applied to the bottom surface of the BT-epoxy resin (substrate) while the ambient temperature is defined as  $23^\circ\text{C}$ . For the mass diffusion analysis, a concentration boundary condition of  $M_{1\infty} = 0.2647\%$  and  $M_{2\infty} = 0.3823\%$  is applied to the bottom surface of the BT-epoxy resin. The temperature, moisture and the resulting stress distribution are evaluated after a time of 20 hours.

## V. RESULTS AND DISCUSSION

### A. Material characterization

The results from the DMA and the tensile test results show the temperature dependent modulus for the individual materials. Figure 3 depicts the results for BT epoxy resin for tensile tests (elevated temperatures) and DMA. The plot shows that the elastic modulus obtained from DMA and tensile tests are in good agreement over a wide temperature range. Small discrepancies may be attributed to the higher fixture compliance in the DMA device. Additionally, Figure 3 also shows the DMA results obtained for  $45^\circ$  specimens. The obtained values emphasize the expected anisotropic behavior of the reinforced epoxy resin.

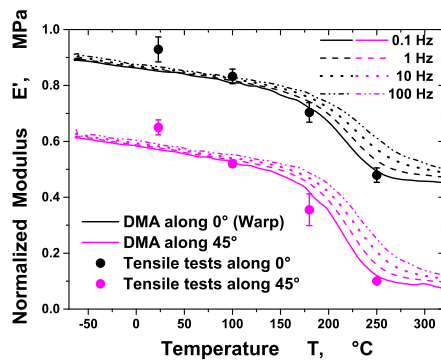


Fig. 3. DMA curves obtained for BT-epoxy resin as a function of frequency and temperature in comparison to tensile tests elastic modulus at different temperatures (normalized to maximum modulus).

On other hand, Figure 4 shows the thermal effects from DMA tests obtained for the considered isotropic insulating and conductive adhesives. The conductive adhesive has a

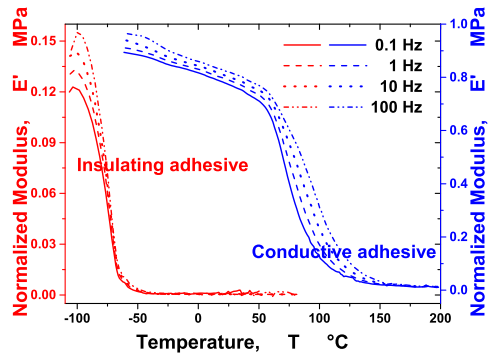


Fig. 4. DMA curves obtained for isotropic insulating and conductive adhesive as a function of frequency and temperature (normalized to maximum modulus).

significantly higher stiffness compared to the insulating adhesive over the measured frequency and temperature range. As expected the frequency dependence is observed to be pronounced in the  $T_g$  region of the individual materials. Modulus differences of up to 20% are measured.

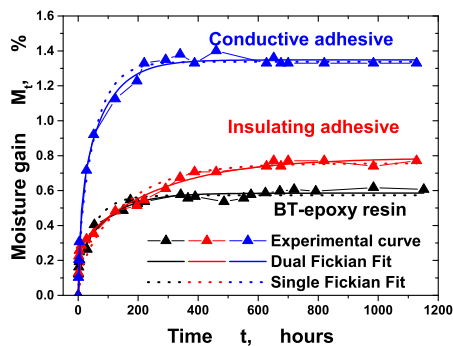


Fig. 5. Typical moisture gain trend and curve fit using the analytical solutions for three representative polymeric materials at  $60^\circ\text{C}$ .

The results obtained for humidity conditioning for conditioning temperatures of  $60^\circ\text{C}$  and  $90^\circ\text{C}$  are depicted in Figures 5 and 6. The plot indicates a typical moisture gain trend, where both diffusion speed and the mass saturation increases at higher temperatures. The conductive adhesive absorbs the highest amount of moisture (1.3% and 1.78%) at both conditioning temperatures. The material reaches its

saturation state at 120 hours. The insulating adhesive absorbs 0.8% and 1.12% and BT-epoxy resin absorbs nearly 0.65% of moisture. The saturation states for the insulation adhesive and the BT-epoxy resin are reached after 620 and 530 hours.

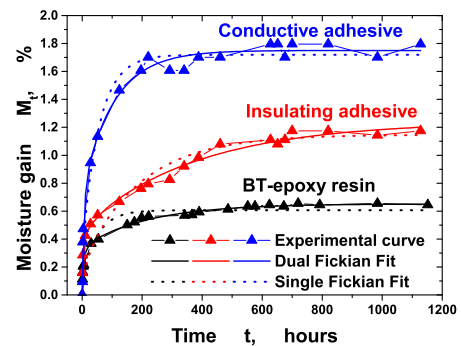


Fig. 6. Typical moisture gain trend and curve fit using the analytical solutions for three representative polymeric materials at  $90^\circ\text{C}$ .

Figures 5 and 6 also depict the obtained curve fits using (3) and (4). The results show that for single Fickian diffusion the model cannot follow the trend of the experimental data in the initial region while the dual Fickian diffusion model fits the overall behavior of the experimental data well. The saturated mass  $M_\infty$  and diffusion coefficient  $D$  obtained from curve fitting using the dual Fickian diffusion model for all polymeric materials are used in the further numerical hygro-thermo-mechanical simulations.

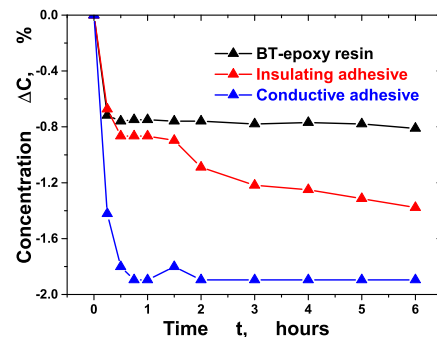


Fig. 7. Change in the moisture concentration  $\Delta C$  from drying process at  $160^\circ\text{C}$  for six hours.

The coefficient of moisture expansion (CME) measurements, resulting from the desorption process are shown in Figure 7. It is observed that the conductive adhesive shows the highest concentration change of about 1.9% compared to the insulating adhesive (1.4%) and the BT-epoxy resin (0.7%).

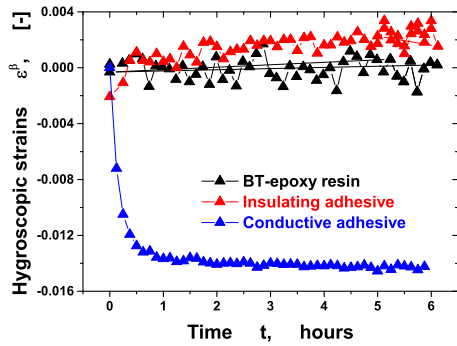


Fig. 8. Measured hygroscopic strains  $\epsilon^\beta$  from digital image correlation (DIC) method from Q400 TCT testing system (Dantec Dynamics, Ulm, Germany).

The measured hygroscopic strains  $\epsilon^\beta$  for the BT-epoxy resin, insulating and conductive adhesives are depicted in Figure 8. The strains measured during the heating phase from  $23^\circ\text{C}$  to  $160^\circ\text{C}$  are neglected as they can be mainly attributed to the thermal expansion. While for the conducting adhesive a significant shrinkage was observed, no changes were measured for the BT-epoxy resin and the insulation adhesive. Further analysis on this behaviour will have to be done. Especially a

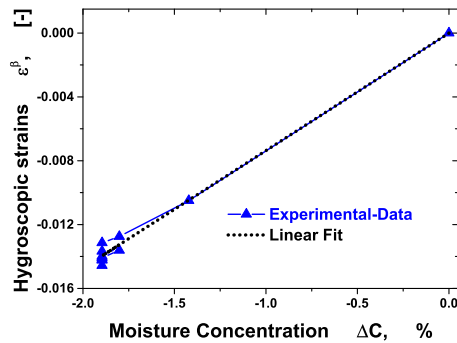


Fig. 9. Linear relation between the hygroscopic swelling strains and change in the moisture content for the conductive adhesive.

potential shrinkage in the heat up phase which is currently not considered will be analysed. In the current simulation model, based on the measurement results only the moisture dependence of the conductive adhesive is considered.

The hygroscopic swelling  $\epsilon^\beta$  behavior of the conductive adhesive over the change of moisture concentration  $\Delta C$  with a linear curve fit is shown in Figure 9. The obtained coefficient of moisture expansion (CME) from the fit is 0.0074.

### B. Simulations

In this section the results from the hygro-thermo-mechanical simulations are discussed. The nodal temperature distribution obtained by the heat transfer simulation for the MEMS package is shown in Figure 10.

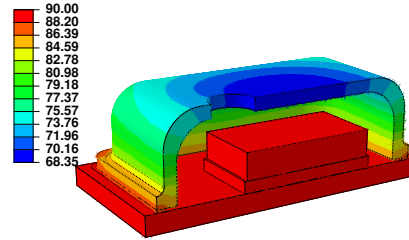


Fig. 10. Nodal temperature distribution [ $^\circ\text{C}$ ] in the MEMS package at  $t = 20$  hours.

The temperature distribution is further used in the mass diffusion analysis which is the second step of the hygro-thermo-mechanical simulation. The obtained moisture distribution in the overall MEMS package is seen in Figure 11. For the silicon die and the metal lid, the moisture diffusion coefficient  $D$  is negligible compared to the polymeric materials used. Therefore, the distribution of moisture is not seen in these materials.

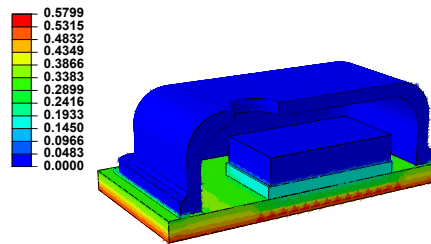


Fig. 11. Moisture distribution [%] in the MEMS package at  $t = 20$  hours.

The determined temperature and moisture distribution are used in the consequent thermo-mechanical step to simulate the induced stresses. The overall stress distribution in the analyzed MEMS package due to hygroscopic strains is depicted in



Figure 12. The hygroscopic swelling behavior of the conductive adhesive contributes to the overall stress distribution in the MEMS package. The stresses are moderately distributed along the MEMS package and is found to be critical in the region between the conductive adhesive and the metal lid. The stresses induced can be further introduced in a deformation analysis for the MEMS package.

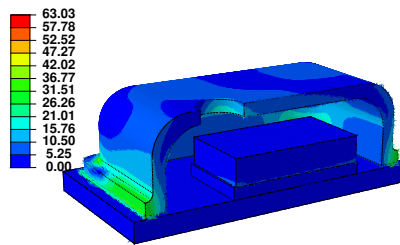


Fig. 12. Von-Mises stress distribution [MPa] in the MEMS package determined from hygro-thermo-mechanical simulation at  $t = 20$  hours.

## VI. CONCLUSION AND OUTLOOK

In this research work, the results from a thermo-mechanical and moisture dependent material characterization for three polymeric materials commonly used in MEMS packages were presented. A dual Fickian mass diffusion model was defined based on the experimental data for all materials. The experimental data were used in a numerical simulation approach to determine the induced hygro-thermo-mechanical stresses in MEMS package. To this end a temperature, two parallel mass diffusion and and hygro-thermo-mechanical simulation was performed. That allows for an evaluation of the effect of temperature and moisture on the deformation behaviour of MEMS packages which can serve as valuable information for reliable systems.

The following open points in the presented research work will be worked on in the future. The elastic modulus is not dependent on the moisture content in the applied model. A moisture-dependent dynamic mechanical analysis will allow for the consideration of this dependence. Furthermore, the temperature dependence of the swelling behavior should be taken into account. That will be done by repeating the CME measurements at different temperature levels. These model improvements will allow for an even more accurate prediction of the deformation behavior in the future.

## ACKNOWLEDGMENT

The research work of this paper was performed at the Polymer Competence Center Leoben GmbH (PCCL, Austria) within the framework of the COMET-program of the Austrian Ministry of Traffic, Innovation, and Technology with contributions by the University of Leoben, by ams AG and by AT&S Austria Technologie & Systemtechnik Aktiengesellschaft. The PCCL is funded by the Austrian Government and the State Governments of Styria and Upper Austria.

## REFERENCES

- [1] Zamik, M. Santo; Belavic, D. (2012); An Experimental and Numerical Study of the Humidity Effect on the Stability of a Capacitive Ceramic Pressure Sensor.
- [2] R. Darveaux, L. Norton, F. Carney, Temperature-dependent mechanical behavior of plastic packaging materials, Proceedings of 45th Electronic Components and Technology Conference, May 1995.
- [3] E. Stellrecht, B. Han, and M. Pecht. Characterization of the hygroscopic swelling behavior of mold compounds and plastic packages. In: IEEE Transactions on Components and Packaging Technologies 27.3 (2004), pp. 499506.
- [4] M.J. Adamson. Thermal expansion and swelling of cured epoxy resin used in graphite/epoxy composite materials. In: Journal of Materials Science 15.7 (1980), pp. 17361745.
- [5] H. Ardebili, E.H. Wong, and M. Pecht. Hygroscopic swelling and sorption characteristics of epoxy molding compounds used in electronic packaging. In: IEEE Transactions on Components and Packaging Technologies 26.1 (2003), pp. 206214.
- [6] S. Yoon, C. Jang, and B. Han. Nonlinear stress modeling scheme to analyze semiconductor packages subjected to combine thermal and hygroscopic loading. In: Journal of Electronic Packaging 130.2 (2008), p. 024502.
- [7] M.Y. Tsai et al. An approach to determining residual strains and moisture diffusion coefficients of cured adhesives in electronic packaging. In: ASME 2007 InterPACK Conference collocated with the ASME/JSM 2007 Thermal Engineering Heat Transfer Summer Conference. American Society of Mechanical Engineers, 2007, pp. 711717.
- [8] Dwight E. Gray ( Ed.) American Institute of Physics Handbook McGraw-Hill Book Company Inc. 1957.
- [9] Handbook of Stainless Steels, Donald Peckner and I. M. Bernstein, McGraw-Hill Book Company, New York, NY, (1977)
- [10] JESD22-A120A, Test method for the measurement of moisture diffusivity and water solubility in organic materials used in electronic devices, JEDEC Standards 2001.
- [11] Stellrecht, E., Han, B., Pecht, M.G., Characterization of the hygroscopic swelling behavior of mold compounds and plastic packages, IEEE Transactions on Components and Packaging Technologies, 27, 499506, 2004.
- [12] Buchholz, R., Nakladal, A., Gerlach, V., Share, K., Eichhorn, K.-J., Miller, M., Reduction of mechanical stress in micromachined components caused by humidity-induced volume expansion of polymer layers, Microsystem Technologies, 5, 312, 1998.
- [13] E. H. Wong, K. C. Chan, R. Rajoo, and T. B. Lim, "The mechanics and impact of hygroscopic swelling of polymeric materials in electronic packaging," 2000 Proceedings. 50th Electronic Components and Technology Conference (Cat. No.00CH37070), Las Vegas, NV, 2000, pp. 576-580.
- [14] Sutton, M.A., McNeill, S.R., Helm, D., Chao, Y.J., Advances in two-dimensional and three dimensional Computer vision, photomechanics, Topics in Applied Physics, 77, 323372, 2000
- [15] Wahab, M.A., Ashcroft, I.A., Crocombe, A.D., and Shaw, S.J., The Journal of Adhesion, 77, 43-80 (2001).
- [16] Brewis, D.M., Comyn, J., and Tredwell, S.T., Int. J. Adhesion and Adhesives, 7, 30-32 (1987).
- [17] Masaro, L. and Zhu, X.X., Prog. Polym. Sci. 24, 731-775 (1999).
- [18] Loh, W.K., Crocombe, A.D., Wahab, M.A., and Ashcroft, I.A., Int. J. Adhesion and Adhesives, 25, 1-12 (2005).
- [19] Crank J. The Mathematics of Diffusion. Clarendon Press, Oxford (1956).

Yalagach et al., ECTC 2019

© 2019 IEEE. Reprinted, with permission, from:  
M. Yalagach et al. **Numerical Analysis of the Influence of Polymeric Materials on a MEMS Package Performance Under Humidity and Temperature Loads**. In: *2019 IEEE 69th Electronic Components and Technology Conference (ECTC)*. 2019, 2029–2035. DOI: [10.1109/ECTC.2019.00311](https://doi.org/10.1109/ECTC.2019.00311)

## Numerical analysis of the influence of polymeric materials on a MEMS package performance under humidity and temperature loads

Mahesh Yalagach\*, Peter Filipp Fuchs\*, Archim Wolfberger\*, Mario Gschwandl\*, Thomas Antretter†, Michael Feuchter‡, Coen Tak§, Tao Qi¶

\*Polymer Competence Center Leoben GmbH  
Leoben, Austria  
mahesh.yalagach@pccl.at

†Montanuniversitaet Leoben, Institute of Mechanics  
Leoben, Austria

‡Montanuniversitaet Leoben, Institute of Material Science and Testing of Polymers  
Leoben, Austria

§ams AG

Premstaetten, Austria

¶Austria Technologie & Systemtechnik Aktiengesellschaft  
Leoben, Austria

**Abstract**—The rapid expansion of the Internet of Things (IoT) and consumer electronics is driving the demand for microelectromechanical systems (MEMS) in the area of wearables, smartphones, and home and building applications. MEMS sensor packages feature a variety of polymeric materials which can significantly affect their behavior under environmental loads as humidity or temperature. A broad range of different polymeric materials can be applied in the packages, but to get a good MEMS sensor performance, an optimized application tailored material combination should be applied. To analyze the effect of the applied material types an advanced simulation approach has to be considered. A hygro-thermo-mechanical simulation based on measured temperature and moisture dependent material properties is presented. As MEMS sensor packages are complex multi-material systems, the main challenge is the modeling of the moisture discontinuities in the interfaces. The discontinuity of moisture concentration has been solved by using the solubility approach.

**Keywords**—hygro-thermal, hygro-mechanical characterization; hygroscopic swelling; solubility; hygro-thermo-mechanical simulation; deformation;

### I. INTRODUCTION

The advancement in MEMS sensor packages towards their applications has gained interests in developing new polymeric materials. In operation, these MEMS sensor packages are often exposed to environmental and mechanical loads like temperature, humidity or bending. Under these loads, the thermo-hygro-mechanical material behavior of the applied polymeric materials strongly affects the MEMS sensor precision due to influences from materials, interfaces and package geometries [1]. The significant difference between the properties of the applied non-polymeric and polymeric

materials leads to a mismatch in hygroscopic swelling, thermal expansion, and bending strain. To optimize the material choice and design, simulation models accurately describing the resulting stress and strain field need to be established. The models can then be used as a basis for the development of tailored polymer materials for MEMS applications by studying the sensitivity on changed properties in the virtual simulation environment.

The effect of material combinations on the MEMS sensor package signal is studied in this work. Doing so, an extensive material characterization was performed, and a thermo-hygro-mechanical simulation strategy for a multi-material system was implemented. To solve the discontinuity in the moisture concentration, the solubility approach [9] is applied. The detailed local die deformation behavior was analyzed using a sub-modeling approach.

### II. EXPERIMENTAL

To understand the behavior of polymeric materials under different temperature and moisture loads, the materials were subjected to thermo-mechanical, hygro-thermal and hygro-mechanical material characterization. The following section explains briefly the different measurement techniques used:

#### A. Thermo-mechanical and Hygro-thermal characterization

The temperature dependent Elastic modulus ( $E$ ) for the critical materials were measured using the uni-axial tensile tests as well the dynamic mechanical analysis (DMA). The thermal conductivity ( $k$ ) was measured using *Netzsch LFA 467 HyperFlash*<sup>®</sup> (Netzsch GmbH, Selb, Germany) and the heat capacity ( $C_p$ ) was measured using differential scanning

calorimetry (DSC). The test conditions and dimensions of the material samples for all the thermo-mechanical analysis were considered according to [2][3][4]. To measure the in-plane coefficient of thermal expansion (CTE) the digital image correlation (DIC) method was employed using the system *Q400 TCT* (Dantec Dynamics, Ulm, Germany) [5]. The hygro-thermal material properties like the moisture diffusion coefficient ( $D$ ) and saturated concentration ( $M_\infty$ ) were determined based on gravimetric humidity conditioning methods according to JEDEC-JESD22-A120B standards [6]. The obtained conditioning curves were fitted using single and dual Fickian diffusion models [2].

### B. Coefficient of moisture expansion (CME)

The hygro-mechanical material parameter CME was measured using an approach based on a DIC system monitoring the hygroscopic strains during the drying process. The hygroscopic swelling strains  $\epsilon^\beta$  have a linear relation with change in moisture concentration  $\Delta C$  [2][7] as shown in (1).

$$\epsilon^\beta = \beta \Delta C, \quad (1)$$

where  $\epsilon^\beta$  is the hygroscopic strain,  $\beta$  is the coefficient of moisture expansion (CME) and  $\Delta C$  is the concentration change.

The following procedure was followed: *a)* humidity conditioning of two samples of the same material and dimension (sample A and sample B) by immersing them in demineralized water, *b)* desorption of moisture at constant temperature using *Q400 TCT* (Dantec Dynamics, Ulm, Germany) using sample A and a conventional temperature oven for sample B. Doing so the swelling strains  $\epsilon^\beta$  and concentration change  $\Delta C$  can be derived from sample A and sample B respectively. The desorption of the saturated material samples is carried out at  $90^\circ C$ ,  $120^\circ C$  and  $160^\circ C$  for six hours. A linear curve fit on the  $\epsilon^\beta$  over the  $\Delta C$  is performed to compute the CME  $\beta$ .

## III. HYGRO-THERMO-MECHANICAL SIMULATION

The hygro-thermo-mechanical simulations were performed using Abaqus (Abaqus 6.17, Dassault Systemes Simulia Corp., Providence, USA). The user-defined sub-routines USDFLD and UEXPAN are used in this model to compute the total moisture concentration and total volumetric strains respectively. The overall simulation approach except for the consideration of the moisture discontinuity is described in detail in a preceding publication [2]. The following section explains briefly an approach to solve the problem of moisture discontinuity in the interface region in multi-material systems using solubility  $S$  approach.

### A. Solubility approach for multimaterial interface

To solve the discontinuities in the multi-materials system, several approaches have been listed in the literature considering the thermal and moisture analogy: wetness theory,

normalization concentration analogy [8], "Direct" analogy [9] and advanced normalized concentration analogy [10]. The normalization concentration analogy was applied in this work because it is best suited to describe our load cases. However, a transient hygro-mechanical load is not possible to be simulated. Therefore, the advanced normalized concentration analogy would have to be used.

The mass diffusion analysis in Abaqus is described by the Fick's second Law as shown in (2)

$$\dot{C} = \nabla \cdot (D \nabla C), \quad (2)$$

where  $C$  is the moisture concentration and  $D$  is the diffusivity. In heterogeneous materials, the normalization concentration method was used to solve the discontinuity. In this approach, the moisture concentration  $C$  is normalized by the solubility  $S$ . The normalized concentration  $\varphi$  [9] is defined as,

$$\varphi = \frac{C}{S} \quad (3)$$

Using Eq.(3) in Eq.(2), and assuming that the solubility  $S$  is both uniform ( $\nabla S = 0$ ) and time independent ( $\dot{S} = 0$ ), the Fick's second law yields,

$$S \dot{\varphi} = \nabla \cdot (D S \nabla \varphi), \quad (4)$$

In the solubility approach, the Henry's Law [11] is used to determine the  $S$ .

$$M_\infty = M_{sat} = S P_{VP}, \quad (5)$$

where  $P_{VP}$  is the ambient vapor pressure, as the saturated concentration  $M_\infty$  at  $23^\circ C$ ,  $60^\circ C$  and  $90^\circ C$  is known from the hygro-thermal material characterization, and the ambient vapor pressure can be adopted from the literature [12] at this temperature levels the solubility  $S$  can be calculated using 4. Using the above definition, the solubility  $S$  was computed. With  $D$  and  $M_\infty$  derived from the experimental data, all parameters needed for the mass diffusion analysis are defined.

### B. Global and local simulation approach

1) *Global simulation approach:* In a global simulation approach, the effect of temperature, moisture and mechanical loads were evaluated considering the printed circuit board (PCB). Since PCB's have a complex structure and detailed FE model of an entire PCB would be computationally very expensive. Hence, a homogenization approach is applied. Doing so, an in-house development for an automated PCB FE-model generation is used [13]. The automated model generation uses segmentation and clustering algorithms to automatically generate FEA-models of arbitrarily complex build-ups using their design data. A conventional PCB (Figure 1) designed according to IPC/ JEDEC-9702 standards [14] with dimensions,  $135 \times 77 \times 0.83 \text{ mm}$  was considered for this modeling approach. The used element type is a linear

hexahedron continuum element of type C3D8R, and the total number of elements is 69692.

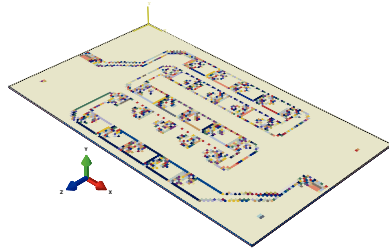


Figure 1. The conventional PCB used for global simulation modeling.

2) *Local simulation approach*: In this approach, the MEMS sensor soldered on to the PCB was considered, and the influence of temperature, moisture and mechanical loads on the MEMS sensor was evaluated. A commonly used MEMS sensor package with dimensions  $2 \times 2 \times 0.7 \text{ mm}$  was considered and the dimensions of the submodel PCB is  $9 \times 9 \times 0.83 \text{ mm}$ . The complete local model setup including the MEMS sensor and PCB with solder lands is depicted in Figure 2. The used element type for MEMS sensor package is a linear tetrahedron continuum element of type C3D4, and the total number of elements are 829724. For the local PCB, 580608 linear hexahedral elements of type C3D8

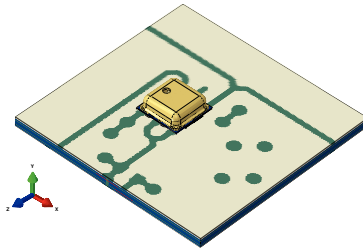


Figure 2. MEMS sensor package soldered on a PCB for local simulation modeling.

### C. Materials

The MEMS sensor is made up of a variety of materials as shown in Figure 3. The material properties for non-polymeric materials like metal-lid, Au-wire, silicon-die and copper were taken from literature [15][16]. The polymeric

materials in this MEMS sensor are the conductive adhesive, insulating adhesive, solder mask, and a prepreg.

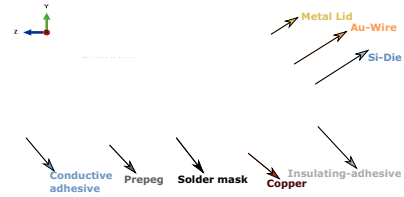


Figure 3. Materials in the considered MEMS sensor package.

The Table I, shows the two different polymeric material combination's (MAT-1 and MAT-2) considered for the MEMS sensor. For prepreg and insulating adhesive two different materials were considered. The prepreg's, CCL-1078 and PP1-1037, are glass fiber fabric woven reinforced epoxy resins. They differ concerning to the matrix resin and the fabric type. PP1-1037 features a higher fiber volume content than CCL-1078.

Table I  
CONSIDERED MATERIAL COMBINATION'S USED IN MEMS SENSOR PACKAGE.

| Materials           | MAT-1    | MAT-2    |
|---------------------|----------|----------|
| Prepreg             | CCL-1078 | PP1-1037 |
| Insulating adhesive | ADH-X-01 | ADH-Y-01 |
| Conductive adhesive | ADH-Z-02 |          |
| Solder mask         | SLM-01   |          |

The insulating adhesives ADH-X-01 and ADH-Y-01 are both made of silicone as a base material, but the curing process for both the materials differs. The insulating adhesive is used in the package to fix the silicon die on to the substrate. The influence of prepreg and the insulating adhesive was chosen to be evaluated as their material properties are expected to have the most significant effect on the MEMS sensor performance.

The conductive adhesive (ADH-Z-02) and the solder mask (SLM-01) were kept the same for both material combinations. The ADH-Z-02 is a silver-filled epoxy resin and is used to fix the metal lid to the substrate. The moisture uptake in these materials is significantly higher compared to other polymeric materials during the humidity conditioning. The PCB used for the global and local sub-modeling approach is made up of multiple layers of commonly used FR4 prepreg (PP2-1037), solder masks (SLM-01) and copper layers.

### D. Evaluation line

The MEMS sensor precision depends on the ability to minimize as much as possible the influence of external

factors as temperature, moisture and mechanical loads on the die deformation. Thus, the criteria for a suitable material combination and package design is the local deformation at the upper die surface. The defined evaluation line in this contribution is shown in Figure 4.

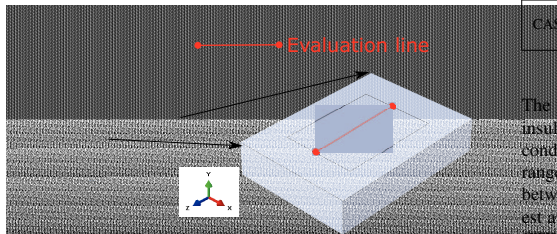


Figure 4. Evaluation line in the silicon die of the MEMS sensor.

#### E. Boundary conditions

The hygro-thermo-mechanical simulation involves a heat transfer simulation, two mass diffusion simulations and a thermo-mechanical step to evaluate the total volumetric strains. All loads were applied in a linear way over 3600 seconds. For the heat transfer simulation, the initial condition is  $23^{\circ}\text{C}$ , and the temperature of  $85^{\circ}\text{C}$  is applied to the surfaces exposed to the environment. For the dual Fickian mass diffusion simulation, the normalized saturated concentrations ( $M_{1\infty}$  &  $M_{2\infty}$ ) are applied to the polymeric materials exposed to the environment. The initial moisture concentration of 0% was considered for all the materials. For the non-polymeric materials like the metal lid, Au-wire, Si-die, and copper, the moisture dependent material properties like  $D$ ,  $M_{\infty}$  and  $S$  are considered to be negligible. In total four different simulations were carried out. For all the simulations, the defined moisture (100% RH) and temperature ( $85^{\circ}\text{C}$ ) loads were considered. In CASE-1 and CASE-2, the simulations are based on a local model only, and the influence of the material combinations (MAT-1 and MAT-2) is analyzed. In CASE-3 the effect of considering the global model is evaluated. In CASE-4 additionally, a bending load in the global model according to the IPC/JEDEC-9702 standards [14] of 3mm is taken into account. The four simulations are summarized in Table II.

### IV. RESULTS AND DISCUSSION

#### A. Material Characterization

The results obtained from thermo-mechanical and hygro-thermal material characterization techniques have been discussed in [2]. The additional results obtained for in-plane CTE ( $\alpha$ ) and CME ( $\beta$ ) are discussed in this contribution.

Table II  
LOAD CASES CONSIDERED IN LOCAL SUBMODELING APPROACH.

|        | Material | Loads  | Simulation approach              |
|--------|----------|--|----------------------------------|
| CASE-1 | MAT-1    | $85^{\circ}\text{C}$ , 100% RH                       | Local model                      |
| CASE-2 | MAT-2    |  |                                  |
| CASE-3 | MAT-1    | $85^{\circ}\text{C}$ , 100% RH                       | Global model +<br>Local submodel |
| CASE-4 |          | $85^{\circ}\text{C}$ , 100% RH +<br>3mm bending load |                                  |

The Figure 5 shows the CTE results obtained for the insulating adhesives ADH-X-01 and ADH-Y-01, and the conductive adhesive ADH-Z-02. Within the measurement range of  $-50^{\circ}\text{C}$  to  $+180^{\circ}\text{C}$  there is a substantial difference between the adhesives behavior. ADH-X-01 shows the highest average CTE and ADH-Y-01 shows the lowest CTE. The CTE of ADH-Z-02 is in between. Maximum differences of about 50% emphasize the importance of the material choice.

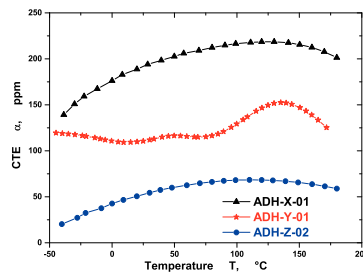


Figure 5. The in-plane CTE measured for different adhesive materials.

For the coefficient of moisture expansion (CME) measurements, the measured change in concentration  $\Delta C$  is depicted in the Figure 6 and 7. It is observed from Figure 6, that the prepreg PP2-1037 shows the highest concentration change of about 1.2% compared to CCL-1078 (0.7%) and PP1-1037 (0.9%).

The moisture adsorption in the adhesives depicted in Figure 7 shows even more pronounced differences between the analyzed materials. Maximum moisture uptakes varied between 1.7% (ADH-Z-02), 1.1% (ADH-X-01) and 0.55% (ADH-Y-01). As the operating temperature for ADH-Y-01 is limited to  $130^{\circ}\text{C}$ , no measurement was performed at  $160^{\circ}\text{C}$  for this material.

The measured dimensional change or the hygroscopic swelling strains  $\epsilon^{\beta}$  for prepreps and adhesives are depicted in Figure 8 and 9. In Figure 8, the prepreg hygroscopic

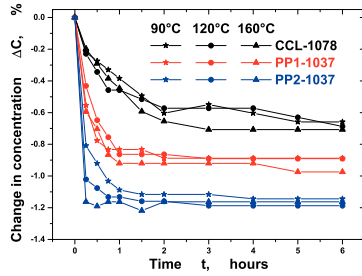


Figure 6. Change in the moisture concentration  $\Delta C$  for prepregs from desorption process at  $90^{\circ}\text{C}$ ,  $120^{\circ}\text{C}$  and  $160^{\circ}\text{C}$  for six hours.

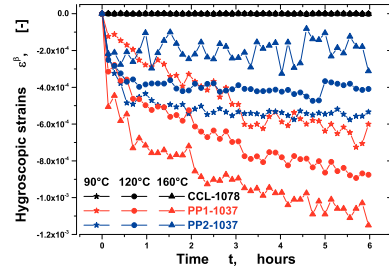


Figure 8. Change in the hygroscopic swelling strains  $\epsilon^{\beta}$  for prepregs at  $90^{\circ}\text{C}$ ,  $120^{\circ}\text{C}$  and  $160^{\circ}\text{C}$  for six hours.

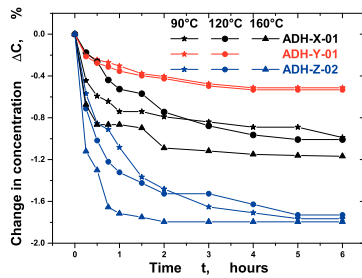


Figure 7. Change in the moisture concentration  $\Delta C$  for adhesives from desorption process at  $90^{\circ}\text{C}$ ,  $120^{\circ}\text{C}$  and  $160^{\circ}\text{C}$  for six hours.

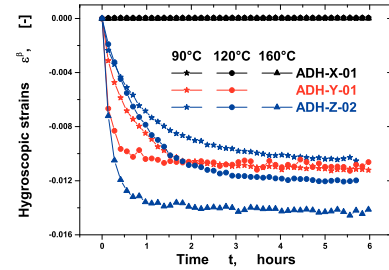


Figure 9. Change in the hygroscopic swelling strains  $\epsilon^{\beta}$  for adhesives at  $90^{\circ}\text{C}$ ,  $120^{\circ}\text{C}$  and  $160^{\circ}\text{C}$  for six hours.

swelling is very low for all materials. However, a maximum hygroscopic strain of 0.12% can be observed for prepreg PP1-1037 while no hygroscopic strain was measured for prepreg CCL-1078 at all. It is interesting to note that the temperature trend for PP1-1037 and PP2-1037 is vice-versa. That is assumed to be caused by the different glass transition ( $T_g$ ) regions. The  $T_g$  values were determined in DMA measurements:  $T_g$  of PP1-1037 is  $270^{\circ}\text{C}$  and the  $T_g$  of PP2-1037 is  $170^{\circ}\text{C}$ . While the tested temperatures for CME are well below the  $T_g$  level for PP1-1037, for PP2-1037 they are within the onset of the transition region. It is known from the literature that the temperature trend changed in this region [8].

The  $\epsilon^{\beta}$  in adhesives are significantly higher (Fig. 9) compared with prepreg materials. For the conductive adhesive ADH-Z-02, the  $\epsilon^{\beta}$  is greatest (1.4%) compared with insulating adhesives ADH-X-01 and ADH-Y-01. The ADH-

Y-01 material showed a  $\epsilon^{\beta}$  of about 1% while the ADH-X-01 did not show any strains. Hence, in this contribution, based on the measurement results, only the moisture dependence from PP1-1037, PP2-1037, ADH-Y-01, and ADH-Z-02 materials has been considered for the hygro-thermo-mechanical simulation.

The CME ( $\beta$ ) was computed from a linear curve fit between the hygroscopic swelling strains  $\epsilon^{\beta}$  and the change in concentrations  $\Delta C$ .

### B. Simulations

In this section, the results from the hygro-thermo-mechanical simulations are discussed. The results obtained from CASE-1 and CASE-2, using different material combinations (MAT-1 and MAT-2) are depicted in the Figure 10. The strain levels in CASE-2 are significantly higher compared to CASE-1. The materials in MAT-2 experience hygro-thermal expansion during the measurements, while

the materials in MAT-1 were observed to show no hygro-thermal expansion in the experiments. Additionally, the materials applied in MAT-1 also show a lower CTE. The simulation results give the expected trend and confirm that a lower thermal and hygroscopic expansion in the polymeric materials is preferable.

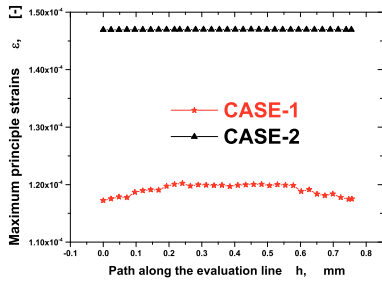


Figure 10. Strain levels along the evaluation line using the CASE-1 (MAT-1) and CASE-2 (MAT-2) material combinations in local modeling approach.

In the Figure 11, a comparison between the CASE-1 and CASE-3, showing the difference in strain levels is given. This difference is due to the submodel boundary conditions in CASE-3. The influence of the deformations in the global model (CASE-3) is significant. Thus, to correctly describe the local deformations of the silicon die, it is essential to consider the global model results.

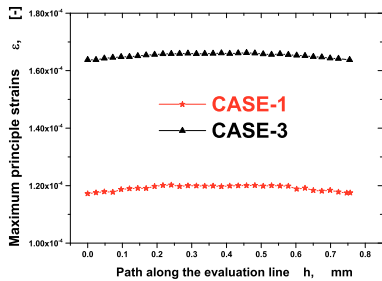


Figure 11. Strain levels along the evaluation line using the MAT-1 in a local (CASE-1) and to local submodeling (CASE-3) approach.

The results obtained from CASE-3 and CASE-4 in a hygro-thermo-mechanical step of the local sub modeling approach using the MAT-1 material combination is depicted in the Figure 12.

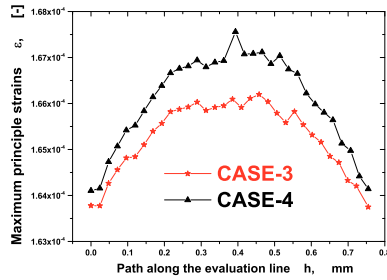


Figure 12. Strain levels along the evaluation line using CASE-3 and CASE-4 in local submodeling approach.

From the Figure 12, the strain levels in the evaluation line are significantly higher for CASE-4 compared with CASE-3. It is shown that already small global mechanical loads affect the local silicon die deformation and have to be considered in detail in local submodeling approach.

## V. CONCLUSION

In this research work, the results from the thermo-mechanical and hygro-mechanical material characterization for different polymeric materials used in MEMS sensor packages are presented. Based on the experimental results, using global and local simulation modeling approaches, hygro-thermo-mechanical simulations were performed. The local deformation of the silicon die under  $85^{\circ}C$  and 100% RH was analyzed in a specified evaluation region. To this end, the influence of different material combinations was evaluated. Obtained results emphasize the importance of considering the total system including the whole PCB could be shown. A submodeling approach featuring the results of a global model gives different results than a local model only. The suitability to include additional mechanical loads on a global level and to derive its influence is also shown by considering a bending load.

The following open points will be worked on in the future. Absorption at different humidity levels is planned to be tested. Additionally to the yet considered 100% RH (immersion in water) conditioning in a climate chamber ( $85^{\circ}C$  and 85% RH) will be performed. Furthermore, validation experiments for the simulation models are planned. The die deformation under defined loads (humidity, temperature, and bending) will be derived from a measured sensor signal and compared to the simulation results.



#### ACKNOWLEDGMENT

The research work was performed within the K-Project "PolyTherm" at the Polymer Competence Center Leoben GmbH (PCCL, Austria) within the framework of the COMET-program of the Federal Ministry for Transport, Innovation and Technology and the Federal Ministry for Digital and Economic Affairs with contributions by University of Leoben, ams AG and by AT&S Austria Technologie & Systemtechnik Aktiengesellschaft. Funding is provided by the Austrian Government and the State Government of Styria.

#### REFERENCES

- [1] Zarnik, M. Santo; Belavic, D. (2012): An Experimental and Numerical Study of the Humidity Effect on the Stability of a Capacitive Ceramic Pressure Sensor.
- [2] M. Yalagach et al., "Influence of environmental factors like temperature and humidity on MEMS packaging materials,," 2018 7th Electronic System-Integration Technology Conference (ESTC), Dresden, 2018, pp. 1-6. doi: 10.1109/ESTC.2018.8546484.
- [3] M. Gschwandl et al., "Modeling of manufacturing induced residual stresses of viscoelastic epoxy mold compound encapsulations," 2017 IEEE 19th Electronics Packaging Technology Conference (EPTC), Singapore, 2017, pp. 1-8. doi: 10.1109/EPTC.2017.8277557.
- [4] M. Morak, P. Marx, M. Gschwandl, P. Fuchs, M. Pfost, and F. Wiesbrock, "Heat dissipation in epoxy/amine-based gradient composites with alumina particles: A critical evaluation of thermal conductivity measurements," *Polymers*, vol. 10, no. 10, p. 1131, 2018.
- [5] M. Gschwandl et al., "Evaluation of Digital Image Correlation Techniques for the Determination of Coefficients of Thermal Expansion for Thin Reinforced Polymers.," *Proceedings of 20th International Conference on Electronic Materials and Packaging*, 2018.
- [6] JESD22-A120A, Test method for the measurement of moisture diffusivity and water solubility in organic materials used in electronic devices, JEDEC Standards 2001.
- [7] Stellrecht, E., Han, B., Pecht, M.G., "Characterization of the hygroscopic swelling behavior of mold compounds and plastic packages", *IEEE Transactions on Components and Packaging Technologies*, 27, 499506, 2004.
- [8] E.H. Wong, Y.C. Teo, T.B. Lim, Moisture diffusion and vapor pressure modeling of IC packaging Proc. of Electronic Components and Technology Conference 1998, pp. 1372-1378.
- [9] Yoon, S., Han, B., and Wang, Z., 2007, "On Moisture Diffusion Modeling Using Thermal Diffusion Analogy," *J. Electron. Packag.*, 129, pp. 421-426.
- [10] Jang C, Park S, Han B, Yoon S. Advanced Thermal-Moisture Analogy Scheme for Anisothermal Moisture Diffusion Problem. *ASME. J. Electron. Packag.* 2008;130(1):011004-011004-8. doi:10.1115/1.2837521.
- [11] Osswald, T., and Menges, G., 1996, *Materials Science of Polymers for Engineers*, Hanser-Gardener, Munich.
- [12] <http://www.wiredchemist.com/chemistry/data/vapor-pressure>
- [13] M. Gschwandl et al., "Finite Element Analysis of Arbitrarily Complex Electronic Devices," In: *IEEE 18th Electronics Packaging Technology Conference (EPTC) 2016*, S. 497-500.
- [14] IPC/JEDEC-9702, *Monotonic Bend Characterization of Board-Level Interconnects*, JEDEC Standards 2004.
- [15] Dwight E. Gray (Ed.) *American Institute of Physics Handbook* McGraw-Hill Book Company Inc. 1957.
- [16] *Handbook of Stainless Steels*, Donald Peckner and I. M. Bernstein, McGraw-Hill Book Company, New York, NY, (1977)

© 2020 IFSA. Reprinted, with permission, from:

M. Yalagach et al. **Characterization and Modeling of Prepregs Applied in MEMS Sensor Packages with a Focus on Moisture Dependence**. In:

*Microelectronic Devices and Technologies*. Vol. 3. Online: International

Frequency Sensor Association (IFSA) Publishing, S. L., Oct. 2020, 5–10. ISBN:

978-84-09-24422-5. URL:

[https://sensorsportal.com/MicDAT\\_2020/MicDAT\\_2020\\_Proceedings.pdf](https://sensorsportal.com/MicDAT_2020/MicDAT_2020_Proceedings.pdf)



## **Microelectronic Devices and Technologies**

**Proceedings of the 3<sup>rd</sup> International Conference  
on Microelectronic Devices and Technologies (MicDAT '2020)**

**22-23 October 2020**

**Edited by Sergey Y. Yurish**



Sergey Y. Yurish, *Editor*  
Microelectronic Devices and Technologies  
MicDAT '2020 Conference Proceedings

Copyright © 2020  
by International Frequency Sensor Association (IFSA) Publishing, S. L.

E-mail (for orders and customer service enquires): [ifsa.books@sensorsportal.com](mailto:ifsa.books@sensorsportal.com)

Visit our Home Page on <http://www.sensorsportal.com>

All rights reserved. This work may not be translated or copied in whole or in part without the written permission of the publisher (IFSA Publishing, S. L., Barcelona, Spain).

Neither the authors nor International Frequency Sensor Association Publishing accept any responsibility or liability for loss or damage occasioned to any person or property through using the material, instructions, methods or ideas contained herein, or acting or refraining from acting as a result of such use.

The use in this publication of trade names, trademarks, service marks, and similar terms, even if they are not identifies as such, is not to be taken as an expression of opinion as to whether or not they are subject to proprietary rights.

ISBN: 978-84-09-24422-5  
BN-20191019-XX  
BIC: TJFD

## Contents

|  |           |
|--|-----------|
| Contents .....   | 3         |
| Foreword .....   | 4         |
| <b>Characterization and Modeling of Prepregs Applied in MEMS Sensor Packages with a Focus on Moisture Dependence .....</b>   | <b>5</b>  |
| <i>Mahesh Yalagach, Peter Filipp Fuchs, Thomas Antretter, Michael Feuchter, Markus Weber, Tao Qi</i>   |           |
| <b>Determination of Temperature Dependent Optical Properties of Amorphous Silicon Thin Films at High Heating Rates for CMOS Compatible Laser Crystallization Processes .....</b> | <b>11</b> |
| <i>F. Fuchs, C. Vedder, J. Stollenwerk, J. H. Schleifenbaum</i>  |           |
| <b>Digital Single-electron Astrocyte Signaling Implementation .....</b>  | <b>14</b> |
| <i>B. O. Câmara and J. G. Guimarães</i>  |           |
| <b>Mont-Blanc 2020 NoC: A Low-power and High Bandwidth Network on Chip Generator .....</b>   | <b>18</b> |
| <i>P.-A. Lagadec, S. Derradji, A. Nocua and Z. Menyhart</i>  |           |
| <b>Digital Micromirror Design for Manufacturing and High Performance .....</b>   | <b>23</b> |
| <i>C. Gong</i>   |           |
| <b>Pupil Position Estimation Error in an Eye Tracking System Based on the MEMS Mirror Scanning Method .....</b>  | <b>28</b> |
| <i>M. Pomianek, M. Piszczek, M. Maciejewski and P. Krukowski</i>   |           |
| <b>TCAD-SPICE Investigation of SEU Sensitivity for SOI and DSOI CMOS SRAM Cells in Temperature Range up to 300 °C .....</b>  | <b>31</b> |
| <i>K. O. Petrosyants, D. A. Popov, B. Li and Y. Wang</i>   |           |
| <b>Physical Alloying of Carbide Nanocomposite Coating by Carbon Nanostructures .....</b>   | <b>35</b> |
| <i>P. I. Vysikaylo, V. S. Mitin, V. I. Mashchenko</i>  |           |
| <b>Detection of Toxic Gas in Dust-filled Environment Using Integrated Microwave-microfluidics .....</b>  | <b>42</b> |
| <i>H. Sadabadi, A. Bostani and A. Esmaeili</i>   |           |
| <b>Thin-layer Microfluidics with Modular Microwave Sensing: A Sensitive Platform for Biomedical and Organ-on-Chip Applications .....</b>   | <b>46</b> |
| <i>H. Sadabadi, M. Zarifi and A. S. Nezhad</i>   |           |
| <b>Nanoporous Anodic Alumina Membranes as Passive Luminance Enhancers for LCD .....</b>  | <b>48</b> |
| <i>D. Shimanovich, V. Yakovtseva, V. Shulgov and G. Basov</i>  |           |
| <b>Internal Stress in Aluminum Layers Deposited on Dielectric Substrates .....</b>   | <b>51</b> |
| <i>V. Shulgov, D. Shimanovich, V. Yakovtseva and G. Basov</i>  |           |

## Foreword

On behalf of the MicDAT' 2020 Organizing Committee, I introduce with pleasure these proceedings devoted to contributions from the 3<sup>rd</sup> International Conference on Microelectronic Devices and Technologies (MicDAT'2020), 22-23 October 2020. The conference is the third of a series of annual International Conferences on Microelectronic Devices and Technologies (MicDAT) held in Barcelona (Spain) in 2018, and in Amsterdam (The Netherlands) in 2019. The conference is organized by the International Frequency Sensor Association (IFSA) in a technical cooperation with our sponsors IFSA Publishing, S.L., (Barcelona, Spain) and media partner - MDPI 'Micromachines' (ISSN 2072-666X) journal (Switzerland). The conference program provides an opportunity for researchers interested in microelectronics to discuss their latest results and exchange ideas on the new trends and challenges. The main objective of the MicDAT' 2020 conference is to encourage discussion on a broad range of microelectronics related topics and to stimulate new collaborations among the participants.

The proceedings contains all papers presented at the conference. We hope that these proceedings will give readers an excellent overview of important and diversity topics discussed at the conference. Based on the proceeding's contributions, selected and extended papers will be submitted by the authors to the 'Sensors & Transducers' open access journal (ISSN: 2306-8515, e-ISSN 1726-5479) or 'Micromachines' open access journal. The limited number of articles, published in the 'Sensors & Transducers' journal will be invited to be extended for 'Advances in Microelectronics: Reviews', Vol. 3, Book Series.

We thank all authors for submitting their latest work, thus contributing to the excellent technical contents of the conference. Especially, we would like to thank the individuals and organizations that worked together diligently to make this conference a success, and to the members of the International Program Committee for the thorough and careful review of the papers. It is important to point out that the great majority of the efforts in organizing the technical program of the conference came from volunteers.

*Prof., Dr. Sergey Y. Yurish*  
*MicDAT' 2020 Chairman*

## Characterization and Modeling of Prepregs Applied in MEMS Sensor Packages with a Focus on Moisture Dependence

**Mahesh Yalagach<sup>1</sup>, Peter Filipp Fuchs<sup>1</sup>, Thomas Antretter<sup>2</sup>, Michael Feuchter<sup>2</sup>, Markus Weber<sup>3</sup> and Tao Qi<sup>4</sup>**

<sup>1</sup> Polymer Competence Center Leoben GmbH (PCCL), Leoben, Austria

<sup>2</sup> Montanuniversität Leoben, Leoben, Austria

<sup>3</sup> ams AG, Premstätten, Austria

<sup>4</sup> Austria Technologie & Systemtechnik Aktiengesellschaft, Leoben, Austria

Tel.: + 43 3842 42962 716

E-Mail: mahesh.yalagach@pccl.at

---

**Summary:** The use of Micro-Electro-Mechanical Semiconductor (MEMS) sensor packages has revolutionized the automotive, home, and building applications (HABA) and Internet of Things (IoT) industries. However, increasing demands on their functionality and reliability necessitates an improved behavior of the packaging materials concerning thermal and hygroscopic changes. Only a low material sensitivity to environmental influences will ensure the reliable performance of the sensors during their application lifetime. To this end, the potentially applied materials undergo defined humidity and temperature-dependent experimental tests. In this contribution, the influence of humidity and temperature has been studied for five different prepreg materials, which are commonly applied as a substrate material in a MEMS sensor. The measured humidity dependent material properties are the basis for a numerical diffusion analysis and a virtual hygro-thermo-mechanical reliability assessment.

**Keywords:** Moisture uptake, Gravimetric method, Hygroscopic swelling, Coefficient of moisture expansion, Humidity tensile tests.

---

### 1. Introduction

The MEMS sensor packages are a multi-material composite system. These packages comprise polymeric materials like prepregs, solder-mask, insulation, and conductive adhesives. The materials involved in MEMS sensor packages show significant effects like thermal expansion and hygroscopic swelling when exposed to harsh environmental loads. Due to these effects, during the application of the packages, stresses are introduced. The induced stresses cause deformation, potentially delamination, and cracks in the materials [1, 10]. In this contribution, the dependence of moisture absorption of five different prepregs, which are commonly used in MEMS sensors, is analyzed. The prepreg materials serve as a substrate material for a MEMS sensor build-up. The moisture absorption of prepregs has a significant impact on the MEMS sensor package reliability [7]. Many failures in MEMS sensor packages are due to the absorption of moisture. Therefore, the characterization of moisture absorption and diffusion in these packages needs to be accounted for modeling the reliability behavior of the sensor package. In doing so, the prepreg materials have been extensively studied using different humidity dependent material characterization techniques. The obtained humidity and temperature-dependent material properties are prepared to be used in hygro-thermo-mechanical simulations [1, 2] to assess the deformation and changes in stress conditions. This information serves as vital information for material and design optimization to eliminate moisture-related failures.

### 2. Hygroscopic Material Characterization

The material characterization involves analyzing the effect of moisture absorption and its impact on the physical and chemical properties of the polymeric materials involved in this contribution. Different moisture dependent characterization techniques like gravimetric humidity conditioning, Coefficient of Moisture Expansion (CME), and humidity dependent Young's modulus were performed. Five different prepregs, CCL-1037, CCL-1078, PP1-1037, PP2-7628, and PP3-1037, were considered for the characterization. They vary in their matrix material, fabric reinforcement type, and thickness. The thickness of the prepregs varied from 60  $\mu\text{m}$  to 1.5 mm.

#### 2.1. Gravimetric Humidity Conditioning

The moisture dependent properties like moisture diffusion coefficient  $D$  and saturated mass  $M_{sat}$  for the prepregs were measured using the gravimetric humidity conditioning method [3]. Apart from conditioning the prepregs in a distilled water bath [1], a climate chamber was used to measure the moisture uptake at 85 °C and 85 % R.H. (Relative Humidity). Before starting the humidity conditioning, the prepregs were conditioned in a temperature oven at 125 °C until they were completely dried (constant weight) To monitor the weight change during the conditioning, the prepregs were repeatedly shortly removed at

predefined points in time from the plastic container or the climate chamber. The surface of the prepregs was cleaned using paper tissue, and they were weighed using a high precision balance. The prepregs tend to follow single Fickian diffusion law above their glass transition temperature ( $T_g$ ) [4]. But, at a temperature below  $T_g$ , these materials follow a non-Fickian or dual Fickian diffusion model. In this contribution, the experimental conditioning curves were analytically approximated using both single and dual Fickian diffusion models.

## 2.2. Coefficient of Moisture Expansion (CME)

The hygroscopic swelling strains  $\varepsilon^\beta$  developed during the gravimetric humidity conditioning are supposed to have a linear relationship with the change in concentration  $\Delta C$  [5] according to (1):

$$\varepsilon^\beta = \beta \Delta C, \quad (1)$$

where  $\beta$  is the CME. The effect of hygroscopic swelling strains  $\varepsilon^\beta$  in the prepregs is measured using a Digital Image Correlation (DIC) approach. In this process, the hygroscopic strains are monitored during drying at defined temperature levels [2]. The moisture changes or changes in concentration are measured using a high-resolution balance. The CME measurements are carried out on the prepregs, which have reached their maximum mass saturation during the humidity conditioning process. The desorption of the saturated material samples was carried out at 70 °C, 90 °C, 120 °C, 140 °C, and 160 °C for six hours. The CME ( $\beta$ ) is computed from a linear curve fit between the hygroscopic swelling strains  $\varepsilon^\beta$  and the change in concentration  $\Delta C$ .

## 2.3. Humidity Dependent Young's Modulus

In order to assess the effect of humidity and temperature on Young's modulus, humidity and temperature-controlled tensile tests were performed on the prepregs. Before the humidity dependent testing, the prepregs were dried in a temperature chamber at 125 °C for 24 hours in a first step and conditioned using a climate chamber in the second step. The defined temperature and humidity levels were 23 °C (50 % and 85 % RH), 60 °C (50 % and 85 % RH), and 85 °C (50 % and 85 % RH). The temperature-dependent tensile tests were performed for the defined temperatures 23 °C, 100 °C, 180 °C and 250 °C. The tests were performed using a Weiss Technik climate chamber and an Instron 4505 universal testing system. For the strain data acquisition, a Mercury 3D DIC system was used. The dimensions of the tensile specimens were prepared according to ISO 527 – 1BA. The measured Young's modulus was compared with results from Dynamic Mechanical Analysis (DMA) performed using Mettler Toledo DMA

(Mettler-Toledo, Columbus, Ohio, USA) in a tensile mode under controlled displacement load.

The prepreg materials were tested at a frequency of 1 Hz and over a temperature range of -100 °C to 300 °C with a heating rate of 2 K/min. Fig. 1 shows the test setup used for the measurement of humidity dependent tensile tests for the prepregs.

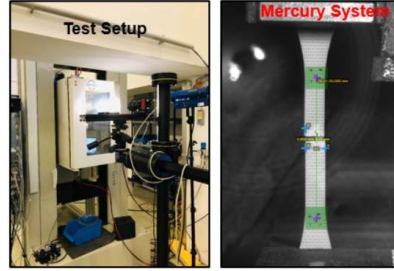


Fig. 1. Experimental setup for the humidity-controlled tensile test with climate chamber and a Mercury 3D DIC system

## 3. Verification Simulation Model

To determine the moisture absorption in prepregs numerically, a verification simulation model was set up in Abaqus (Abaqus 2017, Dassault Systemes Simulia Corp., Providence, USA) using a mass diffusion analysis at test specimen level. As Abaqus uses Fick's law to model the mass diffusion analysis [8, 9], this analysis was numerically solved using a dual Fickian diffusion model approach [1]. This diffusion model was solved using two parallel single Fickian mass diffusion analyses using the analytical fitted parameters moisture diffusion coefficient  $D$  and saturated mass  $M_{sat}$  as boundary conditions. The resulting single Fickian moisture concentrations were saved as field variables and were summed up using the USDFLD subroutine.

## 4. Results and Discussion

The results from the gravimetric humidity conditioning for prepregs show a temperature and humidity dependent moisture uptake trend for the considered prepregs. Fig. 2. represents the typical moisture uptake curve for the prepregs conditioned at 85 °C and 85 % R.H. The maximum moisture uptake of nearly 0.8 % was observed in PP3-1037 material, and a minimum of 0.5 % was found in CCL-1078.

Figs. 3, 4 and 5 depicts the typical moisture gain trend obtained by immersing the prepregs in a distilled water bath and conditioning them at 90 °C, 60 °C and 23 °C. The PP3-1037 material absorbed the maximum moisture (1.3 %) compared with other prepreg materials at all conditioning temperatures. This



prepreg is made up of substandard matrix material, which tends to absorb more moisture during the humidity conditioning.

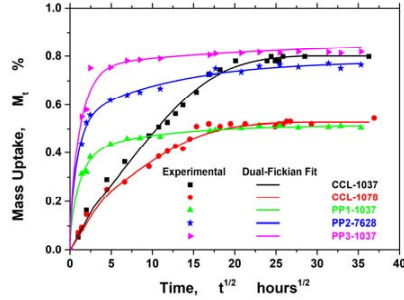


Fig. 2. Typical moisture gain trend and curve fit using an analytical solution (dual Fickian diffusion model) for prepregs at 85 °C and 85 % R.H.

Alternatively, a minimum of 0.6 % of moisture absorption was noticed in CCL-1078 material. The prepregs CCL-1037 and CCL-1078 have similar matrix material but differ in their resin content, fabric reinforcement type, and thickness. The CCL-1037 has a higher resin content of 27 % compared with CCL – 1078 (23 %). Therefore CCL-1037 absorbs more moisture compared with CCL-1078.

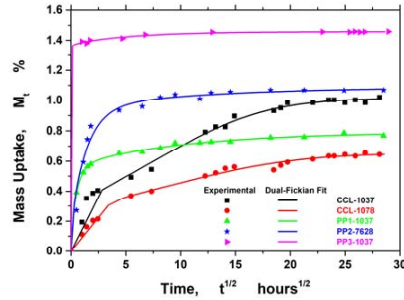


Fig. 3. Typical moisture gain trend and curve fit using an analytical solution (dual Fickian diffusion model) for prepregs at 90 °C immersion.

Additionally, the materials PP1-1037 and PP2-7628 have a similar moisture gain trend, but differ in the amount of maximum moisture absorbed. From Fig. 2 and Fig. 3, a maximum of 0.7 % and nearly 1 % was observed for PP1-1037 and PP2-7628 prepregs, respectively. Consequently, Figs. 2-5 depict that the dual Fickian diffusion model fits the overall behavior of the experimental data.

Furthermore, in Fig. 5 the dotted lines represent the nonlinear fit from the single Fickian diffusion model. On more detailed evaluation, the fit from the single Fickian model cannot follow the trend of the

experimental data in the initial region. The obtained saturated mass  $M_{sat}$  and the diffusion coefficient  $D$  obtained from dual Fickian fit were further used in "Hygro-thermo-mechanical simulations" [2] and in the verification simulation model, to compute the total concentration change numerically. To summarize, from the typical moisture gain trend, both the diffusion coefficient and saturated mass increase with an increase in temperature and humidity.

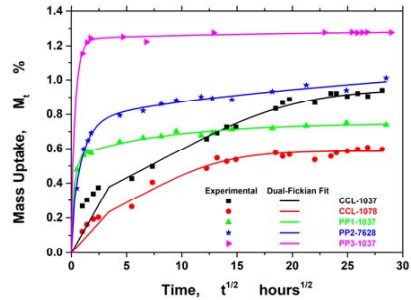


Fig. 4. Typical moisture gain trend and curve fit using an analytical solution (dual Fickian diffusion model) for prepregs at 60 °C immersion.

For the Coefficient of Moisture Expansion (CME), the change in concentration  $\Delta C$  measured using desorption or drying process is depicted in Fig. 6. It can be observed that the prepreg PP3-1037 and PP2-7628 show the highest concentration change of nearly 1.2 % compared with PP1-1037 (0.8 %), CCL-1078 (0.6 %), and CCL-1037 (1 %). The desorption measurements were also carried out at 140 °C and 160 °C for six hours.

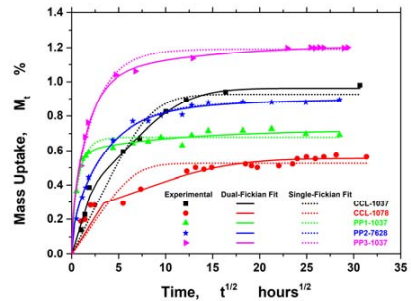


Fig. 5. Typical moisture gain trend and curve fit using an analytical solution (single and dual Fickian diffusion model) for prepregs at 23 °C immersion.

The measured hygroscopic swelling strains  $\epsilon^{\beta}$  for the prepregs are depicted in Fig. 7. The swelling strains are very low for all the prepregs considered. However, significant shrinkage of 0.12 % was observed for prepreg PP2-7628 at 70 °C. Moreover, the CCL-1037

and CCL-1078 did not show any hygroscopic swelling strains at all conditioning temperatures. Henceforth, the desorption and hygroscopic swelling measurements were not performed at 70 °C. The prepreg PP2-7628 and PP3-1037 follow a similar temperature trend, i.e., the swelling strains decrease with an increase in temperature. The temperature trend for PP1-1037 is vice versa. This effect is mainly caused by the different glass transition temperature ( $T_g$ ) regions for the prepregs. The prepregs PP1-1037, PP2-7628, and PP3-1037 have a  $T_g$  of 270 °C, 170 °C and 150 °C respectively.

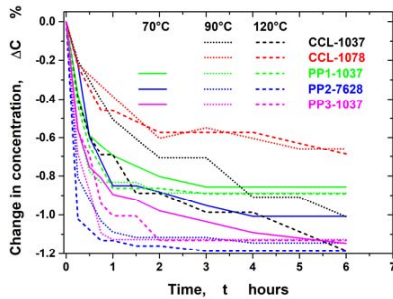


Fig. 6. Change in moisture concentration  $\Delta C$  for prepregs from the desorption process at 70 °C, 90 °C and 120 °C for six hours.

While the considered conditioning temperatures to measure CME is below the  $T_g$  level for PP1-1037, they are within the onset of the transition region for PP2-7628 and PP3-1037. Therefore, a different temperature dependence trend can be observed for these materials [6].

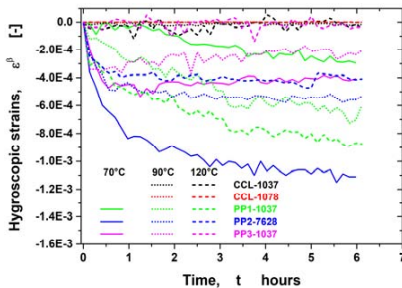


Fig. 7. The measured CME at different temperatures for the prepregs.

The computed CME ( $\beta$ ) at different temperatures for the prepregs is depicted in Fig. 8. As the prepregs CCL-1037 and CCL-1078 did not show any swelling strains, no CME is presented for these materials in the figure. The figure also depicts the change decrease in the value of CME with an increase in temperature for

PP2-7628 and PP3-1037. The decrease is mainly in the glass transition region for both the prepregs.

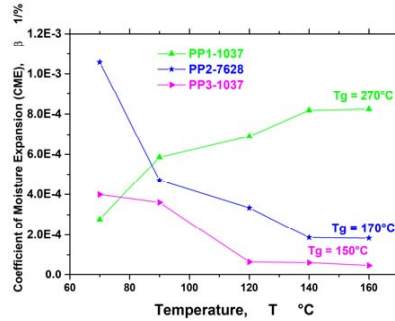


Fig. 8. The measured CME at different temperatures for the prepregs.

The results obtained from humidity and temperature controlled tensile tests for the considered prepregs are presented exemplarily. They are compared against Dynamic Mechanical Analysis (DMA) and the temperature-controlled tensile test results. (See Figs. 9-13). The solid lines in Figs. 9-13 represent the DMA curve measured at 1 Hz; the square symbols represent Young's moduli measured using a temperature oven, and the dot symbols and the star symbols represent Young's moduli measured using a climate chamber with a controlled humidity level of 50 % R.H. and 85 % R.H. respectively.

Overall, Young's moduli  $E$  obtained from temperature-controlled tensile tests are in good agreement with DMA results at increased temperatures for the prepregs considered for both Warp (0°) and 45° test specimens. Discrepancies at room temperature for CCL-1037, CCL-1078, PP2-7628, and PP3-1037 can be attributed due to possible unstable humidity conditions when not using the climate chamber.

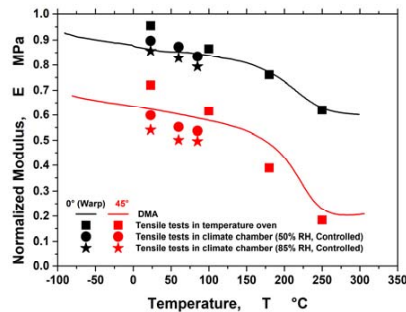


Fig. 9. Comparison of controlled humidity tensile tests with DMA and tensile tests in temperature oven for CCL-1037 prepreg.

To quantify the effects of relative humidity, the preregs were tested at 50 % R.H. and 85 % R.H. conditions at temperature levels of 23 °C, 60 °C, and 85 °C. A decrease in Young's moduli E for all the preregs was observed at 50 % R.H. and 85 % R.H., respectively, at all considered temperature levels. This decrease is mainly attributed due to the presence of moisture in the preregs during the humidity conditioning. The E value for 85 % R.H. is relatively smaller compared with E at 50 % R.H. The lower value of E is mainly due to the presence of higher moisture content at 85 % R.H. than at 50 % R.H. at the same temperature. This hydration difference explains the difference as excess moisture lowers the mechanical strength and stiffness of the preregs. An increased humidity level leads to a reduced stiffness.

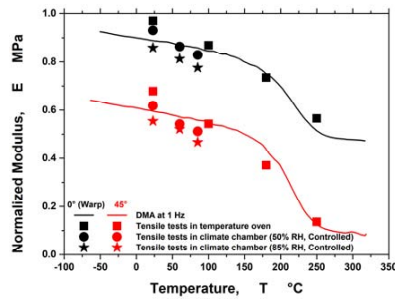


Fig. 10. Comparison of controlled humidity tensile tests with DMA and tensile tests in temperature oven for CCL-1078 prepreg.

The prepreg PP2-7628 is most commonly used in MEMS and PCB manufacturing. This prepreg has a higher resin content compared with other prepreg materials. Therefore, this material absorbs more moisture and affects the strength of the material by lowering Young's moduli E (see Fig. 12 for 0° (Warp)) compared with the results from DMA and temperature controlled tensile tests.

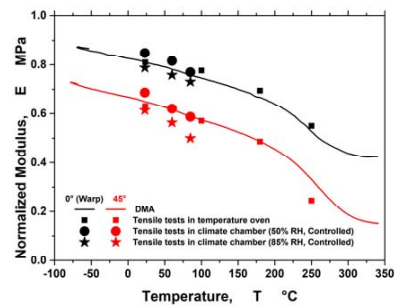


Fig. 11. Comparison of controlled humidity tensile tests with DMA and tensile tests in temperature oven for PP1-1037 prepreg.

Fig. 13 shows the tensile test results obtained for PP3-1037. The temperature controlled tensile tests were only performed at room temperature of 23 °C. Therefore, the results from humidity dependent tensile tests are compared with E values at 23 °C and with DMA along 0° (Warp) and 45° test specimens.

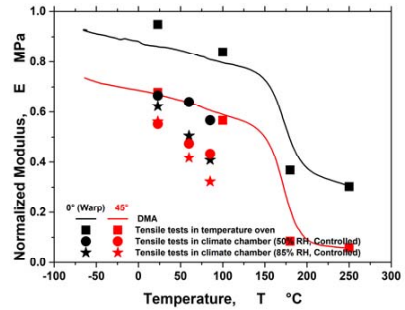


Fig. 12. Comparison of controlled humidity tensile tests with DMA and tensile tests in temperature oven for PP2-7628 prepreg.

The results from the verification simulation have been depicted in Fig. 14. The verification simulation was performed at the specimen level for the preregs immersed in a distilled water bath and conditioned at 90 °C. The solid red lines represent the result obtained from a verification simulation; the black dotted lines represent the curve from the analytical fit, and the black and blue squared symbols represent the experimental humidity conditioning curves for CCL-1037 and PP2-7628, respectively. The humidity verification simulation, using the dual Fickian diffusion model is in good agreement with the overall behavior of both experimental and analytical fit curves. Therefore, this verification simulation model serves as a basis to model in the hygro-thermo-mechanical modeling approach.

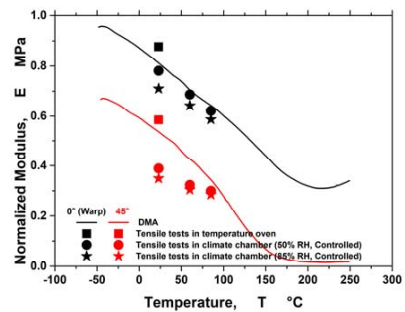


Fig. 13. Comparison of controlled humidity tensile tests with DMA and tensile tests in temperature oven for PP3-1037 prepreg.

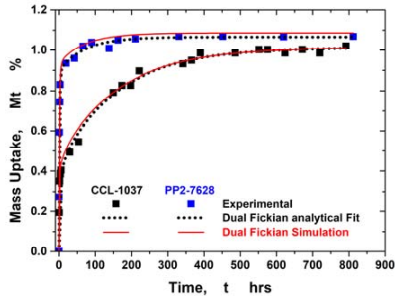


Fig. 14. Comparison of moisture absorption curve between experimental, analytical and numerical simulation using humidity conditioning simulation for CCL-1037 and PP2-7628

#### 4. Conclusions

In this research work, the results from moisture absorption, CME, and humidity and temperature-dependent Young's Moduli  $E$  for five different prepreg materials are presented. The measured moisture diffusion coefficient  $D$  and saturated mass  $M_{sat}$  are in good agreement with the analytical fit and verification simulation. The calculated values of CME serve as a material property to analyze the moisture and thermal mismatch in the MEMS sensor package in further reliability studies. The measured humidity and temperature-dependent  $E$  value provide critical information on shifts in the mechanical properties of the prepreps due to moisture absorption. The measured experimental data will further be used in a numerical simulation to determine the moisture and temperature-induced deformation and stresses in a MEMS sensor package. Thereby the measured material behavior is the crucial basis for a reliable sensor system design.

#### Acknowledgments

The research work was performed within the K-Project 'PolyTherm' at the Polymer Competence Center Leoben GmbH (PCCL, Austria) within the framework of the COMET-program of the Federal Ministry for Transport, Innovation, and Technology,

and the Federal Ministry for Digital and Economic Affairs with contributions by the University of Leoben, ams A.G. and by AT&S Austria Technology & Systemtechnik Aktiengesellschaft. Funding is provided by the Austrian Government and the State Government of Styria.

#### References

- [1]. M. Yalagach, et al., Influence of environmental factors like temperature and humidity on MEMS packaging materials, in *Proceedings of the 7<sup>th</sup> Electronic System-Integration Technology Conference (ESTC'18)*, Dresden, 2018, pp. 1-6.
- [2]. M. Yalagach, et al., Numerical analysis of the influence of polymeric materials on a MEMS package performance under humidity and temperature loads, in *Proceedings of the IEEE 69<sup>th</sup> Electronic Components and Technology Conference (ECTC'19)*, Las Vegas, NV, USA, 2019, pp. 2029-2035.
- [3]. JESD22-A120A, Test Method for the Measurement of Moisture Diffusivity and Water Solubility in Organic Materials Used in Electronic Devices, JEDEC Standards, *JEDEC*, 2001.
- [4]. L. Masaro, X. X. Zhu, Physical models of diffusion for polymer solutions, gels and solids, *Prog. Polym. Sci.*, Vol. 24, 1999, pp. 731-775.
- [5]. E. Stellrecht, B. Han, M. G. Pecht, Characterization of the hygroscopic swelling behaviour of mould compounds and plastic packages, *IEEE Transactions on Components and Packaging Technologies*, Vol. 27, 2004, pp. 499-506.
- [6]. E. H. Wong, Y. C. Teo, T. B. Lim, Moisture diffusion, and vapour pressure modelling of IC packaging, in *Proceedings of the of Electronic Components and Technology Conference (ECTC'98)*, 1998, pp. 1372-1378.
- [7]. Y. He, X. Fan, In-situ characterization of moisture absorption and desorption in a thin BT core substrate, in *Proceedings of the Proceedings 57<sup>th</sup> Electronic Components and Technology Conference*, Reno, NV, 2007, pp. 1375-1383.
- [8]. J. Crank, *The Mathematics of Diffusion*, Clarendon Press, Oxford, 1956.
- [9]. D. M. Brewis, J. Comyn, S. T. Tredwell, Diffusion of water in some modified phenolic adhesives, *Int. J. Adhesion and Adhesives*, Vol. 7, 1987, pp. 30-32.
- [10]. P. F. Fuchs, G. Pinter, K. Fellner, Local damage simulations of printed circuit boards based on in-plane cohesive zone parameters, *Circuit World*, Vol. 39, Issue 2, 2013, pp. 60-66.

© 2021 IEEE. Reprinted, with permission, from:  
M. Yalagach et al. **Numerical analysis of a MEMS sensor's deformation behavior considering dynamic moisture conditions**. In: *2020 IEEE 22nd Electronics Packaging Technology Conference (EPTC)*. 2020, 380–385. DOI: [10.1109/EPTC50525.2020.9315091](https://doi.org/10.1109/EPTC50525.2020.9315091)

# Numerical analysis of a MEMS sensor's deformation behavior considering dynamic moisture conditions.

Mahesh Yalagach\*, Peter Filipp Fuchs\*, Thomas Antretter†, Tao Qi‡, Markus Weber¶

\*Polymer Competence Center Leoben GmbH  
Leoben, Austria  
mahesh.yalagach@pccl.at

†Montanuniversitaet Leoben, Institute of Mechanics  
Leoben, Austria

‡Austria Technologie & Systemtechnik Aktiengesellschaft  
Leoben, Austria

¶ams AG  
Premstaetten, Austria

**Abstract**—Micro Electro Mechanical Semiconductors (MEMS) functionalities have been continuously extended during the last years, and they are applied in a wide range of industrial sectors, including the automotive, consumer electronics, and Internet of Things (IoT) markets. These MEMS sensor packages are a multi-materials composite system. The composite materials involved in MEMS sensor packages show significant effects like thermal expansion and hygroscopic swelling when exposed to environmental loads like temperature and moisture. Due to these effects, the MEMS sensing performance is affected. To understand the effects on sensing performance and mechanical behavior, an advanced simulation approach, "hygro-thermo-mechanical simulation," needs to be accounted for. This approach considers not only the dynamic changes in temperature and moisture loads but also generalized solubility, which is a function of both temperature and saturated mass concentration. This numerical model helps in optimizing and understanding the sensing performance of the MEMS sensor packages.

**Index Terms**—Moisture diffusion, advanced hygro-thermo-mechanical simulation, pressure sensor, die deformation, four-point bending.

## I. INTRODUCTION

MEMS sensors commonly feature a die, adhesives, wiring, encapsulation, and a substrate as a link to the Printed Circuit Board (PCB). The applied adhesives and the insulating layers in the substrate and PCB are polymeric materials. They absorb moisture when they are exposed to ambient temperature and humidity. The absorption of moisture in the polymeric materials leads to undesirable effects like aging [1], hygroscopic swelling [2], and popcorn failures [3] [4]. Additionally, the polymeric materials have different hygro, and thermo-mechanical properties, a thermal and hygroscopic mismatch leads to unwanted stresses during the application. These stresses causes deformation [5], delamination and cracks [6] in the MEMS sensor packages. Therefore, a proper investigation is necessary to account for moisture absorption and diffusion

in the MEMS sensor devices.

Numerous research contributions have been published on the experimental analysis [7] [8] and numerical description of moisture absorption and discontinuity [9] [10] [12] under dynamic changes in humidity. These numerical models consider thermal and moisture analogy to understand the concentration change under dynamic humidity loads. The advanced "hygro-thermo-mechanical simulation" listed in this contribution considers this analogy to determine the moisture-induced deformation.

Within this contribution, the following new aspects in this field of research have been focused on:

- Influence of geometric design on the local die deformation behavior.
- Influence of material combination on the local die deformation behavior.
- Local die deformation under thermal, moisture, and four-point bending loads.

Furthermore, the silicon die deformation is also compared with the capacitance signals from the MEMS sensors obtained during the experimental tests.

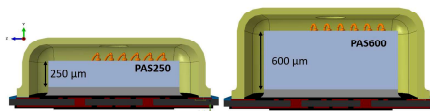


Fig. 1. Two types of capacitive pressure sensor MEMS systems considered for the advanced hygro-thermo-mechanical simulation.

## II. EXPERIMENTAL TESTS

To analyze the thermal, humidity, and four-point bending loads on the MEMS sensor performance, the experimental

tests were performed. The tests were carried out on two types of MEMS sensor packages. The considered MEMS sensors vary in their silicon die thickness (see Figure 1). The test board with the two flavors of MEMS sensors were kept inside the climate chamber, and the readings from the sensors were measured under different temperature, humidity, and bending conditions. The Table I shows the different temperature and dynamic humidity loads used for the experimental tests. In test condition-1, at a constant temperature field of  $23^{\circ}\text{C}$ , and the moisture loads were varied from  $30 \rightarrow 85 \rightarrow 30\%$  RH. While in the test condition-2, the humidity loads were similar to that of the condition-1, but the temperature was increased from  $23^{\circ}\text{C}$  to  $85^{\circ}\text{C}$  at  $2\text{K}/\text{min}$ . Furthermore, in test condition-3, additional to temperature ( $23^{\circ}\text{C}$ ) and humidity loads (50% RH), a four-point bending load of 5 mm displacement at 2 mm/min was considered.

TABLE I  
DIFFERENT TEMPERATURE AND DYNAMIC HUMIDITY LOADS USED FOR THE VALIDATION TESTS.

| Test Condition | Temperature [ $^{\circ}\text{C}$ ] | Humidity[%]                        |
|----------------|------------------------------------|------------------------------------|
| 1              | Constant 23                        | $30 \rightarrow 85 \rightarrow 30$ |
| 2              | $23 \rightarrow 85$                | $30 \rightarrow 85 \rightarrow 30$ |
| 3              | 23                                 | 50                                 |

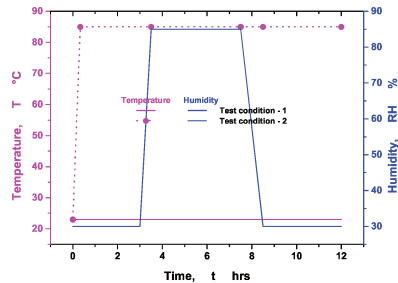


Fig. 2. Different temperature and dynamic humidity loads used for the tests 1 and 2.

The MEMS sensors used in this contribution are capacitive pressure sensors. To read the capacitance signals from the sensors, the readout scripts from LabVIEW [16] software along with USB- $I^2C$  dongles were used. The Figures 2 and 3 represent the environmental and mechanical loads used for the experimental tests. Additionally, Figure 4 shows the validation test setup inside the climate chamber.

### III. ADVANCED HYGRO-THERMO-MECHANICAL SIMULATION

The advanced hygro-thermo-mechanical simulations presented in this contribution uses thermal-moisture analogy [12]

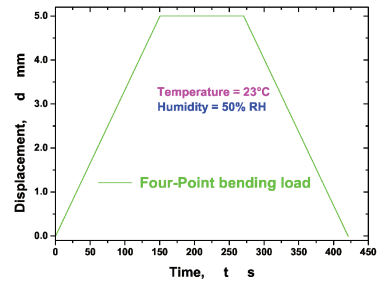


Fig. 3. The four-point bending displacement load experimental test 3.

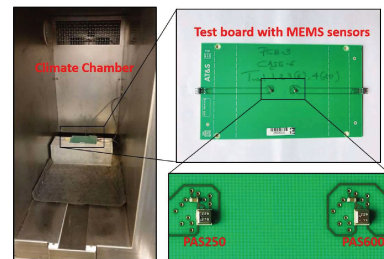


Fig. 4. Validation test setup inside the climate chamber with test board and MEMS sensors.

to describe dynamic changes in a polymeric system under temperature and moisture loads. This numerical approach was performed using Abaqus (Abaqus 6.17, Dassault Systemes Simulia Corp., Providence, USA). A thermal-moisture analogy is established by considering moisture diffusion in polymeric materials based on water activity. The water activity is a thermodynamic state variable and considered as a field variable. The water activity based diffusion model is evaluated using generalized sorption isotherm [11]. In the water activity method, the moisture concentration is computed as a product of water activity and generalized solubility  $K$  [14]. The generalized solubility is evaluated using Henry's law [15]. The moisture dependent properties, i.e., saturated concentration  $C_{sat}$  and diffusion coefficient  $D$  in Henry's Law, are derived from moisture conditioning experiments [13]. This simulation approach considers a generalized solubility approach to compute the amount of moisture absorbed. The value  $K$  depends on the applied temperature and humidity. The dual-Fickian diffusion model [7] was used to calculate the total moisture concentration in the polymeric materials used in the MEMS sensor.

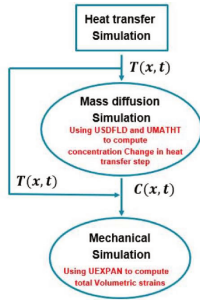


Fig. 5. Advanced hygro-thermo-mechanical stimulation modeling approach.

The modeling approach for the advanced hygro-thermo-mechanical simulation is explained in the block diagram in Figure 5. This advanced numerical approach starts with a heat transfer simulation. The resulting nodal temperature values are considered as a predefined field variable in a humidity simulation to account for the influence of a dynamic temperature change. The humidity simulation is evaluated using a heat transfer step to making use of the thermal-moisture analogy again. To this end, a combination of user-defined subroutines USDFLD and UMATHT are applied. The USDFLD subroutine is used to compute the incremental temperature change from the heat transfer simulation. This temperature change is further used in a UMATHT subroutine to calculate the total concentration change using the water activity method [14]. Furthermore, in the last step, the resulting temperature field and moisture concentration are used in the subroutine UEXPAN to compute the thermal and moisture-induced deformation under dynamic temperature and moisture loads.

#### A. Materials

The capacitive pressure sensor used in this research is made up of multiple materials [12]. The material properties for non-polymeric materials were considered from literature [17] [18]. While the properties for the polymeric materials were determined by performing an extensive experimental thermal and moisture dependent material characterization [13] [12]. Table II shows the two different polymeric material combination's (MAT-1 and MAT-2) considered for the MEMS sensor. For prepreg, insulating adhesive, and solder mask, two different material types were considered.

The materials listed in MAT-1 and MAT-2 have the following properties:

- MAT-1 shows lower hygro-thermal expansion and is expected to be best in performance. Therefore, this combination is considered in the experimental tests.
- MAT-2 shows the highest moisture influence during material characterization and lower Young's Moduli ( $E$ ) than MAT-1. Henceforth, this combination is used for

TABLE II  
CONSIDERED MATERIAL COMBINATION'S USED IN MEMS SENSOR PACKAGE.

| Materials           | MAT-1    | MAT-2    |
|---------------------|----------|----------|
| Prepreg             | CCL-1037 | PP3-1037 |
| Insulating Adhesive | ADH-X-01 | ADH-Y-01 |
| Conductive Adhesive | ADH-Z-02 |          |
| Solder Mask         | SLM-01   | SLM-02   |

the virtual study of the material behavior in the proposed simulation models.

#### B. Evaluation region

To understand the local silicon-die deformation behavior, an evaluation region was defined on the upper surface of the silicon die. The maximum principal strains were evaluated in this region.

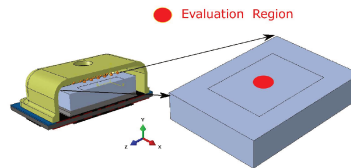


Fig. 6. Evaluation region in the silicon die of the MEMS sensor.

#### C. Boundary conditions

TABLE III  
BOUNDARY CONDITIONS FOR THREE SIMULATIONS CASE-1, 2 AND 3.

| CASE  | Material      | Loads                       |                                      |
|---|---------------|-----------------------------|--------------------------------------|
|   |               | Temperature [ $^{\circ}$ C] | Humidity [%]                         |
| 1   | MAT-1 & MAT-2 | Constant 23                 | 30 $\rightarrow$ 85 $\rightarrow$ 30 |
| 2   | MAT-1 & MAT-2 | 23 $\rightarrow$ 85         | 30 $\rightarrow$ 85 $\rightarrow$ 30 |
| 3   | MAT-1 & MAT-2 | Constant 23                 | Constant 50                          |
| Additional bending load of 5mm displacement |               |                             |                                      |

The advanced hygro-thermo-mechanical simulation involves a heat transfer, mass diffusion, and thermo-mechanical simulation to evaluate the total volumetric strains. A global and local sub-modeling simulation approach was applied considering the loading situation of the whole systems, including PCB, solder pads, substrate, sensor, and encapsulation. The detailed procedure has been described in a preceding publication [12].

All loads in the simulation were applied in step with the experimental tests performed. Three sets of simulations (CASE - 1, 2 and 3) were performed considering the test condition -



1, 2 and 3, respectively from the experimental tests. The loads were applied for 12 hours or 43200 seconds for CASE - 1 and 2. In CASE-1, a constant temperature of  $23^{\circ}\text{C}$  is applied on to the surfaces exposed to the environment in heat transfer simulation. For the mass diffusion simulation, dynamic humidity of  $30 \rightarrow 85 \rightarrow 30 \text{ RH}$  (see figure 2) is applied on the polymeric materials exposed to the environment. However, for CASE-2, the initial condition of  $23^{\circ}\text{C}$ , and the temperature of  $85^{\circ}\text{C}$  is applied in the heat transfer simulation. The humidity loads for the mass diffusion simulation remained the same as in CASE - 1. Furthermore, for CASE-3, a four-point bending load of 5 mm displacement at 2 mm/min was applied for 420 seconds. For all the simulations, the temperature, humidity, and the bending loads were considered from the signals obtained from experimental tests.

For all the simulation models, the moisture dependent material properties are considered negligible for the non-polymeric materials. The material properties for the polymeric materials have been described in preceding publications [12] [13]. The boundary conditions considered in the simulations are summarized in Table III.

#### IV. RESULTS AND DISCUSSION

In this section, the results obtained from experimental tests and advanced hygro-thermo-mechanical simulations have been discussed. The results from experimental tests 1, 2 and 3 are compared with the simulations CASE - 1, 2 and 3, respectively. For all the simulation models (CASE-1, 2 and, 3), the solid lines represent the strain levels for MAT-1 and the dashed lines for MAT-2. The black-colored lines are the strain levels obtained for PAS250, while the red lines are for PAS600.

The results obtained for test condition 1 of the experimental test are depicted in the Figure 7. The capacitance  $C$  of the two flavors of MEMS sensors is compared over time  $t$  under temperature and humidity loads. The test condition 1 did not show any influence on the capacitance readout under varying humidity loads. The capacitance readout was nearly zero for both PAS250 and PAS600 under dynamic humidity levels. Only a minor shift towards negative capacitance values can be observed for both sensors.

The strains obtained from the simulation CASE-1, using the different material combinations (MAT-1 and MAT-2) for the evaluation region (see figure 6) is depicted in Figure 8. The strain levels for MAT-2 are significantly higher compared to the strain levels for MAT-1. The materials listed in combination MAT-2 have a higher tendency to experience hygro-thermal expansion, while the materials in MAT-1 do not show any expansion during the humidity conditioning. Additionally, the strain levels for PAS250 sensor are higher compared with PAS600 due to the change in the silicon die thickness.

The simulation results showed relatively low strain levels for both sensors types. The scattering in the strain levels is mainly attributed to the scatter of temperature and humidity during the experimental test. In comparison with the experimental test condition - 1 (see Figure 7), no influence on the capacitance signal due to change in humidity was observed. However, in

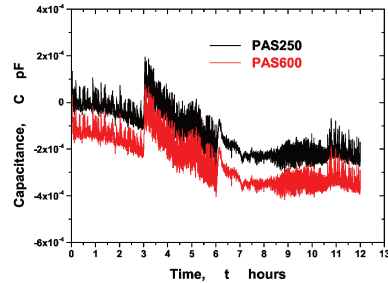


Fig. 7. Experimental test results for test condition 1.

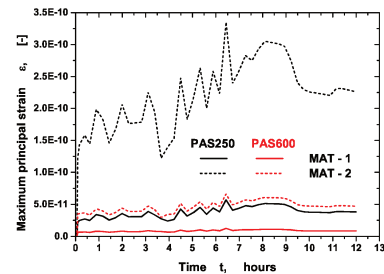


Fig. 8. Strain levels in the evaluation region using MAT-1 and MAT-2 material combinations for MEMS sensors in CASE-1.

the simulation, a small change in strains was observed at the end of the simulation due to a decrease in humidity from  $85 \rightarrow 30 \text{ RH}$ . Additionally, for the MAT-1 combination, no humidity effects on the capacitance signal are expected, while for the MAT-2 combination for PAS250 sensor, a small influence on the capacitance can be expected.

The results obtained for the test condition 2 of the experimental test are shown in Figure 9. The test condition 2 does not show any influence on the capacitance readout under varying humidity loads. The initial increase in capacitance for both PAS250 and PAS600 sensors can be attributed to the rise in temperature from  $23^{\circ}\text{C}$  to  $85^{\circ}\text{C}$ . The variation in the capacitance readout was higher for PAS250 compared to PAS600.

The simulation results obtained for CASE-2 are illustrated in Figure 10. The figure shows the strain levels obtained for PAS250 and PAS600 sensors using the different material combinations for the evaluation region, as shown in Figure 6. The increase in CASE-2 compared to CASE-1 is mainly due

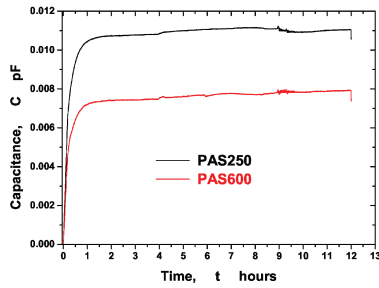


Fig. 9. Experimental test results for test condition 2.

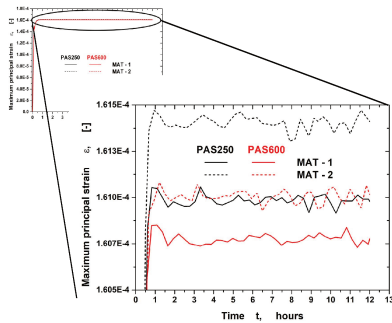


Fig. 10. Strain levels in the evaluation region using MAT-1 and MAT-2 material combinations for MEMS sensors in CASE-2.

to an increase in temperature from  $23^{\circ}\text{C}$  to  $85^{\circ}\text{C}$ . On closer evaluation in Figure 10, higher strains were observed for the material combination MAT-2 compared to MAT-1. This behavior is mainly due to hygro-thermal expansion during the conditioning experiments.

The results from the simulation CASE-2 showed significantly higher strain levels for both MEMS sensors compared with CASE-1. Additionally, comparing the results from simulation to the validation test condition - 2 (see Figure 9), both capacitance and strains increased with an increase in temperature. The trends in simulation and experimental tests are in good agreement. Even in the CASE-2, scattering in strain values is due to scatter in temperature in the experimental test. On closer observation, any potential changes in MAT-2 of PAS250 due to humidity loads are overlaid by the significantly larger temperature influence. Therefore, no influence on strain levels is seen for MAT-2 of PAS250 under humidity change. From the experiments and simulations, the effect of dynamic

humidity changes is negligible compared with temperature effects,

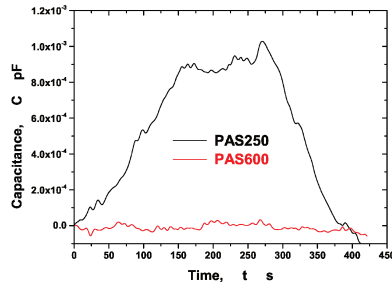


Fig. 11. Experimental test results for test condition 3.

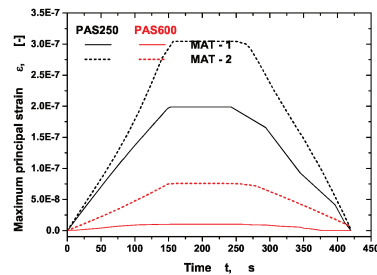


Fig. 12. Strain levels in the evaluation region using MAT-1 and MAT-2 material combinations for MEMS sensors in CASE-3.

The test condition 3 of the experimental tests showed an influence of bending load on the capacitance readout from PAS250 and PAS600 MEMS sensors. The results obtained are shown in Figure 11. The results depict that the capacitance values for PAS250 sensor show a significant increase under a four-point bending load. In contrast, the PAS600 sensor does not show any influence under the bending load. The increase in capacitance for PAS250 is mainly due to the lower silicon die thickness of  $250\mu\text{m}$ . The higher thickness silicon die (PAS600) minimizes the bending effects during the temperature and humidity loads compared with PAS250. Therefore, the MEMS sensor PAS600 has a lower capacitance.

The simulation results obtained for CASE-3 are illustrated in Figure 12. The figure shows the strain levels obtained for PAS250 and PAS600 sensors and the different material combinations. The PAS250 sensor showed a higher strain under bending compared to PAS600 sensor. Additionally,

the principal strain from material combination MAT-2 shows an increase in strains compared with MAT-1. This can be attributed to the lower Young's Modulus (mechanical properties) of the materials used in MAT-2. The bending effect is minimized by using a thicker silicon die, i.e., PAS600. As a result, the maximum principal strain for PAS250 is higher compared with PAS600. As both temperature and humidity were constant throughout the bending load, these factors did not show any influence on the strain levels.

The strain levels from the simulation CASE-3 is compared to the experimental test condition - 3 (see Figure 11). Both capacitance and strain levels increases under the bending load for the PAS250 sensor. Consequently, For the PAS600 sensor, neither the capacitance nor the strains show a significant change under bending. Additionally, the strain levels from the simulation follow a similar trend in comparison with the experimental test. Therefore, both the simulation CASE-3 and experimental test 3 are in good agreement.

#### V. CONCLUSION

In this research work, the results obtained from an advanced hygro-thermo-mechanical simulation considering three different boundary conditions for MEMS packages are presented. The influence of dynamic changes in the humidity by considering thermal and moisture analogy was presented. The local die deformation under the prescribed boundary conditions for two flavors of capacitive pressure sensors (PAS250 and PAS600) was analyzed in a defined region of interest. In doing so, the influence of the considered different material combinations (MAT-1 and MAT-2) was evaluated. The simulation results also gave an expected trend and confirmed that a lower thermal and hygroscopic expansion in the materials is preferred. Additionally, the silicon die thickness plays a vital role in the evaluation of strains and capacitance. Higher silicon die thickness (PAS600) showed minimal influence under environmental and mechanical loads compared to the PAS250 MEMS sensor.

Furthermore, the obtained silicon die deformation from the numerical approach was compared with the capacitance readout from the experimental tests. The trends for die deformation from the simulation and capacitance values from the experimental test were in good agreement. In simulation CASE-1, both the sensor types showed a minor influence of humidity on strain levels for MAT-2. From experimental test 2 and simulation CASE-2, the temperature loads significantly influenced both capacitance and strains. Additionally, the bending load had a significant effect on the die deformation behavior, i.e., with an increase in bending load, both capacitance (experimental test) and strain (simulation) showed an increasing trend. The influence of lower Young's Modulus materials MAT-2 showed a significant and increasing trend on strain levels in the simulation.

#### ACKNOWLEDGMENT

The research work was performed within the K-Project "PolyTherm" at the Polymer Competence Center Leoben

GmbH (PCCL, Austria) within the framework of the COMET-program of the Federal Ministry for Transport, Innovation and Technology and the Federal Ministry for Digital and Economic Affairs with contributions by University of Leoben, ams AG and by AT&S Austria Technologie & Systemtechnik Aktiengesellschaft. Funding is provided by the Austrian Government and the State Government of Styria.

#### REFERENCES

- [1] X. Q. Shi, Y. L. Zhang, W. Zhou and X. J. Fan, "Effect of Hygrothermal Aging on Interfacial Reliability of Silicon/Underfill/FR-4 Assembly," in *IEEE Transactions on Components and Packaging Technologies*, vol. 31, no. 1, pp. 94-103, March 2008, doi: 10.1109/TCAPT.2008.916801.
- [2] Zhou J., Tee T., Fan X. (2010) Hygroscopic Swelling of Polymeric Materials in Electronic Packaging: Characterization and Analysis. In: Fan X., Suhir E. (eds) *Moisture Sensitivity of Plastic Packages of IC Devices. Micro- and Opto-Electronic Materials, Structures, and Systems*. Springer, Boston, MA. [https://doi.org/10.1007/978-1-4419-5719-1\\_7](https://doi.org/10.1007/978-1-4419-5719-1_7)
- [3] A. A. Gallo and R. Munamarty, "Popcorning: a failure mechanism in plastic-encapsulated microcircuits," in *IEEE Transactions on Reliability*, vol. 44, no. 3, pp. 362-367, Sept. 1995, doi: 10.1109/24.406565.
- [4] Xuejun Fan, Jiang Zhou and A. Chandra, "Package structural integrity analysis considering moisture," 2008 58th Electronic Components and Technology Conference, Lake Buena Vista, FL, 2008, pp. 1054-1066, doi: 10.1109/ECTC.2008.4550106.
- [5] E. Stellrecht, B. Han, and M. Pecht. "Characterization of the hygroscopic swelling behavior of mold compounds and plastic packages". In: *IEEE Transactions on Components and Packaging Technologies* 27.3 (2004), pp. 499-506.
- [6] Zarnik, Marina & Belavič, Darko. (2012). An Experimental and Numerical Study of the Humidity Effect on the Stability of a Capacitive Ceramic Pressure Sensor. *Radioengineering*, 21. 201-206.
- [7] Placetie, M. D., Fan, X., Zhao, J.-H., & Edwards, D. (2012). Dual stage modeling of moisture absorption and desorption in epoxy mold compounds. *Microelectronics Reliability*, 52(7), 1401-1408. <https://doi.org/10.1016/j.microrel.2012.03.008>
- [8] X. Fan and Jie-Hua Zhao, "Moisture diffusion and integrated stress analysis in encapsulated microelectronics devices," 2011 12th Intl. Conf. on Thermal, Mechanical & Multi-Physics Simulation and Experiments in Microelectronics and Microsystems, Linz, 2011, pp. 1/8-8/8, doi: 10.1109/ESIME.2011.5765793.
- [9] S. Yoon, B. Han and Z. Wang, "On Moisture Diffusion Modeling Using Thermal Diffusion Analogy", *J. Electron. Packag.*, vol. 129, pp. 421-426, 2007.
- [10] C Jang, S Park, B Han and S. Yoon, "Advanced Thermal-Moisture Analogy Scheme for Anisothermal Moisture Diffusion Problem", *ASME. J. Electron. Packag.*, vol. 130, no. 1, pp. 011004-011004-8, 2008.
- [11] Blahovec, J., Yanniotis, S. GAB Generalized Equation for Sorption Phenomena. *Food Bioprocess Technol* 1, 82-90 (2008). <https://doi.org/10.1007/s11947-007-0012-3>
- [12] M. Yalagach et al., "Numerical Analysis of the Influence of Polymeric Materials on a MEMS Package Performance Under Humidity and Temperature Loads," 2019 IEEE 69th Electronic Components and Technology Conference (ECTC), Las Vegas, NV, USA, 2019, pp. 2029-2035, doi: 10.1109/ECTC.2019.00311.
- [13] M. Yalagach et al., "Influence of environmental factors like temperature and humidity on MEMS packaging materials," 2018 7th Electronic System-Integration Technology Conference (ESTC), Dresden, 2018, pp. 1-6. doi: 10.1109/ESTC.2018.8546484.
- [14] L. Chen, J. Zhou, H. Chu, G. Zhang and X. Fan, "Modeling nonlinear moisture diffusion in inhomogeneous media," *Microelectronics Reliability*, vol. 75, 2017, pp. 162-170.
- [15] Osswald, T., and Menges, G., 1996, *Materials Science of Polymers for Engineers*, Hanser-Gardener, Munich.
- [16] The LabVIEW Platform—Core Technical Advantages of NI LabVIEW (<http://zone.ni.com/devzone/conceptd.nsf/webmain/>).
- [17] Dwight E. Gray ( Ed.) *American Institute of Physics Handbook* McGraw-Hill Book Company Inc. 1957.
- [18] *Handbook of Stainless Steels*, Donald Peckner and I. M. Bernstein, McGraw-Hill Book Company, New York, NY, (1977)

Reprinted, with permission, from:

M. Yalagach et al. **Thermal and Moisture Dependent Material Characterization and Modeling of Glass Fiber Reinforced Epoxy Laminates**. *Sensors & Transducers* 248:1 (Jan. 2021), 1–9. ISSN: 2306-8515. URL: [https://www.sensorsportal.com/HTML/DIGEST/P\\_3196.htm](https://www.sensorsportal.com/HTML/DIGEST/P_3196.htm)



## Thermal and Moisture Dependent Material Characterization and Modeling of Glass Fiber Reinforced Epoxy Laminates

<sup>1,\*</sup> Mahesh Yalagach, <sup>1</sup> Peter Filipp Fuchs, <sup>2</sup> Thomas Antretter, <sup>3</sup> Michael Feuchter, <sup>4</sup> Tao Qi and <sup>5</sup> Markus Weber

<sup>1</sup> Polymer Competence Center Leoben GmbH (PCCL), Leoben, Austria

<sup>2</sup> Montanuniversität Leoben, Institute of Mechanics, Leoben, Austria

<sup>3</sup> Montanuniversität Leoben, Institute of Material Science and Testing of Polymers, Leoben, Austria

<sup>4</sup> Austria Technologie & Systemtechnik Aktiengesellschaft, Leoben, Austria

<sup>5</sup> ams AG, Premstätten, Austria

<sup>1</sup> Tel.: + 43 3842 42962 716

E-mail: mahesh.yalagach@pccl.at

*Received: 30 November 2020 / Accepted: 31 December 2020 / Published: 29 January 2021*

**Abstract:** The Micro-Electro-Mechanical Semiconductor (MEMS) sensor packages are an advanced multi-material composite system. These packages comprise polymeric materials like prepregs, solder-mask, insulation, and conductive adhesives. Prepregs are glass fiber reinforced epoxy laminates. Only a low material sensitivity to environmental influences will ensure the sensors' reliable performance during their application lifetime. To this end, the potentially applied materials undergo defined thermal and moisture-dependent material characterization. In this contribution, the influence of moisture and temperature has been studied for five different prepreg materials, which are commonly applied as a substrate material in a MEMS sensor. The measured thermal and moisture dependent material properties are the basis for a numerical diffusion analysis and a virtual hygro-thermo-mechanical reliability assessment.

**Keywords:** Thermo-mechanical characterization, Hygroscopic swelling, Thermal and moisture expansion, Tensile tests.

### 1. Introduction

The use of MEMS sensor packages has revolutionized the automotive, home, and building applications (HABA) and Internet of Things (IoT) industries [1, 13]. However, increasing demands on their functionality and reliability necessitates improved packaging materials concerning thermal and moisture changes. The temperature and moisture are the essential parameters associated with the electronic packages' reliability and performance [2]. The materials involved in MEMS sensor packages show significant effects like thermal expansion and

hygroscopic swelling when exposed to harsh environmental loads. Due to these effects, during the application of the packages, stresses are introduced.

The induced stresses cause deformation, potentially delamination, and cracks in the materials [4, 11]. In this contribution, the dependence of thermal distribution and moisture absorption in five different prepregs, commonly used in MEMS sensors, is analyzed. The prepreg materials serve as a substrate material for a MEMS sensor build-up. The moisture absorption and thermal mismatch due to the difference in the coefficient of thermal expansion (CTE) of the individual materials significantly impact the MEMS

sensor package reliability [7]. Therefore, the characterization of thermal effects, moisture absorption, and diffusion in these packages need to be accounted for modeling the sensor package's reliability behavior. In doing so, the prepreg materials have been extensively studied using different temperature and moisture dependent material characterization techniques. The obtained moisture and temperature-dependent material properties are prepared to be used in hygro-thermo-mechanical simulations [4, 5] to assess the deformation and stress conditions changes. This information serves as vital information for material and design optimization to eliminate moisture-related failures.

## 2. Experimental

An extensive thermo-mechanical and hygroscopic material characterization was performed to understand the materials' behavior under different temperature and moisture loads. These characterization techniques involve understanding the thermal distribution, moisture absorption, and its impact on the physical, chemical, and mechanical properties of the prepreg materials. Different thermal and moisture dependent characterization techniques like dynamic mechanical analysis (DMA), thermo-mechanical analysis (TMA), gravimetric humidity conditioning, Coefficient of Moisture Expansion (CME), and humidity dependent Young's modulus were performed. Five different prepregs, CCL-1037, CCL-1078, PPI-1037, PP2-7628 and PP3-1037, were considered for the characterization. They vary in their matrix material, fabric reinforcement type and thickness. The thickness of the prepregs varied from 60  $\mu\text{m}$  to 1.5 mm [13]. The following sections explain briefly the different measurement techniques used:

### 2.1. Temperature-Dependent Young's Modulus

The temperature-dependent Young's Modulus ( $E$ ) for the prepreg materials was measured using tensile tests and DMA. The temperature-dependent tensile tests were performed for the defined temperatures 23 °C, 100 °C, 180 °C and 250 °C using Zwick Z010 (Zwick Roell AS, Ulm, Germany) universal test system. The acquisition of strains was performed using the digital image correlation (DIC) method. The measured Young's modulus  $E$  was compared with results from Dynamic Mechanical Analysis (DMA) performed using Mettler Toledo DMA (Mettler-Toledo, Columbus, Ohio, USA) in a tensile mode under controlled displacement load. The materials were tested at a frequency of 1 Hz and over a temperature range of -100 °C to 300 °C with a 2 K/min heating rate.

### 2.2. Thermo-Mechanical Analysis (TMA)

The in-plane CTE was measured using Q400 TCT (Dantec Dynamics, A/S, Skovlunde, Denmark), which utilizes the DIC measurement technique to acquire a change in strain with an increase in temperature. Furthermore, the thermal conductivity  $\lambda(T)$  measurements were performed using Light Flash Analysis (LFA). LFA utilizes a non-destructive and contact-free approach to measure the thermal diffusivity  $a(T)$ . The measurement was performed using – Netzsch LFA 467 HyperFlash® (Netzsch GmbH, Selb, Germany). Based on this approach, the thermal conductivity can be computed using (1):

$$\lambda(T) = a(T) c_p(T) \rho(T), \quad (1)$$

where density  $\rho(T)$  and heat capacity  $c_p(T)$  were measured using high-resolution balance and differential scanning calorimetry (DSC), respectively. The dimensions of the material samples and test parameters for in-plane CTE and thermal conductivity measurements were considered according to [4, 12].

### 2.3. Gravimetric Humidity Conditioning

The moisture dependent properties like moisture diffusion coefficient  $D$  and saturated mass  $M_{sat}$  for the prepregs were measured using the gravimetric humidity conditioning method [5]. Apart from conditioning the prepregs in a distilled water bath [3], a climate chamber was used to measure the moisture uptake at 85 °C and 85 % RH (Relative Humidity) [13]. Before starting the humidity conditioning, the prepregs were conditioned in a temperature oven at 125 °C until they were completely dried (constant weight). To monitor the weight change during the conditioning, the prepregs were repeatedly removed at predefined points in time from the plastic container or the climate chamber. The prepregs' surface was cleaned using paper tissue, and they were weighed using a high precision balance. The prepregs tend to follow single Fickian diffusion law above their glass transition temperature  $T_g$ . But, at a temperature below  $T_g$ , these materials follow a non-Fickian or dual Fickian diffusion model [7]. In this contribution, the experimental conditioning curves were analytically approximated using single and dual Fickian diffusion models.

### 2.4. Coefficient of Moisture Expansion (CME)

The hygroscopic swelling strains  $\varepsilon^\beta$  developed during the gravimetric humidity conditioning are supposed to have a linear relationship with the change in moisture concentration  $\Delta C$  [5, 13] according to (2):

$$\varepsilon^\beta = \beta \Delta C, \quad (2)$$

where  $\beta$  is the CME. The effect of hygroscopic swelling strains  $\epsilon^{\beta}$  in the prepregs is measured using a Digital Image Correlation (DIC) approach. In this process, the hygroscopic strains are monitored during drying at defined temperature levels [4]. The moisture changes or changes in concentration are measured using a high-resolution balance. The CME measurements are carried out on the prepregs, which have reached their maximum mass saturation during the humidity conditioning process. The desorption of the saturated material samples was carried out at 70 °C, 90 °C, 120 °C, 140 °C and 160 °C for six hours. The CME ( $\beta$ ) is computed from a linear curve fit between the hygroscopic swelling strains  $\epsilon^{\beta}$  and the change in concentration  $\Delta C$ .

### 2.5. Humidity Dependent Young's Modulus

To assess the humidity effects on Young's modulus, humidity-controlled tensile tests were performed on the prepregs [13]. Before the humidity dependent testing, the prepregs were dried in a temperature chamber at 125 °C for 24 hours in the first step and conditioned using a climate chamber in the second step. The defined temperature and humidity levels were 23 °C (50 % and 85 % RH), 60 °C (50 % and 85 % RH) and 85 °C (50 % and 85 % RH). The tests were performed using a Weiss Technik climate chamber and an Instron 4505 universal testing system. For the strain data acquisition, a Mercury 3D DIC system was used.

The dimensions of the tensile specimens were prepared according to ISO 527 – 1BA [14]. Fig. 1 shows the test setup used for the measurement of humidity dependent tensile tests for the prepregs. The Change in Young's modulus ( $E$ ) due to absorption of moisture was also measured by performing DMA.

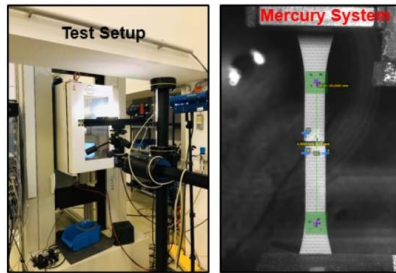


Fig. 1. Experimental setup for the humidity-controlled tensile test with climate chamber and a Mercury 3D DIC system [13].

The prepregs materials pre-conditioned by immersing in distilled water were considered. The saturated materials were subjected to testing in DMA.

The testing parameters for DMA measurement remained the same as considered in thermo-mechanical characterization. These DMA measurements were performed for CCL-1078 prepreg materials due to the difficult measurement technique, and the moisture from the conditioned materials are lost during the clamping and stabilization of the measurement system.

### 3. Verification Simulation

To determine the moisture absorption in prepregs numerically, a verification simulation model was set up in Abaqus (Abaqus 2017, Dassault Systemes Simulia Corp., Providence, USA) using a mass diffusion analysis at test specimen level. As Abaqus uses Fick's law to model the mass diffusion analysis [8, 9], this analysis was numerically solved using a dual Fickian diffusion model approach [3]. The block diagram in Fig. 2 depicts the modeling approach for the verification simulation.

The simulation model is initially started with the heat transfer simulation. The resulting nodal temperature is used in a mass diffusion simulation to access the conditioning's temperature effects as a predefined boundary condition. The mass diffusion model was solved using two parallel single Fickian mass diffusion analyses using the analytically fitted parameters moisture diffusion coefficient  $D$  and saturated mass  $M_{sat}$  as boundary conditions. The resulting single Fickian moisture concentrations were saved as field variables and were summed up using the USDFLD subroutine. The resulting temperature distribution and moisture concentration were used in a subroutine UEXPAN to compute the total volumetric strains due to moisture uptake and thermal effects.

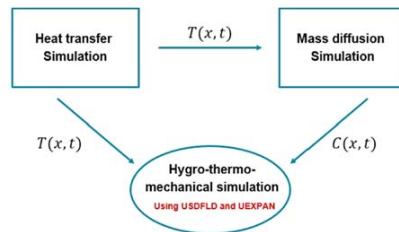


Fig. 2. Verification simulation modeling approach [4].

### 4. Results and Discussion

The results obtained from thermo-mechanical and hygroscopic material characterization are discussed in this section. Initially, the results obtained for in-plane CTE  $\alpha(T)$  and thermal conductivity  $\lambda(T)$  are discussed, followed by hygroscopic material characterization results [13].

Fig. 3 shows the in-plane CTE  $\alpha(T)$  results obtained for the prepreg materials. The CCL-1037 and CCL-1078 show a similar CTE trend for the overall temperature range of -50 °C to 250 °C. The CCL-1037 has a higher resin content of 27 % than CCL - 1078 (23%). Therefore, CCL-1078 has a lower CTE in the initial temperature range (-50 °C – 150 °C). Also, a lower CTE value was measured for PP1-1037 compared with other materials. The PP2-7628 and PP3-1037 showed a higher CTE value in the initial temperature ramp. On close observation, the CTE values decrease due to  $T_g$  for both materials. The CTE values for PP3-1037 is higher than other prepreg materials. Therefore, PP3-1037 is a poor material choice as a substrate in microelectronic packages. The maximum difference of 20 % in all the materials emphasize the importance of the material choice.

Fig. 4 illustrates a wide range of thermal conductivity  $\lambda(T)$  values for the considered prepreg materials. The  $\lambda(T)$  values measure the ability of the material to conduct heat. The CCL-1037 and CCL-1078 show a similar trend for the measured temperature range.

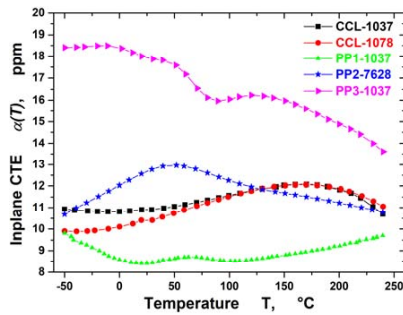


Fig. 3. The in-plane CTE  $\alpha(T)$  measured for different prepreps as a function of temperature.

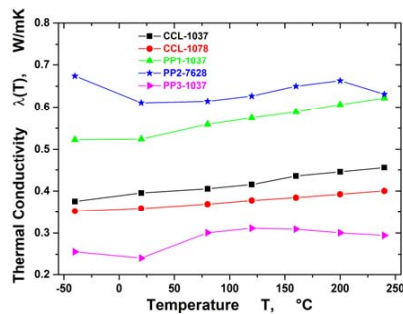


Fig. 4. The thermal conductivity  $\lambda(T)$  measured for different prepreps as a function of temperature.

Furthermore, both PP1-1037 and PP2-7628 depict a higher  $\lambda(T)$ . Heat transfer through these prepreg materials occurs at a higher rate compared with other prepreps. Additionally, PP3-1037 shows relatively lower  $\lambda(T)$ ; this is mainly attributed to this prepreps' substandard matrix material.

The gravimetric humidity conditioning results for prepreps show a temperature and humidity dependent moisture uptake trend for the considered prepreps. Fig. 5 represents the typical moisture uptake curve for the prepreps conditioned at 85 °C and 85 % RH. A maximum moisture uptake of nearly 0.8 % was observed in PP3-1037 material, and a minimum of 0.5 % was found in CCL-1078.

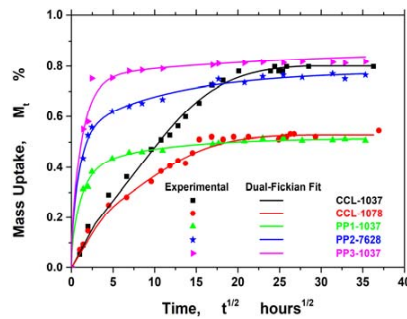


Fig. 5. Typical moisture gain trend and curve fit using an analytical solution (dual Fickian diffusion model) for prepreps at 85 °C and 85 % RH [13].

Figs. 6, 7 and 8 depict the typical moisture gain trend obtained by immersing the prepreps in a distilled water bath and conditioning them at 90 °C, 60 °C and 23 °C. The PP3-1037 material absorbed the maximum moisture (1.3 %) compared with other prepreg materials at all conditioning temperatures. This prepreg is made up of substandard matrix material, which tends to absorb more moisture during the humidity conditioning.

Alternatively, a minimum of 0.6 % of moisture absorption was noticed in CCL-1078 material. The prepreps CCL-1037 and CCL-1078 have similar matrix material but differ in their resin content, fabric reinforcement type, and thickness. The absorption of moisture in CCL-1037 is higher than in CCL-1078. The increase in absorption in CCL-1037 is due to the presence of higher resin content than CCL-1078.

The materials PP1-1037 and PP2-7628 have a similar moisture gain trend but differ in maximum moisture absorbed. From Fig. 6 and Fig. 7, a maximum of 0.7 % and nearly 1 % was observed for PP1-1037 and PP2-7628 prepreps, respectively. Consequently, Fig. 5 - Fig. 8 depict that the dual Fickian diffusion model fits the experimental data's overall behavior.



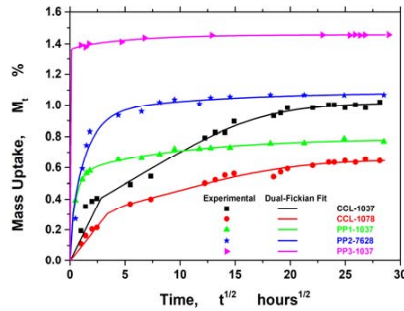


Fig. 6. Typical moisture gain trend and curve fit using an analytical solution (dual Fickian diffusion model) for preregs at 90 °C immersion [13].

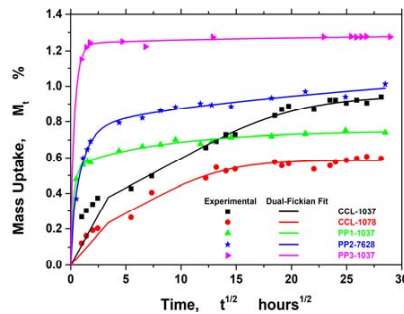


Fig. 7. Typical moisture gain trend and curve fit using an analytical solution (dual Fickian diffusion model) for preregs at 60 °C immersion [13].

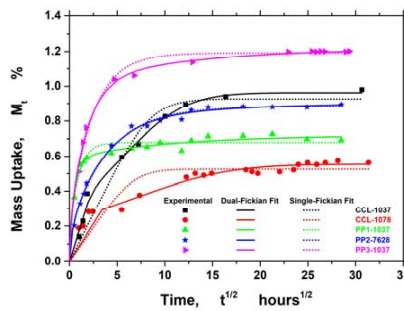


Fig. 8. Typical moisture gain trend and curve fit using an analytical solution (single and dual Fickian diffusion model) for preregs at 23 °C immersion [13].

Furthermore, in Fig. 8, the dotted lines represent the single Fickian diffusion model's nonlinear fit. The fit from the single Fickian model cannot follow the

experimental data trend in the initial region. The obtained saturated mass  $M_{sat}$  and the diffusion coefficient  $D$  obtained from dual Fickian fit were further used in "Hygro-thermo-mechanical simulations" [4, 5] and in the verification simulation model to compute the total concentration change numerically. To summarize, from the typical moisture gain trend, both the diffusion coefficient and saturated mass increase with an increase in temperature and humidity.

For the Coefficient of Moisture Expansion (CME), the change in concentration  $\Delta C$  measured using desorption or drying process is depicted in Fig. 9. It can be observed that the prepreg PP3-1037 and PP2-7628 show the highest concentration change of nearly 1.2 % compared with PP1-1037 (0.8 %), CCL-1078 (0.6 %) and CCL-1037 (1 %).

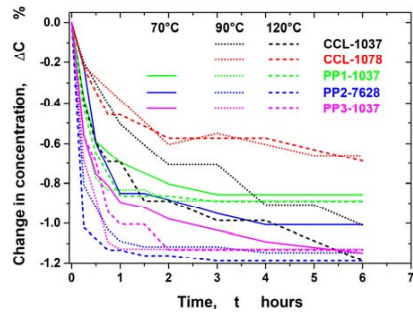


Fig. 9. Change in moisture concentration  $\Delta C$  for preregs from the desorption process at 70 °C, 90 °C and 120 °C for six hours [13].

The moisture desorption concentration trend is in good agreement with the moisture absorption trend (Fig. 5 - Fig. 8) during the gravimetric humidity conditioning.

The desorption measurements were also carried out at 140 °C and 160 °C for six hours.

The measured hygroscopic swelling strains  $\epsilon^{\beta}$  for the preregs are depicted in Fig. 10. The swelling strains are very low for all the preregs considered. However, significant shrinkage of 0.12 % was observed for prepreg PP2-7628 at 70 °C. Moreover, the CCL-1037 and CCL-1078 did not show any hygroscopic swelling strains at all conditioning temperatures. Henceforth, the desorption and hygroscopic swelling measurements were not performed at 70 °C. The prepreg PP2-7628 and PP3-1037 follow a similar temperature trend, i.e., the swelling strains decrease with an increase in temperature. Conversely, PP1-1037 shows the opposite trend. This effect is mainly caused by the different glass transition temperature ( $T_g$ ) regions for the preregs. The preregs PP1-1037, PP2-7628 and PP3-1037 have a  $T_g$  of 270 °C, 170 °C and 150 °C, respectively.

While the considered conditioning temperatures to measure CME is below the  $T_g$  level for PP1-1037, they are within the onset of the transition region for PP2-7628 and PP3-1037. Therefore, a different temperature dependence trend can be observed for these materials [8].

The computed CME ( $\beta$ ) at different temperatures for the prepregs is depicted in Fig. 11. As the prepregs CCL-1037 and CCL-1078 did not show any swelling strains, no CME is presented for these materials in the figure. The figure also depicts the decrease in CME's value with an increase in temperature for PP2-7628 and PP3-1037. The decrease is mainly in the glass transition region for both the prepregs.

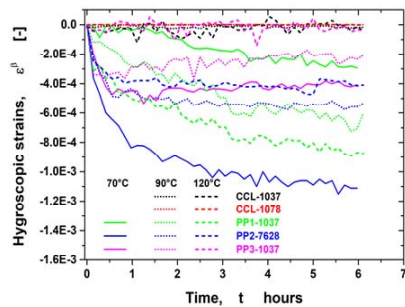


Fig. 10. The measured CME at different temperatures for the prepregs [13].

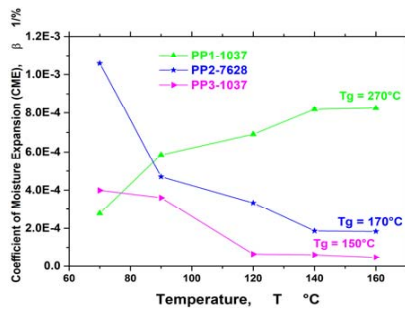


Fig. 11. The measured CME at different temperatures for the prepregs [13].

The results obtained from humidity-controlled tensile tests for the considered prepregs are presented exemplarily. They are compared against the results from thermo-mechanical DMA, the temperature-controlled tensile test results. (See Figs. 12-16). The solid lines in Fig. 12 - Fig. 16 represent the DMA curve measured at 1 Hz, the square symbols represent Young's moduli measured using a temperature oven, and the dot symbols and the star symbols represent

Young's moduli measured using a climate chamber with a controlled humidity level of 50 % RH and 85 % RH respectively.

Overall, Young's moduli  $E$  obtained from temperature-controlled tensile tests are in good agreement with DMA results at increased temperatures for the prepregs considered for both Warp ( $0^\circ$ ) and  $45^\circ$  test specimens. Discrepancies at room temperature for CCL-1037, CCL-1078, PP2-7628 and PP3-1037 can be attributed to possible unstable humidity conditions when not using the climate chamber.

To quantify relative humidity effects, the prepregs were tested at 50 % RH and 85 % RH conditions at temperature levels of 23 °C, 60 °C and 85 °C. A decrease in Young's moduli  $E$  for all the prepregs was observed at 50 % RH and 85 % RH, respectively, at all considered temperature levels.

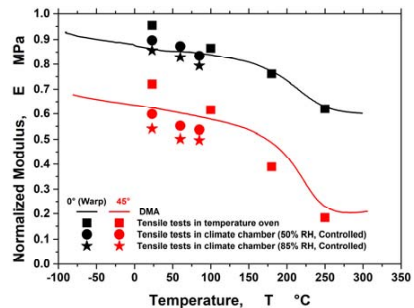


Fig. 12. Comparison of controlled humidity tensile tests with DMA and tensile tests in temperature oven for CCL-1037 prepreg (normalized to maximum modulus) [13].

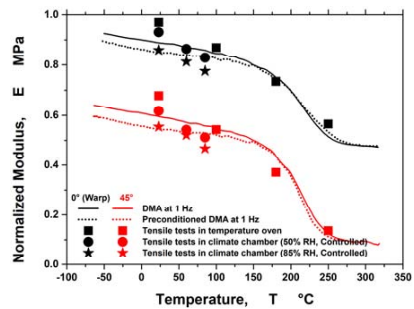


Fig. 13. Comparison of controlled humidity tensile tests with DMA and tensile tests in temperature oven for CCL-1078 prepreg (normalized to maximum modulus) [13].

This decrease is mainly attributed due to the presence of moisture in the prepregs during the humidity conditioning. The Young's modulus  $E$  value

for 85 % RH is relatively smaller than  $E$  at 50 % RH. The lower value of  $E$  is mainly due to the presence of higher moisture content at 85 % RH than at 50 % RH at the same temperature. This hydration difference explains the difference as excess moisture lowers the mechanical strength and stiffness of the prepregs. An increased humidity level leads to a reduced stiffness.

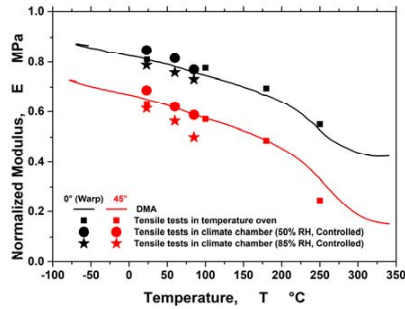


Fig. 14. Comparison of controlled humidity tensile tests with DMA and tensile tests in temperature oven for PP1-1037 prepreg (normalized to maximum modulus) [13].

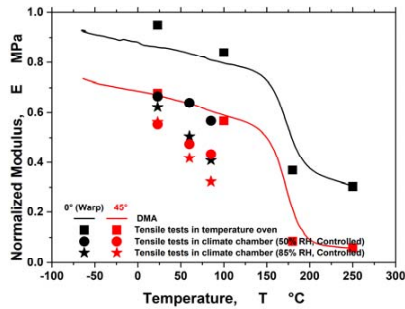


Fig. 15. Comparison of controlled humidity tensile tests with DMA and tensile tests in temperature oven for PP2-7628 prepreg (normalized to maximum modulus) [13].

The Young's Modulus  $E$  obtained by performing DMA of the pre-conditioned material (CCL-1078) is shown in Fig. 13 with black ( $0^\circ$ ) and red ( $45^\circ$ ) dotted lines. CCL-1078 absorbs nearly 0.6 % of moisture during the pre-conditioning using gravimetric humidity conditioning. A deviation in the Young's moduli values of 1 % in the temperature range of  $-80^\circ\text{C} - 150^\circ\text{C}$  was observed for both  $0^\circ$  and  $45^\circ$  directions test specimen. Furthermore, the increase in temperature from  $150^\circ\text{C}$  desorbs moisture in the specimen. Therefore, the modulus  $E$  above  $150^\circ\text{C}$  follows the DMA trend at 1 Hz without any pre-conditioning. Additionally, Young's moduli measured

by DMA are in close agreement with those from humidity-controlled tensile tests.

The prepreg PP2-7628 is most commonly used in MEMS and PCB manufacturing. This prepreg has a higher resin content compared with other prepreg materials. Therefore, this material absorbs more moisture and affects the material's strength by lowering Young's moduli  $E$  (see Fig. 15 for  $0^\circ$  (Warp)) compared with DMA and temperature-controlled tensile results tests.

Fig. 16 shows the tensile test results obtained for PP3-1037. The temperature-controlled tensile tests were only performed at room temperature of  $23^\circ\text{C}$ . Therefore, the results from humidity dependent tensile tests are compared with  $E$  values at  $23^\circ\text{C}$  and with DMA along  $0^\circ$  (Warp) and  $45^\circ$  test specimens.

The results from the verification simulation have been depicted in Fig. 17.

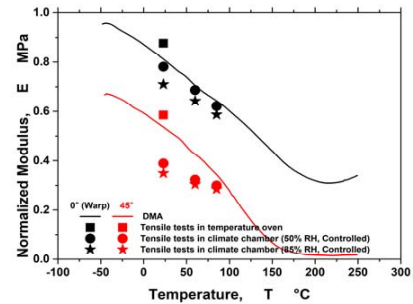


Fig. 16. Comparison of controlled humidity tensile tests with DMA and tensile tests in temperature oven for PP3-1037 prepreg (normalized to maximum modulus) [13].

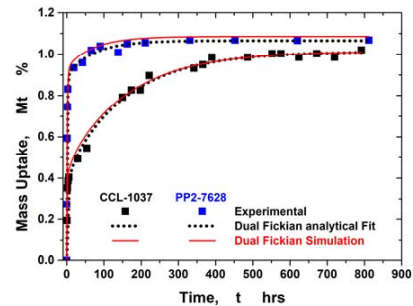


Fig. 17. Comparison of moisture absorption curve between experimental, analytical, and numerical simulation using humidity conditioning simulation for CCL-1037 and PP2-7628 [13].

The verification simulation was performed at the specimen level for the prepregs immersed in a distilled water bath and conditioned at  $90^\circ\text{C}$ . The solid red

lines represent the result obtained from a verification simulation; the black dotted lines represent the curve from the analytical fit, and the black and blue squared symbols represent the experimental humidity conditioning curves for CCL-1037 and PP2-7628, respectively. The verification simulation using the dual Fickian diffusion model agrees with both experimental and analytical fit curves' overall behavior. Therefore, this verification simulation model serves as a basis to the hygro-thermo-mechanical modeling [4, 5] approach. The verification simulation was also performed for all the five prepregs considered in this contribution. Overall, the simulation results agree with the experimental data and the analytical fit parameters for all the prepregs.

## 5. Conclusions

In this research work, the results from thermo-mechanical and hygroscopic material characterization for five different prepreg materials are presented. The thermal material properties like in-plane CTE  $\alpha(T)$  and thermal conductivity  $\lambda(T)$  help predict the right material choice for the substrate in microelectronic packages. Based on the experimental gravimetric conditioning for all the prepregs, a dual Fickian moisture diffusion model was defined. The measured moisture diffusion coefficient  $D$  and saturated mass  $M_{sat}$  are in good agreement with the analytical fit and verification simulation.

Furthermore, the measured in-plane CTE  $\alpha(T)$  and calculated CME values  $\beta$  serve as a material property to analyze the thermal and moisture mismatch in the MEMS sensor package in further reliability studies. The measured humidity and temperature-dependent Young's moduli provide critical information on shifts in the prepregs' mechanical properties due to moisture absorption and thermal distribution, respectively. The measured experimental data will be used in a numerical simulation to determine the moisture and temperature-induced deformation and stresses in a MEMS sensor package. Thereby the measured material behavior is the crucial basis for a reliable sensor system design.

## Acknowledgments

The research work was performed within the K-Project "PolyTherm" at the Polymer Competence Center Leoben GmbH (PCCL, Austria) within the framework of the COMET-program of the Federal Ministry for Transport, Innovation, and Technology, and the Federal Ministry for Digital and Economic Affairs with contributions by the University of Leoben, ams AG and by AT&S Austria Technology & Systemtechnik Aktiengesellschaft. Funding is provided by the Austrian Government and the State Government of Styria.

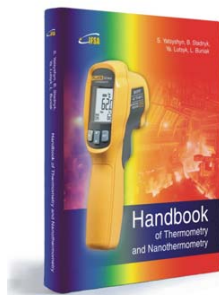
## References

- [1]. Stellrecht E., Han B., Pecht M. G., Characterization of the hygroscopic swelling behavior of mold compounds and plastic packages, *IEEE Transactions on Components and Packaging Technologies*, Vol. 27, Issue 3, 2004, pp. 499-506.
- [2]. Kim H., *et al.*, Investigation of moisture-induced delamination failure in a semiconductor package via multi-scale mechanics, *Journal of Physics D: Applied Physics*, Vol. 44, 2011, 034007.
- [3]. Y. He, *et al.*, In-situ Characterization of Moisture Absorption and Desorption in a Thin BT Core Substrate, in *Proceedings of the 57<sup>th</sup> Electronic Components and Technology Conference (ECTC'07)*, Reno, NV, 2007, pp. 1375-1383.
- [4]. M. Yalagach, *et al.*, Influence of environmental factors like temperature and humidity on MEMS packaging materials, in *Proceedings of the 7<sup>th</sup> Electronic System-Integration Technology Conference (ESTC)*, Dresden, 2018, pp. 1-6.
- [5]. M. Yalagach, *et al.*, Numerical Analysis of the Influence of Polymeric Materials on a MEMS Package Performance Under Humidity and Temperature Loads, in *Proceedings of the IEEE 69<sup>th</sup> Electronic Components and Technology Conference (ECTC)*, Las Vegas, NV, USA, 2019, pp. 2029-2035.
- [6]. JESD22-A120A, Test method for the measurement of moisture diffusivity and water solubility in organic materials used in electronic devices, JEDEC Standards, 2001.
- [7]. L. Masaro, X. X Zhu, Physical models of diffusion for polymer solutions, gels and solids, *Progress in Polymer Science*, Vol. 24, Issue 5, 1999, pp. 731-775.
- [8]. E. H. Wong, Y. C. Teo, T. B. Lim, Moisture diffusion, and vapor pressure modeling of IC packaging, in *Proceedings of the Electronic Components and Technology Conference*, 1998, pp. 1372-1378.
- [9]. Macdonald D. D., 1977, *The Mathematics of Diffusion*, in: *Transient Techniques in Electrochemistry*, Springer, Boston, MA. [https://doi.org/10.1007/978-1-4613-4145-1\\_3](https://doi.org/10.1007/978-1-4613-4145-1_3).
- [10]. Brewis D. M., Comyn J., Tredwell S. T., Diffusion of water in some modified phenolic adhesives, *Int. J. Adhesion and Adhesives*, Vol. 7, Issue 1, 1987, pp. 30-32.
- [11]. Fuchs P. F., Pinter G., Fellner K., Local damage simulations of printed circuit boards based on in-plane cohesive zone parameters, *Circuit World*, Vol. 39, Issue 2, 2013, pp. 60-66.
- [12]. Morak M., Marx P., Gschwandl M., Fuchs P. F., Pfost M., Wiesbrock F., Heat Dissipation in Epoxy/Amine-Based Gradient Composites with Alumina Particles: A Critical Evaluation of Thermal Conductivity Measurements, *Polymers*, Vol. 10, Issue 10, 2018, 1131.
- [13]. M. Yalagach, *et al.*, Characterization and Modeling of Prepregs Applied in MEMS Sensor Packages with a Focus on Moisture Dependence, in *Proceedings of the 3<sup>rd</sup> International Conference on Microelectronic Devices and Technologies (MicDAT' 2020)*, 22-33 October 2020, pp. 5-10.
- [14]. ISO 527-1:2019, *Plastics – Determination of tensile properties – Part 1: General principles*.

# Handbook of Thermometry and Nanothermometry



S. Yatsyshyn, B. Stadnyk, Ya. Lutsyk, L. Buniak



Hardcover: ISBN 978-84-606-7518-1  
e-Book: ISBN 978-84-606-7852-6

*The Handbook of Thermometry and Nanothermometry* presents and explains of main catchwords in the field of temperature measurements and nanomeasurements. This the first, well illustrated in full color, encyclopedia contains more than 800 articles (vocabulary entries) in thermometry and nanothermometry, and covers nearly every type of temperature measurement device and principles. At the end of book the authors provide a useful list of references for further information.

Written by experts, the book at the first place is destined for all who are not acquainted enough with specificity of temperature measurement but are interested in it and study literary sources in this realm. The authors tried to enter maximally on catchwords list the issues, which refer directly or indirectly to thermometry as well as to nanothermometry. The last one is the most modern chapter of thermometry and simultaneously of nanometrology. *The Handbook of Thermometry and Nanothermometry* is a 'must have' guide for both beginners and experienced practitioners who want to learn more about temperature measurements in various applications: engineers, students, researchers, physicists and chemists of all disciplines. In addition, this book will influence the next decade or more of road design in the nanothermometry.

Order: <http://www.sensorsportal.com/HTML/BOOKSTORE/Thermometry.htm>



**Universal Frequency-to-Digital Converter  
(UFDC-1 and UFDC-1M-16)  
in MLF (5 x 5 x 1 mm) package**

**SMALL WORLD -  
BIG FEATURES**

SWP, Inc., Toronto, Ontario, Canada,  
Tel. + 34 696067716, fax: +34 93 4011989, e-mail: [sales@sensorsportal.com](mailto:sales@sensorsportal.com)  
[http://www.sensorsportal.com/HTML/E-SHOP/PRODUCTS\\_4/UFDC\\_1.htm](http://www.sensorsportal.com/HTML/E-SHOP/PRODUCTS_4/UFDC_1.htm)



Published by International Frequency Sensor Association (IFSA) Publishing, S. L., 2021  
(<http://www.sensorsportal.com>).